Politecnico di Milano

PhD in Bioengineering

Structural and fluid dynamic assessment of stenting procedures for coronary bifurcations

Author:
Stefano Morlacchi

Supervisor:
Prof. Francesco Migliavacca

Tutor:
Prof. Gabriele Dubini

PhD Coordinator:
Prof. Maria Gabriella Signorini

April 5, 2013

It could work!
- Young Frankenstein -

Acknowledgements

I would like to express my gratitude to my supervisor prof. Francesco Migliavacca for always pushing me to obtain my best and for always being positive and inspiring. I wish also to acknowledge all the other professors and researchers working at LaBS for the shared knowledge and useful comments.

A special thank goes to prof. Pavlos Valchos who accepted me in his laboratory at Virginia Tech for his important insights on PIV and patience with my Italian scheduling. This collaboration could not be possible without the help of my american labmates, especially Jaime. Our chats on gmail have been a fundamental step for a better understanding of the PIV methods and the worldwide political problems.

For a biomedical engineer, clinical opinions are essential to correctly direct his research activities. I wish to acknowledge prof. Francesco Burzotta and prof. Julian Gunn for their help and insights on stenting procedures for coronary bifurcations.

A big thank goes to all the present and past students of LaBS working in Milan and all around the world. Thank you for all the coffees, beers, jokes and wonderful moments spent together.

Last, a special thank goes to my family and friends from university and from Villastanza for their love and support.

Stefano

Contents

Abstract

Despite their wide success and acceptance, stenting procedures are still an open problem in the clinical field, especially in complex vascular tracts such as coronary bifurcations. These regions are a very atheroprone environment because of a peculiar hemodynamic field characterized by recirculation and stagnation zones. Moreover, the anatomical complexity of bifurcated lesions and the technical difficulties during stent deployments concur in lower procedural success rates and higher risk of post-stenting clinical problems, such as sub-acute stent thrombosis and in-stent restenosis, respect to common linear lesions. Different options and interventional strategies have been proposed but, currently, an optimal solution has not been identified, yet.

In this light, the main objective of this PhD thesis is the development of both structural and fluid dynamic engineering methods able to better investigate the biomechanical effect of stenting procedures in coronary bifurcations. After describing the main modelling techniques developed by means of finite element analyses, computational fluid dynamics or digital particle image velocimetry, several case studies are presented to examine and compare the most adopted stenting procedures and the currently available stents for coronary bifurcations. Two main findings arise from the models here presented: i) the importance of new dedicated devices specific for bifurcations and ii) the worse biomechanical influence of double-stenting procedures respect to single-stenting procedures are the main findings proposed in this thesis. Particular attention is finally dedicated to the implementation of image-based patient specific models able to replicate real interventions. In summary, the results obtained show that such models may provide useful insights for both the industry to improve the commercially available devices and for the clinical world to enhance the current stenting procedures and facilitate the interventional planning.

Extended Abstract

This PhD thesis has been developed at the Laboratory of Biological Structure Mechanics (LaBS) of Politecnico di Milano within the PhD program in Bioengineering. The main topic of this work is stenting procedures for coronary bifurcations. These regions are still considered an open problem in the clinical field as a peculiar biomechanical environment occurs both before and after stent implantation leading to higher probability of cardiovascular disease and lower clinical rates. In this light, structural and fluid dynamic engineering methods have been developed in this PhD project to provide a better understanding of the stent-induced biomechanics alterations.

The development of this research project has involved the fundamental contribution from several national and international collaborations. In particular, PIV experiments developed in Chapter 5 have been carried out at the AEThER (Advanced Experimental Thermofluid Research) Lab at Virginia Tech where I spent 6 months following the expert indications from prof. Pavlos Vlachos, Jaime Schmieg, Dan Cooper and Dr. John Charonko during the development of the experimental setup and the post-processing of the data. In Chapter 6, image-based reconstructions have been carried out at the Universitat Pompeu Fabra in Barcelona by Dr. Ignacio Larrabide and Dr. Rubén Cardenes. Moreover, a biomedical engineering research cannot lack the essential opinions from the clinical side. In this sense, clinical insights provided by Prof. Francesco Burzotta from Universitá Cattolica del Sacro Cuore, Rome and by Dr. Julian Gunn from University of Sheffield helped me to give a useful direction to this research. Lastly, a major contribution has been given by the collaboration with my supervisors prof. Francesco Migliavacca and prof. Gabriele Dubini and the shared knowledge provided by the colleagues at LaBS, especially Claudio Chiastra, Sebastian Colleoni and Roberto Nichetti.

The contents developed in this thesis are presented according to the following outline.

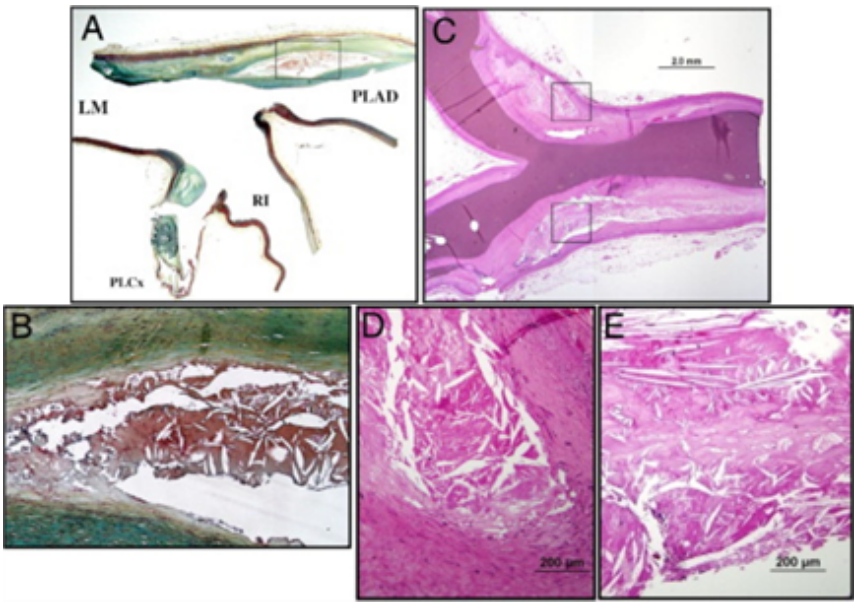

Figure 1: *Representative histological images of coronary plaque in bifurcation lesions. (A) Longitudinal section of trifurcation: LM/proximal LAD coronary artery/ramus intermedicus/proximal LCX. (B) Atherosclerotic plaques were observed in the lateral wall, whereas the flow divider regions were spared. (C) Longitudinal section obtained from the region of the left circumflec/left obtuse marginal bifurcation. Note the severe luminal narrowing proximal and distal to the bifurcation. (D, E) Low-shear regions show atherosclerotic plaque development, including necrotic core formation, whereas flow divider regions (the carina) have minimal intimal thickening. Reprinted with permission from Nakazawa et al.[157]*

Chapter 1. Coronary bifurcations: an atheroprone environment

Despite the systemic influence of several risk factors such as genetic predisposition, sedentary lifestyle, smoking, diabetes mellitus, and hypertension, atherosclerosis is manifested locally in the vasculature; regions such as coronary bifurcations have been demonstrated to be more prone to develop atherosclerotic plaques. This occurrence together with the lower clinical outcomes related to the interventional difficulties in these complex anatomies make the treatment of coronary bifurcations a remarkable open challenge for interventional cardiologists and the main topic of this thesis.

This introductory chapter is divided in five sections. First, the main anatomic features of the coronary arteries are described together with the particular hemodynamic conditions that make coronary bifurcations a very atheroprone environment. Briefly, recirculation and stagnation zones occurring in coronary bifurcations result in altered endothelial shear stress conditions in the lateral arterial walls increasing the risk of plaque formation (Fig. 1). Then, the main percutaneous coronary intervention techniques currently used for the treatment of coronary bifurcated lesions are described in the third and fourth sections, highlighting the main clinical consensus statements and their current unsolved issues. In particular, section 3 outlines the main approaches involving the use of conventional coronary devices while,

in section 4, the new dedicated stents specifically designed to be implanted in bifurcations are reviewed. Lastly, the role of biomechanics in the development of post-stenting clinical drawbacks such as in-stent restenosis or stent thrombosis are described. These clinical drawbacks and open technical challenges related to stenting procedures in coronary bifurcations continuously provide a vital stimulus to carry on the research on this topic.

Chapter 2. Numerical modelling of stenting procedures: state of the art[i]

Besides clinical investigations, in the recent years, both experimental and numerical engineering methods emerged as useful tools to investigate stenting procedures. These techniques have the potential to complement the results obtained with traditional clinical studies and provide new insights both in the development of new devices and in the optimal planning of the interventional procedures.

In particular, recently, numerical models have become a well-recognized and widely adopted tool to investigate biomechanical issues due to its advantages in terms of reduced costs, high flexibility and ability of assessing important biomechanical quantities. Especially, several research groups started to implement numerical models focusing on the cardiovascular system and its interactions with the implanted endovascular devices. At first, researchers focused on developing structural models able to investigate the mechanics of stent expansion (foreshortening, scaffolding properties, flexibility, stress fields and deformation rates) and its influence on the arterial wall during deployment. Simultaneously, the influence of stent presence on blood flow started to be investigated by means of computational fluid dynamics (CFD) models, mainly due to the importance of hemodynamic factors like wall shear stresses on in-stent restenosis, the main clinical drawback of stenting procedures. Moreover, in the drug-eluting stent era, new insights on drug elution capabilities are becoming essential in the stent development. This topic, hardly analysable with experimental campaigns, has become a wide application of numerical models as well.

Chapter 2 follows this pathway describing the current state of the art of numerical modelling of stenting procedures and highlighting their main advantages, current applications and potential future developments. Deeper attention is paid to those studies involving complex geometries such as curved vessels or coronary bifurcations that are characterized by lower clinical success rates and still represent open clinical issues. Structural, fluid dynamics and drug elution models are described separately even if most of the newest studies involve sequential implementations of these numerical models responding to the accepted evidence of the multifactorial nature of this topic.

In the end, a section on verification and validation of numerical models in biomechanics is proposed, being this issue their current major concern and limit.

[i]The content of this chapter has been partially published in:
- Morlacchi S and Migliavacca F. *Modelling stented coronary arteries: where we are, where to go.* Annals of Biomedical Engineering. 2012. In press.

Chapter 3. A sequential numerical model of stenting procedures in coronary arteries[ii]

In the recent literature, numerical models have been recognized as a widely used and adopted tool to investigate stenting procedures but always from either a purely structural or fluid dynamic point of view. As a consequence, the main scope of this thesis is the implementation of a sequential structural and fluid dynamic numerical model (Fig. 2) to provide a better understanding of the biomechanical influence of stenting procedures in coronary arteries, mainly focusing on complex regions such as coronary bifurcated arteries. This sequential model is thoroughly described in Chapter 3 highlighting the main modelling choices and potential results. It is divided into two main parts: (1) the implementation of structural finite element models of the analysed stenting procedures and (2) the execution of transient CFD simulations with particular attention to the construction of the fluid domain based on the structural finite element results.

- Structural model

The commercial finite element code developed by ABAQUS (Dassault Systemes Simulia Corp., RI, USA) is used to simulate the stent deployment in a atherosclerotic coronary arteries. Three main components (artery, angioplasty balloon and stent) are involved in the modelling of stenting procedures. First, idealized coronary bifurcations are created with a CAD software while their mechanical behaviour is described by means of an hyperelastic reduced polynomial strain energy density function, differentiating the three layers of the arterial wall. Atherosclerotic plaques are then included and describe with hyperelastic-plastic material models. Angioplasty balloons are created in the expanded configuration and then deflated by applying an internal negative pressure, thus obtaining a multi-folded configuration. Elastic material model and membrane elements are used to define the balloon model. Stent models are created to resemble commercial devices and their mechanical behaviour is described with en elastic plastic model mimicking the material properties of a medical Co-Cr alloy. Before final simulations of stenting procedures, preliminary simulations of stent crimping and advancement are implemented to correctly position the devices.

- Fluid dynamic model

The fluid volume of the CFD analyses is based on the geometrical configurations obtained by means of the structural simulations. In this way, the volume takes into account the different mechanical behaviours of the artery and the stent and the interactions of the different parts during the stenting procedure, considering interesting phenomena like tissue prolapse or strut malappositions. CFD analyses are implemented within ANSYS commercial

[ii]The content of this chapter has been partially published in:
- Morlacchi S, Chiastra C, Gastaldi D, Pennati G, Dubini G, Petrini L, Migliavacca F. *Sequential structural and fluid dynamic numerical simulations of a stented bifurcated coronary artery.* Journal of Biomechanical Engineering. 2011;133(12):121010.
- Gastaldi D, Morlacchi S, Nichetti R, Capelli C, Dubini G, Migliavacca F. *Modelling of the provisional side-branch stenting approach for the treatment of atherosclerotic coronary bifurcations: effects of stent positioning.* Biomechanics and modelling in mechanobiology. 2010;9(5):551-561.
- Chiastra C, Morlacchi S, Pereira S, Dubini G, Migliavacca F. *Computational fluid dynamics of stented coronary bifurcations studied with a hybrid discretization method.* European Journal of Mechanics, B/Fluids. 2010. 35:76-84.

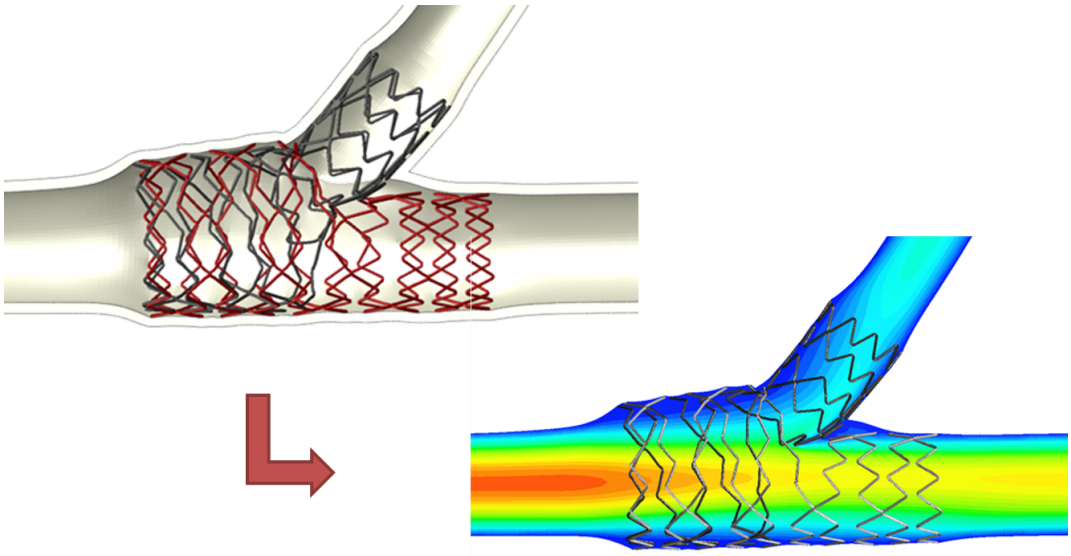

Figure 2: *Example of sequential structural and fluid dynamic numerical model implemented to investigate a double stenting procedure for coronary bifurcations.*

code (Ansys Inc., Canonsburg, PA, USA) using the ICEM CFD package to create a computationally efficient hybrid discretization and the Fluent package to solve the models. Both transient and steady simulations are carried out, describing blood as a non-Newtonian fluid and paying attention to the implementation of realistic boundary conditions.

For sake of clarity, a stenting expansion in a simplified curved atherosclerotic coronary artery with no branches is taken as an example in Chapter 3 while the case studies involving coronary bifurcations are thoroughly discussed in Chapter 4.

Chapter 4. Stenting procedures for coronary bifurcations: three case studies[iii]

The main reasons to more deeply investigate stenting procedures for coronary bifurcations are widely discussed in Chapter 1. Despite a wide consensus on some topics related to coronary bifurcations has been reached, several issues are still under debate and the optimal procedure or device suitable for all the different lesions and anatomic variations of coronary bifurcations has not been found, yet. Moreover, the new findings on the pathobiology of

[iii] The content of this chapter has been partially published in:

- Morlacchi S, Chiastra C, Gastaldi D, Pennati G, Dubini G, Migliavacca F. *Sequential structural and fluid dynamic numerical simulations of a stented bifurcated coronary artery.* Journal of Biomechanical Engineering. 2011;133(12):121010.

- Morlacchi S, Chiastra C, Cutri E, Zunino P, Burzotta F, Dubini G, and Migliavacca F. *Stent deformation, physical stress, and drug elution obtained with provisional stenting, conventional culotte and Tryton-based culotte to treat bifurcations: a virtual study* Eurointervention. In first round of review.

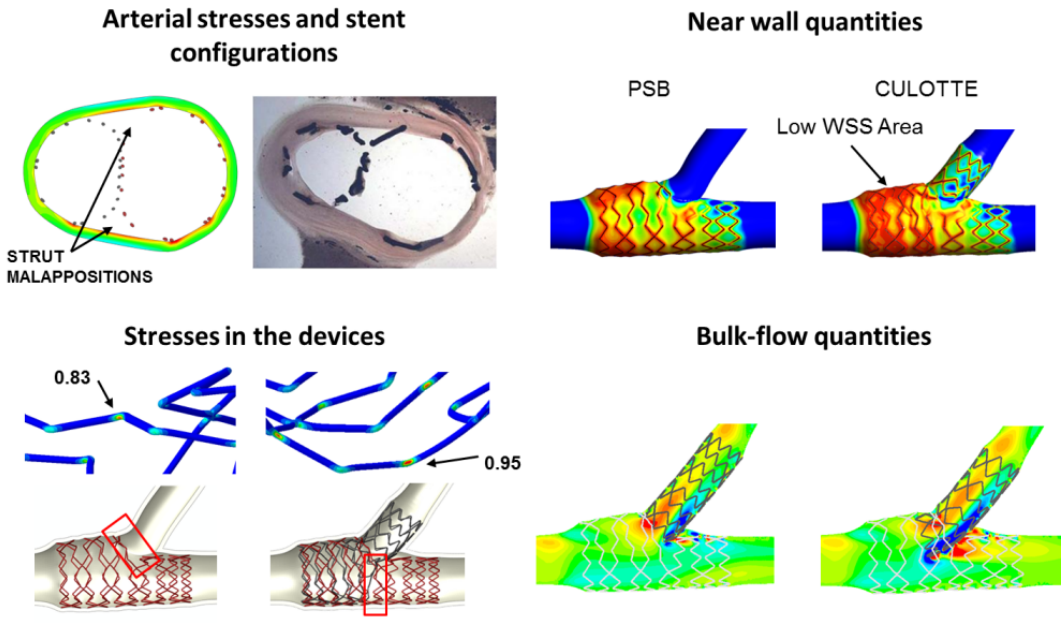

Figure 3: *Different biomechanical quantities assessed by means of the sequential numerical model.*

cardiovascular diseases or technical innovations such as the new dedicated devices may lead to an improvement of the current clinical state of the art.

As a consequence, the sequential numerical model described in Chapter 3 has been used to provide a better investigation of the biomechanical influence of different stenting procedures for coronary bifurcations. In particular, three different case studies are presented. First, a new tapered balloon is proposed to improve the Final Kissing Balloon inflation within the Provisional Side Branch approach; second, different single- or double-stenting procedure involving conventional devices are simulated and compared in terms of structural and hemodynamic quantities; lastly, a new dedicated device designed to facilitate the double-stenting culotte technique is investigated highlighting its main advantages and drawbacks.

The different case studies have been investigated through comparisons and quantitative assessments of several biomechanical quantities, concisely represented in Fig. 3. The ability of this model to simultaneously investigate both structural and fluid dynamic quantities eventually provided new interesting insights on the influence of stenting procedures and biomechanical justification to known post-stenting phenomena.

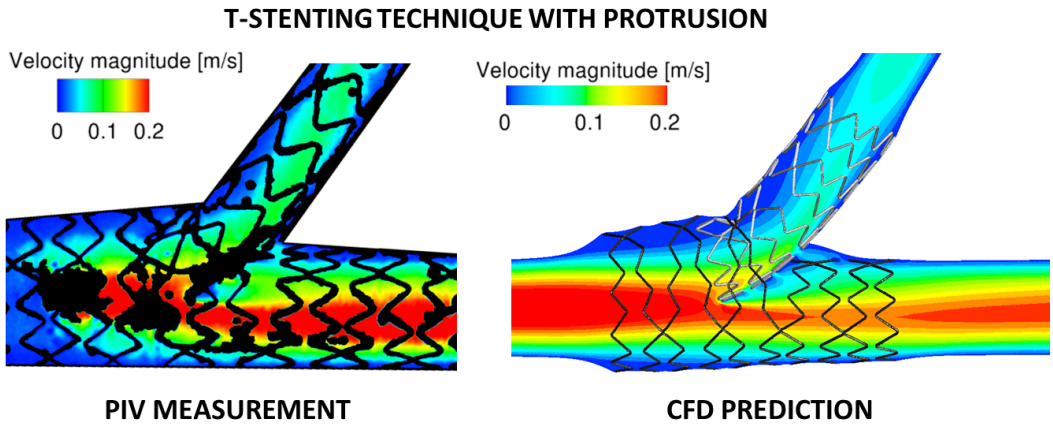

Figure 4: *Velocity magnitude fields in m/s in the transversal plane after the T-stenting technique with protrusion (T-PR). The experimental DPIV measurements are shown on the left, while the CFD results are reported on the right.*

Chapter 5. Flow patterns in stented and non-stented coronary bifurcations: an experimental and numerical study[iv]

The study presented in Chapter 5 is divided in two parts and aims to compare digital particle image velocimetry measurements and structural-based CFD predictions of blood flows in stented and non-stented coronary bifurcation models.

The experimental study involves the fabrication of silicone models of different coronary bifurcations and subsequent *in vitro* bench tests of four single- or double-stenting procedures. Subsequently, non-stented and stented bifurcations are inserted in a DPIV setup to perform flow visualization and measure the influence of stenting procedures and bifurcations angles on local blood flow patterns. In the second part, numerical replica of the experimental cases is performed by means of CFD simulations. The sequential structural and CFD model described in Chapter 3 is implemented to replicate the *in vitro* bench tests of the stenting procedures. Beside intrinsic differences and modelling assumptions of the two approaches, both CFD and DPIV analyses are able to capture the main features of the fluid flows, highlighting the influence of different bifurcation angles and stenting procedures (Fig. 4).

These findings suggest that the hemodynamic scenario before and after stenting procedures might be accurately assessed with both methods. Nonetheless, both approaches still require a challenging direct validation against *in vivo* measurements to fully demonstrate their ability to describe the existent hemodynamics of coronary flows.

[iv]The content of this chapter has been partially used for:
- Morlacchi S, Schmieg J, Migliavacca F, Vlachos P. *Local blood flow patterns in stented and non-stented coronary bifurcations.* In preparation.

Chapter 6. Patient specific simulations of real clinical cases[v]

Important limitations still prevent the current routine application of computational models in the clinical field. Among these limits, the majority of numerical studies until today is still based on highly idealized geometries and only aims at replicating standard stenting procedures. Therefore, such studies can only provide general guidelines and not patient-specific indications for the planning of each treatment. Conversely, the possibility to compare different procedural options considering the specific anatomical and mechanical properties of each patient before its treatment might help the improvement of the interventional planning and clinical outcome. Recent developments in coronary imaging have paved the way to new methods that are able to create realistic image-based reconstructions of vascular districts, potentially useful for patient-specific simulations of stenting procedures.

As a consequence, in this chapter, a review of the most important methods to create image-based coronary models is firstly presented, highlighting the most recent applications to image-based models of stenting procedure. Secondly, a feasibility study where two real clinical cases are simulated by means of finite element models is presented. Attention is focused on the open problems of coronary bifurcations and its main treatment, the PSB approach. Image-based reconstructions are created by the Universitat Pompeu Fabra in Barcelona combining the information from conventional coronary angiography and computed tomography angiography while structural finite element models are implemented by means of the ABAQUS commercial code following the main modelling techniques presented in Chapter 3 (Fig. 5). In both simulations, the straightening of the arterial wall due to stent implantation is in agreement with previous experimental studies and with the image-based post-stenting configurations of the second case studied, reconstructed after the 6 months follow-up. Also, the presence of overlapping stents proved to be a critical occurrence from a biomechanical point of view because of higher mechanical stresses both in the device and the arterial wall and a higher metal-to-artery ratio due to the double metallic layer. These findings seem to be in agreement with past *in vivo* studies that recognized overlapping stents as an independent factor of coronary stent fractures and delayed healing.

In summary, this work proved the feasibility of patient-specific numerical models that uses image-based reconstructions of coronary bifurcations and is able to replicate real cases of stenting procedures. This step may be considered a step forward towards the routine application of such models in the clinical field that, however, is still limited by some restrictions such as the computational cost and complex preparation of the models itself.

Chapter 7. Final remarks

The main hypothesis of this thesis is that biomechanics plays a major role both in the formation of atherosclerotic diseases in coronary bifurcations and the development of post-stenting drawbacks such as in-stent restenosis and stent thrombosis. As a consequence, a sequential structural and fluid dynamic model is implemented to better investigate clinically interesting issues related to stenting procedures for coronary bifurcations. The results ob-

[v]The content of this chapter has been partially published in:
- Morlacchi S, Colleoni SG, Cardenes R, Chiastra C, Diez JL, Larrabide I, and Migliavacca F. *Patient-specific simulations of stenting procedures in coronary bifurcations:two clinical cases.* Medical Engineering and Physics. In second round of review.

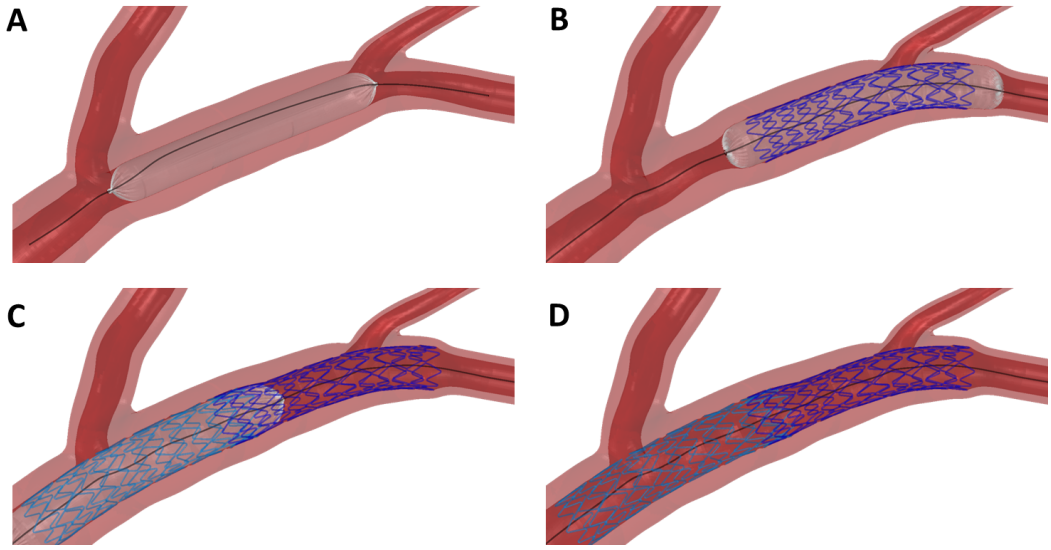

Figure 5: *Image-based finite element simulation of a real clinical case. Steps of the final numerical simulation: A) Angioplasty procedure with a 2.5 mm balloon expanded at 13atm; B) Expansion of an Endeavor stent across the distal bifurcation with a 2.75 mm balloon inflated at 12 atm; C) Deployment of a second Endeavor stent across the proximal bifurcation with a 3.0 mm balloon at 14 atm; D) Final geometrical configuration at the end of the stenting procedure.*

tained prove that such models provide useful insights for both the industry to optimize the commercially available devices (including the new dedicated stents) and for the clinical world to better understand the different outcome of both single- and double-stenting procedures. Moreover, a feasibility study of image-based numerical models demonstrates their ability to replicate real cases of stenting procedures.

Further developments of this research activity should be directed to better investigate the new remarkable frontiers of cardiovascular interventions, such as degradable stents and arising clinical issues, such as coronary stent fracture due to fatigue failure. Efforts should be directed to overcome the major limits (the computational cost and complex preparation of the models) that currently restrict the routine use of such models for a patient-specific interventional planning.

Chapter 1

Coronary bifurcations: an atheroprone environment

Contents

Coronary artery diseases are among the main causes of death in the developed western world. They involve the accumulation of fatty deposits known as plaques within the walls of the coronary arteries which supply the myocardium with oxygen and nutrients. As time passes, the plaques thicken and the arteries narrow (atherosclerosis), resulting in a reduction of the blood flow perfusing the downstream tissues. If untreated, a complete obstruction of coronary arteries leads to the interruption of blood supply to a portion of the heart, causing heart cells to die and a myocardial infarction.

Despite the systemic influence of several risk factors such as genetic predisposition, sedentary lifestyle, smoking, diabetes mellitus, and hypertension, atherosclerosis is manifested locally in the vasculature; regions such as coronary bifurcations have been demonstrated to be more prone to develop atherosclerotic plaques. Clinical evidence proves that almost 20% of all coronary interventions involves a bifurcation [114]. This occurrence together with the lower clinical outcomes related to the interventional difficulties in these complex anatomies make the treatment of coronary bifurcations a remarkable open challenge for interventional cardiologists and the main topic of this thesis.

In this introductory chapter divided in 5 sections, the main anatomic features of coronary arteries will be firstly described together with the particular hemodynamic conditions that make coronary bifurcations a very atheroprone environment. Subsequently, the main percutaneous coronary intervention techniques currently used for the treatment of coronary bifurcated lesions will be described in the third and fourth sections. Lastly, the role of biomechanics in the development of post-stenting clinical drawbacks such as in-stent restenosis (ISR) or stent thrombosis (ST) will be outlined.

1.1 Anatomy of healthy coronary arteries

The coronary tree originates from the root of the aorta with two separate coronary arteries: the right coronary artery (RCA) and the left coronary artery (LCA). After a relatively small initial common tract, called left main artery (LM), the LCA divides into the left anterior descending artery (LAD) and the left circumflex artery (LCX). RCA, LM, LAD and LCX are the most important coronary arteries and, if affected by atherosclerotic diseases, they necessarily need to be treated to restore an adequate blood flow to the wide myocardial regions that they supply. According to the data published by Dodge et al. [44] in 1992, the mean diameters of the proximal segments of the RCA, LM, LAD and LCX are respectively 3.0 ± 0.5, 4.4 ± 0.4, 3.6 ± 0.4 and 3.4 ± 0.5 mm. These branches course over the surface of the heart (epicardial arteries) and divide into gradually smaller branches that then progress inward to penetrate the epicardium and supply blood to the transmural myocardium (subendocardial arteries). Then, after the capillary bed, coronary vessels merge into the cardiac veins to reach the vena cava and, at last, the right atrium. A graphical representation of the main coronary arteries is shown in Fig. 1.1. During the heart beating, the strong interaction between coronary arteries and cardiac wall highly affects the biomechanical environment of coronary arteries. In particular, during contraction of the ventricular myocardium (systole), the subendocardial coronary vessels are compressed due to the high intra-ventricular pressures and blood flow stops. As a result most of the myocardial perfusion mainly occurs during heart relaxation (diastole) when the subendocardial coronary vessels are patent and

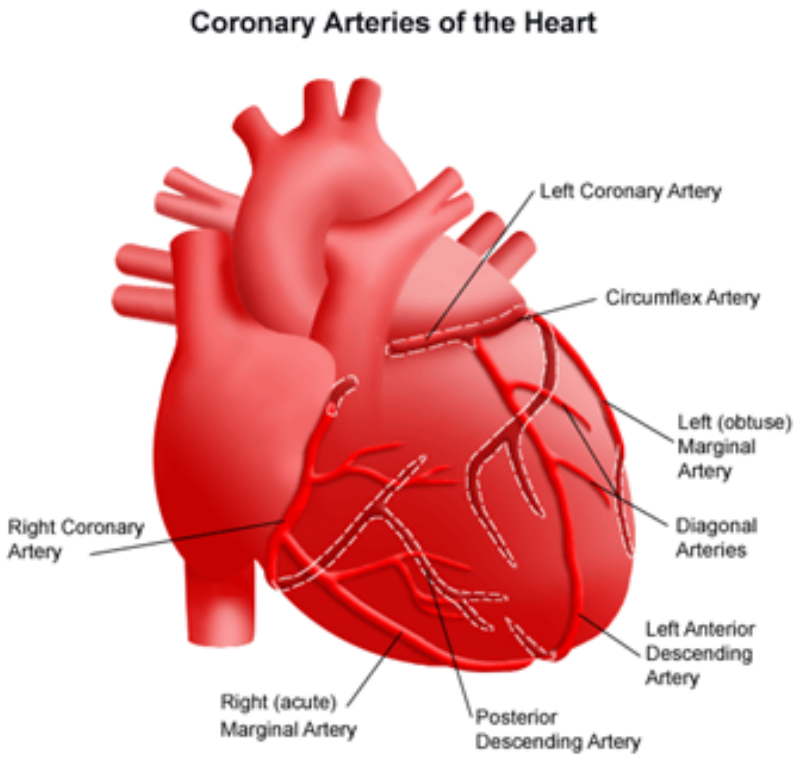

Figure 1.1: *Anatomy of the heart and major coronary vessels.*

under low pressure. As a consequence, coronary flow is also defined as a diastolic flow whose phase shift is visible in Fig. 1.2 in case of the LAD artery; other example of flow tracings for different coronary regions can be found in Davies et al. [36] Mean coronary blood flow in a healthy adult male is about 225 ml/min accounting for the 4-5% of the total cardiac output.

The coronary wall is characterized by three different layers or tunicae, called intima, media, and adventitia (Fig. 1.3). The intima is composed of an inner endothelial lining sitting on an elastic lamina. The media, the thickest layer in coronaries, is composed of spiral smooth muscle cells held together by elastic fibres and an encircling elastic lamina. The adventitia is composed of fibroelastic connective tissue aiming to protect the integrity of the vessel, with much of its elastic component contributing to the creation of the external elastic lamina surrounding the media. The thickness of the three layers varies along the coronary tree even if the media always represents the major portion of the arterial wall thickness. Due to the dissimilar tissue compositions and functional purposes, the intima, media and adventitia are characterized by highly different mechanical behaviours contributing to the complex anisotropic nonlinear mechanical response of the whole coronary wall as demonstrated by different experimental campaigns [92].

In each living being, structure and function of the organs are always strictly related.

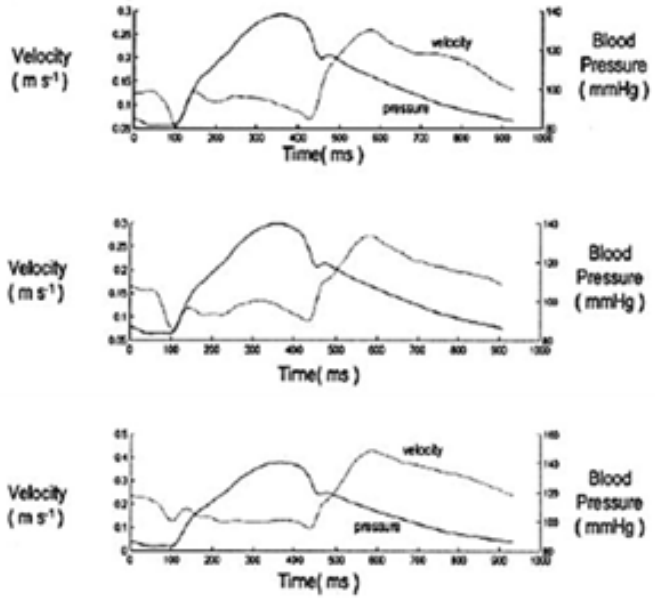

Figure 1.2: *Blood pressure and velocity tracings measured in adult human circumflex artery (upper panel), left anterior descending (middle panel), and left main artery (lower panel). Modified with permission from Davies et al. [36].*

Looking at the coronary tree, its basic structure is the coronary bifurcation that represents an elegant solution to its main function: the 3D spatial distribution of blood-flow throughout the myocardium [103]. This apparently complex structure is driven by energetic efficiency principles aiming to minimize the work necessary for blood transport. In this regard, in 1926 Murray proposed a cost function (applicable to the whole vascular tree) that is the sum of friction power loss and metabolic power dissipation proportional to blood flow [155]. The main result of this minimum energy hypothesis is Murray's law which states that the sum of the cubes of the daughter vessels (D_{d1} and D_{d2}) is equal to the cube of the mother (D_m) vessel as: $D_m^3 = D_{d1}^3 + D_{d2}^3$. More recently, another research group [203] proposed a new empirical model that was based on flow measurements performed by Doriot et al. [45] in angiographically normal coronary arteries. The fit based on these measurements showed that the flow ratio through the daughter branches can best be described with a power of 2.27.

1.2 Hemodynamics stimulates atherosclerosis in coronary bifurcations

Since systemic factors of atherosclerosis are essentially identical along the whole arterial bed, the non-casual distribution of atherosclerosis in the proximity of branching points or curved vessels [129, 157, 215] has to be related to specific local effects. Hemodynamic forces and, in particular, low and oscillating wall shear stress (WSS) have been demonstrated to

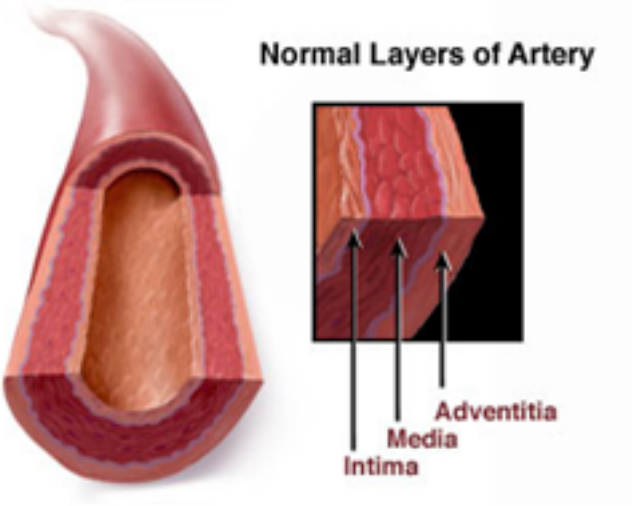

Figure 1.3: *Three-layered structure of the coronary arteries. In the magnification, intima, media and adventitial layers are showed. Source: http://www.unc.edu/*

play a fundamental role in the localization and progression of atherosclerotic plaques. Both *in vitro* and *in vivo* studies gave experimental validation to this evidence originally proposed by Caro et al. [26] in 1969. Nowadays, the endothelium is no longer considered as a passive, non-thrombogenic surface but is now regarded as an active, dynamically responsive, vascular element reactive to local hemodynamic forces. According to this theory, high physiological shear stresses maintain endothelial cells in a quiescent, atheroprotective and polygonal-shaped phenotype, while low and oscillatory shear stresses induce an atheroproliferative and rounded-shaped phenotype. In this latter circumstance, the endothelium seems to be more liable to recruit monocytes and uptake low density lipoproteins.

Hemodynamic complexity of coronary bifurcations is motivated by different factors such as wide branching angles, high curvature of the coronaries, highly pulsatile flow and the contraction and movement of the cardiac wall. This particular environment dictates the plaque distribution and progression in these regions and leads to large WSS variations, as well (Fig. 1.4). In particular, in both autopsy [157] and intravascular studies [164], it was reported that atherosclerosis in coronary bifurcations is very recurrent and mostly occurs at the outer walls of bifurcations where recirculation regions, secondary flows and flow separations occur (Fig. 1.5). Geometrical factors like greater angulation of the side branch (SB) [43] and ratio of SB dimensions [130] were associated to increased plaque formation. The typical pulsatile coronary flow characterized by very low or even reverse flow in systole and forward flow in diastole also contributes to create an extremely atheroprone environment by inducing a highly oscillatory character to WSS. High heart rate was also recognized as an independent risk factor for atherogenesis. In fact, at high heart rates, the reduction of the cardiac cycle duration occurs at the expense of the diastolic phase (high flow) respect to systole (low flow). Consequently, a higher heart rate prolongs the exposure of the endothelium to low and oscillatory WSS [68].

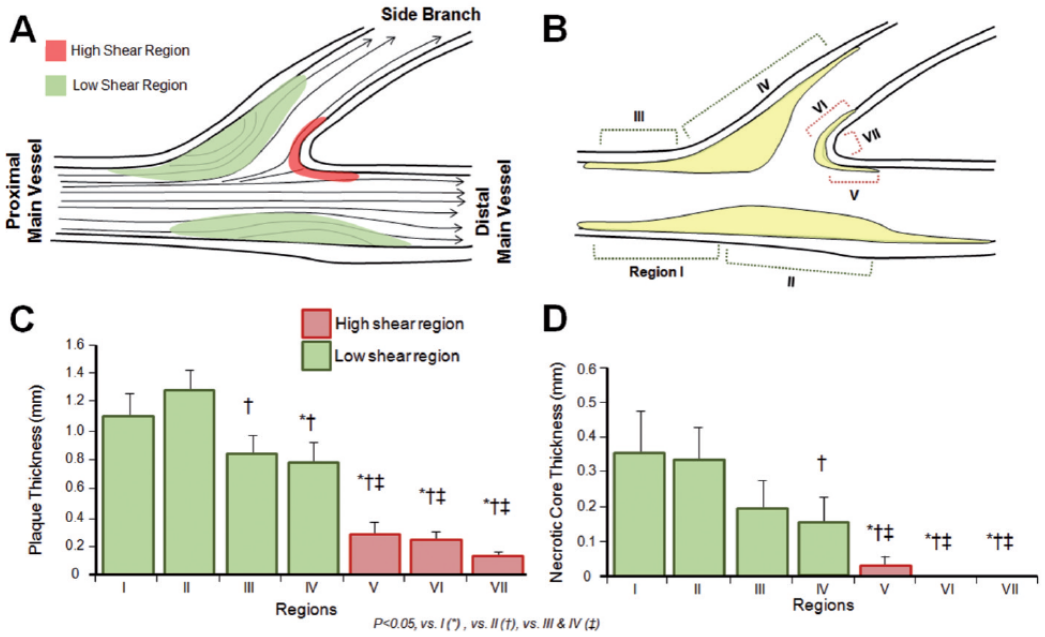

Figure 1.4: *Morphometric analysis of native coronary bifurcations. (A) Schematic diagram illustrating flow behaviour within a coronary branch with low shear regions observed in the lateral walls and high shear regions observed at the carinal region. (B) Sections of non-stented atherosclerotic lesions. (C) Plaque thickness was greater in regions of low shear as compared to high shear. (D) Similarly, necrotic core thickness was significantly greater in low shear regions as compared to high shear. Reprinted with permission from Yazdani et al. [215].*

In conclusion, both anatomical complexity and hemodynamic factors concur in making coronary bifurcations a very atheroprone environment where the outer regions of the bifurcation are a recurrent site of plaque formation. However, the great intra-individual variations and different personal predisposition lead to the development of a wide range of bifurcated lesions that were recently classified (Fig. 1.6) by Medina et al. [133] according to the position of the atherosclerotic plaques. For instance, following the Medina classification, a true bifurcation lesion affecting both the main branch (MB) (proximal and distal) and the SB is named a 111 lesion while a lesion affecting the SB only is called a 001 lesion.

1.3 Treatment of coronary bifurcation lesions with conventional stents

Stenting procedures appeared in 1986 as a novel method to treat atherosclerosis becoming a valid alternative to older methods like coronary artery bypass graft and balloon angioplasty. Main advantages offered by the use of stents are the minor invasiveness respect to coronary artery bypass and the major long- term clinical outcomes respect to balloon angioplasty.

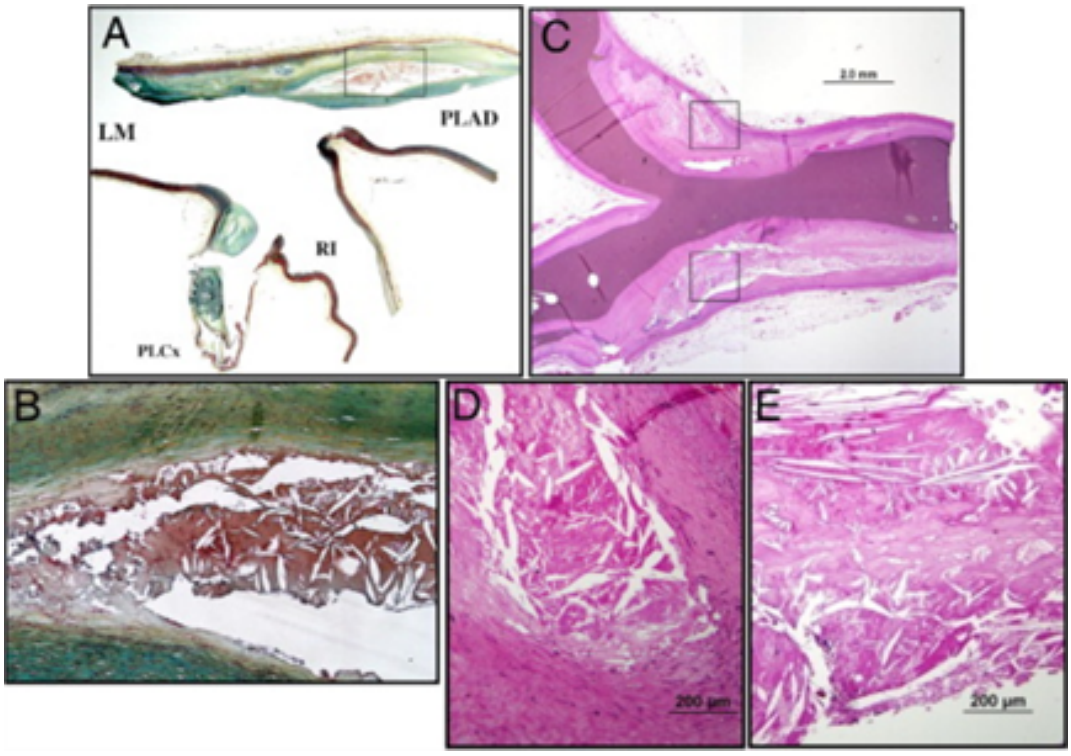

Figure 1.5: *Representative histological images of coronary plaque in bifurcation lesions. (A) Longitudinal section of trifurcation: LM/proximal LAD coronary artery/ramus intermedicus/proximal LCX. (B) Atherosclerotic plaques were observed in the lateral wall, whereas the flow divider regions were spared. (C) Longitudinal section obtained from the region of the left circumflex/left obtuse marginal bifurcation. Note the severe luminal narrowing proximal and distal to the bifurcation. (D, E) Low-shear regions show atherosclerotic plaque development, including necrotic core formation, whereas flow divider regions (the carina) have minimal intimal thickening. Reprinted with permission from Nakazawa et al. [157].*

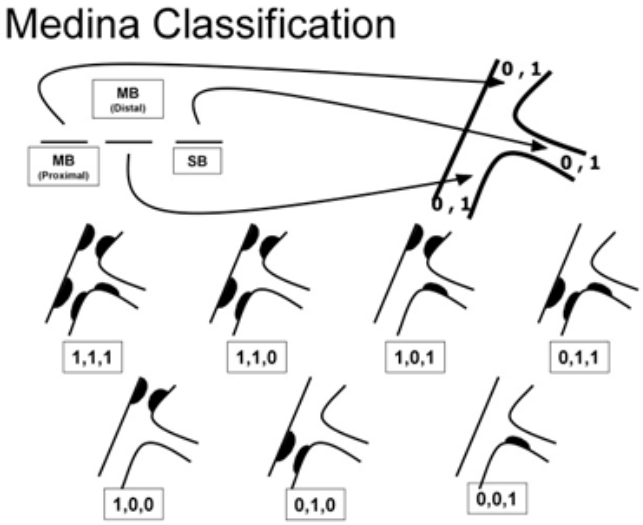

Figure 1.6: *Classification of atherosclerotic lesions in coronary bifurcations proposed by Medina et al. [133].*

Stents are metallic tubular structure that are expanded across the atherosclerotic lesion via a percutaneous access opening the narrowed artery and providing a structural support to maintain the patency of the vessels. In the 1990s, stent gradually became the most common option in interventional cardiology even if coronary artery bypass and balloon angioplasty are still considered valid options for specific cases. A key step in the development of metallic stents is the introduction into the market of the drug-eluting stents (DES) in 2002. These devices are able to elute anti-proliferative drugs in the diseased area preventing negative clinical outcomes as ISR and gradually replaced the previous generation of stents, the bare metal stents (BMS).

However, while the clinical and procedural outcomes are in most of the cases acceptable in case of linear arteries, current treatment with stenting procedures of atherosclerotic coronary bifurcations is still an open challenge for percutaneous cardiology interventionist mainly due to lower procedural success rates and a higher clinical event rates [180]. Part of the complexity of stenting coronary bifurcations relates to the wide variety of anatomies, location of the plaques and severity of the disease. Many techniques have been proposed in the literature involving one or more conventional stents. At present, the MADS classification (Main, Across, Distal, Side) is unanimously accepted within the European Bifurcation Club (EBC) and divides the techniques into four major groups depending on which arterial segment a first stent is implanted (see Fig. 1.7) [124].

The first family (M for Main) starts by implanting a stent in the proximal MB relatively close to the carina. This initial step may be followed by the opening of the stent towards both branches (SKIRT technique), with subsequent successive or simultaneous stent placement in one or both distal branches. The second family (A for Across) starts with the stenting of the MB across the SB. This may be the first and the last step of the procedure but may

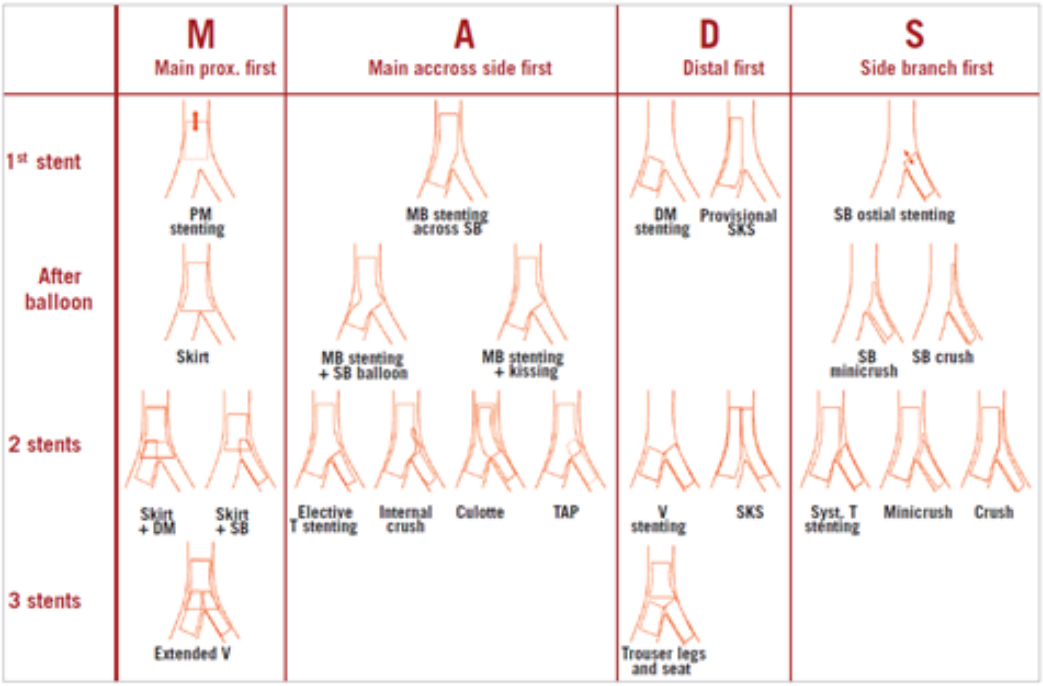

Figure 1.7: *Classification of stenting procedures for coronary bifurcations proposed by Louvard et al. [124] as a consensus statement from the 2007 EBC.*

also be followed by the opening of a stent cell with or without FKB inflation towards the SB, and if necessary by the delivery of a second stent in the SB in a T, TAP (T And small Protrusion), culotte, or Internal Crush configuration. The third family (D for Distal) involves the distal branches and historically starts with simultaneous stent placement at the ostium of both distal branches (V stenting). A recent variant consists in creating a new carina by implanting a stent in the proximal segments (Simultaneous Kissing Stent or SKS). A V stenting configuration can also be achieved by successive delivery of the stents. The fourth family (S for Side) involves strategies where the SB is stented first, either at ostium level, or with relatively pronounced protrusion into the MB. The SB stent may be crushed with a balloon inflated in the MB or a second stent may be deployed in the MB across the SB.

Each of these techniques has advantages and disadvantages and none of them perfectly fits for all the potential clinical cases. Main problems involving stenting of bifurcated lesions are potential multiple metallic layers, incomplete coverage of the SB and high interventional times that increase the amount of liquid of contrast needed for coronary imaging. Moreover, procedural errors caused by technical difficulties, especially in multiple-stents techniques, could lead to wire wrap during stent advancement, compromise of the SB during stent implantations and stent malappositions.

However, besides this complex scenario of potential clinical cases and numerous clinical options, in the recent years, consensus on some issues is reached with the emphasis that "simpler is better". In particular, the annual meetings of the EBC were able to bring together

physicist, engineers and clinician and produce final consensus statements after detailed discussion on some of the main issues of bifurcated lesions. In 2010 Hildick-Smith et al. [89] summarized the main agreements found during the 5th EBC meeting that are hereby listed:

- Provisional T-stenting (stenting of the MB and optional stenting of the SB if the clinical conditions are sub-optimal) remains the gold standard technique for most of the bifurcations.
- Large SBs with ostial disease extending >5 mm from the carina are likely to require a two-stent strategy.
- SB whose access is particularly challenging should be secured by stenting once accessed.
- When two stents are required, the culotte technique, where appropriate, offers some advantages over the crush technique.
- Current evidence suggests that an optimal two-stent technique does not predict a significantly higher rate of ST.
- Bifurcations with angulation of >60° between the daughter vessels should be approached with single stent strategies where possible.
- In single stent techniques, the primary stent should be sized according to the distal MB diameter.
- Postdilatation, or FKB inflations, are required to optimise the proximal MB stent diameter.
- Proximal optimization technique should be used in any case of difficulty recrossing into a SB with either a wire or a balloon.
- Stent balloon inflation duration of 30 seconds minimum is encouraged.
- When using a single stent technique, in the absence of FKB inflations, the proximal MB should be postdilated to an appropriate diameter.
- Final Kissing Balloon (FKB) inflations should be used when an angiographically significant (>75%) SB lesion remains after the MB stenting.
- When rewiring a SB, efforts should be made to cross the MB stent distally, thereby ensuring stent coverage of the ostium of the SB.
- FKB inflation for carina reconstruction is mandatory in two stent techniques.
- High pressure proximal stent inflation using a short non-compliant balloon should be considered for correction of possible proximal stent distortion after the FKB inflation.
- Non-compliant balloons are recommended for FKB inflations.

However, all these statements are taken according to available clinical studies that only consider the current state of the art of stenting procedures and existing commercial DES. Final consensus of this EBC meeting is that none of the existing strategies (neither provisional T-stenting or culotte technique) are likely to remain the gold standard in the long term and therefore efforts to produce dedicated bifurcation stent delivery systems should be encouraged and the research on this topic fostered.

1.4 Treatment of coronary bifurcation lesions with dedicated stents

A large variety of dedicated bifurcation stents, both BMS and DES, have been designed and investigated in clinical and pre-clinical trials. Some of them are already available on the market but none of them has become widely adopted, yet. In theory, dedicated stents should be easy to use, intuitive and simplify the procedure by shortening the procedural time and x-ray exposure and decrease the amount of contrast media. They should be safe, allow a permanent access to the second branch and have a high rate of device success. Dedicated stents should also provide an optimal long-term outcome with a lower rate of ISR and ST. Finally, the ideal dedicated stent should be able to treat all kinds of bifurcations [118]. In practice, current dedicated devices are far from being widely adopted in the clinical field. The main reason is that all current devices require multi-step approaches for stent deployment and the adaptation to various anatomies is not optimal. Position of dedicated devices is not easy since their specific design makes stent alignment delicate and a fundamental step towards procedural success. Moreover, concerns are still present about the cost-effectiveness of the development of new devices with such a limited market. Lastly, their clinical validation is a major issue due to the lack of large randomized trials comparing conventional and dedicated devices.

However, in the last years progresses have been made both in the clinical and in the medical industry resulting in a new generation of dedicated devices that apparently overcome some of the previous limitations. The currently available devices may be divided in four groups and an illustration of a device from each group is shown in Fig. 1.8:

- *Devices treating the MB with some degree of SB scaffolding.* These devices are implanted following a strategy of the Provisional Side Branch (PSB) stenting and allow an easy access to SB for a potential second device implantation. This concept of devices could be used for all the lesions except for the Medina 001 lesion (ostial branch lesion). Because of their specific asymmetric design features, most of these stents need for a precise longitudinal or a rotational alignment as for example the Twin-Rail (Invatec S.r.l., Brescia, Italy), Nile (Minvasys, Genevilliers, France), Petal (Boston Scientific, Natick, MA, USA) (Fig. 1.8a) and Abbott's SB access DES (Abbott Vascular Devices, Santa Clara, CA, USA). Thus, positioning of the stent becomes a fundamental and essential step for procedural success. Conversely, Stentys (Stentys S.A.S., Clichy, France) does not need for alignment due to its particular design. It is a linear self-expandable Nitinol stent that has to be deployed across the MB. After deployment, a SB balloon is inserted in a distal position and deployed breaking a strut connection and pushing some metal onto the external wall of the SB.

- *Proximal bifurcation stents.* The only stent of this kind is the Devax stent (Devax, Irvine, California) (Fig. 1.8b). It is a DES fabricated with Nitinol superelastic alloy. The design is ideal for Medina 100 lesions in a Y bifurcation with two similar daughter vessels. Its restricted suitability, the potential need for two or three stents in the more complex lesions and the need for a very accurate positioning are its main limitations.

- *Side branch stents.* These devices are designed to secure the SB and allow an easy deployment of a second stent in the MB. Being routinely implanted with a two stents technique,

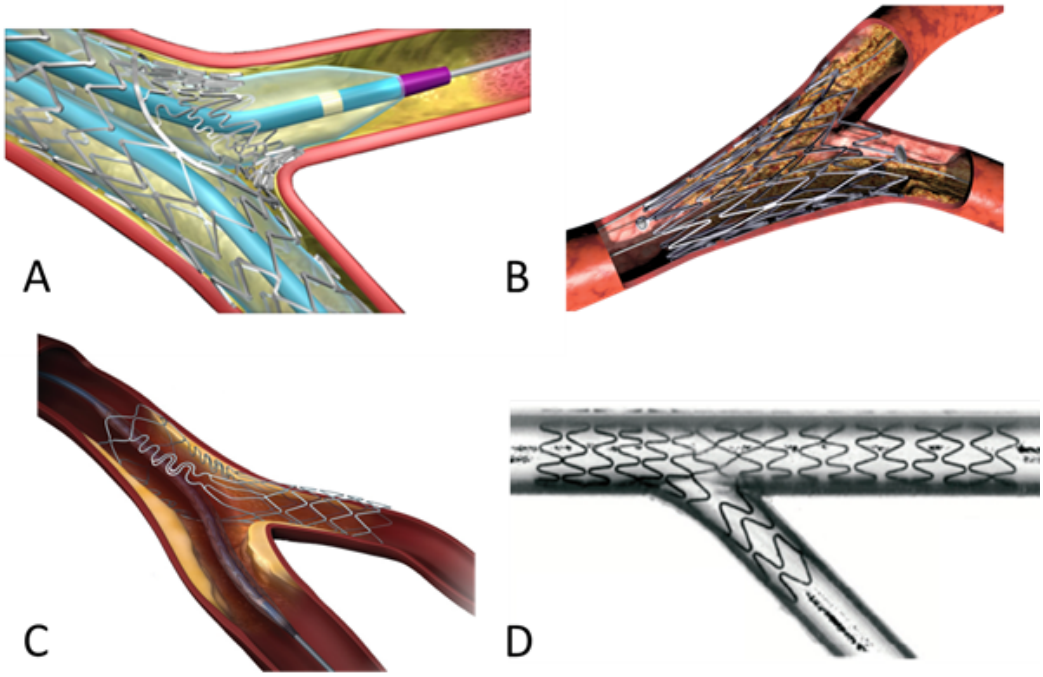

Figure 1.8: *Example of devices from the four families of dedicated stents for coronary bifurcations. A) Petal Stent from Boston Scientific used as MB stent in a provisional approach and allows an easy access to SB; B) Devax stent for proximal MB stenting; C) Tryton SB system used as SB stent in a two-stents technique and characterized by a dedicated design that allows an easy deployment of a second device and a reduced overlapping zone; D) Medtronic Bifurcation Stent System that allows the complete coverage of the whole bifurcation.*

their main limitation is their poor suitability since they should only be used with lesions involving large SB. Among these devices, the Sideguard stent (Cappella Inc, MA, USA) and the Tryton SB system (Tryton Medical, MA, USA) (Fig. 1.8c) seem to be clinically interesting. In particular, Tryton is a balloon expandable cobalt chromium (Co-Cr) BMS characterized by three different specific designs and projected to facilitate the culotte technique. Its design with few struts in the proximal part of the stent reduces the double metallic layer in the proximal part of the MB and allows an easy implantation of a second device in the MB.

- *Bifurcated stents.* This kind of device has always been the interventionalist's dream because of its potential to solve the problems encountered in the majority of the bifurcation lesions. However, since a device with two branches is less flexible than a single stent and requires to be loaded on two wires, the risk of wire wrap and misalignment is high. The new Medtronic bifurcated stent (Medtronic Inc., Minneapolis, MN, USA) (Fig. 1.8d) is under investigation even if the first results did not show optimal rates of device success and proved the existence of some problems during its deployment (difficult alignment and wire wrap) [135]. There is a potential for LM use which should be assessed as well.

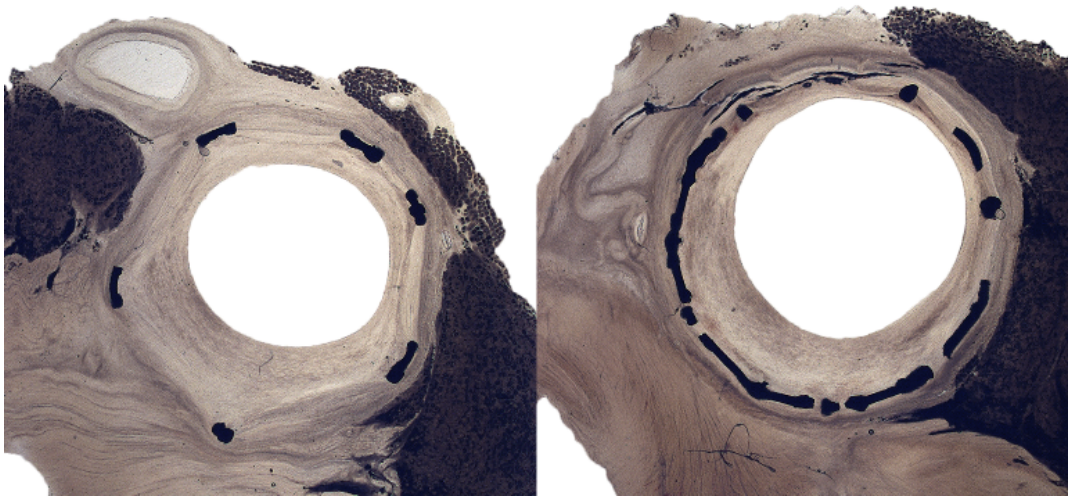

Figure 1.9: *Representative histological images of the in-stent restenosis phenomenon in a pig coronary artery consisting of the renarrowing of the vessel lumen after stent implantation mainly due to hemodynamic disturbances, arterial injury and excessive neo-intimal proliferation. Courtesy of Dr. Julian Gunn, University of Sheffield.*

1.5 Post-stenting clinical drawbacks: role of biomechanics

Despite their success and wide use in the clinical field, stenting procedures are still associated to substantial clinical problems such as ST and ISR (Fig. 1.9). ST is a blood clot formation caused by the activation of platelets that can occur a few days after stent implantation. The main causes leading to thrombosis were recognized as chemical factors like thrombogenicity of metal and mechanical factors like endothelial denudation and medial elastic lamina dissection. Greater injury provoked by stent deployment produces a greater thrombotic response [51, 61]. ISR is the reduction of lumen size as a result of proliferation and migration of vascular smooth muscle cells mostly happening within the first three weeks after stent implantation. Its mechanism and causes are still not fully understood, but three different phenomena seem to be associated with it [206]. Firstly, low WSS induced by the flow to endothelial cells seem to be predominantly significant. A series of *in vivo* and *in vitro* studies [55, 108] proved that stent implantation with strut malappositions and compliance mismatches negatively influences the hemodynamic field and results in low WSS areas, encouraging ISR. Secondly, the implantation of a stent results in the so called "overstretch injury", a persistent non physiological stress state within the arterial wall and potential injuries during stent deployment. In the end, complex interactions between the vessel wall, the blood and the metal materials of the device can generate an inflammatory response. The main outcome of ST and ISR is the re-narrowing of the coronary vessels and the necessity of a new treatment to restore blood flow and perfusion to downstream tissues. This second intervention is not always possible and straightforward due to the presence in the diseased region of the previously implanted device paving the way to complex scenarios

such as invasive coronary artery bypasses [70].

1.6 Main conclusions

In summary, biomechanical factors are critical not only in the process of plaque localization and plaque growth (see Section 1.2) but also in the main clinical drawbacks affecting stent implantation. This brief introduction shows how both hemodynamic and structural factors are associated in the post-stenting drawbacks proving the importance of simultaneously investigating both kind of influences. This occurrence is even more amplified in those regions like coronary bifurcations that are characterized by intrinsic technical difficulties during the percutaneous treatment and more frequently result in procedural complications and sub-optimal clinical outcomes [42]. As a consequence, these clinical drawbacks and open challenges related to stenting procedures in coronary bifurcations continuously provide a vital stimulus to carry on the research on this topic.

Besides clinical investigations, in the recent years, both experimental and numerical engineering methods emerged as useful tools to investigate stenting procedures. These techniques have the potential to complement the results obtained with traditional clinical studies and provide new insights both in the development of new devices and in the optimal planning of the interventional procedures. In this light, the major numerical studies on the biomechanical influence of stenting procedures in coronary bifurcations proposed in the literature will be reviewed in the following chapter.

Chapter 2

Numerical modelling of stenting procedures: state of the art

Contents

In the last two decades, numerical models have become a well-recognized and widely adopted tool to investigate biomechanical issues mainly due to its advantages in terms of reduced costs, high flexibility and ability of assessing important biomechanical quantities. In particular, several research groups started to implement numerical models focusing on the cardiovascular system and its interactions with the implanted endovascular devices. Since 2000, coronary stents have become a wide research area for numerical modelling specialists aiming to optimize their design and to understand their influence on the surrounding biological scenario.

At first, researchers focused on developing structural models able to investigate the mechanics of stent expansion (foreshortening, scaffolding properties, flexibility, stress fields and deformation rates) and its influence on the arterial wall during deployment. Simultaneously, the influence of stent presence on blood flow started to be investigated by means of computational fluid dynamics (CFD) models, mainly due to the importance of near-wall hemodynamic factors like WSS on ISR, the main clinical drawback of stenting procedures. Subsequently, in the DES era, new insights on drug elution capabilities have become essential requirements in the stent development. This topic, hardly analysable with experimental campaigns, has become a wide application of numerical models as well.

This chapter follows this pathway describing the current state of the art of numerical modelling of stenting procedures and highlighting their main advantages, current applications and potential future developments. Deeper attention is paid to those studies involving complex geometries such as curved vessels or coronary bifurcations that are characterized by lower clinical success rates and still represent open clinical issues. Structural, fluid dynamics and drug elution models are described separately even if most of the newest studies involve sequential implementations of these numerical models responding to the accepted evidence of the multifactorial nature of this topic. In the end, a section on verification and validation of numerical models in biomechanics is proposed, being this issue their current major concern and limit.

2.1 Advantages of numerical modelling in biomechanics

Modelling is the process by which a simplified mathematical reality is constructed to describe a more complex physical reality and quantitatively evaluate some of its features. In this process, analytical exact solutions of mathematical models are not always available, especially for complex *in vivo* physical realities. In this light, numerical methods (or models) are often used to overcome this limitation by providing an approximated solution of the problem. However, the goodness of this solution is not always assured and great caution must be taken during the implementation of such models.

Biomechanics and, in particular, cardiovascular mechanics are a research area where mathematical modelling and numerical methods have been widely exploited and frequently preferred respect to *in vitro* studies. The high complexity of the components of the cardiovascular system and their interactions with the endovascular devices seem to have a primary role on this choice. Nonetheless, numerical modelling provides other important advantages that are hereby listed:

- *Reduction of costs due to virtual modelling.* The creation of virtual geometrical mod-

els of the objects that compose the physical system investigated may be pursued by means of virtual prototyping methods, CAD software or image-based reconstructions from medical images. The last technique paves the way to easily setup patient-specific studies, more and more important in the virtual planning of clinical procedures. Main advantage of virtual modelling is the reduction of costs if compared to *in vitro* tests that require the physical production of the regions of interest. In computational biomechanics, this issue is particularly relevant since the objects investigated are frequently expensive medical devices or complex anatomical regions. Moreover, experimental campaigns often require expensive instruments used to setup external loadings, boundary conditions and measurements of quantities.

- *Flexibility and prediction of results.* By means of virtual modelling, it is feasible to setup the model in order to easily modify some of its parameters, including geometrical features, boundary conditions or external loadings. In this way, different cases may be fastly investigated paving the way, for instance, to the construction of response surfaces able to predict results and propose optimized solution to the given problems.

- *Ability of assessing important biomechanical quantities.* Measurement is always a critical point in experimental campaigns due to challenging calibration of the instruments and measurement errors (bias, sensor resolution, accuracy), often leading to the necessity of complex statistical treatment of the dataset. Sometimes, direct measurements of the desired quantities are not feasible and complex post-processing of the data may be required. Additionally, experimental measurements may be limited by the number of instruments available to a reduced number of points. Conversely, numerical models provide direct and continuous access to several quantities during the whole simulation of the process. For instance, structural finite element models easily provide calculation of stress fields and deformation rates in all the physical domain while CFD models provide accurate estimations of velocity fields and shear stress calculations.

Beside these advantages, confidence in numerical methods is only possible after the verification of the mathematical foundation of the model and validation of the results against experimental data. This issue is particularly complicated in computational biomechanics and is discussed in details in the last section of this chapter.

2.2 Structural models of stenting procedures

In the last 15 years, modelling of stent expansion has been tackled with different strategies not always explicitly considering the balloon and the vessel presence [24, 53, 106, 137, 138, 150, 169, 197, 199, 216]. The results obtained by the earlier studies are discussed in more details in the publication proposed by Martin and Boyle in 2011. [132] Conversely, only the main findings from recent studies involving complex geometries such as curved vessels and coronary bifurcations, or presenting the newest modelling techniques are considered here.

First of all, the majority of the recent studies where coronary stents interact with the arterial wall consider the presence of a balloon during their deployment. The construction of the balloon geometrical model and the selection of the boundary conditions and external loadings applied to the angiography balloons are key choices that need to be accurately

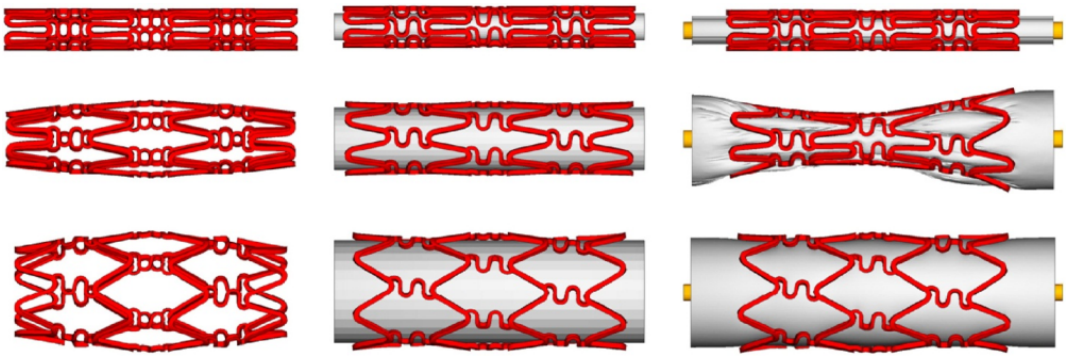

Figure 2.1: *Stent deployment patterns resulting from (left) imposition of a normal uniform pressure on the stent struts; (middle) expansion by a rigid cylinder and (right) expansion by a trifolded balloon. Views are reported prior (top), during (centre) and after (bottom) the stent expansion. Image copied with permission from De Beule et al. [37].*

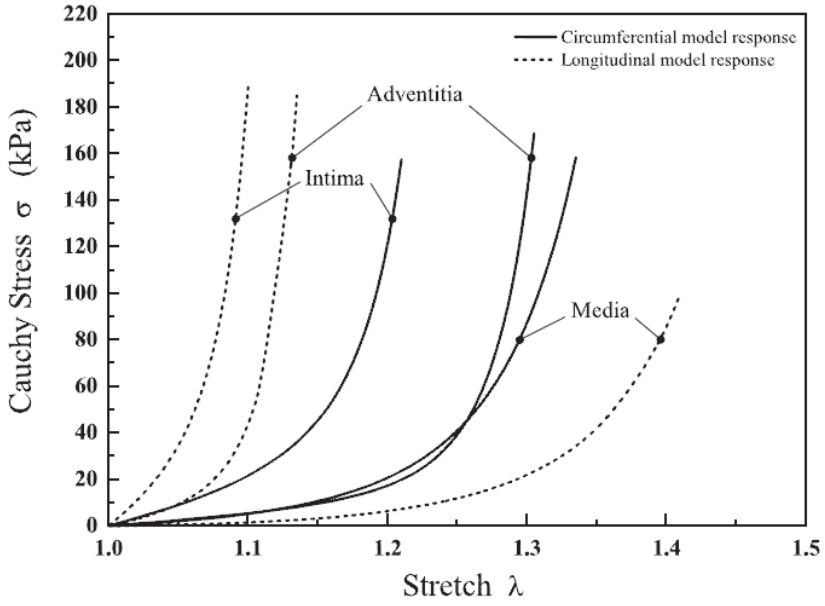

Figure 2.2: *Stress-stretch model response representing mean of all mechanical data of adventitia, intima, and media in circumferential and longitudinal directions obtained from the midportion of human LAD coronary specimens. Reproduced with permission from Holzapfel et al. [92].*

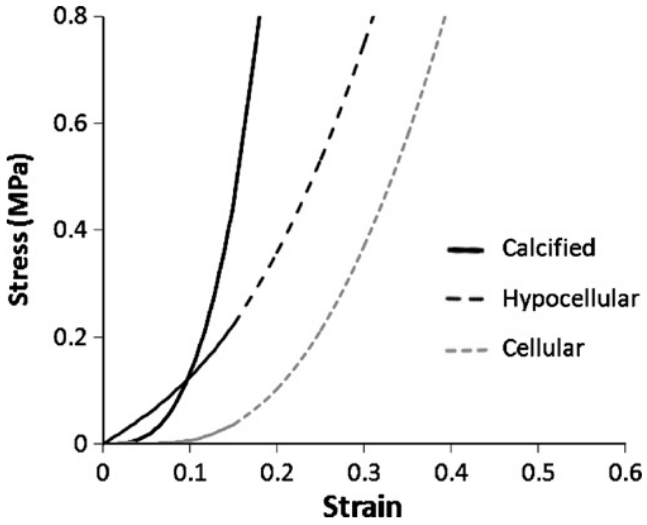

Figure 2.3: *Uniaxial tensile stress strain data represented by the strain energy density functions for the three different plaque types. The models were determined by fitting mean stress/strain curves from Loree et al. [123]. Reprinted with permission from Pericevic et al. [168].*

made when simulating the stenting deployment. The first computational works studying the effect of different modalities of stent expansion (nodal displacements, internal pressure, cylindrical surface displacement) were proposed by De Beule et al. [37] and by Gervaso et al. [67]. In 2008, De Beule et al. [37] analysed different modelling strategies of stent expansion (Fig. 2.1) using the Cypher stent. These authors concluded that deployment with a tri-folded balloon configuration showed a better qualitative and quantitative agreement with both manufacturer's data and experiments. Similar results were obtained by Gervaso and colleagues [67] adopting a multi-folded balloon and including a model for the arterial wall. Their main result was that the expansion strategy highly affected stress patterns in the arterial wall provoked by the stent insertion. Consequently, in the current state of the art, a commonly accepted finding is that a balloon model is necessary to better describe the stent-artery interaction during stent deployment. Expansions with cylindrical surfaces should only be accepted in structural models that are highly focused on the structural behaviour of a single (central) link and do not aim to investigate the whole stent-artery interaction.

Nowadays, the inclusion of the vessel wall has been recognized as central in coronary stenting modelling as well. The definition of constitutive laws for the vessel wall, including the dissimilar arterial layers, is often based on the work carried out by Holzapfel et al. [92] whose results are adopted as a standard for modelling coronary arteries. In that work, authors firstly performed an experimental investigation of the passive mechanical properties of arterial strips from each of the three layers of human LAD coronary arteries in both the axial and circumferential directions (Fig. 2.2); secondly, they implemented specific constitutive laws for the description of the mechanical response of each tissue.

Pathological coronary arteries are characterized by the presence of atherosclerotic plaques

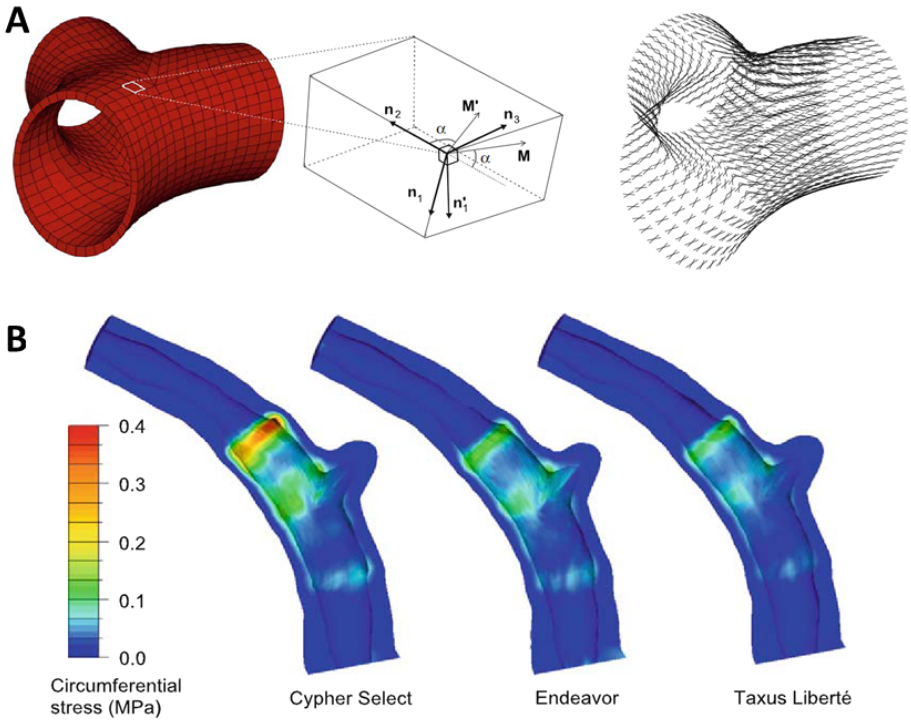

Figure 2.4: *A) Left: outermost layer of the structured hexahedral discretization in the location of the bifurcation with an enlarged view of the indicated element and its local material orientations. Right: illustration of the (local) mean fiber directions for the finite elements at the bifurcation. B) Comparison of the circumferential (Cauchy) stress distribution after implantation of the Cypher Select, the Endeavor and the Taxus Liberteť stents, with maximal stresses of 0.38, 0.15, and 0.15* MPa *from left to right. Modified with permission from Mortier et al. [149].*

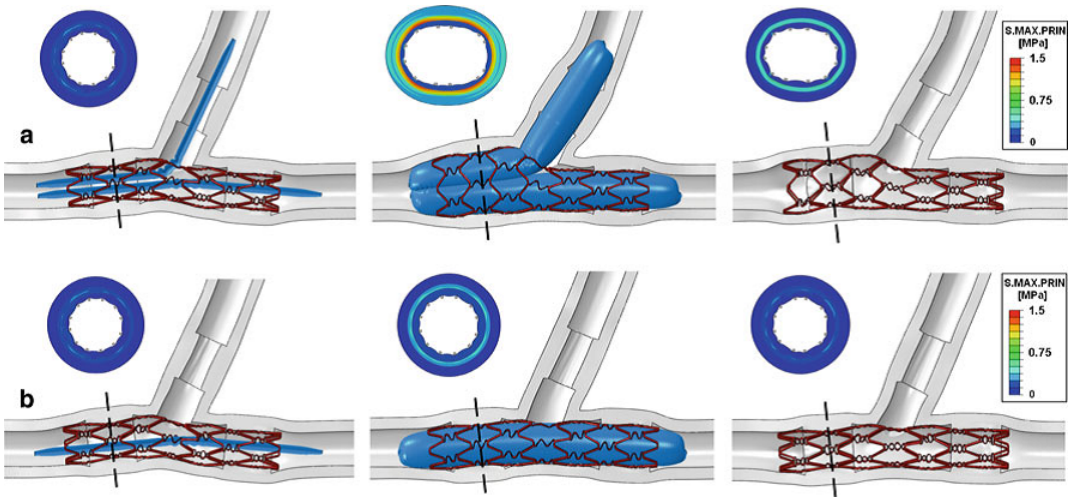

Figure 2.5: *Structural model investigating the final step strategies after the SB access: a) FKB procedure: insertion of two balloons, simultaneous expansion and elastic recoil. b) Dilatation of the MB only: insertion of one balloon in the MB, expansion and elastic recoil. Cross-sections show maximum principal stresses in the arterial wall during the different steps of the procedures. Image copied with permission from Gastaldi et al. [65].*

which could strongly influence the mechanical behaviour of the arteries and the post-stenting structural outcomes [65, 168, 217]. Indeed, the mechanical properties exhibited by plaque tissue components are highly responsible for lumen widening after stent expansion. However, only a few studies involving stenting simulations considered their presence. Commonly, the constitutive laws used to model atherosclerotic plaques are based on the experimental data presented in 1994 by Loree et al. [123], who found a large variation in the mechanical behaviour within each plaque type (cellular, hypocellular or calcified) (Fig. 2.3). Numerical studies considering the presence of plaque used isotropic hyperelastic [168, 217] or hyperelastic-plastic [65] constitutive models to describe in a simple way a mechanical behaviour that, in reality, is characterized by very complex phenomena such as rupture, plaque shift and delamination. In fact, another study from Maher et al. [128] proved the high in-specimen and inter-patient variability of the mechanical properties of fresh carotid plaque samples. This study is based on uniaxial circumferential tension and radial compression tests performed less than 2h after endarterectomy. In-specimen variability suggests that, in the future, much more localised mechanical testing should be performed while inter-patient variability underlines the importance of patient-specific modelling of biological tissues.

Recently, much attention has also been paid to complex geometries like coronary bifurcations. Indeed, stent implantation in complex geometries such as coronary bifurcations is still a challenging clinical problem, with a higher rate of procedural complications [32]. Different techniques (provisional side branch, crush technique, culotte technique, T-stenting, V-stenting, etc.) that imply the insertion of one or two devices are described in the literature [98] and new dedicated devices are emerging as potential options [118], however, an optimal procedure has not been found, yet.

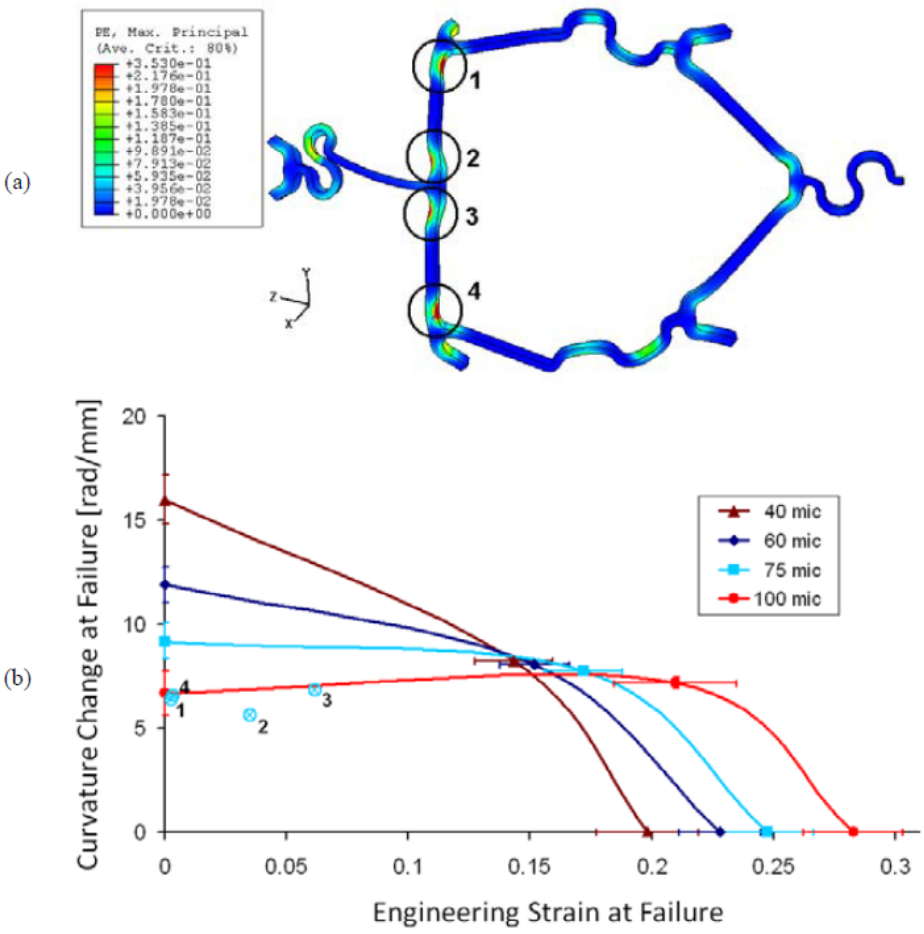

Figure 2.6: *A) Plot of max principal plastic strain in the region of the stent deformed after SB access with the deployment of a balloon angioplasty in the SB. Numbered regions correspond to the hinges at which strains are highest. B) Safe design chart for a plastic hinge from Harewood and McHugh [85] that is appropriate for the plastic hinges of interest here. The chart identifies safe and unsafe regions, on axes of curvature change vs engineering strain, for hinges of different indicated thicknesses. Points corresponding to curvature changes and strains in hinges 1-4 are included for hinges of 75* μm *thickness. Reprinted with permission from Harewood et al. [84].*

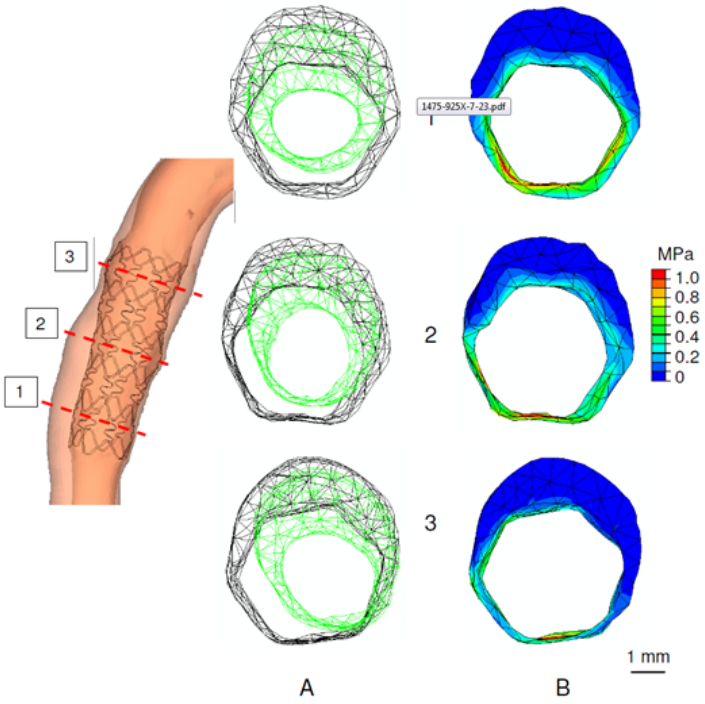

Figure 2.7: *A) Initial shape of the lumen (green) and configuration at the maximum inflation pressure of 1.0* MPa *(black) for three different axial locations (shown in the middle left side). B) Corresponding von Mises contour maps. Reprinted with permission from Gijsen et al. [69].*

In 2009 and 2010, Mortier and colleagues used finite element analyses to investigate stenting procedures in coronary bifurcations. In their studies, the authors observed the behaviour of different stent designs in terms of strut distortion at the SB access after balloon dilation [148] and compared three different stents in the curved MB of a coronary bifurcation built using rotational angiography aiming to provide better insights into the related changes of the mechanical environment [149]. Peculiarity of that work is the implementation of a new algorithm to assign fibre orientation to elements and consider the anisotropic mechanical behaviour of the three different coronary layers described by Holzapfel et al. [92] (Fig. 2.4).

In 2010, Gastaldi et al. [65] investigated the PSB approach focusing their attention on the effects of different procedural options. At first, three different accesses to the SB were simulated; then, the comparison between the FKB procedure and the dilatation of the MB only as final step of the interventional procedure (Fig. 2.5) was proposed in order to assess their influence on the arterial wall stress state. Atherosclerotic plaques were included in this model and described with a hyperelastic-plastic behaviour using a polynomial strain energy density function. In 2010, Harewood and colleagues [84] proposed a multiscale approach, incorporating the results of microscale modelling of failure in individual stent struts [85] and macroscale modelling of stent deployment in realistic arterial geometries (Fig. 2.6). In particular, authors proved how stenting procedures for coronary bifurcations such as the

PSB approach or the crush technique may provoke critical changes of curvatures and strains at some locations of the devices leading to higher risks of failure.

More recently, Morlacchi et al. [143] proposed a model to investigate the behaviour of a new tapered balloon to be used within the FKB inflation and able to reduce the critical overexpansion of the proximal part of the MB. The novelty of that work is that the final geometrical configurations obtained after the structural analyses can be used to create a realistic fluid domain to perform transient fluid dynamic analyses. In such a way, the effects on the hemodynamic field of several geometrical factors such as malapposition of stent struts, tissue prolapse or non-uniform expansion of the vessel wall may be detected.

Lastly, most of the studies make use of idealized geometries and simulate standard cases and techniques that can only provide general guidelines to improve coronary stenting treatment. The use of realistic patient-specific reconstructions might help physicians in a case-by-case surgical planning process by enabling virtual implantation and analysis of different treatments prior to the actual procedure. A feasibility study of such approach was firstly proposed by Gijsen et al. [69] (Fig. 2.7). In the future, advancements in coronary imaging may provide new opportunities to improve these models and allow the study of more complex scenarios.

2.3 Fluid dynamic models of stenting procedures

Hemodynamic factors play a fundamental role in post-operative clinical issues such as in-stent restenosis and stent thrombosis. This idea was proven in several clinical studies [108] and led to the development and use of numerical modelling techniques to better understand these aspects. Due to very high computational costs required for transient CFD simulations, most of the earliest studies were related to reduced or highly simplified anatomies (i.e. straight vessels) and stent models [154]. Recently, more complex cases have been approached.

From a modelling point of view, if within a structural analysis the geometrical configuration of the stented vessel is the final result of the simulation itself, when investigating the fluid dynamics or drug transport behaviours, the deformed configuration of the stented vessel is the starting point and, probably, the most influencing modelling assumption. Different strategies to study hemodynamics in stented arteries were proposed in the recent literature and are hereby briefly reviewed.

The first strategy is the construction of idealized stented arteries using CAD programs. This very idealized approach was adopted in the first CFD studies involving stented arteries. In the authors' opinion, this method should only be used in the cases of straight arteries with no plaques or complex geometries, where an idealized configuration can return acceptable accuracy. Deplano and colleagues [41] in 2004 investigated the effects of two deployed Palmaz stents inserted in an idealised 90° coronary bifurcation, simulating a double stent implantation. They showed how the arterial walls opposite to the bifurcation are affected by low WSS and that protrusion of SB stent struts in the MB results in flow disturbances and higher shear rates. In 2010, Murphy et al. [153] proposed an innovative numerical method to create geometries of stented arteries characterized by a tissue prolapse between stent struts that depends on the distance between the struts and on a specific coefficient of prolapse. Then, Williams et al. [211] aimed to quantify altered hemodynamics due to MB stenting

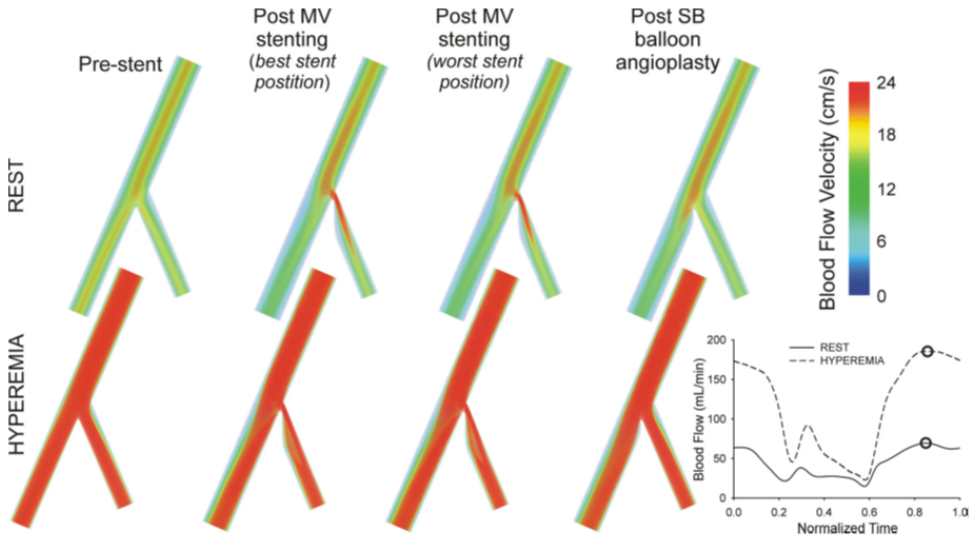

Figure 2.8: *Volume rendering of changes in blood flow velocity magnitude introduced by bifurcation stenting. Blood flow velocity nearest the wall (values 0.1* cm/s*) was made transparent to reveal velocity magnitude during maximum blood flow under resting (top) and hyperemic (bottom) flow conditions in the MB and SB. Inflow waveform contours previously obtained from a canine LAD coronary artery under normal resting and hyperemic conditions during continuous adenosine infusion are shown at bottom right and were imposed at the inlet of CFD models. The temporal locations for volume renderings are denoted by circles. Reprinted with permission from Williams et al. [211].*

and subsequent virtual SB angioplasty. Their models were idealized both in the anatomy and in the stent configuration, which was uniformly shaped. Authors concluded that MB stenting, even if followed by a SB angioplasty, causes abnormal hemodynamic modifications in the bifurcated area. This might be one of the reasons for higher occurrence of adverse clinical event rates in those regions (Fig. 2.8). Lastly, a very recent paper by Gundert et al. [80] analysed the relationship between vessel diameter and the hemodynamically optimal number of crowns using a derivative-free optimization algorithm coupled with CFD in idealized vessels. Objective of the optimization process was the minimization of the low WSS area; results indicate that the current design of commercial stents incorporate a greater number of crowns compared to the hemodynamically optimal stent designs.

The second strategy for reconstructing a CFD domain is based on medical images. In 2011, Gundert et al. [81] created their stented bifurcations based on a standard reconstruction of the internal arterial wall from medical images and used an innovative geometrical method to subtract a patient-specific virtually expanded stent from the fluid volume (Fig. 2.9). Despite being a step forward in the state of the art, these models still have some limitations since they are not able to describe potential non-uniform expansion of stent cells in complex anatomies. Moreover, stent design may not be realistic in highly curved vessels resulting in erroneously shorter or longer stent struts. The suitability of this method was verified with patient-specific models of a stented coronary artery bifurcation constructed from OCT imaging data by Ellwein et al. [52]. In this paper, the arterial wall surface was

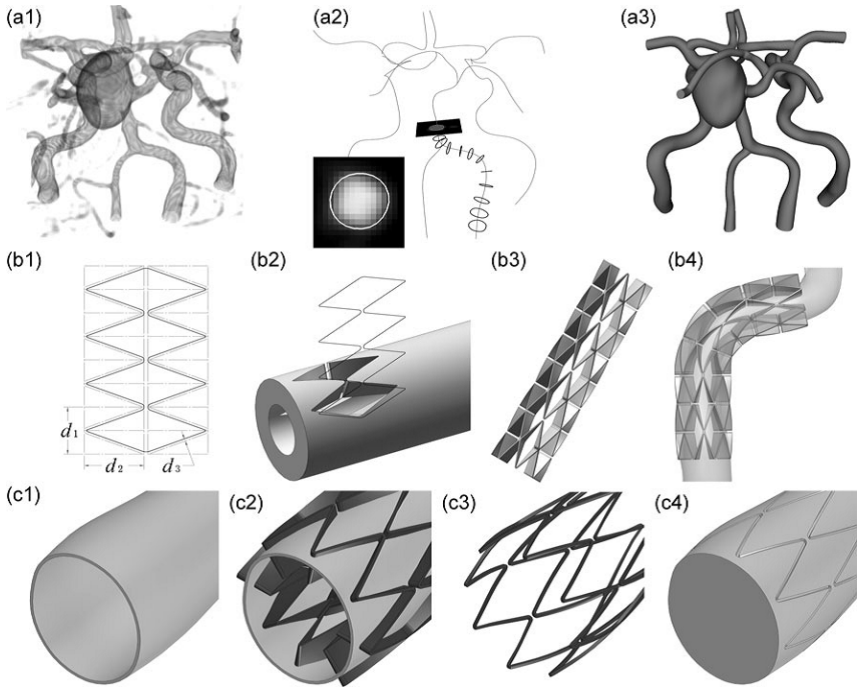

Figure 2.9: *Method of patient–specific model construction for CFD simulations of stented coronary arteries. a) workflow from imaging data to 3D solid model of a patient-specific coronary tree; b) Preparation of an idealized model of a thick stent matching the arterial geometry; c) production of the fluid domain of the stented coronary artery by subtracting the stent volume from the coronary solid model. Image copied with permission from Gundert et al. [81].*

reconstructed by registering OCT cross sectional images to the pathway of the guide wire that was estimated by applying a shortest path algorithm to a graph representation of the artery. Stent implantation was obtained with the previously described virtual method [81]. In 2012, Foin et al. [58] reconstructed the numerical fluid volumes by means of microCT scans of *in vitro* bench tests where different stents were deployed into silicone coronary bifurcations (Fig. 2.10). In that work, the authors compared a typical FKB procedure with a sequential 2-step post-dilation of the SB and the MB. These treatments were performed after MB stenting aiming to open SB ostium and reduce strut malapposition. Their analyses showed that the latter option may offer a simpler and more efficient alternative to FKB technique by reducing some of the FKB drawbacks such as low WSS areas and high wall stresses caused by the overexpansion and elliptical configuration obtained in the proximal part of the MB.

The third alternative for the reconstruction of the CFD geometries is the creation of deformed configurations of vessel and stents by means of structural simulations of stenting procedures. This strategy allows the simultaneous biomechanical assessment of stenting procedures both from a structural and a fluid dynamic point of view and provides a more realistic representation of the fluid volume since it is able to perceive geometrical features such as tissue prolapse, strut malapposition or overlapping metallic layers. This method was

firstly proposed in 2008 by Balossino et al. [12] who investigated the influences of different commercial stents expanded in straight idealized vessels (Fig. 2.11). In 2011 Pant et al. [166] developed a method to perform single-objective stent optimization considering both structural and fluid dynamic analyses. The same strategy was adopted by Morlacchi et al. [143] in more complex cases of stenting procedures involving coronary bifurcations. Structural and transient CFD simulations highlighted the drawbacks of standard FKB in terms of overexpansion of the MB and consequential increase of low WSS areas. Hemodynamic improvements resulting from the use of a tapered balloon lead, to a reduction of the critic low WSS areas. In 2011, Chiastra et al. [31] used the same approach to investigate the differences provoked by a distal or a proximal SB access after MB stenting. According to clinical practice, CFD simulations showed that a distal access should be preferred to reduce the hemodynamic disturbances of the stenting procedures. Besides coronary arteries, similar methodologies were adopted by De Santis et al. [38] and Bernardini et al. [15] for carotid artery and cerebral aneurysms stenting, respectively.

Lastly, a method combining the second and third strategies was proposed in 2011 by Morlacchi et al. [145]. In this paper, microCT images were used to reconstruct coronary stents implanted in *in vivo* pig models while finite element simulations were used to obtain the geometrical configuration of the explanted coronary arteries (Fig. 2.12). The realistic geometry obtained from microCT images and computer simulations was characterized by proximal overexpansion and asymmetric deployment of the stent leading to a markedly non-uniform distribution of WSS values. Authors found a good correlation between the computed hemodynamic parameters and the asymmetric neo-intimal growth evaluated by means of histomorphometric analyses of the explanted vessels. This correlation could not be appreciated with studies characterized by idealized geometries.

After the creation of the fluid volume, the definition of appropriate boundary conditions is the other crucial modelling choice in CFD simulations. Due to the complexity of *in vivo* measurements, patient-specific boundary conditions are frequently lacking. As a consequence, in most of the studies, boundary conditions are usually based on standard velocity tracings measured in human coronary arteries [36] or empirical/morphometric relationships associating flow rates with arterial diameters [96, 155, 203]. An example of velocity tracings in different human coronary districts can be found in Davies et al. [36] while van der Giessen et al. [203] recently presented an empirical relationship (Eq.1) between the average flow (q) and the coronary diameter (d) fitting experimental measurements [45] in healthy human coronary arteries:

$$q = 1.43 \cdot d^{2.55} \tag{1}$$

In presence of bifurcated geometries, the choice of the flow split among the daughter branches is another critical point. In 1926, Murray presented a study [155] based on the Poiseuille's law to determine the vessel radius requiring minimum expenditure of energy by the organism. The result of this study is valid for the whole vascular tree and lead to the following formula (Eq.2):

$$q_{D2}/q_{D1} = (d_{D2}/d_{D1})^3 \tag{2}$$

where q_{D1} and q_{D2} are the mean flows through the diameters of the two daughter branches (d_{D2} and d_{D2}). Recently, different studies [96, 203] showed that, specifically for the coronary

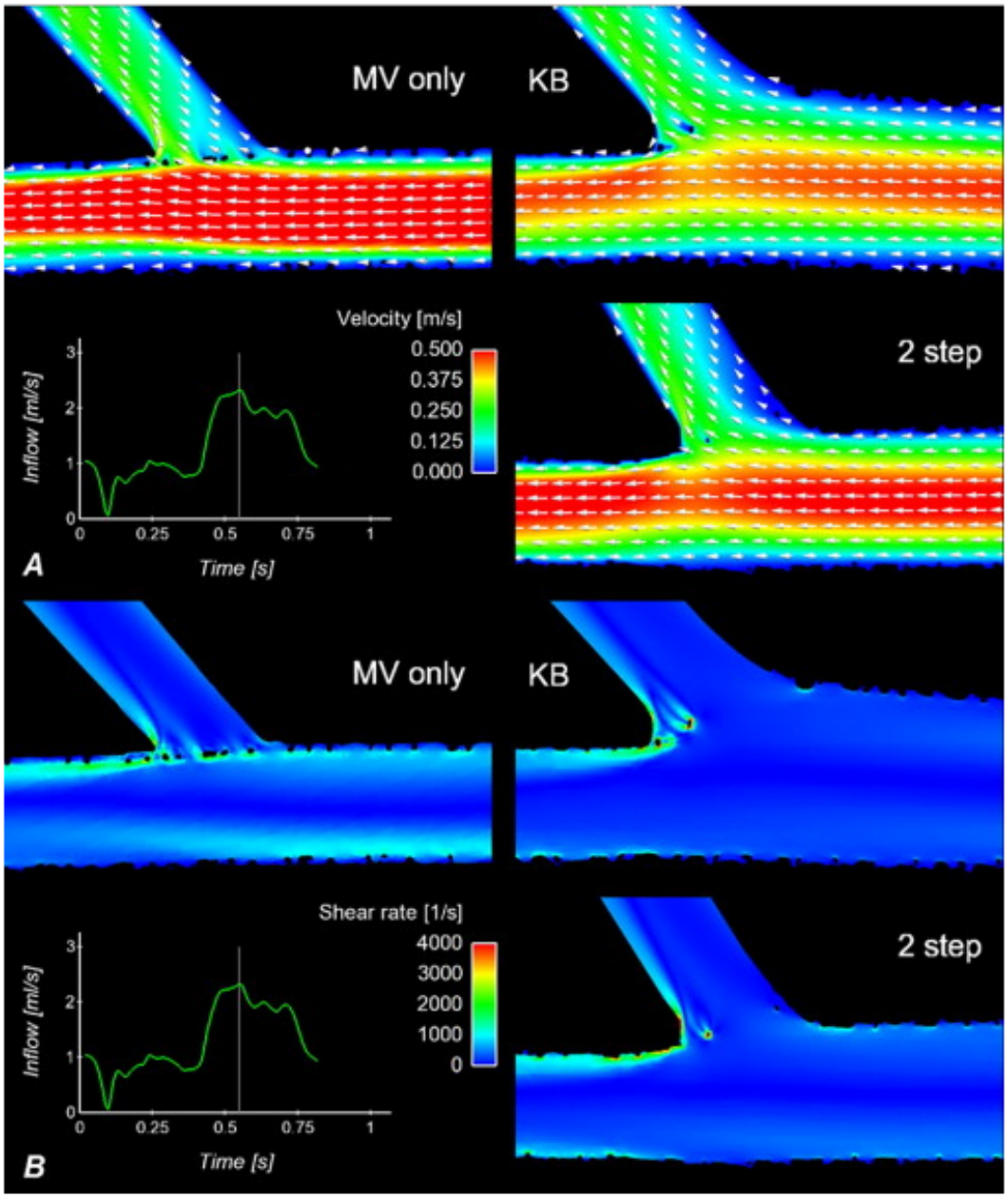

Figure 2.10: *Computational flow simulation of the velocity field (A) and shear rate (B) in cases representative of provisional technique with MB stenting only and post-dilation with FKB or the sequential 2–step SB/MB dilation. Reprinted with permission from Foin et al. [58].*

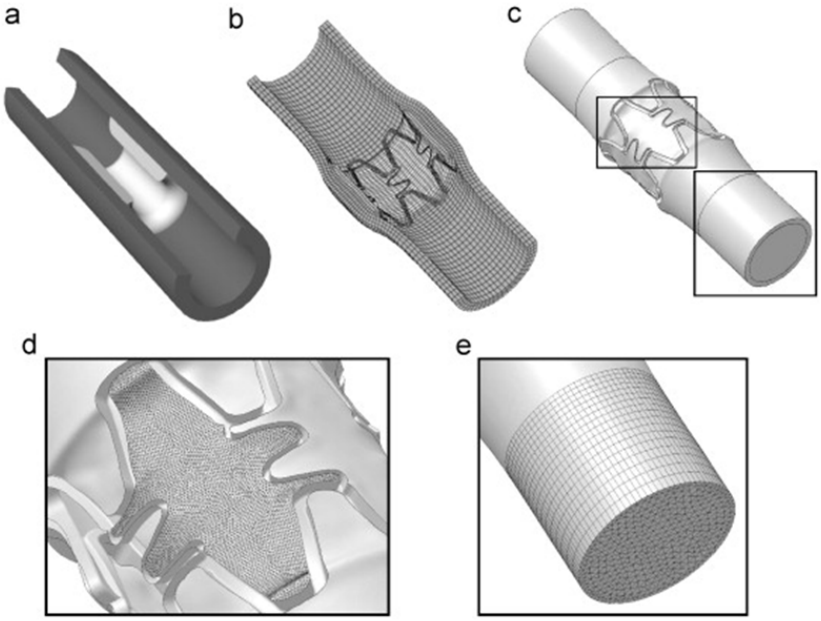

Figure 2.11: *3D CAD geometry of the plaque and the artery (a); deformed configuration after stent expansion (b); fluid domain (c); particular of the fine discretization in the vessel area within the stent struts (d) and of the coarser mesh in the area outside the stented region. Reprinted with permission from Balossino et al. [12].*

tree, the flow ratio between daughter branches is best described with lower exponential values. In particular, van der Giessen et al. [203] found that a power value of 2.27 results in a better agreement with the previously mentioned experimental measurements. However, the presence of obstructive cardiovascular diseases or medical devices may influence these flow distributions in the coronary tree. In this light, Morlacchi et al. [143] and Williams et al. [211] implemented 0D lumped parameter models that account for the impedance of the downstream vascular systems and were coupled at the outlets of the 3D fluid volumes of the stented regions. In this way, they verified that flow split is not highly influenced by the presence of a stent or a mild plaque. Moreover, it remains almost constant during the entire cardiac cycle. These findings are in agreement with what reported in Lee et al. [116] who stated that the resistances in epicardial coronaries accounts for only 10% of the total resistance of the coronary bed leaving to the downstream regions the capability of regulating the flow distribution among the branches. Obviously, this occurrence is not valid in presence of a very severe stenosis or complete obstructions of vessels and has to be carefully evaluated for each case under investigation.

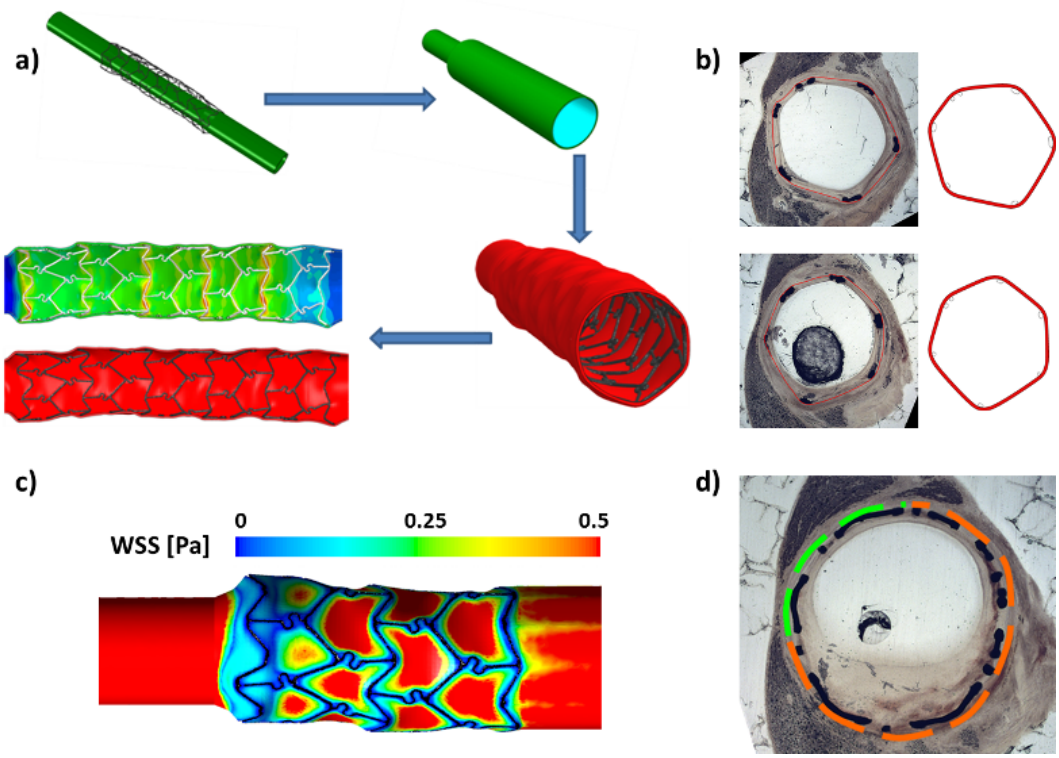

Figure 2.12: *A) Structural model implemented to identify the geometrical configuration of the stented arteries of in vivo porcine coronary models: CAD model of the undeformed artery and of the stent reconstructed from microCT, expansion of the artery through a cylindrical surface dilatation, stent-artery coupling obtained after the recoil of the artery, and longitudinal section of the final configuration. B) Comparison between two histological images and the corresponding sections obtained with the structural simulation showing the good agreement between the histological images (left) and the numerical geometrical configuration (right). C) Results of the CFD simulations in terms of spatial distribution of WSS magnitude over the arterial wall. D) Correlation between areas characterized by low WSS (orange lines) and the in-stent restenosis phenomenon after 14 days in a proximal section of the stented artery. Image adapted with permission from Morlacchi et al. [145].*

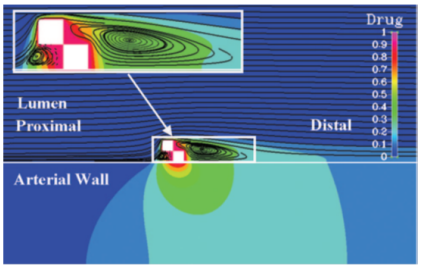

Figure 2.13: *Visual representation of drug concentration distribution (in color) and blood flow streamlines (black curves). Influence of the presence of two DES struts in which the top strut is staggered upstream relative to bottom. White line separates lumen (above) and tissue (below). Reprinted with permission from Balakrishnan et al. [11].*

2.4 Drug elution models of stenting procedures

After the successful introduction of drug eluting stents (DES) to overcome restenosis, the ability to correctly release drug into the arteries has become an important factor in the development of stent devices.

Several computational models have been recently proposed using one dimensional (1D) [125, 174], bi-dimensional (2D) (Fig. 2.13) [9–11, 18, 75, 97, 139, 140, 202, 218], or three-dimensional (3D) approaches. The 3D models consist of either simplified geometry [94, 107] or derived from structural simulations of stent expansion [34, 35, 136, 166, 219]. The majority of these studies considers the arterial wall as a homogenous porous medium, and drug advection due to plasma leakage. In addition to this model setting, some authors account for drug binding to tissue proteins, others include anisotropic drug diffusivity or the presence of atherosclerotic plaque. A recent review on mass transport models for stented arteries has been proposed in 2010 by O'Connell et al. [159] Due to high computational costs, those studies investigated reduced arterial models with simplified geometries of arteries with no branches. Complex geometries like coronary bifurcations have been analysed in only three recent papers [34, 35, 107]. The effects of complex luminal flows have been demonstrated to strongly affect drug deposition in the arterial walls. In particular, Kolachalama et al. [107] constructed a two-phase computational model of stent-deployed in ideal arterial bifurcations simulating blood flow and drug transport. Simulations predicted that heterogeneous drug distribution patterns are sensitive to relative stent position and luminal flow (Fig. 2.14). The study by D'Angelo et al. [35] used a deformed configuration of the stented arterial bifurcation obtained through structural simulations and found that the highest concentrations are located in the opposite part of the artery with respect to the bifurcation branch. Such an effect can be explained by a combination of fluid dynamics and mass transport phenomena and might reside in a specific feature of the elliptical arterial configuration caused by the implantation of a stent with the FKB technique. Such a configuration is responsible for promoting low axial velocities and possible blood recirculations in the lower part of the lumen, augmenting the effects of the bifurcation subtracting a considerable part of the flow from the upper part of the artery. The same model has been subsequently exploited in Cutrí et al. [34] (Fig. 2.15) to study the influence of different stenting configurations (the Provisional

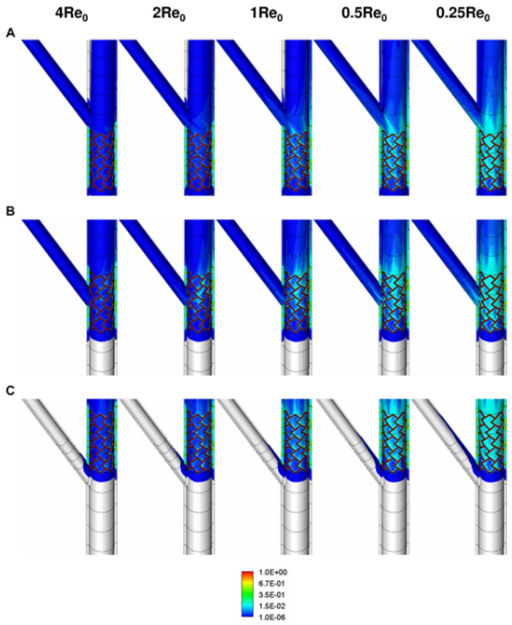

Figure 2.14: *Snapshots of arterial drug deposition patterns for three different stent placement scenarios (upstream (A), midstream (B) and downstream (C)) and five different flow conditions are shown. Reprinted with permission from Kolachalama et al. [107].*

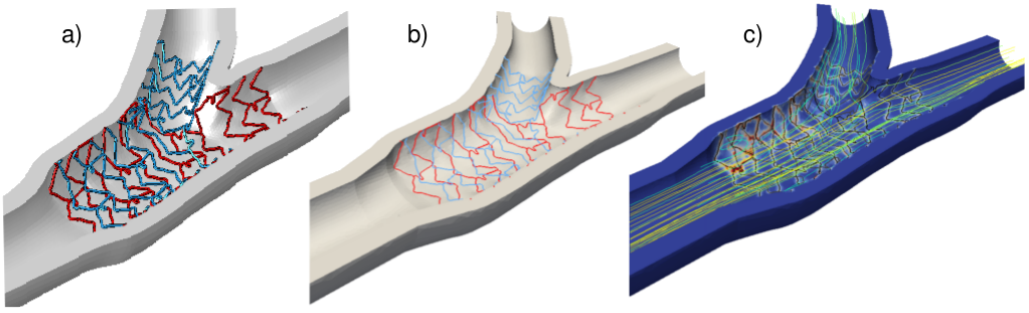

Figure 2.15: *Computational model of DES for a two stents technique: a) 3D geometry of the DESs implanted in the coronary bifurcation via a structural finite element model; b) 1D model of DESs built from the 3D geometry; c) drug concentration in the arterial wall (blue to red code), blood velocity in the arterial lumen (streamlines) and 1D geometry of the two DESs. Courtesy of prof. Paolo Zunino and Dr. Elena Cutrí et al. [34].*

Side Branch, the culotte and the inverted culotte techniques), thus suggesting improvements in the treatment of coronary bifurcation lesions. Clinical issues such as the effectiveness of drug delivery to lesions in the SB, as well as the influence of incomplete strut apposition and overlapping stents involving one or two conventional stents are addressed in these studies.

Experimental validation is a fundamental step for each numerical model. However, the complexity of the biological phenomena affecting DES implantation makes this phase particularly challenging in these models. Among the experimental evidences described in the literature, particularly interesting is the paper proposed by O'Connell et al. [160] in 2011 where authors revealed that increased compressive forces on a porous media reduced the ability of species to diffuse through that media. This finding suggests that arterial deformation could affect the ability of a DES to release correct therapeutic levels of drug *in vivo*. Thus, in the future, drug transport models should not only be focused on the effects of modified hemodynamics but should also consider the deformations provoked by stent implantations on the arterial wall.

2.5 Verification and validation of computational models in biomechanics

Confidence in numerical methods is only possible after the verification of the mathematical foundation of the models and the validation of the results against experimental data. This issue is particularly complicated in computational biomechanics mainly due to the complexity of biological systems and uncertainties related to the experimental campaigns [87]. Accordingly, their verification and validation is, at the moment, the most challenging concern about numerical models of stenting procedures.

The ASME Committee for Verification and Validation in Computational Solid Mechanics defines verification as "the process of determining that a computational model accurately represents the underlying mathematical model" while validation is "the process of determining the degree to which a model is an accurate representation of the real world". Briefly, verification is "solving the equations right" while validation is "solving the right equations" [185].

Among the two, validation is the most demanding issue in this field since most of the current studies make use of commercial software that are expected to have been verified by the code developers (code verification). Instead, calculation verification focuses on errors arising from discretization of the numerical domains and has now become a conventional step via mesh convergence studies.

On the other hand, direct validation of numerical models of stenting procedures is a costly and time consuming process and faces some challenging problems. The high complexity and variability of the biomechanical systems, the lack of standard experimental guidelines and the incapacity/difficulties to accurately measure the quantities of interests are the main issues that currently limit the execution of a proper validation. Some previous studies [37, 65, 67] have performed indirect validations of their models using experimental results or data available in the literature or from manufacturer reports. In those cases, experimental quality control, sources of error, and the degree of variability are not typically known nor controllable. As a consequence, more efforts in the verification and validation processes would

certainly be useful and desirable in order to provide numerical models of stenting procedures a higher reliability and wider acceptance. In this thesis, the issue has been considered mainly focusing on the validation of the fluid dynamic models. In particular, local blood flow patterns in stented coronary bifurcations have been investigated by means of both CFD simulations (Chapters 3 and 4) and Particle Image Velocimetry (PIV) experiments (Chapter 5). Results of both studies have been used to compare the two methods and to study diffrent stenting procedures.

Chapter 3

A sequential numerical model of stenting procedures in coronary arteries

Contents

Despite their success, stenting procedures are still associated to some clinical problems like sub-acute thrombosis and in-stent restenosis. As highlighted in Chapter 1, several clinical studies associate these phenomena to a combination of both structural and hemodynamic alterations caused by stent implantation. In the recent literature, numerical models have been recognized as a widely used and adopted tool to investigate stenting procedures but always from either a purely structural or fluid dynamic point of view. The main scope of this thesis is the implementation of a sequential structural and fluid dynamic numerical model to provide a better understanding of the biomechanical influence of stenting procedures in coronary arteries, mainly focusing on complex regions such as coronary bifurcated arteries. This sequential model is divided into two main parts: (1) the implementation of structural finite element models (FEM) of the analysed stenting procedures and (2) the execution of transient fluid dynamic simulations with particular attention to the construction of the fluid domain based on the structural FEM results. In this way, the fluid volume of the CFD simulation is not only based on some geometrical assumptions but takes into account the different mechanical behaviours of the artery and the stent and the interactions of the different parts during the stenting procedure. Following this method, interesting phenomena such as tissue prolapse or strut malappositions may be considered as well.

In this chapter, this sequential numerical model is thoroughly described highlighting the main modelling choices and potential results. For sake of clarity, a stenting expansion in a simplified curved artery with no branches is here examined while the case studies involving coronary bifurcations will be discussed in the next chapter.

3.1 Structural model of a stenting procedure

The commercial finite element code developed by ABAQUS (Dassault Systemes Simulia Corp., RI, USA) is used to simulate the stent deployment in a curved atherosclerotic coronary artery. Three main components (artery, angioplasty balloon and stent) are involved in the modelling while the preliminary simulations of stent crimping and advancement are implemented to correctly position the devices before the final analysis of the stent deployment. In the end, two paragraphs discussing the choice of the solution scheme and the balloon models are added to more deeply discuss these issues.

3.1.1 Coronary artery model

The geometry created resembles a portion with no branches of a human LAD coronary artery and is characterized by the length of the centreline (44 mm), the curvature radius (28 mm), the internal diameter (2.78 mm) and the thickness of the arterial wall (0.9 mm) that is assumed to be uniform throughout the model (Fig. 3.1a). The tortuosity index (TI) is calculated as:

$$\mathrm{TI} = \frac{\mathrm{L}}{\mathrm{L}'} - 1 \tag{1}$$

where L is the length of the centreline of the coronary artery and L' is the straight distance between the extremes of the region of interest. In this case, the TI is equal to 0.11 and represents a low curvature usually characterizing the coronary arteries in the diastolic

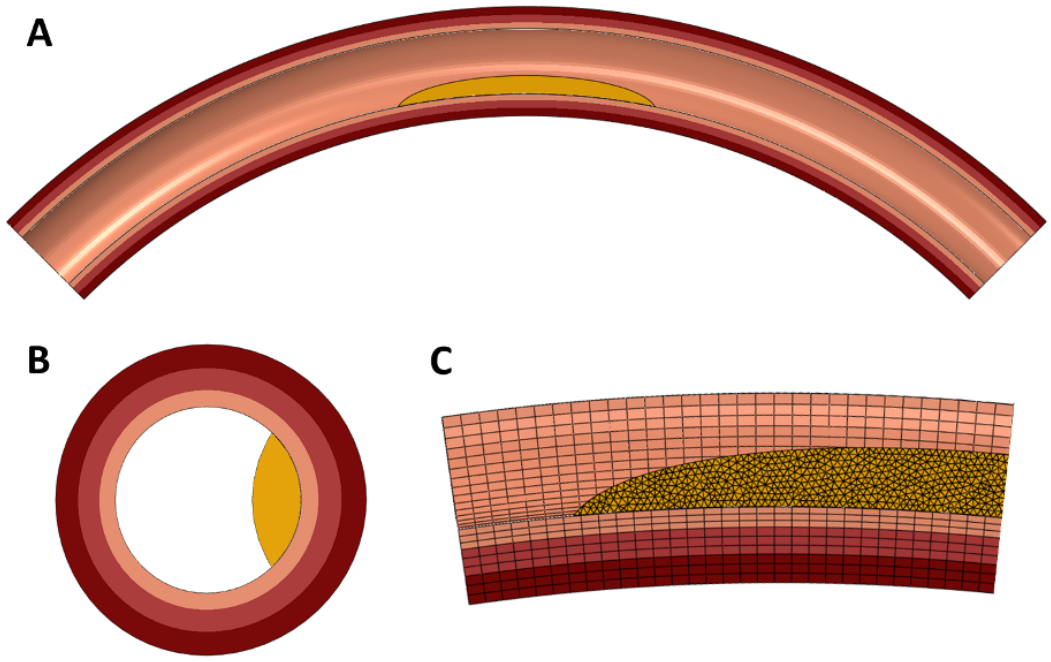

Figure 3.1: *A) Geometric model of an atherosclerotic curved coronary artery. B) Central section of the arterial wall highlighting the thicknesses of three arterial layers and of the atherosclerotic plaque. Dimensions are specified in the text. C) Discretization of the coronary artery: 9 layers of hexahedral elements are used to discretize the thickness of the arterial wall while a fully tetrahedral mesh is used for the atherosclerotic plaque.*

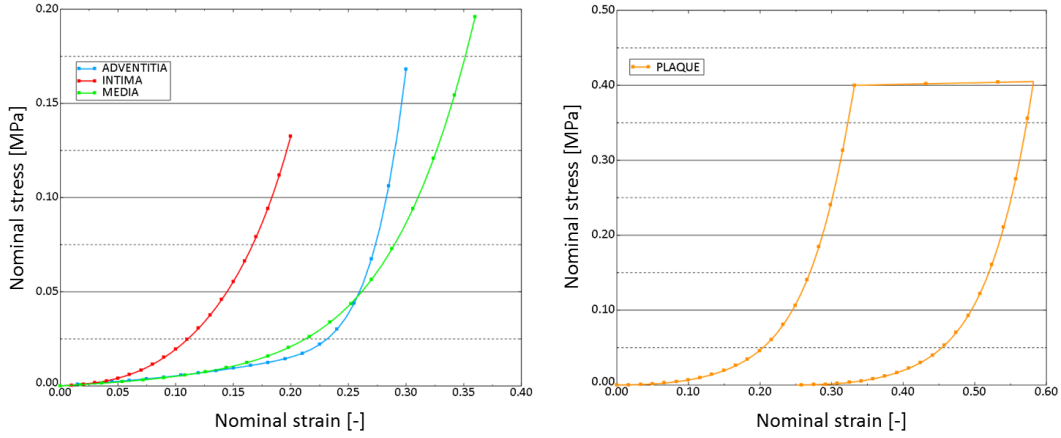

Figure 3.2: *Mechanical behaviour of the isotropic material models implemented in Abaqus to describe the biological tissues of the atherosclerotic coronary artery by means of reduced polynomial strain energy density functions. On the left, the hyperelastic models of the three arterial layers. On the right the hyperelastic-plastic model used for cellular atherosclerotic plaques. Experimental data obtained by Holzapfel et al. [92] and Loree et al. [123] are used to implement such models.*

Table 3.1: *Coefficients of the reduced polynomial strain energy density function used to model the materials of the arterial wall layers and cellular atherosclerotic plaques.*

Layer	C_{10}[MPa]	C_{20}[MPa]	C_{30}[MPa]	C_{40}[MPa]	C_{50}[MPa]	C_{60}[MPa]
Intima	6.79	5.40	1.11	10.65	7.27	1.63
Media	6.52	4.89	9.26	0.76	0.43	8.69
Adventitia	8.27	1.20	5.20	5.63	21.44	0.00
Plaque	2.38	1.89	3.88	3.73	2.54	5.73

phase of the cardiac cycle, when most of the blood flow occurs [175]. The arterial wall is divided into three layers with different thicknesses (Fig. 3.1b) corresponding to the intima (0.24 mm), the media (0.32 mm) and the adventitia (0.34 mm) according to the data obtained by Holzapfel et al. [92]. An atherosclerotic plaque is positioned along the internal wall of the curved artery and is characterized by a length of 10.636 mm and a maximal width of 0.75 mm provoking a mild stenosis (area reduction of almost 20%) in the arterial lumen as illustrated in Fig. 3.1b. The artery is discretized using about 115,200 reduced-integration 8-node hexahedral elements (C3D8R). The accuracy of the mesh density used in the analyses is guaranteed by the mesh sensitivity study performed and published in a recent paper by Capelli et al. [24] on a similar arterial wall. Conversely, the atherosclerotic plaque is discretized using 117,288 4-node tetrahedral elements (Fig. 3.1c).

A hyperelastic isotropic constitutive law, suitable for nearly incompressible materials accounting for large strains, is adopted to describe the mechanical behaviour of healthy human arterial layers in accordance with the experimental data obtained by Holzapfel et al. [92] in stress-strain tests in the circumferential direction (Fig. 3.2). The adopted constitutive law is based on the following sixth-order reduced polynomial strain energy density function:

$$\begin{aligned} U = {} & C_{10}(\overline{I_1} - 3) + C_{20}(\overline{I_1} - 3)^2 + C_{30}(\overline{I_1} - 3)^3 + \\ & + C_{40}(\overline{I_1} - 3)^4 + C_{50}(\overline{I_1} - 3)^5 + C_{60}(\overline{I_1} - 3)^6) \end{aligned} \tag{2}$$

where C_{i0} are material parameters (Table 3.1), and $\overline{I_1}$ is the first deviatoric strain invariant defined as

$$\overline{I_1} = \overline{\lambda_1}^2 + \overline{\lambda_2}^2 + \overline{\lambda_3}^2 \tag{3}$$

with the deviatoric stretches $\overline{\lambda_i}$ related to the principal stretches λ_i and total volume ratio J by the relation

$$\overline{\lambda_i} = J^{1/2}\lambda_i \tag{4}$$

With the aim of approximately describing the mechanical failure of an atherosclerotic plaque, its material is described coupling an isotropic hyperelastic model with a plasticity model: it allows consideration of stenosis reduction after stent expansion and arterial elastic recoil. The hyperelastic part of the stress-strain curve is implemented using the previous strain energy density function (Eq.2) in which the parameters C_{i0} (Table 3.1) are modified

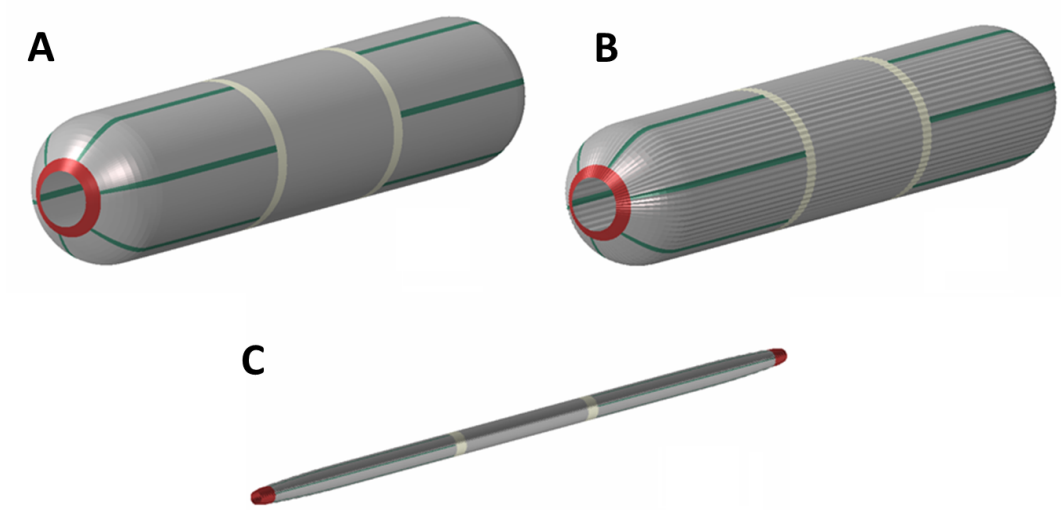

Figure 3.3: *Steps of the balloon deflation simulation: A) Initial expanded configuration , B) first step where alternate nodes are given a small radial displacement and C) final deflated multi-folded configuration obtained by applying a negative pressure to the balloon internal surface. Green and white zones represent the planes used to facilitate the seeding process and the nodes constrained in the circumferential direction; the red areas are the elements at the extremities that are pulled in the longitudinal direction.*

to describe the stress-strain curve obtained by Loree et al. [123] for cellular plaques. For strain values greater than 34%, a plasticity model was assumed for the plaque response. The stress plateau value was fixed at 0.4 MPa, accordingly with the rupture stress measure in the same experimental campaign (Fig. 3.2). A density value of 1120 kg/m^3 is used for both the artery and the plaque.

3.1.2 Angioplasty balloon model

Most of the stents currently implanted in coronary arteries are balloon-expandable devices, being deployed by means of a high pressure inflation of polymeric balloons placed inside the stent. In this model, polymeric balloons are designed in the inflated configuration. In Fig. 3.3a, an example of a 3.0 mm balloon is shown. Reduced integration 4-nodes membrane elements with a thickness of 0.03 mm are used to discretize the balloon. Such elements neglect the influence of one dimension, i.e. thickness, with respect to the other two, so that forces are transmitted only on the element plane, setting flexional rigidity to zero. Membrane elements are commonly used to characterize thin surfaces, and appear adequate for the studied case. Considering commercially available medical devices, the material model reproduces polyethylene terephthalate (PET) mechanical properties. The density is assumed equal to 1256 kg/m^3. The material is considered linear elastic, having Young modulus of 1455 MPa; Poisson's ratio is assumed to be 0.3.

The multi-folded deflated geometry is obtained by means of a preliminary analysis performed within ABAQUS/Explicit. After a first step in which alternate nodes in the cir-

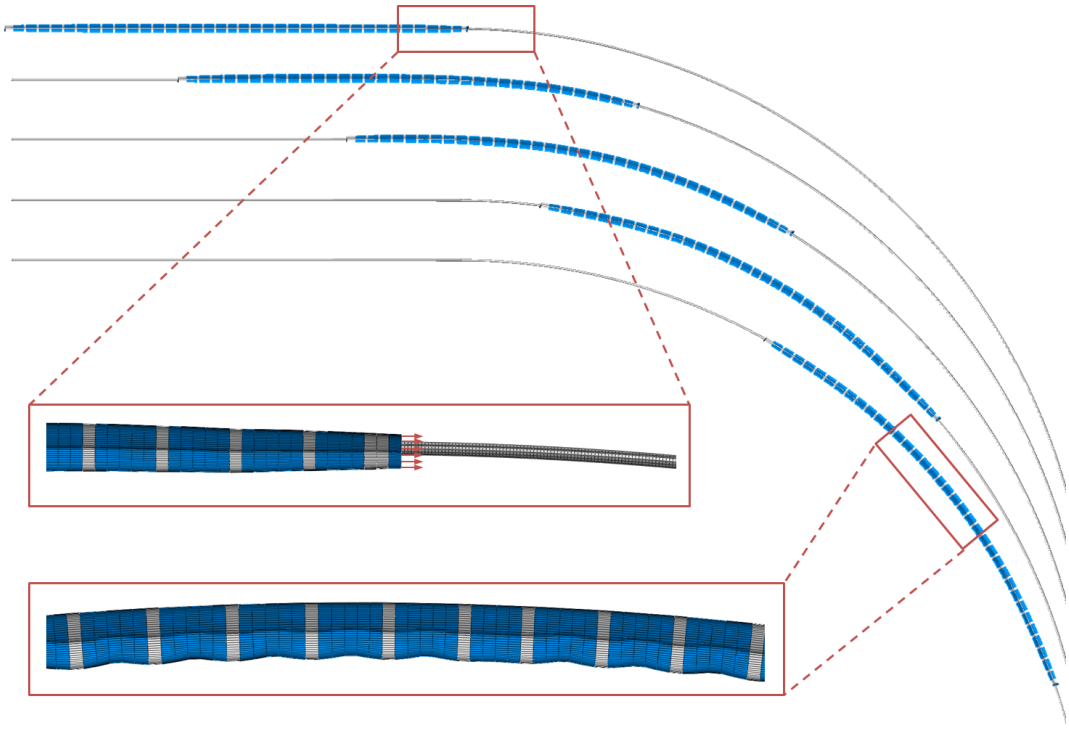

Figure 3.4: *Advancement of an angioplasty balloon model. In the magnification areas: initial assembly with concentrated loads displayed (above); rigid body properties assigned to balloon elements (grey area, below).*

cumferential direction undergo a small radial displacement (Fig. 3.3b), an internal negative pressure (0.03 MPa) is applied, obtaining a regular deformed configuration that fitted inside the crimped stent (Fig. 3.3c). During the deflation process, the nodes at the balloon extremities (red zone) are pulled imposing longitudinal displacement to lengthen the deflated balloon while some nodes (white and green areas) are constrained in the circumferential direction.

In order to simulate angioplasty procedures or stent expansions in curved or bifurcated arteries, the balloon models need to be bent and advanced along curved guides. In these simulations, the multi-folded balloons are firstly imported in their deformed deflated configuration. Then, adequate CAD geometries of internal guides are generated considering the curvature needed. Subsequently, the nodes composing a balloon extremity are subjected to concentrated loads pulling the whole balloon model along the encastred internal guide. Contacts between the balloon internal surface and the guide are implemented with the general contact algorithm, imposing a hard frictionless contact. Self-contact is assumed for the whole balloon model. In order to bend the balloon maintaining the multi-folded configuration, several elements are constrained as rigid bodies. The simulations are performed using the finite element package ABAQUS/Explicit. The initial assembly and several steps of the

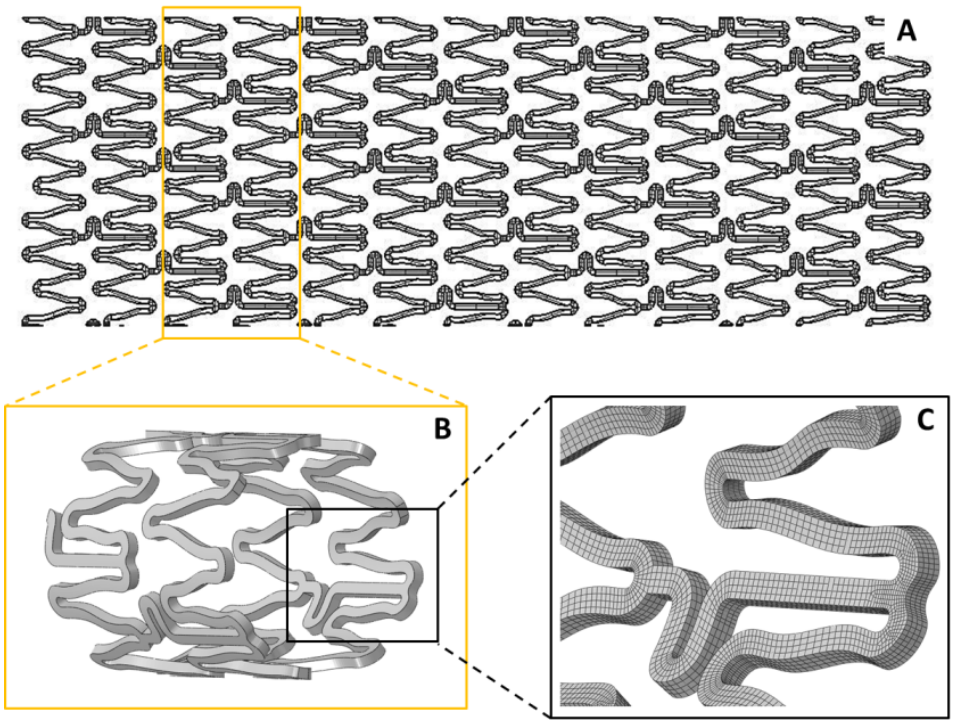

Figure 3.5: *Xience V stent model creation and discretization: A) 2D sketch of the stent design taken from a public patent; B) identification of the central repetitive unit and creation of the 3D modular stent ring; C) hexahedral discretization of the stent. Finer elements are used in proximity of curved regions.*

balloon advancements are shown in Fig. 3.4; detailed views of the regions subjected to the concentrated forces and rigid body constraints (grey area) can be appreciated as well.

3.1.3 Stent model

Geometrical models of coronary stents are created using the CAD software Rhinoceros 4.0 Evaluation (McNeel & Associates, Indianapolis, IN, USA) aiming to resemble commercial devices currently available on the market. The creation of all stent models mainly follows the same pathway with exceptions for some devices characterized by particular designs. In this section, the process used to create a stent model resembling the Xience V coronary stent system by Abbott Vascular (Abbott Laboratories, Abbott Park, IL, USA) is described. The starting point of this process is typically the 2D sketch of the stent design usually available in public patents or company publications (Fig. 3.5a). This information is then integrated with more precise measurements of actual devices performed with a Nikon SMZ800 stereo microscope (Nikon Corporation, Tokyo, Japan). In order to fasten the creation of the model, the symmetries and the modular nature of the stents are usually exploited; a central repetitive unit is identified, rolled along a central axis and given an offset equal to the stent thickness (91 μm) to achieve the 3D geometry of the modular ring of the stent (Fig. 3.5b). Once obtained

the central, initial and final modular sections, the whole stent is assembled by connecting the desired number of repetitive units. In case of the Xience V stent used in the expansion in the curved artery, a final length of 15.5 mm is achieved while the external diameter in the nominal configuration is set equal to 1.76 mm. The whole model is visible in Fig. 3.6b. Afterwards, in order to generate a high-quality mesh, the CAD surface representing the stent is firstly partitioned, dividing the curved and the straight regions, thus facilitating the regular discretization of the stent. Secondly, a cross section of the device is meshed by means of a 2D quadrilateral regular mesh. Such mesh is dragged along the strut surface to create solid elements. Due to stress concentrations and high stress gradients, the curved parts are usually more finely discretized, while the straight regions are characterized by a coarser mesh to decrease the computational cost of the analyses. After a sensitivity analysis, the mesh used in this particular case resulted in 16 cross-sectional elements and a total amount of 211,468 C3D8R elements (Fig. 3.5c).

In Fig. 3.6, the three stent models resembling the commercial devices investigated within this thesis are illustrated together with their main geometrical dimensions. In particular, the Endeavor Resolute coronary stent system (Fig. 3.6a) is developed by Medtronic (Medtronic, Minneapolis, MN, USA) and characterized by a circular cross section. The third device is Tryton SB stent (Fig. 3.6c) (Tryton Medical, Durham, NC, USA) which is a BMS dedicated stent specifically designed to be implanted in the SB of coronary bifurcations; it facilitates the culotte stenting technique.

All these devices are made of a Co-Cr alloy. The material model is created using the typical mechanical properties of biocompatible Co-Cr alloys, which are defined in the work of Poncin et al. in 2004 [173]. Specifically, the Co-Cr alloy behaviour is assumed isotropic and elasto-plastic. The material constants used are listed below:

- Young's modulus (E) = 233 GPa
- Poisson's ratio (ν) = 0.35
- Yield stress = 414 MPa
- Fracture stress = 933 MPa
- Deformation at break = 44.8%
- Density (ρ) = 8,500 kg/m^3

3.1.4 Implicit vs Explicit: choice of the solution scheme

The ABAQUS finite element commercial code comprehends two different tools to solve structural problems: ABAQUS/Standard and ABAQUS/Explicit. The main difference among the two solvers is that ABAQUS/Standard uses an implicit solution scheme while ABAQUS/Explicit is based on an explicit scheme that solves a dynamic equilibrium. For several analyses, it is clear whether Abaqus/Standard or Abaqus/Explicit should be used. For instance, ABAQUS/Standard is more efficient for solving smooth nonlinear problems; on the other hand, ABAQUS/Explicit is originally developed to model high-speed impact events in which inertia plays a dominant role in the solution. However, some cases, such as quasi-static nonlinear problems, may be correctly simulated with either methods and the choice among the two solvers is not trivial. In this section, the main characteristics and

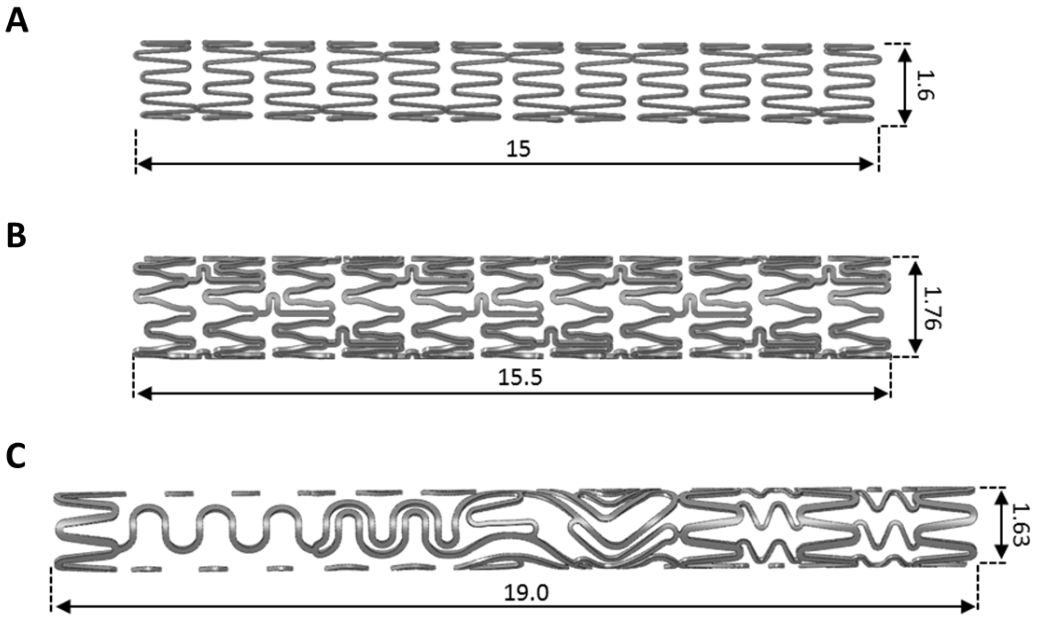

Figure 3.6: *CAD models of the three commercial devices investigated in this thesis: A) Endeavor Resolute coronary stent system by Medtronic (Medtronic, Minneapolis, MN, USA); B) Xience V stent by Abbott Vascular (Abbott Laboratories, Abbott Park, IL, USA); Tryton SB stent system by Tryton Medical Inc. (Tryton Medical Inc., Durham, NC, USA) which is a BMS explicitly dedicated to coronary bifurcations. Dimensions are in millimetres.*

differences of the two solvers are discussed, thus justifying the solver choice in case of the simulations presented in this thesis.

Within an implicit solution scheme, the variables depend both on the solution at the current ($t + \Delta t$) and the previous (t) time increments. As a consequence, this approach requires the solution of a complex nonlinear system through iterative numerical methods and the inversion of the global mass matrix at each increment. On the other hand, within an explicit solver, the solution at the current time increment ($t + \Delta t$) is only based on the solutions at the previous increment (t). ABAQUS/Explicit, for instance, is based on the central difference rule to integrate the equations of motion:

$$\ddot{\mathbf{u}}^{(i)} = \mathbf{M}^{-1} \cdot (\mathbf{F}^{(i)} - \mathbf{I}^{(i)}) \tag{5}$$

$$\dot{\mathbf{u}}^{(i+\frac{1}{2})} = \dot{\mathbf{u}}^{(i-\frac{1}{2})} + \frac{\Delta t^{(i+1)} + \Delta t^{(i)}}{2} \ddot{\mathbf{u}}^{(i)} \tag{6}$$

$$\mathbf{u}^{(i+1)} = \mathbf{u}^{(i)} + \Delta t^{(i+1)} \dot{\mathbf{u}}^{(i+\frac{1}{2})} \tag{7}$$

where $\dot{\mathbf{u}}$ and $\ddot{\mathbf{u}}$ represent the velocity and acceleration fields, (i) is the index defining the current increment, $\mathbf{M}$ is the diagonal mass matrix, $\mathbf{F}$ is the vector of the applied loads and $\mathbf{I}$ is the vector of the internal forces. As a consequence, the computational cost and memory

usage for each increment is lower for every explicit integration scheme if compared to implicit methods.

However, from a numerical point of view, explicit schemes are only conditionally stable and may require a large number (even two orders of magnitude higher) of very small time increments to guarantee the numerical stability of the solution. An estimate of the stable time increment size is given by the following formula:

$$\Delta t_{stable} = \frac{L_e}{c_d} \tag{8}$$

where L_e is the smallest characteristic element length and c_d is the dilatational wave speed of the material. The dilatational wave speed for a linear elastic material with Poisson's ratio equal to zero is given by

$$c_d = \sqrt{\frac{E}{\rho}} \tag{9}$$

where E is the Young modulus of the material and ρ is the material density. In case of nonlinear materials, dilatational wave speed in the element is calculated as:

$$c_d = \sqrt{\frac{\hat{\lambda} + 2\mu}{\rho}} \tag{10}$$

where $\hat{\lambda}$ e μ are an estimate of the Lamé constants used to calculate the effective moduli representing the element stiffness at the current strain values.

From this brief description, it is clear that the limit of stability depends both on the material and calculation grid properties. For instance, meshes characterized by very small elements or stiff materials will be characterized by very small stable time increment. Density plays a major role as well, since increasing material density may be useful to increase the stable time increment and to reduce the computational time. However, this method may lead to inaccuracies in the computed solution especially while solving quasi-static phenomena. Indeed, higher densities may generate unwanted inertial effects within the dynamic equilibtium solved by ABAQUS/Explicit, thus undermining the accuracy of the computed results. Instead, implicit methods, as those implemented in ABAQUS/Standard, use a stiffness-based solution technique that is unconditionally stable and the time increments for the solution only depend on the convergence of the numerical problems.

Another important difference among the two methods concerns their ability on solving contact problems. In particular, ABAQUS/Standard has great difficulties in solving highly nonlinear models characterized by complex 3D contact problems, potentially requiring a great number of iterations and increasing the computational cost of the solution. On the other hand, explicit schemes are characterized by a robust contact functionality that readily solves even the most complex contact simulations.

Lastly, in explicit solution schemes the computational cost is linearly proportional to the number of elements and roughly inversely proportional to the smallest element dimension. Instead, using the implicit method, experience shows that for many problems the computational cost is roughly proportional to the square of the number of degrees of freedom. As a

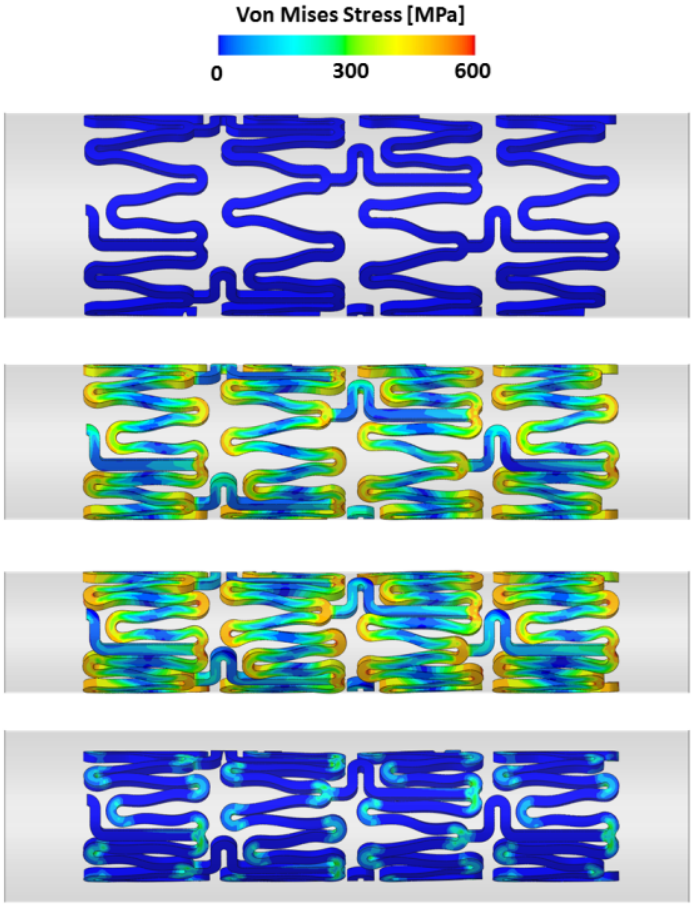

Figure 3.7: *Preliminary simulation: stent crimping. An external rigid cylinder is used to gradually reduce the stent external diameter until an value of 1.05* mm. *The cylinder is then released to allow recoil of the structure. Contours of Von Mises stresses occurring in the crimping process are shown. For sake of clarity, only four central rings opf struts are depicted.*

consequence, the computational cost of the analysis for models characterized by a large number of degrees of freedom is expected to be higher for implicit solution schemes. Conversely, with small number of degrees of freedom, implicit solution schemes could be more efficient. This deduction, however, should be taken with caution due to the problem-dependent relationship between element connectivity and solution cost within implicit solution methods, a relationship that conversely does not exist in the explicit method.

In this thesis, three kinds of simulations are implemented: stent crimping, stent advancement and stent deployment in coronary arteries. The first two analyses are efficiently solved by means of ABAQUS/Standard mainly due to the relatively low number of elements in the model (stent and cylindrical surfaces) and unsophisticated contact conditions. Conversely, the simulation of stent deployment in coronary arteries is characterized by a very large number of degrees of freedom since several parts (one or two stents, angioplasty balloons, catheter guides, coronary arteries) with highly nonlinear mechanical behaviours are necessary to simulate the complex procedures in coronary bifurcation. Moreover, multiple self-contact and contact conditions among the parts are included in the model enhancing the difficulties of the system. Hence, ABAQUS/Explicit is adopted. Details of the simulation parameters for both approaches are proposed in the next paragraphs, focusing in particular on the strategies adopted for quasi-static analyses of balloon-expandable stent deployment with an explicit dynamics procedure.

3.1.5 Preliminary simulations: stent crimping and advancement

To precisely position the stents in the curved and bifurcated idealized arteries or in complex patient-specific anatomies, preliminary simulations of crimping and bending of the devices are performed using the implicit finite element commercial code ABAQUS/Standard (Dassault Systemes Simulia Corp., RI, USA). At the end of each simulation, the stressed configurations of the devices are passed to the subsequent analysis in order to keep track of the whole history of stress modifications.

At first, the initial configuration of the stent is crimped to a reduced external diameter by controlling the radial displacement of a cylindrical surface in contact with the stent (Fig. 3.7). Whether the stent design is characterized by simmetries, circumferential boundary conditions are applied to fasten the solution of the problem and assure accurate results. After the elastic recoil, plastic deformations occurring at the stent hinges allow the maintaining of the reduced the stent diameter, thus facilitating their insertion in the coronary vasculature. All contacts are modelled by means of a hard contact model in the normal direction and a tangential behaviour, with friction coefficient set to 0.2 [1].

Crimped configurations of the stents are then imported in the advancement simulation. Since the arterial tracts preceding the coronary bifurcations usually have greater diameters and higher curvature radii, stent advancement in these regions was assumed to be negligible for the stent final positioning. Thus, only the final part of the stent insertion is simulated. Internal cylindrical guides are created following the vessel centreline and discretized with rigid homogeneous shell elements. At this point, to simulate the stent advancement (Fig. 3.8) and obtain realistic stress distributions on the bent struts, the stents are pushed against the guide imposing longitudinal displacement to a series of nodes positioned close to the links (yellow arrows). Such boundary conditions are removed once the links approach the first

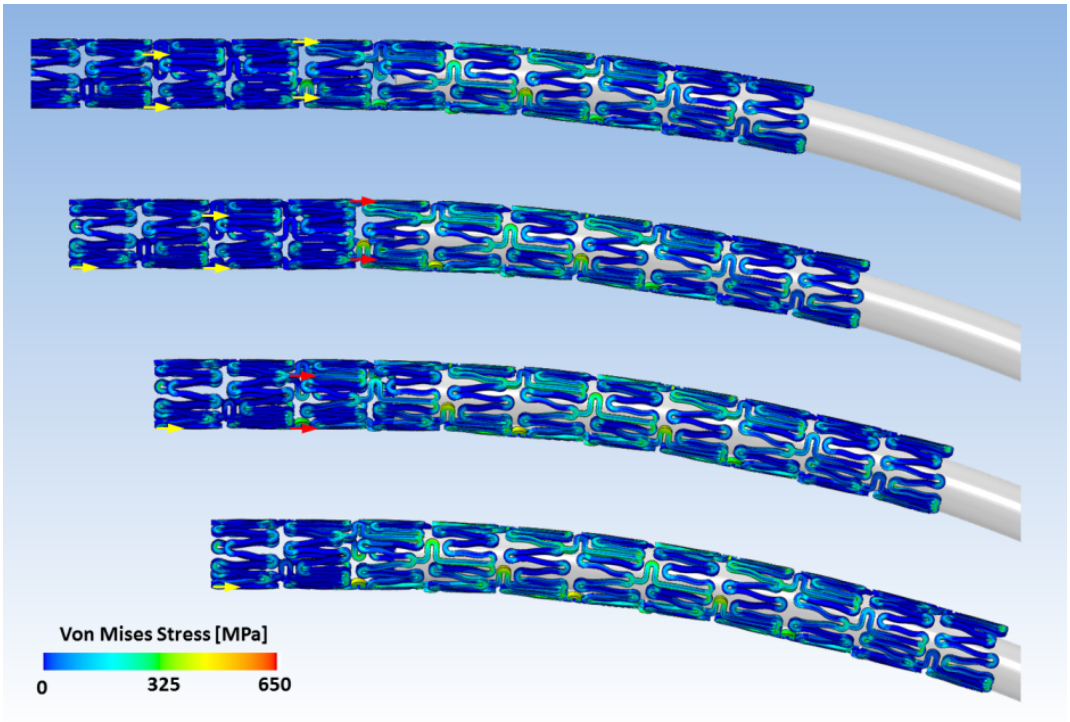

Figure 3.8: *Preliminary simulation: stent advancement. The stent is advanced along an internal cylindrical guide by applying displacement boundary conditions to a series of stent nodes (yellow arrows). Once these nodes approach the curved region (red arrows), the boundary conditions are removed to allow the free bending of the device. In the last step, all the boundary conditions are removed.*

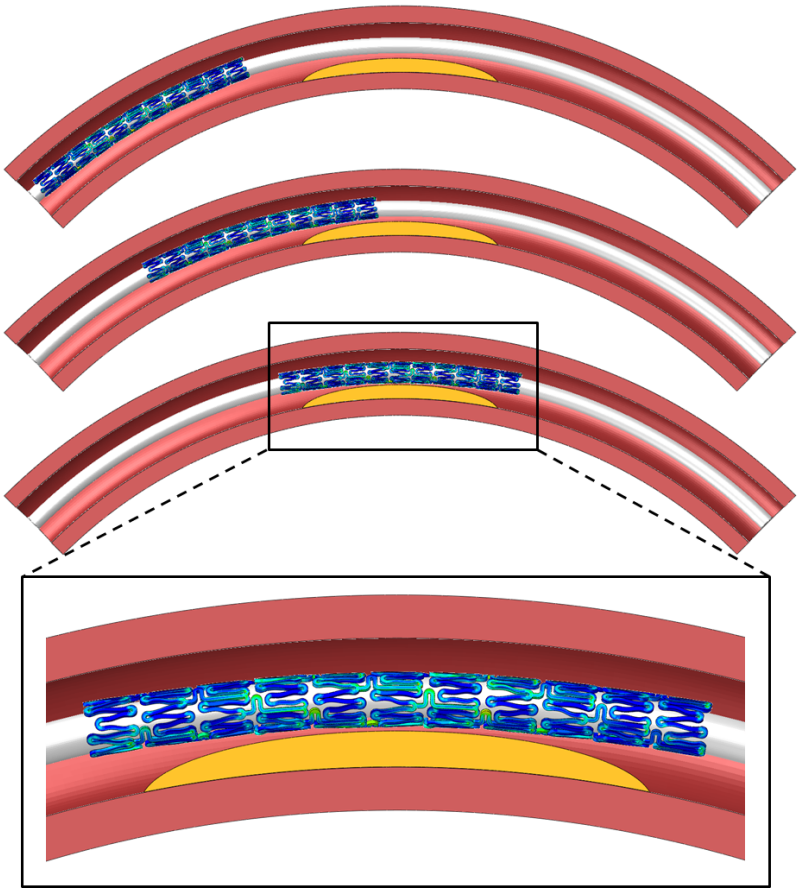

Figure 3.9: *Stent advancement in the curved atherosclerotic coronary artery. Contour maps shown reprenent von Mises stresses in the device and range from 0* MPa *(blue zone) to 650* MPa *(red zone).*

curve (red arrows) in order to let the stent free to bend along the guide. Contacts are set to have friction coefficient equal to 0.3 and the normal behaviour is modelled with a "softened" contact relationship in which the contact pressure is a linear function of the clearance between the surfaces. In the last step of the bending simulations, all the displacement boundary conditions are removed and only one node of the stent's distal end is constrained to its current position allowing the structure to adapt to the bending guide and reach a minimum-energy final static equilibrium.

In Fig. 3.9, the crimped Xience V stent model used in this example case is advanced within the curved artery previously described. If compared to the crimped configuaration of Fig. 3.7, a slight increase in the stress state of the device is evident in the magnification below while plastic deformations remain constant, thus justifying the choice of simulating the final path only. The stent is now ready to be deployed within the artery.

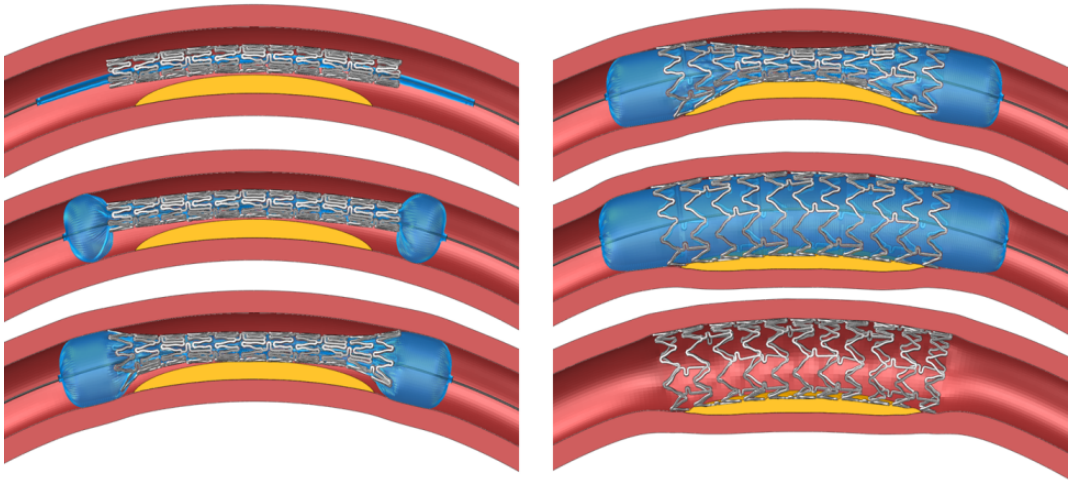

Figure 3.10: *Final simulation of stent deployment. The Xience V stent model is deployed in the atherosclerotic coronary artery by means of the inflation of a 3.0* mm *angioplasty balloon at 15* atm. *Starting from the initial assembly (above, on the left) and arriving to the final geometrical configuration (below, on the right), different stages of the stent deployment are depicted.*

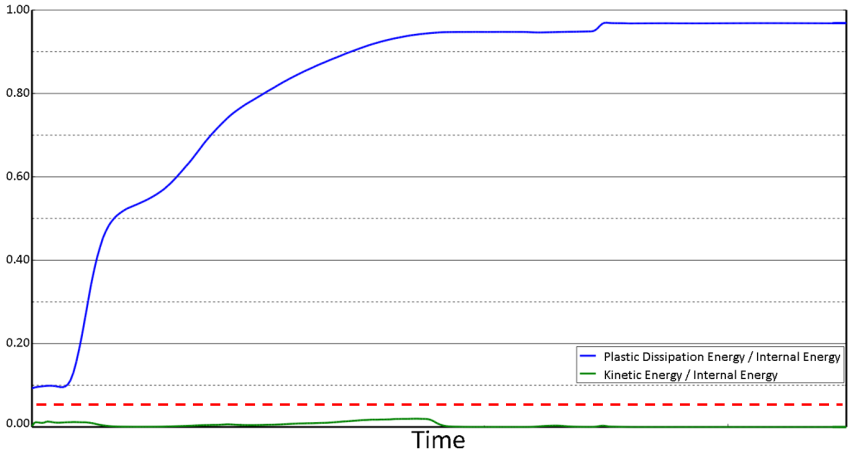

Figure 3.11: *Plot of the ratios between the plastic dissipation and internal energies (solid blue line) and between the kinetic and internal energies (green solid line). The quasi-static regime is ensured through the whole simulation since the Kinetic Energy / Internal Energy ratio is always maintained below the 5% limit (red dotted line).*

3.1.6 Final simulation: stent deployment

Due to the high nonlinearity of the problem (mainly a result of the nonlinear material behaviour and complex contact conditions), a quasi-static analysis of the stent deployment is implemented using an explicit dynamics procedure: the commercial code ABAQUS/Explicit (Simulia Corp., RI, USA) is adopted. Since ABAQUS/Explicit solves a dynamic equilibrium, in order to assure the quasi-staticity of the simulation and avoid that inertial effects become predominant in the solution, special care needs to be done while choosing the simulation parameters. Also, a check on the energy balance of the simulation has to be performed at the end of each analysis to verify the accuracy of the solution. In particular, the energy balance can be defined by the following equation:

$$\begin{aligned} \mathrm{E_I} + \mathrm{E_V} + \mathrm{E_{FD}} + \mathrm{E_{KE}} + \mathrm{E_{IHE}} - \mathrm{E_W} - \\ + \mathrm{E_{PW}} - \mathrm{E_{CW}} - \mathrm{E_{MW}} - \mathrm{E_{HF}} = \mathrm{E_{total}} = \text{constant} \end{aligned} \tag{11}$$

where $\mathrm{E_I}$ is the internal energy, $\mathrm{E_V}$ is the viscous energy dissipated, $\mathrm{E_{FD}}$ is the frictional energy dissipated, $\mathrm{E_{KE}}$ is the kinetic energy, $\mathrm{E_{IHE}}$ is the internal heat energy, $\mathrm{E_W}$ is the work done by the externally applied loads, and $\mathrm{E_{PW}}$, $\mathrm{E_{CW}}$, and $\mathrm{E_{MW}}$ are the work done by contact penalties, by constraint penalties, and by propelling added mass, respectively. $\mathrm{E_{HF}}$ is the external heat energy through external fluxes. To ensure that inertial effects are not predominant in the calculated solution, as a general rule, the kinetic energy of the deforming material should not exceed a small fraction (typically 5% to 10%) of its internal energy [88]. This control is even more important if permanent plastic deformations may arise in the analysis since inertial forces acting during plastic deformation may result in permanent unrealistic deformations of the structures.

Looking at the simulation parameters, since the explicit integration method (central difference rule) is only conditionally stable, specific attention needs to be paid to the time increment size that depends mainly on the characteristic element length, material constitutive parameters and density. Analysis time-step duration and loading rates are adequately chosen to ensure a static equilibrium along the analysis, mainly decreasing the loading rate during the expansion of the stents. In this work, to follow a cost-saving approach maintaining solution accuracy, an element-by-element stable time increment estimate coupled with a "variable mass scaling technique" is used, allowing an ad hoc adjustment of the material density in space and simulation time. This strategy allows to increase the density of only those elements characterized by lower stable increment time. In such a way, an increase in the global stable increment time is achieved without highly affecting the total mass of the structure and, as a result, the amount of kinetic energy in the simulation. Also, a viscous pressure is applied on the external surface of the different parts to reduce the low-frequency kinematic oscillations.

In the example here presented, the Xience V stent model previously crimped and advanced in the atherosclerotic region, is deployed with a 3.0 mm balloon inflated at 15 atm. Different stages of the simulation are illustrated in Fig. 3.10. Characteristic effects of stent deployment such as, dog-boning of the stent and straightening of the arterial wall are visible. Internal rigid guides are created and used as boundary conditions for the elements at the extrmities of the balloons that are constrained as rigid bodies. The nodes at the end of the

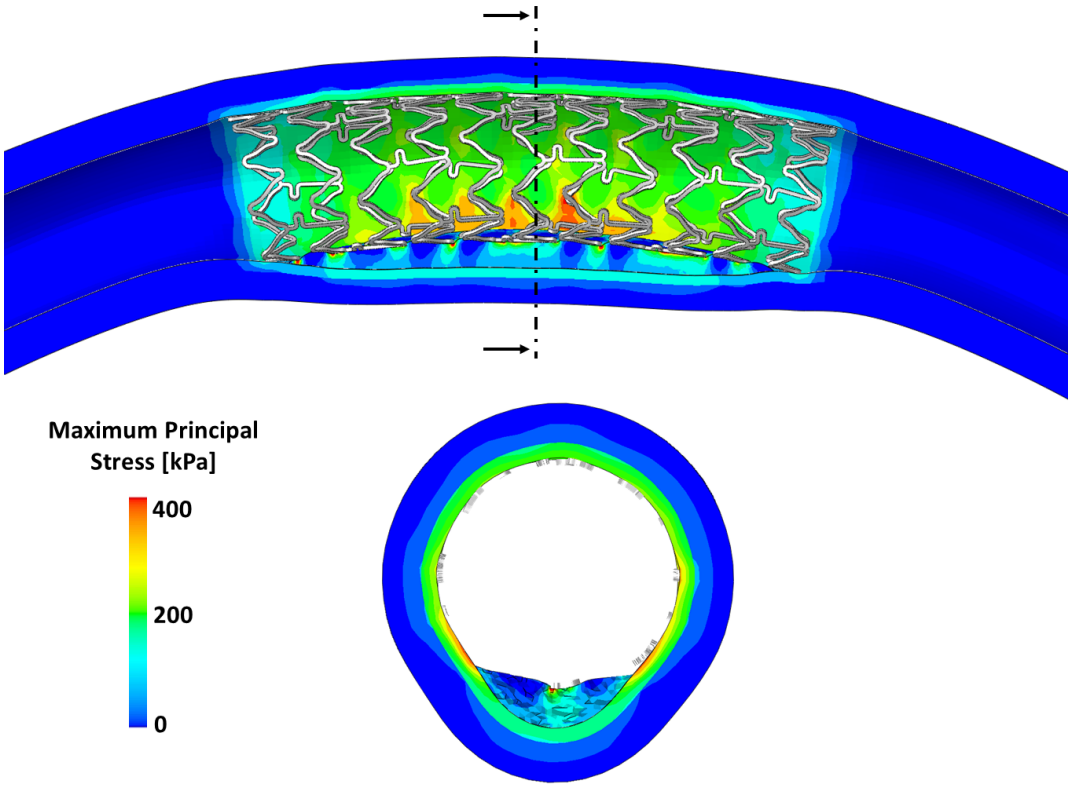

Figure 3.12: *Maximum principal stress contour maps in the arterial wall after the stenting procedure. Longitudinal (above) and cross section (below) images are proposed.*

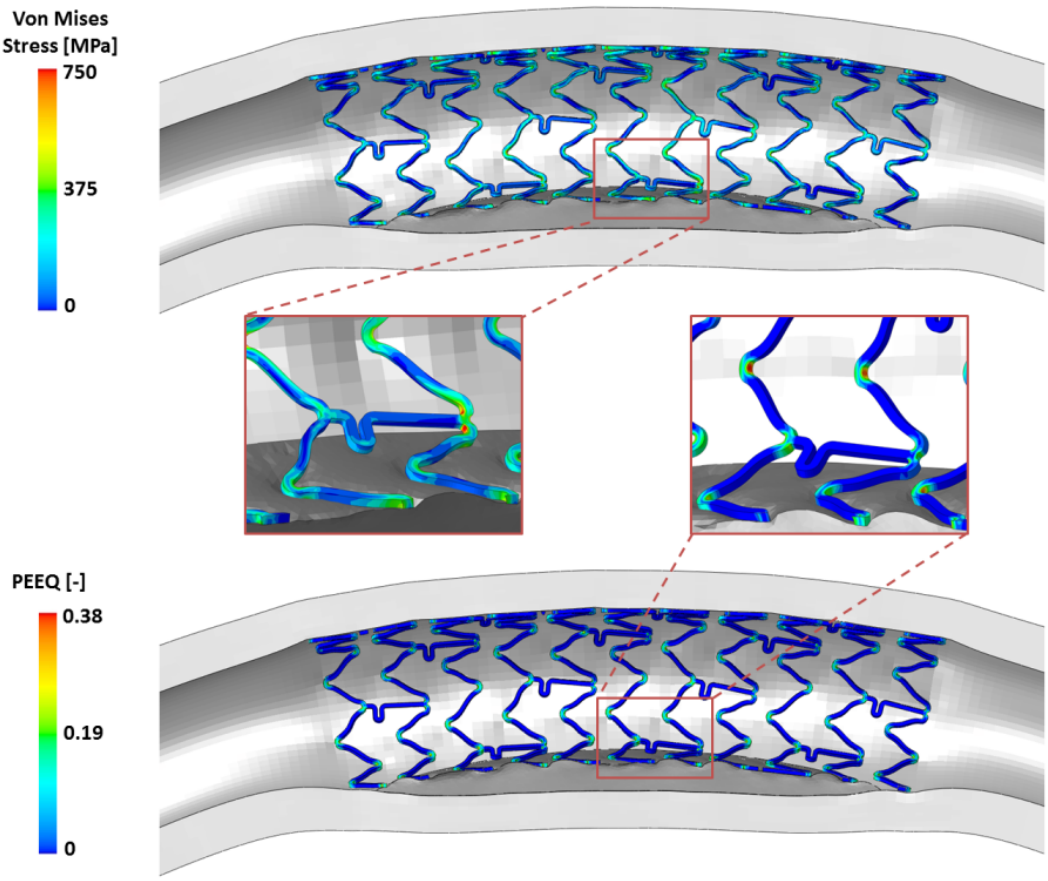

Figure 3.13: *Von Mises stresses on the stent (upper panel) and plastic equivalent deformations (PEEQ) (lower panel) contour maps obtained at the end of the stent deployment. In the magnifications, the areas with highest values are highlighted.*

arterial wall are constrained in the axial direction while no boundary conditions are applied to the stent. Contacts between parts of the model are defined according to the general contact algorithm available in ABAQUS/Explicit using a hard normal behaviour. A frictional tangential behaviour with a friction coefficient of 0.06 [46] is used in contacts involving the biological tissues while all other contacts have a friction coefficient of 0.2 [1]. Lastly, a tie constrain between the internal surface of the artery and the plaque cinematically restrains the relative movement of the two parts.

The first result that needs to be checked at the end of quasi-static simulations performed with an explicit dynamics procedure is the verification of their quasi-static character. In Fig. 3.11, the ratios between kinetic and internal energy (green line) and between plastic dissipation and internal energy (blue line) developed in the simulation are shown, confirming its quasi-static regime and the reliability of the computed results. Afterwards, the influence of stenting procedures on the coronary artery can be evaluated in terms of several geometrical parameters and biomechanical quantities. For instance, in Fig. 3.12 the contour map of the maximum principal stresses arising in the arterial wall is shown. Other important geometrical indexes such as metal-to-artery ratios related to the quantity of metal in contact with the artery, degree of stenosis describing the patency of the arterial lumen or tortuosity indexes associated to the straightening effect of the arterial wall provoked by stent implantation may be used to examine the effects of stenting procedures. Furthermore, looking at the implanted devices, in Fig. 3.13 the Von Mises stress and plastic equivalent deformation (PEEQ) contour maps obtained at the end of the procedure are presented. In the magnification areas, the most stimulated regions are shown as well. Von Mises stress is a geometrical combination of all the stresses (normal stress in the three directions, and all three shear stresses) acting at a particular location and it is defined as:

$$\sigma_{\mathrm{VM}} = \sqrt{\frac{(\sigma_{11}-\sigma_{22})^2 + (\sigma_{11}-\sigma_{33})^2 + (\sigma_{22}-\sigma_{33})^2 + 6\left(\sigma_{12}^2+\sigma_{13}^2+\sigma_{23}^2\right)}{2}} \tag{12}$$

On the other hand, PEEQ gives a measure of the amount of permanent strain occurring in a body. This quantity ($\bar{\varepsilon}^{\mathrm{p}}$) is the time integral of the equivalent plastic strain rate:

$$\bar{\varepsilon}^{\mathrm{p}} = \int_0^{\mathrm{t}} \dot{\bar{\varepsilon}}^{\mathrm{p}} \mathrm{dt} \tag{13}$$

where the equivalent plastic strain rate is calculated as:

$$\dot{\bar{\varepsilon}}^{\mathrm{p}} = \sqrt{\frac{2}{3}\dot{\varepsilon}_{\mathrm{ij}}^{\mathrm{p}}\dot{\varepsilon}_{\mathrm{ij}}^{\mathrm{p}}} \tag{14}$$

Mechanics of implanted stents can also be evaluated in terms of several geometrical parameters such as radial or longitudinal elastic recoil, foreshortening or dog-boning indexes. All these parameters are proposed and described in the study presented by Migliavacca et al. in 2005 [138].

3.1.7 Five-folded vs Multi-folded: choice of the balloon model

Commercially available angioplasty balloons present three to six folds. Computational analyses of stent expansion do not usually take into account the folded configuration of the

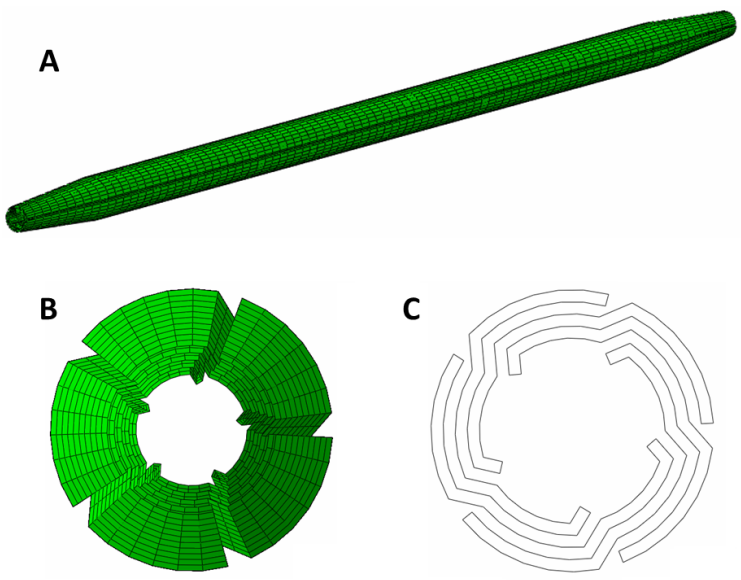

Figure 3.14: *Perspective (A) and radial (B and C) views of the five-folded balloon geometry and its discretization.*

Table 3.2: *Main geometrical and mechanical parameters [138] calculated for the free expansion simulations using five-folded and multi-folded balloon models.*

	Five-folded configuration	**Multi-folded configuration**
Central radial recoil	2.362	2.297
Longitudinal recoil	-0.350	-0.348
Foreshortening	8.285	8.004
Max Von Mises stress at full expansion [MPa**]**	841	802
Max Von Mises stress after recoil [MPa**]**	556	551

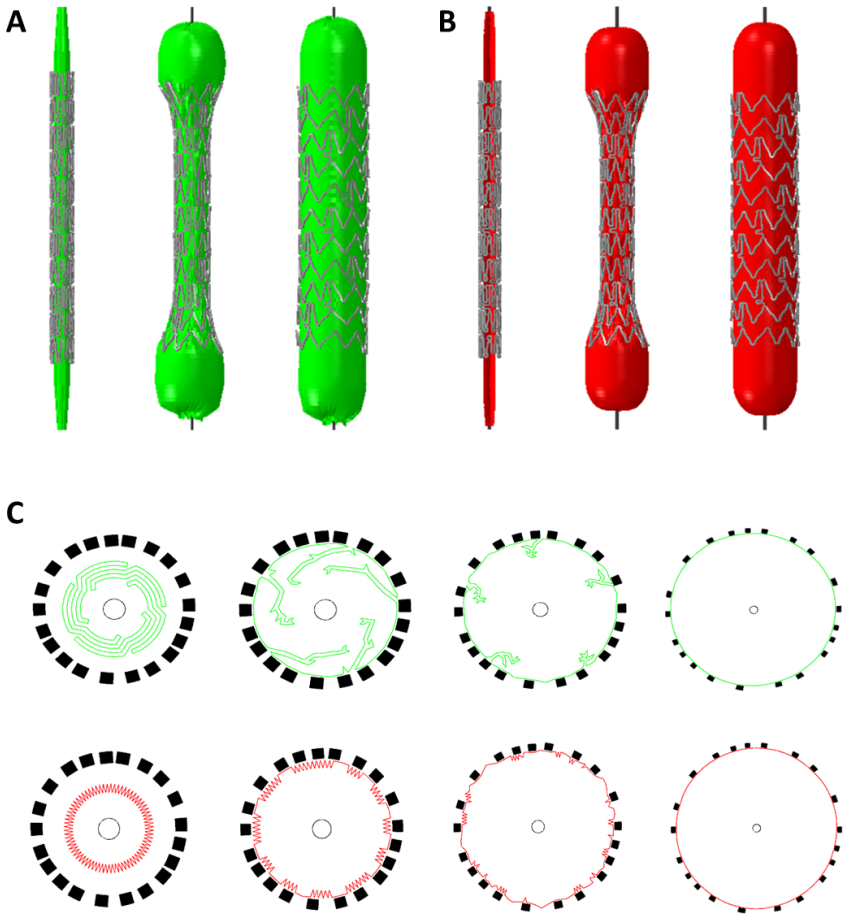

Figure 3.15: *Full view of the two free expansion simulations carried out by inflating the five-folded (A) and the multi-folded (B) balloon models at initial, middle and final configurations. C) Cross sectional cuts of the two stent free expansions at four different instants. For sake of clarity and to better visualize the balloon unfolding process, figures are not scaled.*

balloons [132] and only a few studies have developed folded balloon models [37, 122, 148, 216]. Due to this unsettled modelling choice, a comparison between five-folded and multi-folded balloon models is presented in this section. Free expansions of the Xience V stent models are implemented and both mechanical and geometrical parameters are used to explore the importance of the folded balloon configuration.

In order to obtain the five-folded balloon configuration, the geometry of an unexpanded balloon is created using the commercial CAD software Rhinoceros 4.0 Evaluation (Fig. 3.14). The external diameter of the folded balloon is set to 0.7 mm, and the wing length chosen resulted in an expanded balloon diameter of 3.0 mm, an appropriate coronary stent diameter. The tapered ends replicated the real clinical assembly, with the balloon ends constrained to the catheter. However, the CAD geometry still contained idealizations, such as sharp edges, and the creation procedure resulted highly time-consuming. On the other hand, the multi-folded balloon is created with the process described in section 3.1.2 and is characterized by a 3.0 mm diameter as well. Discretization, element type and material model used are chosen similar for both balloon models.

After crimping, free expansion simulations of the stent models are implemented in ABAQUS/Explicit following the methodologies previously described. The gradual inflation of the two balloon configurations at 15 atm is shown in Fig. 3.15a and Fig. 3.15b, which highlights the different balloon expansion. The unwrapping of the wings makes the five-folded configuration more complicated to fully expand resulting in higher computational requests. The inflation dynamics are remarkably distinguishable. The cross sectional views (Fig. 3.15c) prove that while the five folds are evident until the end, the multi-folded configuration soon takes an almost circular form. As expected, the less uniform expansion induced by the five-folded balloon inflation generated higher stresses during expansion, even though the final Von Mises stresses after recoil in the two simulations are comparable. Nevertheless, despite the different balloon expansions, the stent deployment resulted similar, in terms of both mechanical and geometrical parameters. For a quantitative proof, Table 3.2 provides the comparison details, reporting the values of the parameters considered in a stent deployment assessment. Stent deployments in coronary arteries through these two balloon models were also performed giving rise to similar considerations. As a consequence, these results are not reported here.

In conclusion, a more realistic folded configuration, as the five-folded model presented, is feasible but does not result in an improved assessment of the mechanics of stent expansion. Moreover, the use of the five-folded model causes an increase of the time needed for the preparation of the geometrical model, its discretization and the computational power required for the simulations. In light of these considerations, the balloon models used in this thesis will continue to exploit the multi-folded configuration.

3.1.8 Qualitative validation of structural models

Currently, validation is one of the major issues for biomechanical numerical models. Since a direct validation is not straightforward mainly due to the lacking of accurate experimental studies on stenting procedures, indirect qualitative comparisons among our numerical simulations and *in vitro* expansions of metallic stents found in the recent literature are here proposed. In particular, a qualitative comparison, visible in Fig. 3.16a and published in

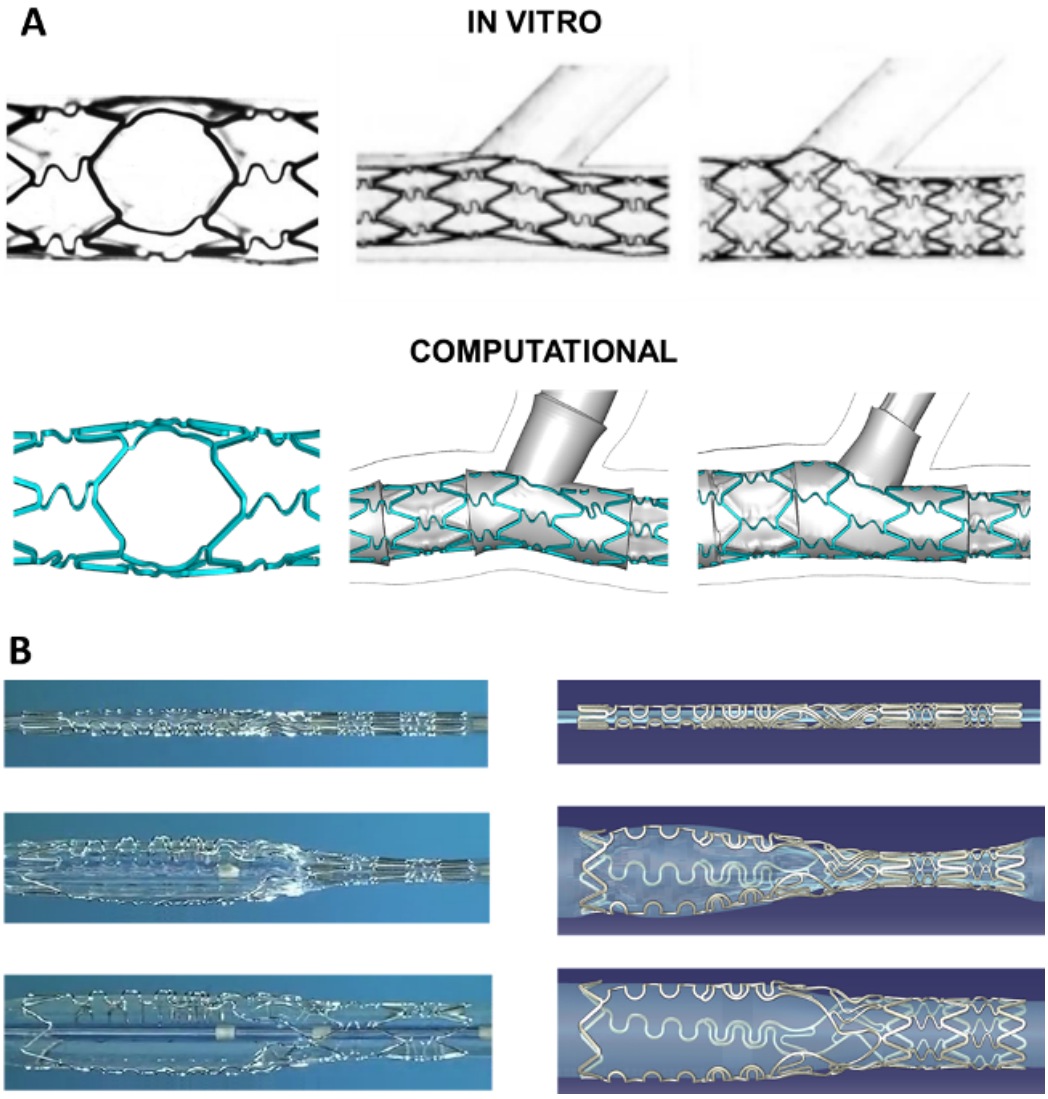

Figure 3.16: *A) Comparison between the results of the experimental data (top, modified by Ormiston et al. [162] and of the computational analysis (bottom). Left and centre the results after the SB stenting in two different views; right the configurations after the FKB. Image copied with permission from Ormiston et al. [162] and Gastaldi et al. [66] B) Comparison between the numerical and in vitro free deployments of the Tryton SB stent. Images of the in vitro expansion are taken from the animation proposed by Dr Schultz and published in the website http://www.pcronline.com.*

Gastaldi et al. [66], shows a good agreement between the numerical results and the geometrical configuations achieved by an experimental stent deployment proposed by Ormiston et al. [162] to analyse the device distortions after expansion of the balloon in the SB and after the FKB. Moreover, in Fig. 3.16b, the finite element expansion of the dedicated device Tryton is compared with an *in vitro* deployment. The peculiar two-steps expansion and final configuration of the dedicated device are caught in both the methods. In conclusion, the similarity between the two solutions provides a first qualitative validation of the implemented numerical models.

3.2 Fluid dynamic model of a stenting procedure

The second part of the sequential numerical model developed in this thesis investigates the effects of stenting procedure on the hemodynamics of coronary arteries starting from the final geometrical configurations of the structural simulations to create realistic fluid domains. CFD analyses are implemented within ANSYS commercial code (Ansys Inc., Canonsburg, PA, USA) using the ICEM CFD package for the discretization and Fluent package for the solution of the models.

3.2.1 Creation and discretization of the fluid domain

To increase the realistic character of the CFD analyses, results of the structural analyses are used to create the fluid domains. At each significant procedural stage, the surfaces of the stents and the biological tissues defining the blood volume are exported from ABAQUS in terms of triangulated surfaces. Afterwards, these surfaces are imported into ANSYS ICEM CFD (Fig. 3.17a). Volume discretization is the subsequent step. Due to the complexity of the stented arteries geometry, the high computational cost required for this kind of analyses usually represents one of the main problems and limiting issues. Thus, in order to reduce the number of nodes and to increase computational speed, a hybrid discretization of the volume is firstly developed using both hexahedral and tetrahedral elements (Fig. 3.17b). Hexahedral elements should be preferred because of higher accuracy and reduced number of elements for a given volume. Nevertheless, hexahedral elements are difficult to be used in highly complex geometrical structures, such as the intersection zones between strut stent and arterial wall, where tetrahedral elements become necessary. The meshing method consists in the creation of internal cylinder along the artery. This cylinder is meshed with only hexahedral elements, while in the region between the cylinder and the arterial wall a fully tetrahedral mesh is created. Lastly, merging of the two meshes is performed through pyramidal elements. The proposed discretization method has been compared with a standard tetrahedral mesh. Results of this comparison and other details on this method are presented in Chiastra et al. [31]. Briefly no significant differences are observed between the two cases in terms of average WSSs in the stented region for this straight artery; however, computational time for hybrid mesh was halved in comparison with that required by the tetrahedral one. In conclusion, improvements offered by this method give the opportunity to simulate the blood flow in a whole stented bifurcation.

In the example case of this section, following the dimensional values suggested by the sensitivity analysis performed in Chisatra et al. [31], the final mesh obtained resulted in a

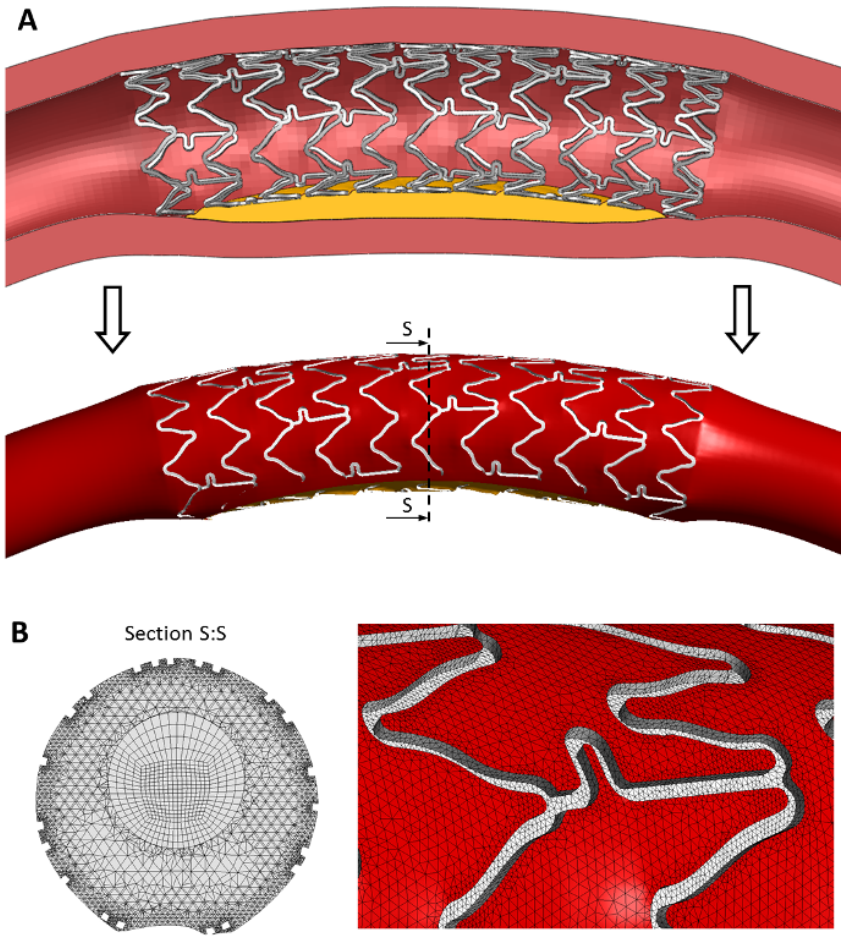

Figure 3.17: *A) Creation of the fluid domain from the geometrical configuration obtained through structural simulations. B) Hybrid discretization method. Example of the mesh of the cross-section S:S located in the middle of the stented artery. It is possible to notice the internal cylinder meshed with only hexahedral elements and connected through pyramid elements to the region of tetrahedrons necessary due to the complexity of the external surface. Tissue prolapse among stent struts is also observable. On the right, detail of the external surface characterized by the track of the stent struts.*

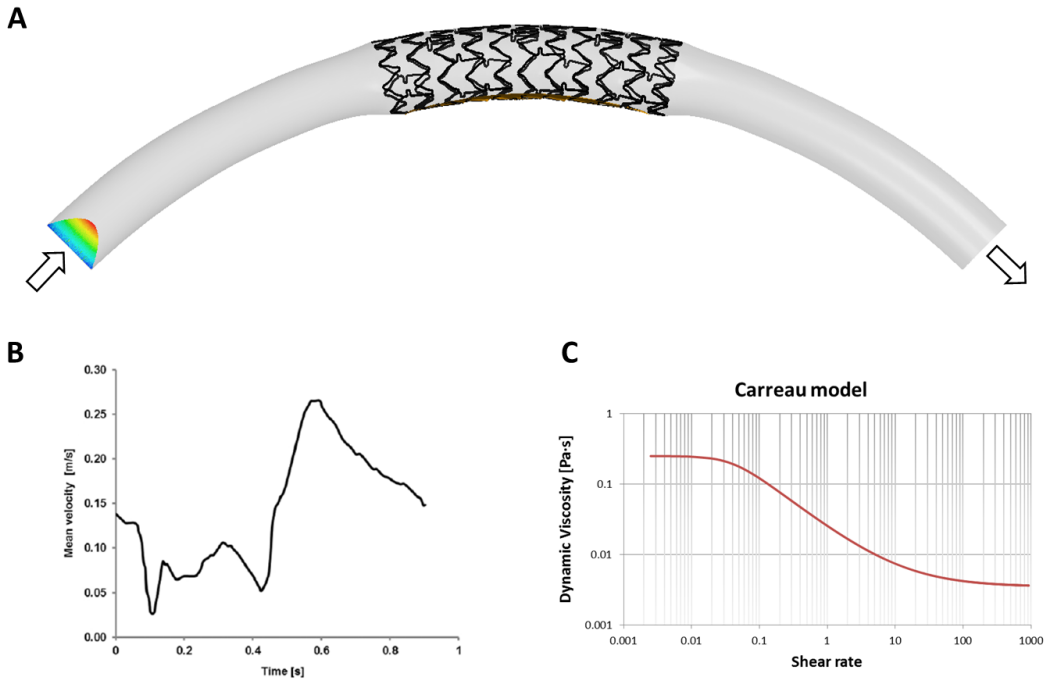

Figure 3.18: *A) Fluid dynamic model of the curved stented artery. B) pulsatile velocity tracing applied at the inlet of the artery. C) Carreau's model used to describe the non-Newtonian character of the blood dynamic viscosity.*

total of 166,005 hexahedral cells and 3,076,968 among tetrahedral and pyramidal cells.

3.2.2 Fluid dynamic model

Fluid dynamic simulations are carried out through solving the continuity and momentum conservation equations, using the commercial package ANSYS Fluent that is based on a finite volume method (Fig. 3.18a). A coupled solver was used with a second-order upwind scheme for the momentum spatial discretization and a first-order time implicit scheme to discretize the governing equations. A time step size of 10^{-2} s was considered after an appropriate temporal sensitivity analysis. Under-relaxation factors of 0.4 for pressure and momentum and 1 for density are used while convergence criterion for continuity and velocity residuals is set to 10^{-6}. Simulations are performed on a desktop computer equipped with a 2.93 GHz quad-core processor with 16 GB RAM using 4 parallel processors.

A pulsatile blood flow tracing according to Davies et al. [36] (Fig. 3.18b) is applied at the inlet as a paraboloid-shaped velocity profile. The average flow rate value is 60 ml/min (mean velocity = 0.13 m/s) and the duration of the cardiac cycle is 0.903 s. The adopted profile is representative of a typical flow tracing of a human LAD coronary artery. A zero pressure condition is applied at the outlet of the fluid volume. Artery and stent struts were assumed to be rigid and defined with a no-slip condition.

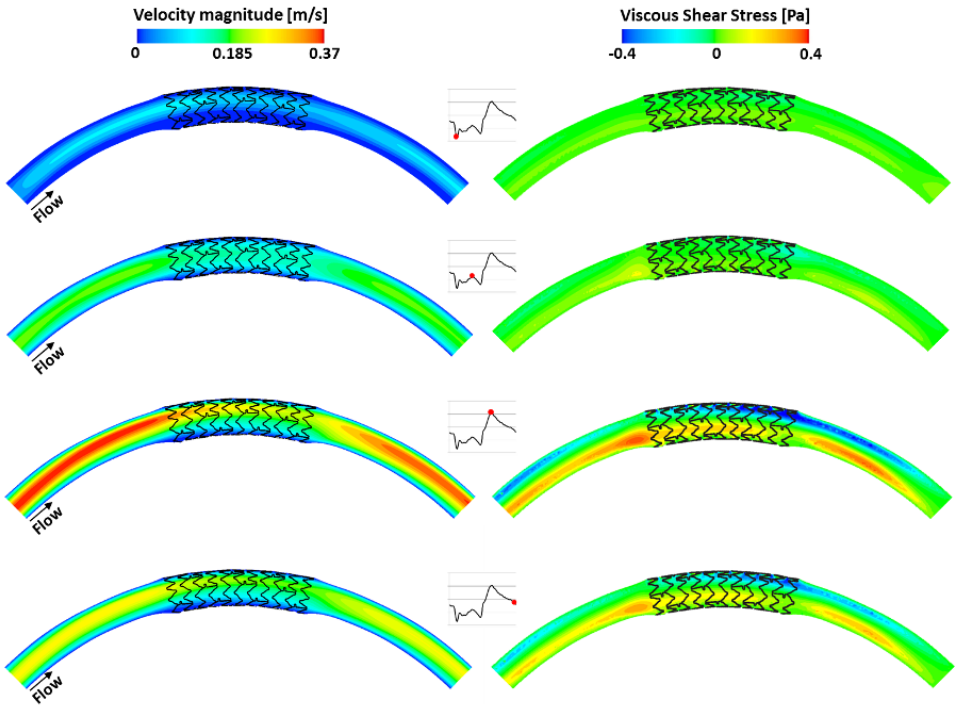

Figure 3.19: *Bulk flow assessment. Velocity magnitude (left) and in-plane VSS (right) fields occurring at four different time steps of the CFD simulation.*

Blood is described as an incompressible, non-Newtonian fluid with a density equal to 1060 kg/m^3 and the viscosity varying according to the Carreau's model (Fig. 3.18c):

$$\mu = \mu_\infty + (\mu_0 - \mu_\infty) \cdot [1 + (\lambda \cdot S)^2]^{n-1/2} \tag{15}$$

where S is the shear rate, μ is the dynamic viscosity, μ_0 and μ_∞ are the viscosity values at S equal to zero and infinite, which, respectively, are equal to 0.25 Pa·s and 0.0035 Pa·s, λ is the time constant equal to 25 s, and n is the Power-Law index equal to 0.25. These values correspond to those proposed by Seo et al. [186].

3.2.3 Fluid dynamic results

The results of the CFD simulations are analysed considering both bulk-flow (Fig. 3.19) and near-wall (Fig. 3.20) hemodynamic quantities.

At the moment, bulk-flow quantities have not been associated to any interesting biological phenomenon related to stenting procedures. However, their investigation is still interesting since they allow to understand the influences of stent implantation on the local blood flow patterns highlighting potential low flow regions, recirculation or stagnation zones. Among bulk-flow quantities, velocity magnitude and in-plane viscous shear stresses (VSS) will be

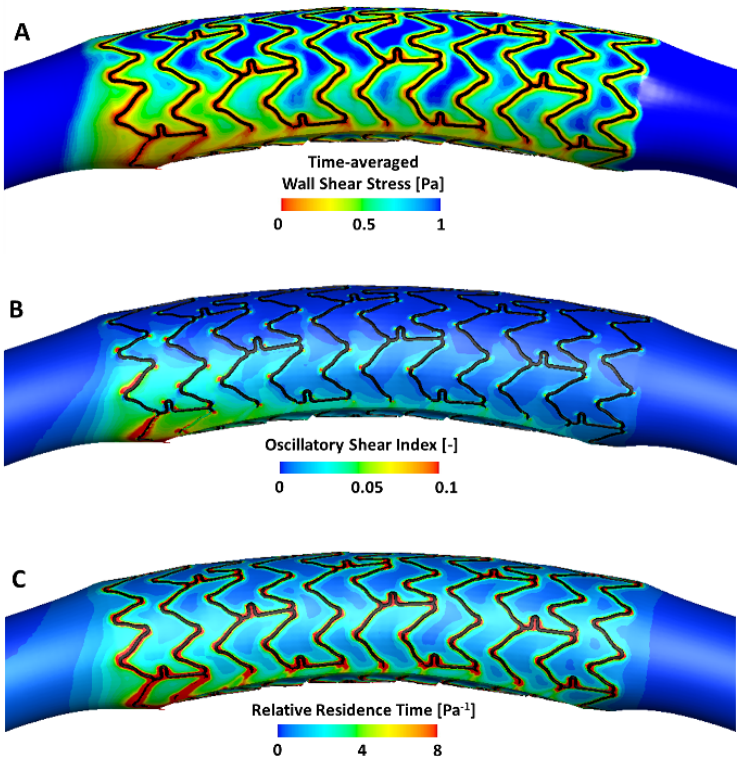

Figure 3.20: *Near wall quantities assessment. A) time-averaged wall shear stress (TAWSS); B) Oscillatory Shear Index (OSI); C) Relative Residence Time (RRT).*

investigated throughout the thesis. In particular, in-plane VSS describe the effects of shearing between adjacent layers of fluid, which roughly represents the force exerted by the fluid on suspended blood cells, and can be defined as:

$$\mathrm{VSS} = \mu \left(\frac{\mathrm{dV_1}}{\mathrm{dU_1}} + \frac{\mathrm{dV_2}}{\mathrm{dU_2}} \right) \tag{16}$$

where μ is the dynamic viscosity and $\mathrm{dV_1}$, $\mathrm{dV_2}$, $\mathrm{dU_1}$ and $\mathrm{dU_2}$ are velocities and displacements in two directions of the plane. On the other hand, near-wall quantities as time-averaged wall shear stress (TAWSS)(Fig. 3.20a), Oscillatory Shear Index (OSI) [111] (Fig. 3.20b) or Relative Residence Time (RRT) (Fig. 3.20c) allow describe the forces exerted by the fluid flow on the endothelial layer and have been associated in several studies to the major clinical issues related to stenting procedures [108]. Particularly, low and oscillating WSS are proven to increase the risks for in-stent restenosis [111].

TAWSS is defined as:

$$\mathrm{TAWSS} = \frac{1}{\mathrm{T}} \int_0^{\mathrm{T}} |\vec{\tau}_{\mathrm{W}}| \, \mathrm{dt} \tag{17}$$

where $\vec{\tau}_W$ is the WSS vector, and T is the duration of one cardiac cycle. OSI values close to 0.5 represent a highly oscillating WSS field [129] and is commonly defined as:

$$OSI = \frac{1}{T}\left(1 - \frac{\left|\int_0^T \vec{\tau}_W dt\right|}{\int_0^T |\vec{\tau}_W| \, dt}\right) \tag{18}$$

Finally, RRT depends on both OSI and TAWSS values and is defined as:

$$RRT = \frac{1}{(1 - 2 \cdot OSI) \cdot TAWSS} \tag{19}$$

Validation of fluid dynamic results in terms of velocity fields will be discussed in the Chapter 5 where numerical studies will be compared to experimental measurements achieved by means of Particle Image Velocimetry (PIV) performed in stented polymeric bifurcated arteries.

3.2.4 Boundary conditions in bifurcated arteries

In case of bifurcated arteries, the sole use of the velocity inlet condition is not sufficient to adequately describe the hemodynamic field. In particular, the flow split between daughter branches has to be defined; two main strategies may be pursued. The former is associated to studies based on experimental measurements of *in vivo* coronary trees that results in empirical laws relating flow rates and dimensions of the bifurcating arteries. An example is the brilliant study from Murray [155] that in 1926 led to the following formula:

$$\frac{q_{D2}}{q_{D1}} = \left(\frac{d_{D2}}{d_{D1}}\right)^3 \tag{20}$$

where q_{D1} and q_{D2} are the mean flows through the diameters of the two daughter branches (d_{D1} and d_{D2}). Recently, different studies [96, 203] proved that, specifically for the coronary tree, the flow ratio between daughter branches is best described with lower exponential values. In particular, van der Giessen et al. [203] found that a power value of 2.27 results in a better agreement with the previously mentioned experimental measurements. The latter strategy used in the scientific literature [211] involves the combination in a multi-domain approach of the 3D CFD model of the stented coronary bifurcations with lumped parameter models of the downstream coronary tree applied at the outlets (Fig. 3.21b) [176]. These models are able to investigate the influence of atherosclerotic plaques and stent implantation in the flow split. Preliminary simulations are carried out for a coronary bifurcation model without and with plaques (limit cases) considering a part of the lumped parameter scheme proposed by Pietrabissa et al. [172] and are presented in Morlacchi et al. [143]. Four cardiac cycles were simulated in order to guarantee accuracy of the multi-domain approach used and a very small time-step (10^{-4}s) was used to allow convergence of the lumped parameter model scheme. Results in terms of flow rates at the outlets were identical for both the two limit cases. This occurrence showed that downstream districts play a dominant role in establishing the blood flow distribution to downstream tissues. In other words, the flow resistances created by mild plaques or the stent struts in the SB area do not influence the flow distribution between the distal MB and the SB. This assumption is in accordance with the results obtained by Balossino et al. [13] in 2009 for a carotid artery bifurcation where

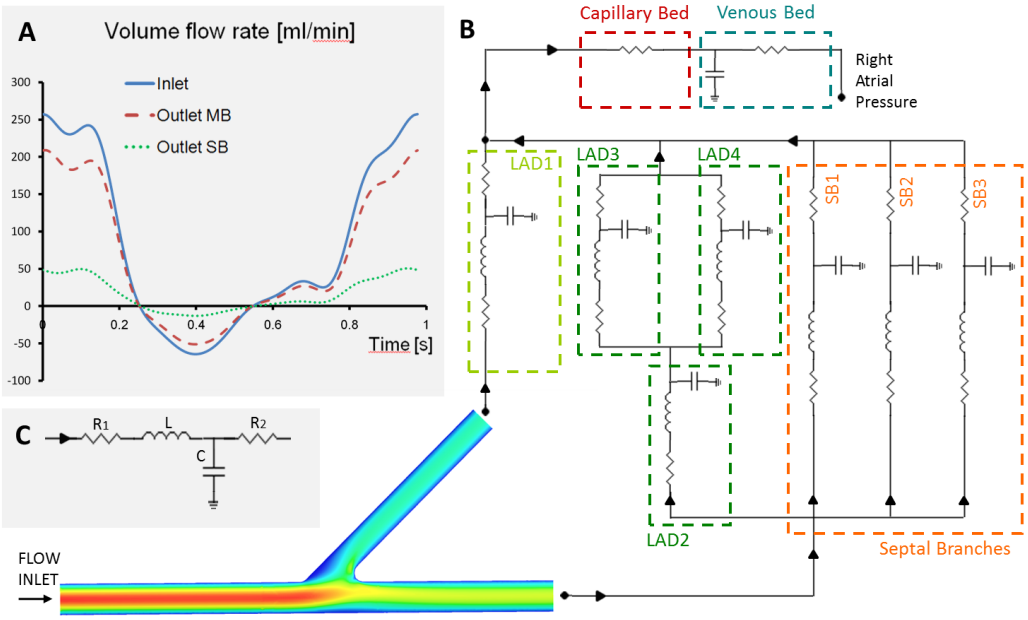

Figure 3.21: *Multi-domain model of the LAD coronary artery. Below on the left, the 3D model of the coronary bifurcation with the lumped parameter model of part of the coronary tree connected to the outlets. (A) Flow tracing used as inlet condition (solid line) proposed by Charonko et al. in 2009 [27] and the flow tracings obtained at the MB (line-dotted model) and at the SB (dotted line). (C) Example of the lumped parameter scheme used to model a segment of a coronary vessel characterized by two resistances, a capacitance and an inductance. Image copied with permission from Morlacchi et al. [143].*

only a stenosis equal to 90% in terms of area reduction affected the flow split between the branches of the carotid bifurcation. As a consequence, flow tracings at boundaries (Fig. 3.21a) characterized by constant flow split seem to be physiological and only depending on the downstream vasculature, allowing the use of stand-alone CFD models. Obviously, this occurrence is not valid in presence of a very severe stenosis or complete obstruction of vessels and has to be carefully evaluated for each case studied. Moreover, neglecting the lumped parameter model at the outlet cross sections allows the opportunity of obtaining accurate results with a greater time step size (10^{-2}s vs 10^{-4}s) and without simulating more consecutive cardiac cycles. This choice strongly reduces the computational time.

3.3 Limitations

Numerical models here presented are built to simulate real physical systems and the relation among its variables. Due to the complexity of biomechanical systems, current numerical models investigating this topics are characterized by several limitation and modelling assumptions. As a consequence, any conclusion, especially clinical considerations, derived from such study should be interpreted with caution bearing in mind all the limitations in-

troduced and hereby reviewed.

3.3.1 Limitations of the structural model

The main limitation of this work is the description of biological tissue constitutive laws. More advanced constitutive models are available in the literature taking into account the anisotropy related to fibre dispersion in the tissue [63, 64, 86, 149]. However, in order to apply these more complex constitutive models, parameters calibration is a crucial issue. Precise information about fibre orientation in the bifurcated region as well as the properties of the plaques are required; they are sensitive to the specific patient and nearly impossible to obtain from routine clinical exams. An additional limitation of our model is the absence of any rupture mechanism in the arterial components. This limitation has effects on the absolute values of the stresses and deformations of the arterial layers. However, the adopted simplified constitutive relations are an efficient and simple comparative framework to estimate the non-physiological state created by the insertion of a stent with multiple balloon expansions. Indeed, results can be useful to evaluate the vessel zones more prone to damage and hence more subjected to the restenotic process. Another imprtant limitation is related to the plaque modelling since it is described as a homogenoeus material while, in reality, it is a highly dishomogenous tissue characterized by the presence of different components (clacifications, lipids, necrotic core etc.). Lastly, the geometries of the artery and the plaques are ideally drawn through CAD software and do not implement in detail the actual anatomy of the human coronary tree. Reconstruction based on the use of medical images, especially for the artery lumen, would have provided more realistic geometries, although hardly providing information on arterial wall thickness. Numerical models of the devices are fully idealized considering both their materials and geometry. In particular, a common medical Co-Cr alloy is used for all the devices even if each stent is characterized by a typical alloy whose specific composition and treatment is most of the times unknown. Lastly, as described in Section 3.1.7, a multi-folded geometry is chosen after a comparison with a more realistic five-folded balloon model. However, this comparison has not been performed in curved arteries yet. Beside not expecting major differences, this issue will be one of the first points that will be investigated in the further developments.

3.3.2 Limitations of the fluid dynamic model

The arterial wall is assumed to be rigid and the movement of the artery due to the presence of the heart is not taken into account. This assumption could result in different WSS distributions and blood flow patterns. Currently, in the literature there is an absence of works on fluid-structure interaction in highly complex geometries, like stented coronary bifurcations. An exploratory, fluid-structure analysis should be performed to evaluate the effects of such fluid dynamic features and their importance in a stented vessels. Moreover, the geometric configuration here analysed refers to the instants immediately subsequent to the stent implantation where stent struts are in a direct contact with the flow stream. In reality, stents are rapidly (a few days) covered by a neo-intimal layer that results in a smoothed fluid volume. This limitation, however, does not prevent our models to identify the regions where in-stent restenosis will more likely initiate even if the progress of the disease may be better investigated by means of mechano-biological model of tissue growth.

Chapter 4

Stenting procedures for coronary bifurcations: three case studies

Contents

The main reasons to more deeply investigate stenting procedures for coronary bifurcations were widely discussed in Chapter 1 and recently published in a review by Moore et al. [142]. Briefly, these regions are associated to a high risk of vascular diseases and lower clinical results mainly due to technical difficulties during the treatments and sub-optimal procedural outcomes. Despite consensus has been reached on some topics related to coronary bifurcations [192], several issues are still under debate and the optimal procedure suitable for all the different lesions and anatomic variations of coronary bifurcations has not been found, yet. Moreover, the new findings on the pathobiology of cardiovascular diseases or technical innovations such as the new dedicated devices may lead to an improvement of the current clinical state of the art.

As a consequence, the sequential numerical model described in Chapter 3 has been used to provide a better investigation of the biomechanical influence of different stenting procedures for coronary bifurcations. In particular, three different case studies are presented. First, a new tapered balloon is proposed to improve the Final Kissing Balloon (FKB) inflation within the Provisional Side Branch (PSB) approach by reducing the overexpansion caused by the simultaneous expansion of two balloons in the proximal part of the MB; second, different single- or double-stenting procedure involving conventional devices are simulated and compared in terms of structural and hemodynamic quantities; lastly, a new dedicated device designed to facilitate the double-stenting culotte technique is investigated highlighting its main advantages and drawbacks.

4.1 Final Kissing Balloon inflation: a new tapered balloon

The FKB inflation was the first technique to be specifically developed for percutaneous interventions in coronary bifurcations and still plays an important role in their treatment. FKB is the simultaneous expansion of two angioplasty balloons in both branches of the bifurcation and its main purposes are the optimization of stent apposition to arterial walls, correction of stent deformation and improvement of the SB access [187]. Clinical studies [3, 30] demonstrated that the FKB procedure causes an improvement in the clinical results of complex double-stenting procedures like crush or culotte techniques. However, the simultaneous deployment of two balloons in the main vessel results in a great arterial overexpansion that could negatively influence the biomechanical environment. As a consequence, uncertainty still remains on the application of the FKB procedure within single-stenting techniques such as the PSB stenting approach [158, 163, 165]. PSB consists of the stenting of the MB and subsequent opening of the SB access by means of a SB balloon deployment. Because of its ease and good clinical outcomes, nowadays PSB is the preferred bifurcation stenting strategy [114]. However, since a better investigation of the biomechanical influences of FKB within the PSB approach is still needed, the sequential numerical model previously described has been applied to this clinical case and presented in this section. Stresses in the arterial wall generated by stent and balloon expansions and hemodynamic forces acting on the intimal layer of the vessels are examined before and after the FKB procedure enlightening both its benefits and drawbacks. Furthermore, a new tapered balloon dedicated to bifurcations is proposed to decrease the overexpansion of the MB, limit the structural

damage induced to the arterial wall and to enhance the fluid dynamic WSS patterns at the internal layers of the bifurcation.

4.1.1 Main features of the sequential model

- Coronary bifurcation model

A CAD model representative of the bifurcation of the LAD coronary artery with its first diagonal branch (Fig. 4.1a) is created using Rhinoceros 4.0 Evaluation CAD program (McNeel and Associates, Indianapolis, IN, USA). The model has an angle of bifurcation of 45° [170] and includes the presence of two asymmetric atherosclerotic plaques corresponding, for the most critical section, to a 2.06 mm hydraulic diameter and a 45% of percentage area stenosis, calculated as:

$$\text{Stenosis}\,[\%] = 100 \cdot \left[1 - \left(\frac{D_h}{D_0}\right)^2\right] \tag{1}$$

where D_h is the hydraulic diameter, and D_0 is the internal diameter of the MB without plaques. The internal diameters of the MB and SB are, respectively, 2.78 mm and 2.44 mm [120] while the thickness of the arterial wall (0.9 mm) is considered constant along the whole artery. The arterial wall is divided into three layers with different thicknesses corresponding to the intima (0.24 mm), the media (0.32 mm), and the adventitia (0.34 mm) in accordance to the work of Holzapfel et al. [92]. The mechanical behaviour of the coronary artery and atherosclerotic plaques is defined in accordance to the hyperelastic or hyperelastic-plastic models described in Chapter 3. Discretization of the model is performed in accordance to the previously described methods as well.

- Angioplasty balloon and stent models

Cylindrical polymeric balloons are created in the expanded shape with a diameter of 3.0 mm (MB) or 2.0 mm (SB) and a thickness of 0.03 mm and then deflated by applying a negative pressure to the internal surface, obtaining a multi-folded geometry. Furthermore, a novel tapered balloon dedicated to the FKB inflation is investigated as well. This balloon is characterized by a proximal conical part, a zone of transition, and a distal cylindrical part with a diameter of 2.0 mm as depicted in Fig. 4.1b. The polymeric material of the balloons (PET polymer) is described using an elastic linear isotropic model with a Young modulus of 1455 MPa and a Poisson coefficient of 0.3. Balloon models (Fig. 4.1b) are discretized using about 20,000 four-node membrane elements with reduced integration. The pressure-diameter curves for the normal and the tapered balloon show a very similar behaviour, comparable to typical experimental data from manufacturers and reported in literature [67].

The model of the stent (Fig. 4.1c) resembles the geometry of the Xience V coronary system (Abbott Laboratories, Abbott Park, IL, USA). Its main geometrical features, mechanical behaviour and discretization process are fully described in Section 3.1.3. Briefly, this stent is fabricated using a Co-Cr alloy and is characterized by a length equal to 15.5 mm, an external diameter in the non-crimped configuration of 1.76 mm and a strut thickness of 90 μm.

- Structural model

The structural numerical simulations are conducted using ABAQUS/Explicit (Dassault Systemes Simulia Corp., RI, USA), modelling the stent expansion as a quasi-static process

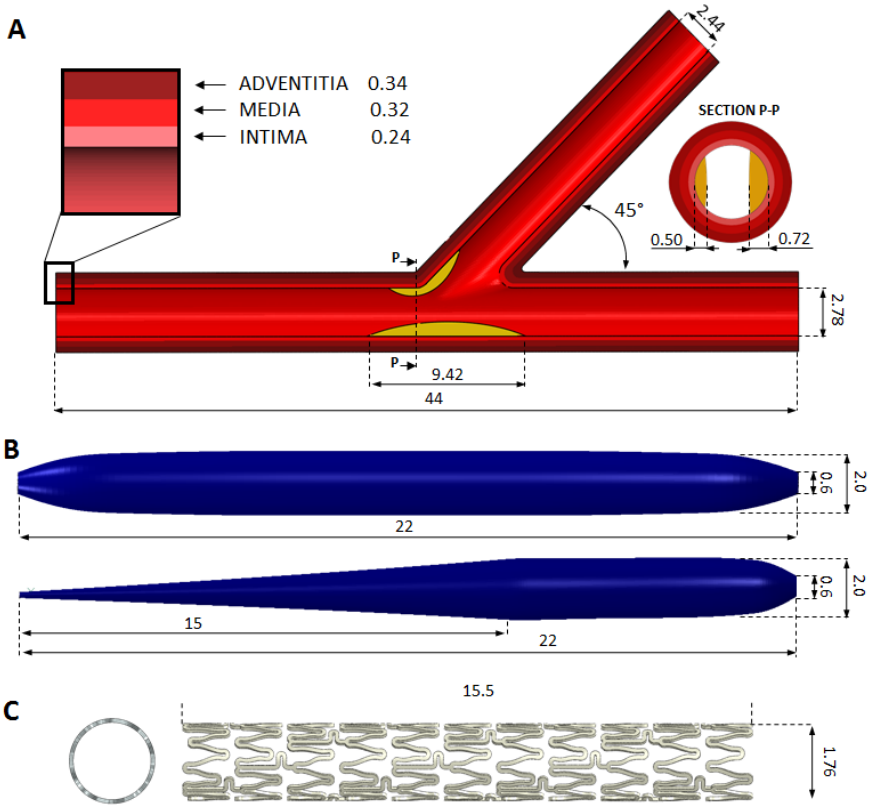

Figure 4.1: *A) Geometric model of the atherosclerotic bifurcation. In the magnification area on the left, the stratification of arterial wall in the three layers (intima, media, and adventitia) is depicted. On the right, the illustration of the section corresponding to the maximal stenosis (45% of stenosis area) provoked by the presence of the two atherosclerotic plaques. B) Example of the two different models of polymeric balloons: a standard cylindrical balloon (top) and a tapered balloon characterized by a conical proximal part and a cylindrical distal part (bottom). C) CAD model of the Multilink Vision stent. On the left, the cross section of the device is depicted. Dimensions are reported in mm. Image copied with permission from Morlacchi et al [143].*

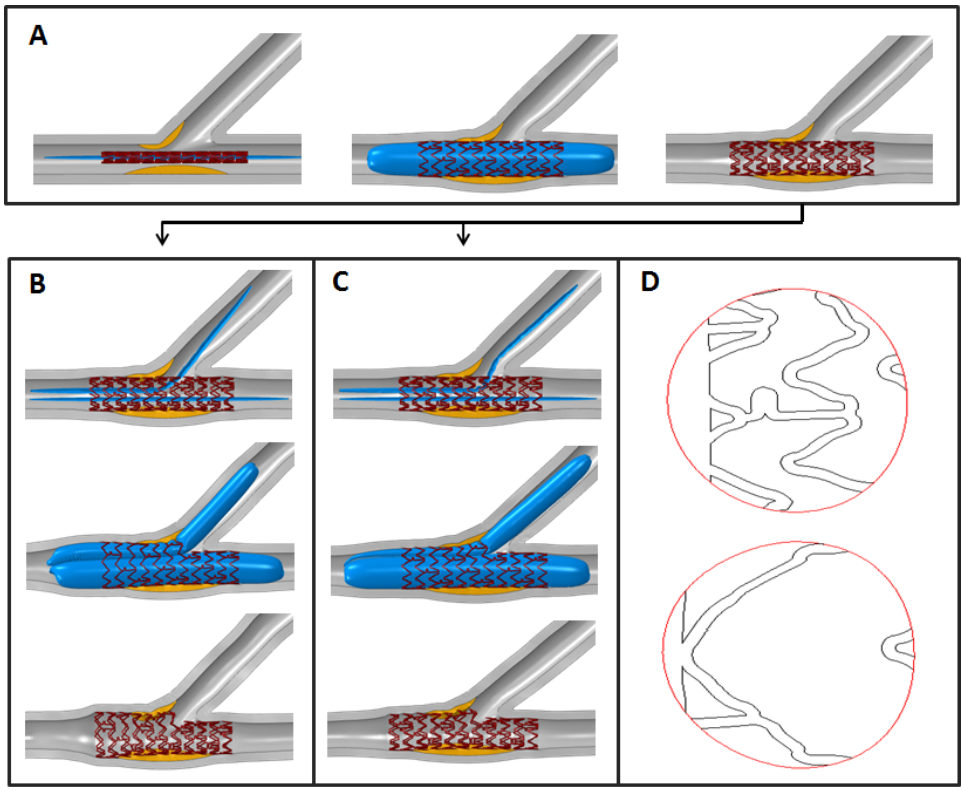

Figure 4.2: *PSB simulation steps. A) Positioning of the crimped stent followed by the implantation in the MB and the elastic recoil. B) Final step called "standard FKB" inflation was performed with two cylindrical balloons in both branches. C) Simulation of the "modified FKB" carried out by deploying a cylindrical balloon in the MB and a tapered one in the SB. D) Deformed configurations of the stent struts in proximity of the bifurcation before (top) and after (bottom) the standard FKB, view from the access to the SB. Image copied with permission from Morlacchi et al. [143].*

as described in Section 3.1.6. In particular, the stenting procedure investigated in this work is the PSB stenting approach, which is simulated through three main numerical steps:

Step 1: Crimping of the stent to an external diameter of 1.04 mm by controlling the displacement of a cylindrical surface in contact with the external surface of the device.

Step 2: Positioning of the crimped device across the bifurcation and implantation of the stent in the MB by applying a uniform pressure of 15 atm to the internal surface of the 3.0 mm balloon (Fig. 4.2a)

Step 3: FKB procedure, which consists in the simultaneous expansion of two balloons in both branches of the bifurcation using a pressure of 15 atm. The SB balloon crosses the device through the most distal strut. This procedure allows the opening of the stent cell across the bifurcation (Figs. 4.2b and 4.2c) maintaining a straight configuration of the device in the MB. In order to better analyse the biomechanical influence of this FKB procedure, two different simulations of Step 3 are carried out: (i) the "standard FKB" operated with two standard cylindrical balloons, a 3.0 mm balloon in the MB and a 2.0 mm balloon in the SB (Fig. 4.2b), and (ii) the "modified FKB" operated with a cylindrical 3.0 mm balloon in the MB and a tapered balloon in the SB (Fig. 4.2c).

After each step previously described, the elastic recoil of the system was allowed by the deflation of the balloons (Steps 2 and 3) or the release of the cylindrical surface (Step 1). The boundary conditions applied to the coronary artery constrain the ends of the vessels in the circumferential and axial directions in order to take into account the coronary tree before and after the region of interest. In these regions, radial displacement is allowed. The lengths of the branches are properly chosen in order to maintain the boundary conditions far from the region of interest. The terminal nodes of the balloons are only constrained in the radial direction. No boundary conditions are directly applied to the stent model, which is driven by the balloon inflation and wall interaction. The highest values of the von Mises stresses in the device and the average value of the maximum principal stresses affecting the intimal layer in the stented area are the quantities of interest analysed in the results.

- Fluid dynamic model

At each significant procedural stage, the surfaces of the stent and the biological tissues defining the blood volume are exported from ABAQUS and used to create the fluid volume for the CFD simulations. Then, hybrid meshes (Section 3.2.1), composed of both hexahedral and tetrahedral elements, regarding the three different cases are implemented: (1) bifurcation after stenting of the MB (model MBst), (2) bifurcation after "standard FKB" (model FKBstd), and (3) bifurcation after "modified FKB" (model FKBmod). Mesh parameters (in particular, maximum element size) are chosen after an appropriate sensitivity analysis on WSS in the region close to the stent, resulting in a number of elements equal to almost 2,600,000 and ensuring that results were independent of the number of mesh elements.

Fluid dynamic simulations are carried out through solving the continuity and momentum conservation equations, using the commercial package ANSYS Fluent 12.1 (Ansys Inc., Canonsburg, PA, USA), based on a finite volume method. A coupled solver is used with a second-order upwind scheme for the momentum spatial discretization and a first-order time implicit scheme to discretize the governing equations. After a temporal sensitivity analysis, a 10^{-2} time step size is chosen and resulted in a computational time equal to almost 40 hours for each transient simulation using a desktop computer equipped with a 2.93GHz quad-core

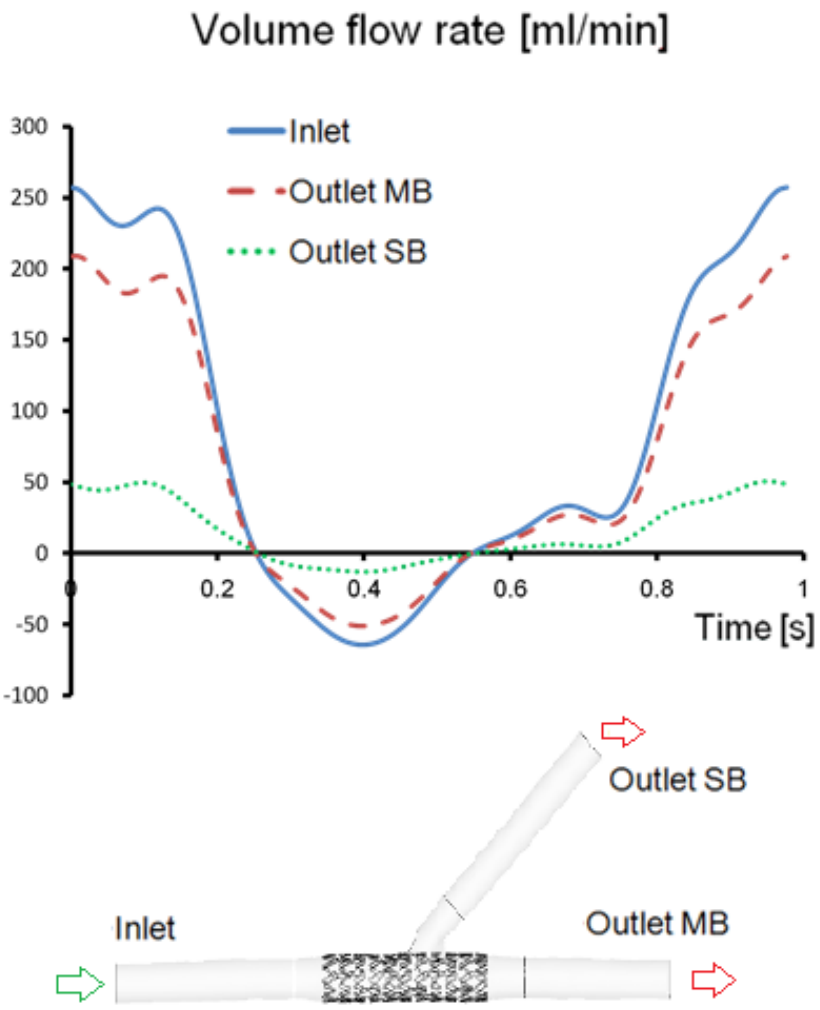

Figure 4.3: *Flow tracing used as inlet condition (solid line) proposed by Charonko et al. [27] and the flow tracings applied at the MB (line-dotted model) and at the SB (dotted line). Image modified with permission from Morlacchi et al. [143].*

processor with 8 Gb RAM. Artery and stent struts are assumed to be rigid and defined with a no-slip condition. Blood is described as a non-Newtonian fluid using the Carreau model proposed by Seo et al. [186]. A pulsatile blood flow tracing is applied at the inlet as a paraboloid-shaped velocity profile with an average flow rate of 80.7 ml/min according to a study by Charonko et al. [27] (Fig. 4.3). Lastly, a constant flow split is imposed at the bifurcation outlets considering the results of preliminary multi-domain analyses described in Section 3.2.4. Results are proposed in terms of TAWSS, OSI and velocity magnitude.

4.1.2 Results

- Structural results

Mechanical stresses and deformation fields in the arterial wall, the plaques, and the stent are examined in each PSB simulation performed. Figure 4.4a shows the contour maps of the maximum principal stresses in the arterial wall at the maximum expansion of solely the MB balloon and after the elastic recoil of the stent. A comparison of these contour maps shows that stenting of the MB provokes a lower stress state in the artery if compared to the standard FKB inflation (Fig. 4.4b). This phenomenon is mainly caused by the simultaneous deployment of two balloons in the MB. However, performing the FKB procedure with a modified tapered balloon reduces the stress state applied to the artery in the corresponding region (Fig. 4.4c). These qualitative considerations are confirmed by the quantitative analysis presented in Fig. 4.5 where the maximum principal stresses affecting the intimal layer are averaged only considering the values in the stented region. Stress values obtained in the MBst case at the maximum expansion and after the elastic recoil are 94.16 kPa and 68.48 kPa, respectively. The same quantities increase until 269.28 kPa and 213.82 kPa following the standard FKB procedure and until 165.68 kPa and 127.31 kPa following the modified FKB procedure. Contour maps of von Mises stresses in the stent are illustrated in Fig. 4.6a after the implantation in the MB while the effects of the standard FKB on the device are depicted in Fig. 4.6b. Considering the MBst case, the highest value of this quantity is 773.2 MPa and is located at the bow of a strut in the middle of the device. After inflation of the standard FKB, both in the proximal part of the device and in the opened strut at the SB access, stress values exceed 900 MPa with a maximum value in the opened strut of 927 MPa. Due to the minor expansion, the modified FKB procedure reduces the stresses in the device in the proximal part of the bifurcation but still does not diminish the stress field in the opened strut region of the stent.

- Fluid dynamic results

Hemodynamic forces acting on the internal layer of the artery are analysed in terms of TAWSS magnitude and OSI (Fig. 4.7). Percentage of area exposed to TAWSS lower than 0.5 Pa is 62.3% for MBst and 79.0% for FKBstd, respectively (Figs. 4.7a and 4.7b). FKBstd creates a wider region characterized by low WSS in the proximal part of the MB and, particularly, at the entrance of the stent. The situation is partially improved by the introduction of the modified balloon (Fig. 4.7c), resulting in a smaller area exposed to low TAWSS (71.3%). Figure 8 illustrates the contours of the OSI, as well. In the end, Fig. 4.8 shows the stent strut influence on the local blood flow pattern in terms of velocity magnitude field before and after inflation of the modified FKB (Figs. 4.8a and 4.8b, respectively). Contours are plotted on the plane transversal to the bifurcation. A qualitative analysis of

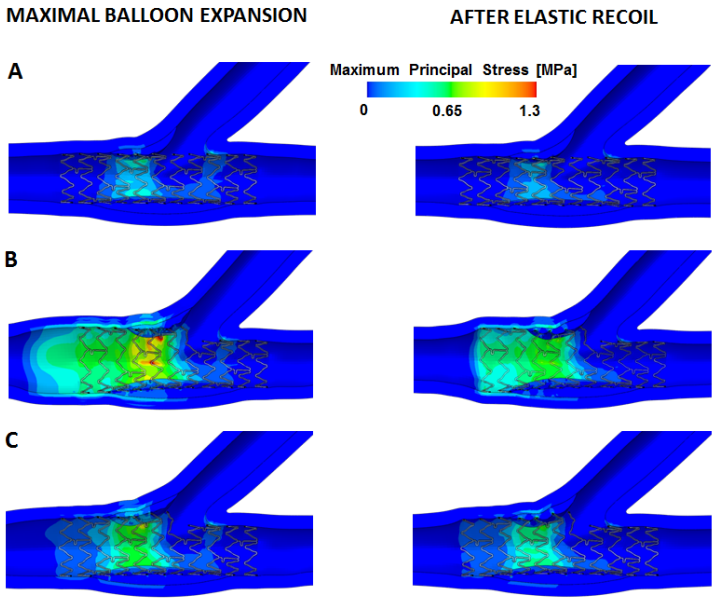

Figure 4.4: *Maximum principal stress contours in the artery during (A) the MB stenting implantation, (B) the standard FKB, and (C) the modified FKB inflation at the maximum balloon expansion (on the left) and after the elastic recoil (on the right). Image copied with permission from Morlacchi et al. [143].*

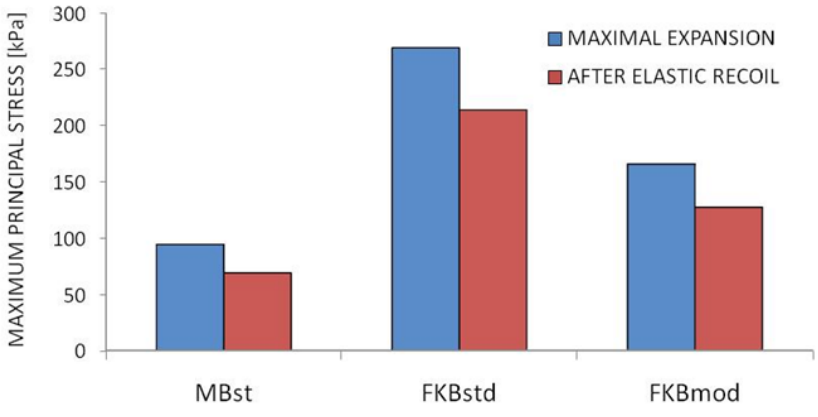

Figure 4.5: *Averaged values of the maximum principal stresses in the intimal layer of the stented region of the MB in the three cases analysed. Image copied with permission from Morlacchi et al. [143].*

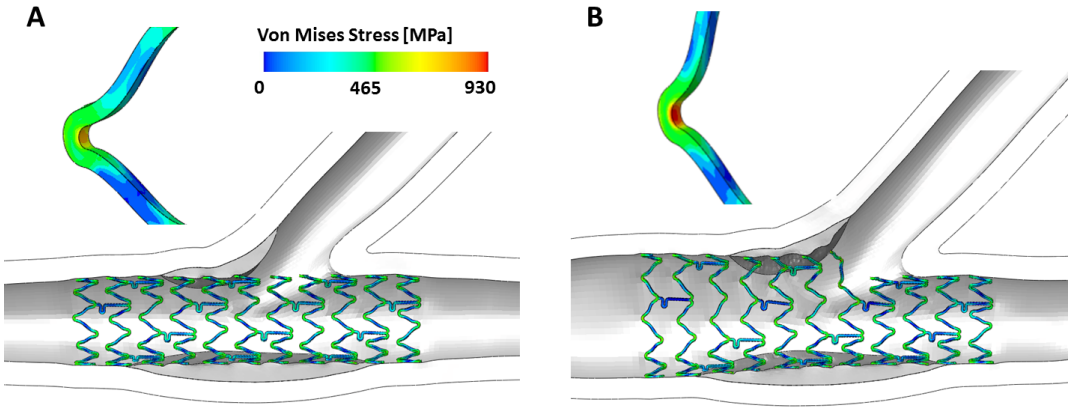

Figure 4.6: *Von Mises stresses contours on the stent before (A) and after (B) the standard FKB inflation at the maximum balloon expansion. In the magnification, example of the different stress state of an expanded strut in the proximal region of the main branch. Image copied with permission from Morlacchi et al. [143].*

the results obtained shows the positive influence of the FKB that removes the stent struts from the blood flow, freeing the access to the SB and lowering the hemodynamic disturbances downstream from the bifurcation.

4.1.3 Discussion

The sequential structural and fluid dynamic numerical model is applied to the PSB stenting approach, regarded as the most commonly used technique for coronary bifurcations. Any clinical consideration derived from this study should be interpreted with caution bearing in mind that only a single geometry is investigated for the coronary bifurcation and stent. However, three different cases are simulated (MBst, FKBstd, FKBmod), corresponding to different stenting procedures or balloon shapes. As expected, the three structural simulations generated very different deformed configurations for the artery and the stent, enhancing the importance of a structural simulation to obtain reasonable geometries for CFD simulation after stenting. These geometries could not have been deduced a priori.

One of the aspects investigated is the overall biomechanical effect of the FKB, performed with two standard cylindrical balloons (3.0 mm in the MB and 2.0 mm in the SB), within the PSB approach. The decision on whether performing or not the FKB after a single-stenting technique like PSB is still an open question. In agreement with this debate, numerical simulations presented in the present work highlight both advantages and limits of performing the FKB procedure. For instance, our results highlight that stenting of the MB permits, in this case, total recovery of the vessel lumen but reduces access to the SB by interposing metallic struts in the midst of the blood flow. Figure 4.8a clearly shows the fluid dynamic alterations caused by the presence of the hanging struts. Execution of the FKB allows the displacement of these struts and frees the access to the SB, while maintaining at the

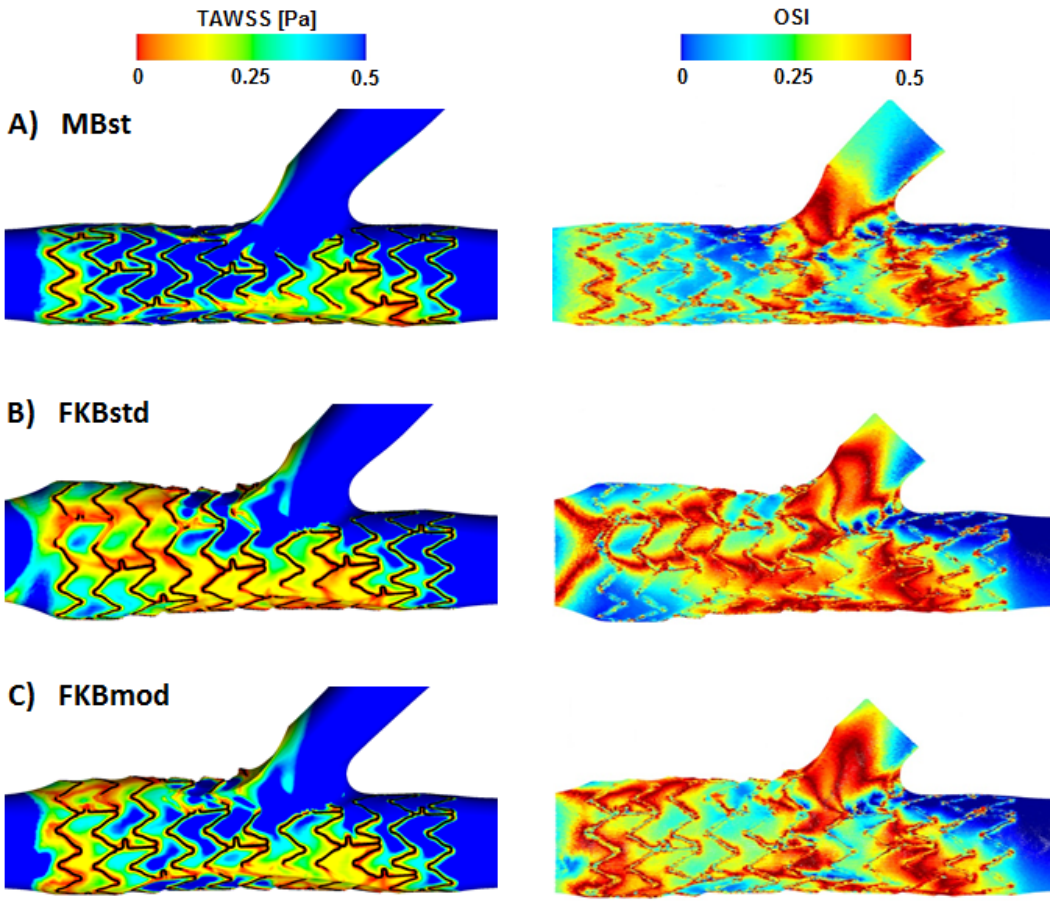

Figure 4.7: *Hemodynamic forces acting on the endothelial layer, contours of TAWSS (on the left) and OSI (on the right) for the analysed cases: (A) stenting of the MB, (B) standard FKB inflation performed with two cylindrical balloons (3.0 mm in the MB and 2.0 mm in the SB), and (C) modified FKB inflation performed with a cylindrical 3.0 mm balloon in the MB and a dedicated conical balloon in the SB. Image copied with permission from Morlacchi et al. [143].*

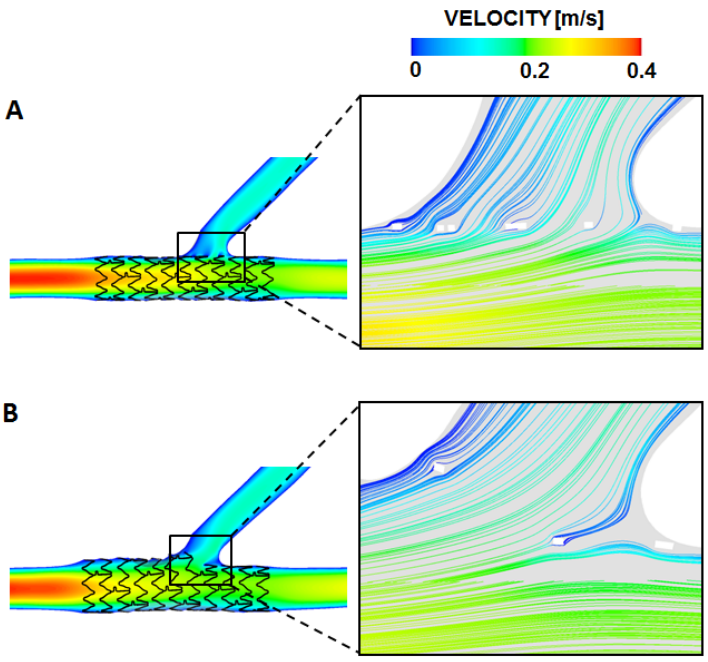

Figure 4.8: *Velocity magnitude contour map and streamlines in the transversal plane after the MB stenting (A) and the modified FKB (B), respectively. Image modified with permission from Morlacchi et al. [143].*

same time a straight configuration of the device (Fig. 4.2). These results highlight the improvements in the local blood flow pattern in terms of a more regular flow downstream of the bifurcation (Fig. 4.8b). On the other hand, FEM simulations demonstrate that FKB inflation (Fig. 4.4b) provokes an overexpansion of the proximal part of the MB if compared to the MB stenting only (Fig. 4.4a) resulting in greater stresses in the arterial wall both at the maximum expansion of the balloons and after its elastic recoil. Figure 4.5 shows the increase from 94.16 kPa to 269.28 kPa of the average maximum principal stresses evaluated in the intimal layer of the stented region. This increase might affect the clinical outcome of the treatment in terms of ST and ISR, respectively. Moreover, FKB influences the stress state in the device as well. In particular, the stent reaches an elevated level of stress and deformation that might significantly exceed the design limit, both in the proximal part of the MB and in the expanded strut at the bifurcation. In particular, the highest value of the von Mises stresses in the device passes from 773.2 MPa to 927 MPa. High stresses are also associated to high deformations in the structure of the device that, as shown by Guerin et al. [79], are related to damage of the polymer coating and a malfunction of the beneficial drug application to the area. Another drawback caused by the FKB procedure is the alteration of hemodynamic forces acting on the endothelial cells. After the FKB (Fig. 4.7b), the area characterized by WSS lower than 0.5 Pa is wider than in the case of MB stenting only (Fig. 4.7a) and rises from 62% to 79%. This phenomenon is more evident in the proximal part of the MB and, particularly, at the entrance of the stented area. A threshold value of 0.5 Pa

was considered because clinical studies [110, 129] suggested that lower values of WSS can promote the ISR phenomena. This region is particularly critical also because of the high OSI values calculated. Elevated values of OSI predict a higher risk of ISR as well [129].

The last considerations proposed in this work are related to the use of a different balloon specifically designed to overcome the major limitation provoked by a standard FKB inflation, the overexpansion in the proximal part of the MB. This balloon is characterized by three different regions: a tapered proximal part, a transition zone, and a distal standard cylindrical part. By performing a modified FKB using the tapered balloon, the overexpansion of the MB decreases while maintaining, at the same time, the positive effects of this procedure from the hemodynamic point of view. Simulations show that the use of a tapered balloon improves the biomechanical influence of the FKB (Fig. 4.4c) by lowering the average stress value calculated in the stented region (Fig. 4.5) and by decreasing the zone characterized by low and oscillating WSS (Fig. 4.7c) if compared to the standard FKB procedure (Fig. 4.7b).

4.1.4 Conclusion

In this case study, the sequential numerical model is used to investigate the biomechanical influences of the FKB during the PSB approach. Results from numerical simulations highlight the advantages of this procedure in terms of better flow pattern and access to the SB but also its drawbacks mainly due to the overexpansion of the proximal part of the MB. In particular, FKB provokes greater stresses in the arterial wall and a wider region characterized by low and oscillating WSS. In the end, this work shows that the use of a tapered balloon deployed in the SB during FKB might improve the main drawbacks of this procedure.

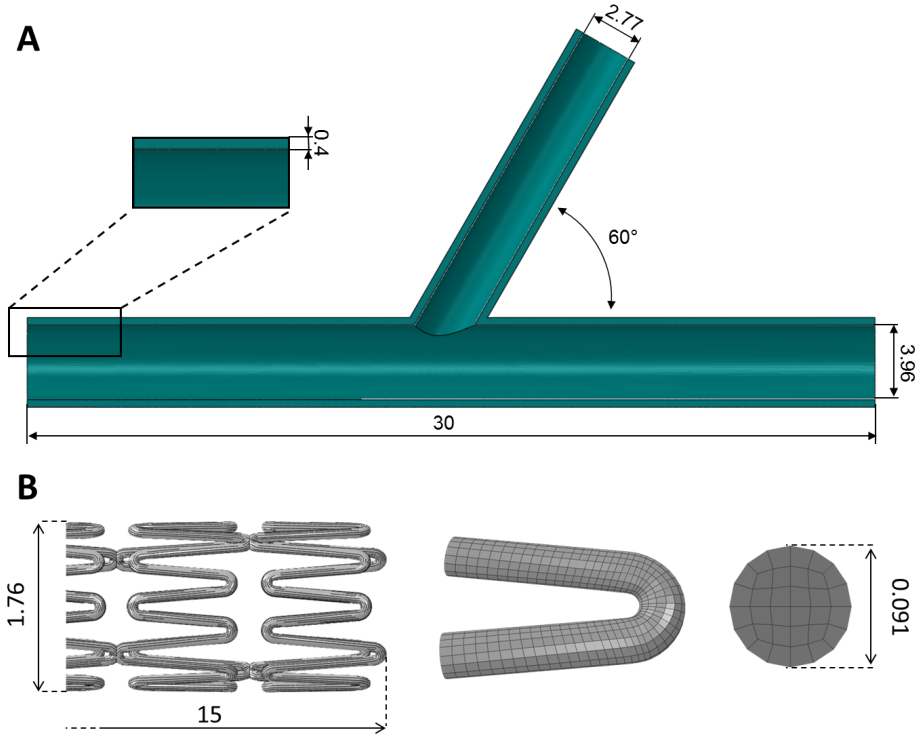

Figure 4.9: *A) CAD model and main geometrical features of the idealized polymeric bifurcation. B) On the left, stent geometrical model resembling the Endeavor stent by Medtronic (only two slides are shown for clarity). On the right, main characteristics of its hexahedral discretization, highlighting a stent strut and the cross-sectional area. Dimensions are in millimetres.*

4.2 Biomechanical influence of single- and double-stenting procedures

The "optimal" stenting procedure for bifurcated lesions is still not defined but should theoretically restore both MB and SB patency, avoiding major myocardial injury and allowing a simple and straight execution. Among the different controversies related to the optimal technique, a major issue is the choice between a single- and a double-stenting approach. At present, available clinical data on BMS and DES suggest that simple strategies are associated with lower rates of long-term adverse clinical events and should be considered as the preferred strategy [192]. However, in some cases, double-stenting techniques remain a mandatory option, either as "intention-to-treat" (LM or diffuse disease in SB 2.5 mm in diameter) or as a "crossover" procedure from the provisional approach (because of dissection, suboptimal result or plaque shift) [113]. Currently, the most commonly adopted double-stenting techniques are characterized by the use of conventional devices, originally designed to be implanted in straight vessels. This "out of the ordinary" use may lead i) to procedural complications with increased technical difficulties, duration, fluoroscopy times and contrast

volume and ii) to negative effects on both on the integrity of the devices themselves (high stresses and deformations) and their biomechanical influence on coronary bifurcations (strut malappositions, multiple metallic layers). Moreover, clinical experience indicates that not all the techniques adequately fit all the potential vascular anatomies of coronary bifurcation.

These evidences suggest that the choice among the different single- and double-stenting procedures is still an open debate and more studies are required to better understand the biomechanics of this topic and provide new insights to either improve the design of devices or guide the cardiologist during the interventions. For these reasons, in this section, the sequential numerical model previously described is implemented to simulate and compare in terms of different biomechanical variables the most commonly used single- and double-stenting procedures involving conventional devices. After showing the main results of the virtual simulations, three comparisons are presented to show the potential use of this numerical tool.

4.2.1 Main features of the sequential model

CAD models of ideal 60° bifurcations (Fig. 4.9a) are built using the commercial software Rhinoceros 4.0 Evaluation (McNeel and Associates, Indianapolis, IN, USA). Internal diameters of the MB and SB are equal to 3.96 mm and 2.77 mm, respectively while wall thickness is set equal to 0.4 mm. The bifurcations are then discretized with 112,720 C3D8R hexahedral elements and its mechanical behaviour is described with a linear elastic material with a Young modulus and a Poisson coefficient typical for polymeric materials and equal to 1 MPa and 0.3, respectively. The choice of using a very idealized arterial geometry is driven by two main purposes. First, very idealized geometries are more appropriate to the comparative nature of the study where general differences depending on the techniques have to be explored and highlighted. Second, these numerical models will be used in a comparison with the results obtained in a PIV experimental campaign presented in Chapter 5 where *in vitro* stent deployments in polymeric bifurcations are used for PIV measurements of local blood flow patterns. Manufacturing problems of the polymeric bifurcations and measurements issues on the PIV setup only allowed simple bifurcated geometries [27].

Stent models (Fig. 4.9b) resemble the commercial devices Endeavor Resolute (Medtronic, USA) used in the *in vitro* bench tests and are characterized by a circular cross section with a diameter of 91 μm. In the uncrimped configuration, stents have an external diameter of 1.6 mm and a length of 15 mm. The meshes of the devices resulted in a total amount of 272,384 C3D8R hexahedral elements. Stents are constructed of a Co-Cr alloy that is described through a Von Mises-Hill plasticity model with isotropic hardening and the following properties: 233 GPa, 0.35, 414 MPa, 933 MPa and 44.5% in terms of Young modulus, Poisson coefficient, yield stress, ultimate stress and deformation at break, respectively [173].

Explicit dynamics finite element models are implemented in ABAQUS/Explicit (v. 6.10, Dassault Systems Simulia Corp., RI, USA) to replicate six among the more common single and double stenting procedures using the methodology described in Chapter 3. An example of the whole structural simulation of the culotte technique is showed in Fig. 4.10 while Figs. 4.12-4.17 present the main results of the six stenting procedures simulated. The geometrical configuration of the stents and bifurcations achieved with structural simulations are then used to create the fluid domain of the stented arteries needed in the CFD study (Fig.4.11) [143].

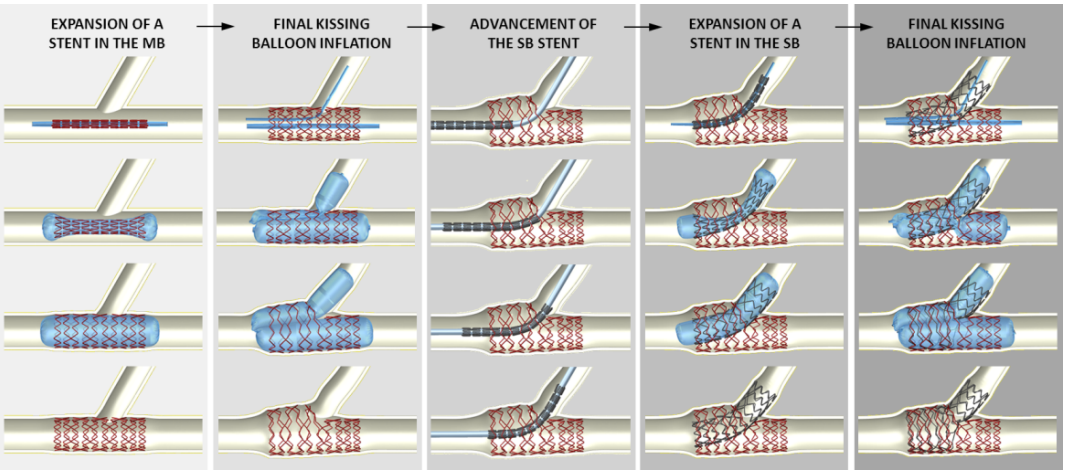

Figure 4.10: *Complete simulation of a double stenting procedure involving two conventional stent models that resemble Endeavor stents by Medtronic and are implanted following the culotte technique. The different steps of the simulation comprise (from left to right): the expansion of a stent in the MB, a FKB inflation, the advancement if the SB stent, the expansion of the SB stent and another FKB inflation.*

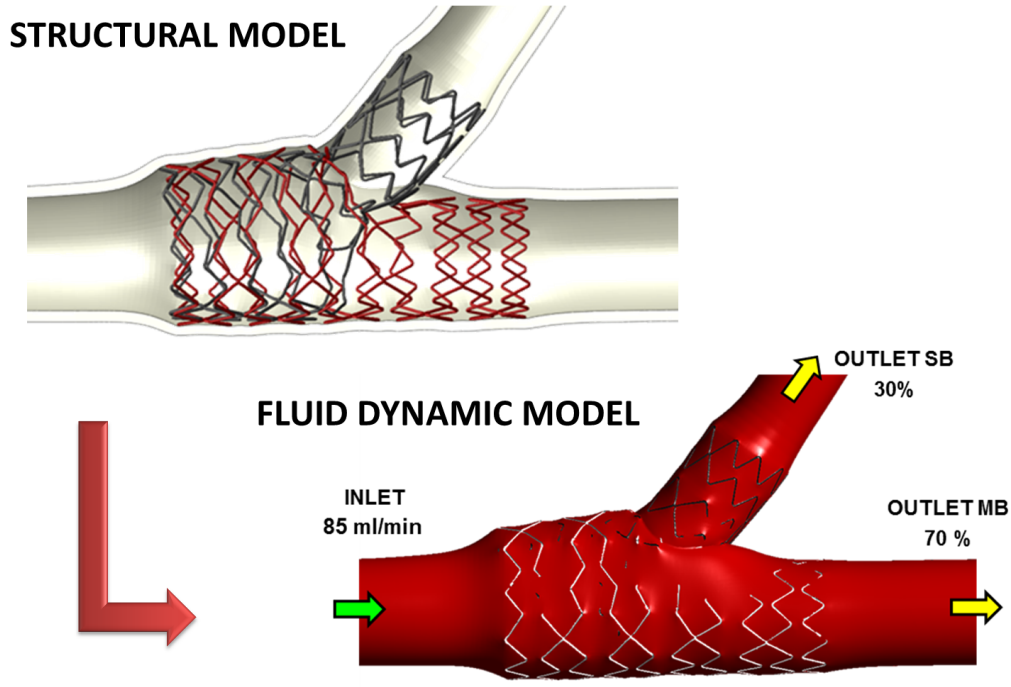

Figure 4.11: *Sequential structural and fluid dynamic model: creation of the fluid domain and boundary conditions implemented for the steady flow simulations.*

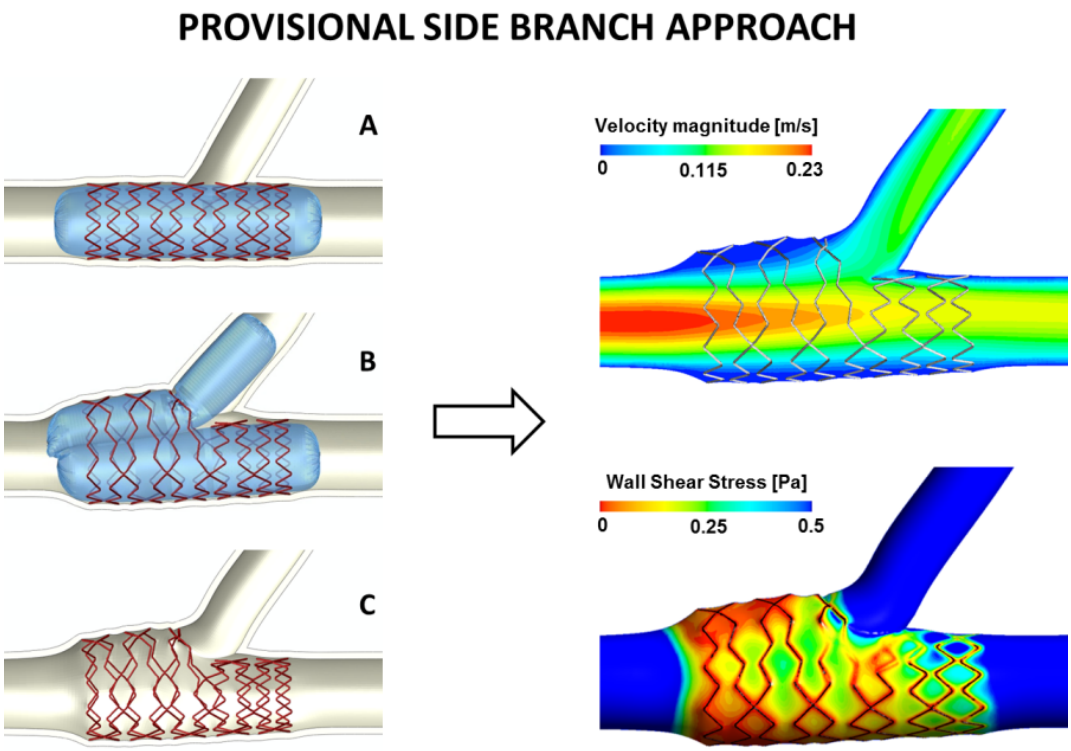

Figure 4.12: *Sequential numerical model of the PSB approach. On the left, the structural simulation of the technique involving three main steps: A) stenting of the MB with a 4.0 mm angioplasty balloon; B) FKB inflation with distal access to the SB; C) final geometrical configurations. On the right, fluid dynamic results: contour maps of the velocity magnitude in the transversal plane (top) and of the WSS field (below).*

A hybrid meshing method composed of hexahedral elements for the core and tetrahedron for the surface [31] is used to obtain a computationally efficient calculation grid. Steady state simulations are carried out by means of the ANSYS/Fluent commercial software using a parabolic velocity profile at the inlet and a constant flow split as outlet condition. In particular, an 85 ml/min flow is divided with a 70/30 split in the MB and SB respectively, following the empirical law proposed by van der Giessen et al. [203]. The working fluid is modeled as a Newtonian fluid characterized by a dynamic viscosity of $3.77\text{x}10^{-3}$ Pa $\cdot$ s and a density equal to 1,100 kg/m^3 replicating the experimental conditions of the PIV study (Chapter 5). A coupled solver is used with a second-order upwind scheme for the momentum spatial discretization. Under-relaxation factors of 0.3 for the pressure and the momentum and 1 for the density were used. The convergence criterion for continuity and velocity residuals was set to 10^{-6}.

4.2.2 Numerical simulation of stenting procedures

Among all the procedures proposed in the literature, the six techniques simulated have been chosen considering the frequency of their adoption in the clinical practice and presence in clinical studies. To correctly simulate the procedures, boundary conditions and loading rates have been applied to stents and balloons following the indications presented in the review by Louvard et al. [124] and its references. As general rules, the same deployment pressure (15 atm) and balloon dimensions (4.0 mm in the MB and 3.0 mm in the SB) are used for all the procedures. Description of the main features of the techniques is found in Movahed et al. [152].

- Provisional SB approach (PSB)

The PSB approach is currently the most commonly used procedure due to its easiness and good clinical outcomes [192]. It involves the implantation of one stent in the MB and the deployment of a balloon angioplasty across the SB when it is compromised after MB stenting (plaque shift) or the SB has significant disease. This inflation aims to free the SB access from stent struts as well. This technique is very simple but can be associated with a higher risk of SB occlusion in case of SB with significant disease. It is important to note that in lesions with angulation of more than 70° the SB can be difficult to rewire. The steps implemented in the simulation are shown in Fig. 4.12 on the left while the right panel presents the velocity magnitude and WSS contour maps from steady fluid dynamic simulations. The main evidences are the relatively low influence of stent implantation on the hemodynamic field and the absence of multiple metallic layers.

- Culotte technique (CUL)

The culotte (CUL) technique is also known as “trouser legs” or “Y” stenting. With this technique, the operator should stent the less-angulated branch first and then wire the other branch vessel through the stent struts and position a second stent back to the proximal part of the previously deployed main stent. FKB inflation is important in order to prevent the protrusion of stent struts into the main vessel and improve the apposition of stent struts to the arterial wall. This technique, which was almost abandoned due to high restenosis rates in the past, is again gaining in popularity as preliminary results with new drug-eluting stents characterized by low profile struts have been encouraging in terms of low restenosis and thrombosis rates [95]. This technique is useful as a bailout technique when a branch vessel is compromised unexpectedly after stenting the MB with inadequate results with SB ballooning alone. Lastly, CUL is particularly suitable when both ostia of the bifurcation branches are diseased. Its main characteristic is the huge overlap area in the proximal part of the MB that results in a highly modified hemodynamic field, especially considering the wide low WSS area visible in Fig. 4.13.

- Crush technique (CRU)

The crush (CRU), pioneered by Colombo et al. [33], consists of simultaneously advancing two stents into both bifurcation branches but with non-simultaneous deployment such that the SB stent is accurately positioned with protrusion of the proximal stent in the main vessel and deployed. This step is followed by deployment of the MB stent across the ostium of the SB crushing against the vessel wall the segment of the SB stent deployed in the main vessel.

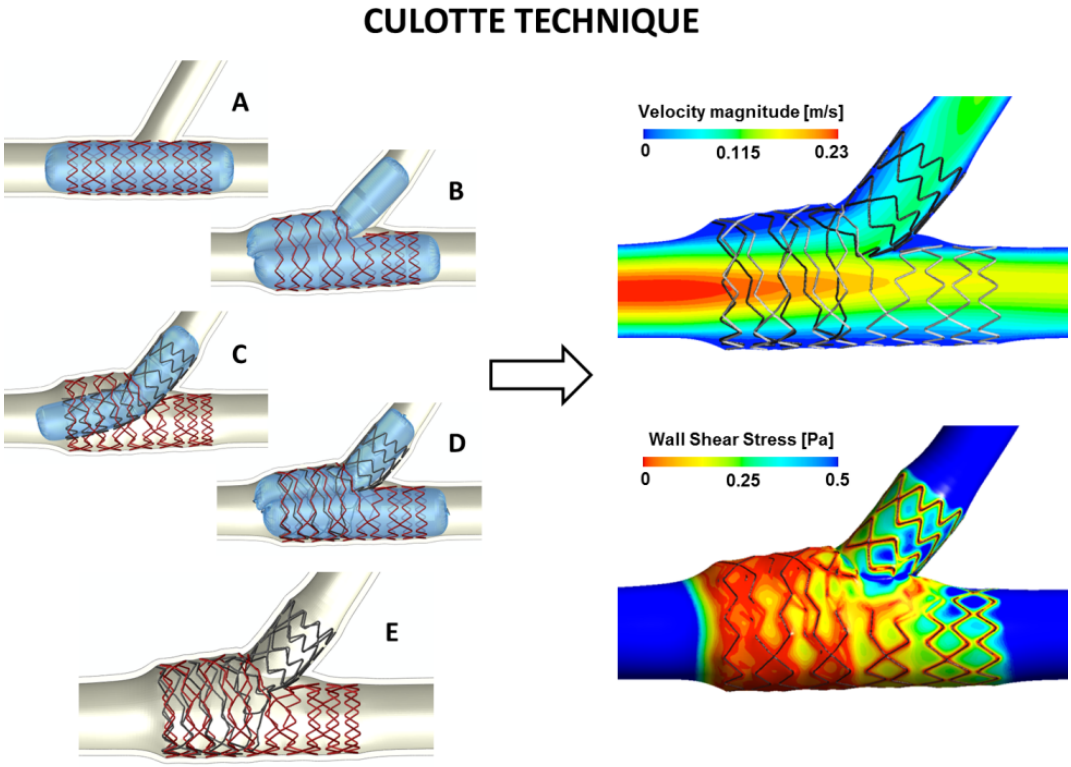

Figure 4.13: *Sequential numerical model of the CUL technique. On the left, the structural simulation of the technique involving five main steps: A) stenting of the MB with a 4.0 mm angioplasty balloon; B) FKB inflation with distal access to the SB; C) stenting of the SB with a 3.0 mm angioplasty balloon; D) second FKB inflation; E) final geometrical configuration. On the right, fluid dynamic results: contour maps of the velocity magnitude in the transversal plane (top) and of the WSS field (below).*

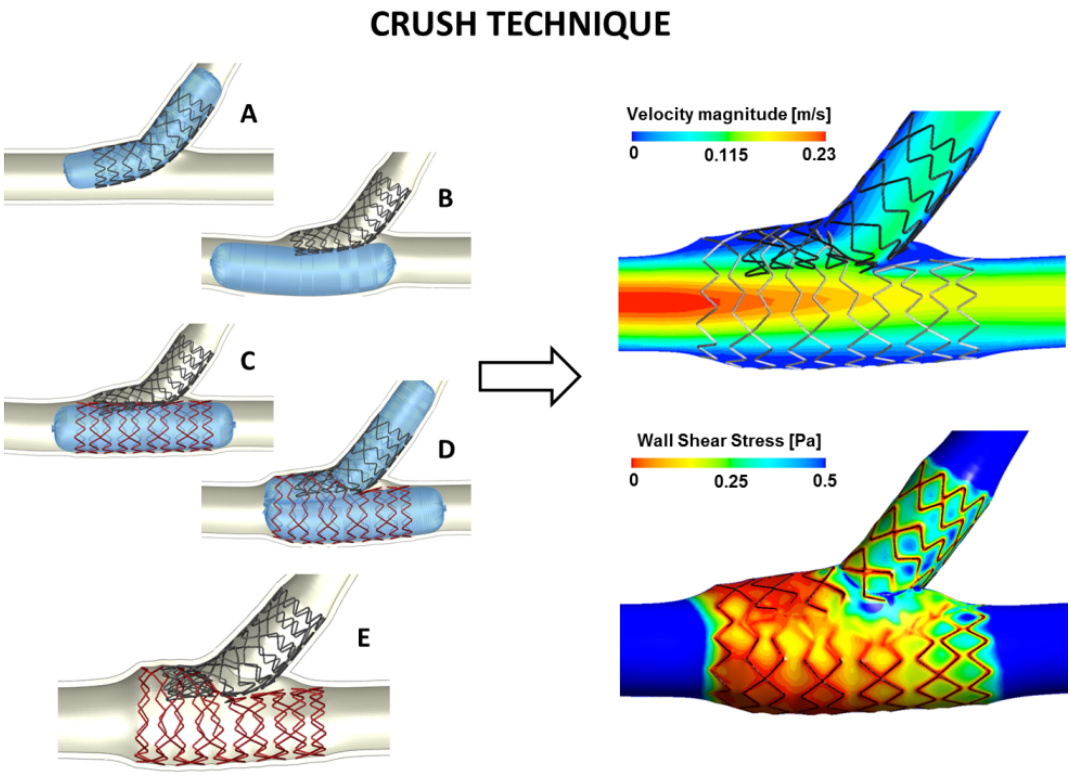

Figure 4.14: *Sequential numerical model of the CRU technique. On the left, the structural simulation of the technique involving five main steps: A) stenting of the SB with a 3.0 mm angioplasty balloon; B) expansion of a 4.0 mm balloon in the MB across the bifurcation; C) stenting of the MB with a 4.0 mm angioplasty balloon with crushing of the proximal end of the SB stent; D) FKB inflation with distal access to the SB; E) final geometrical configuration. On the right, fluid dynamic results: contour maps of the velocity magnitude in the transversal plane (top) and of the WSS field (below).*

To complete the procedure, the SB must be rewired and FKB dilatation of both branches performed. Although this technique can be used to treat most bifurcation lesions, steep angulations such as in all "T" lesions could pose a risk for rewiring the SB. Furthermore, sub-acute stent thrombosis rate has been high [99, 100, 161]. Results of numerical simulations (Fig. 4.14) prove the criticisms of the crushing process in both the stress field in the device and the low WSS area in correspondence of the triple metallic layer.

- Simultaneous Kissing Stents technique (SKS)

The simultaneous kissing stents (SKS) requires the simultaneous advancement of two stents that are positioned side by side into each bifurcation branch with creation of a new carina. This technique is also known as V stenting if only the SB and distal part of the MB are stented leaving the proximal part of the MB untreated. The major advantage of this technique is its ability to maintain access to both branches at all times. However, the

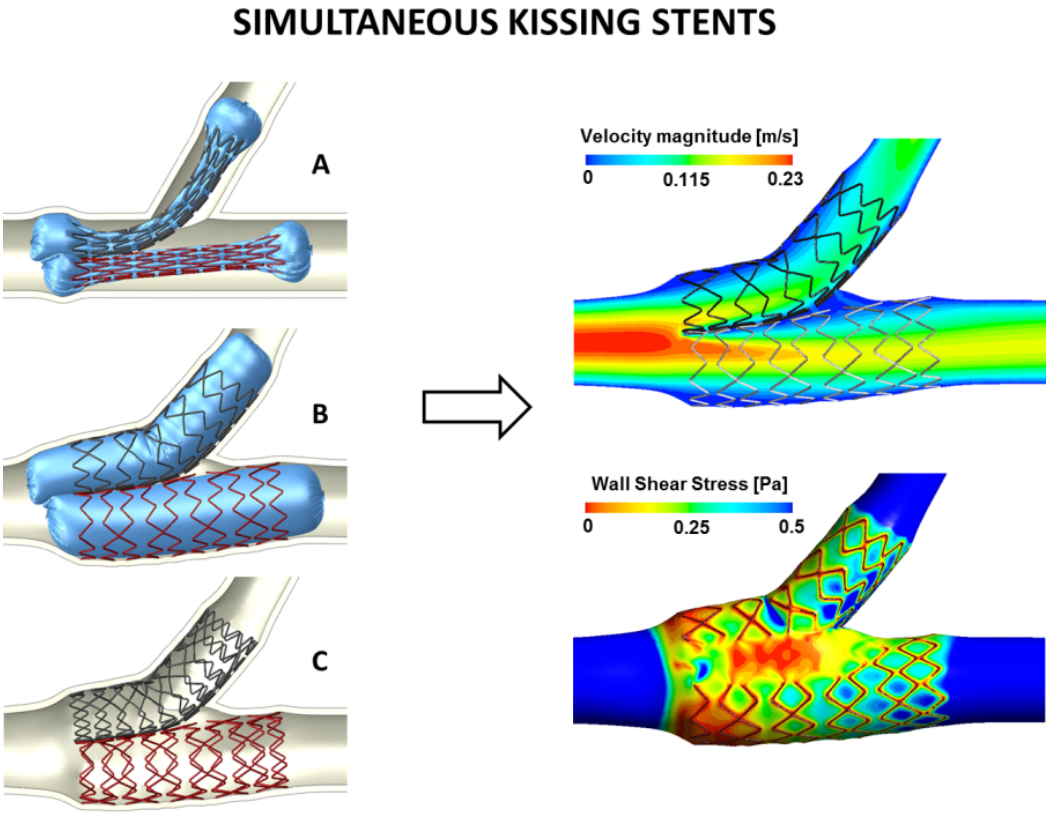

Figure 4.15: *Sequential numerical model of the SKS technique. On the left, the structural simulation of the technique involving three main steps: A) and B) simultaneous insertion and deployment of two conventional devices in both the MB and the SB with a 4.0 mm and a 3.0 mm angioplasty balloons, respectively; C) final geometrical configuration. On the right, fluid dynamic results: contour maps of the velocity magnitude in the transversal plane (top) and of the WSS field (below).*

occurrence of an edge dissection and a big metallic carina in the MB could pose a theoretical risk of stent thrombosis. However, based on two studies reported by Sharma et al. [188] and Kim et al. [105], sub-acute stent thrombosis rate for this technique is low in the drug-eluting stent era. The most important anatomical requirement of this technique is the presence of a large proximal healthy segment in order to accommodate the proximal ends of two stents. Furthermore, steep angulations may cause difficulty in advancing two stents simultaneously. From the results of our simulations (Fig. 4.15), it is clear the effect of the new metallic carina in creating low flow areas and hemodynamic disturbances in the bifurcated region.

- T-stenting technique (TST)

The T-stenting technique (TST) requires positioning of two stents in a "T" fashion. This technique has many other names such as "modified T technique" or "classic T technique" and there are many variations. One of its advantages is that it allows a provisional approach since it is possible to stent the MB first and then stent the SB through the stent struts

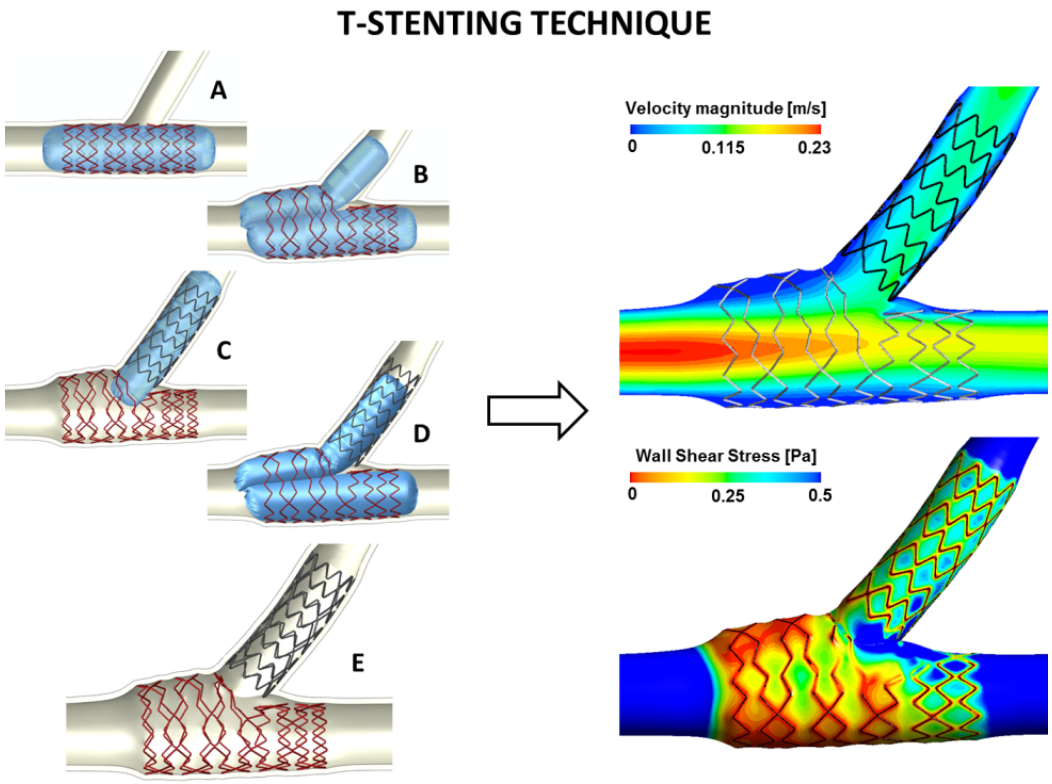

Figure 4.16: *Sequential numerical model of the TST technique. On the left, the structural simulation of the technique involving three main steps: A) stenting of the MB with a 4.0 mm angioplasty balloon; B) FKB inflation with distal access to the SB; C) positioning and deployment of the SB stent with a perfect alignment to the distal part of the SB access; D) second FKB inflation; E) final geometrical configuration. On the right, fluid dynamic results: contour maps of the velocity magnitude in the transversal plane (top) and of the WSS field (below).*

with the possible risk that advancement of the SB stent could be difficult. Another problem of this technique is the loss of direct SB access after MB stenting as opposed to the SKS technique. It is also possible to perform TST within a routine approach by stenting the SB first and then continuing with the stenting of the MB and a FKB inflation. This technique can be best utilized in bifurcation lesions where both ostia are involved and the proximal vessel is too small for the SKS. Important issue of T-stenting is the potential non-stented region in the bifurcated area. For anatomical reasons, this area increases for acute angles and could result in an inhomogeneous distribution of drug in the arterial wall and incomplete scaffolding of the SB. Results of numerical simulations are shown in Fig. 4.16.

- T and small protrusion (TAP) technique

More recently, a new modification of the TST called T and intentional small protrusion (TAP) technique has been recently proposed by Burzotta et al. [20] and clinically validated [21]. This novel modification of the T-stenting technique is based, after stenting of the MB

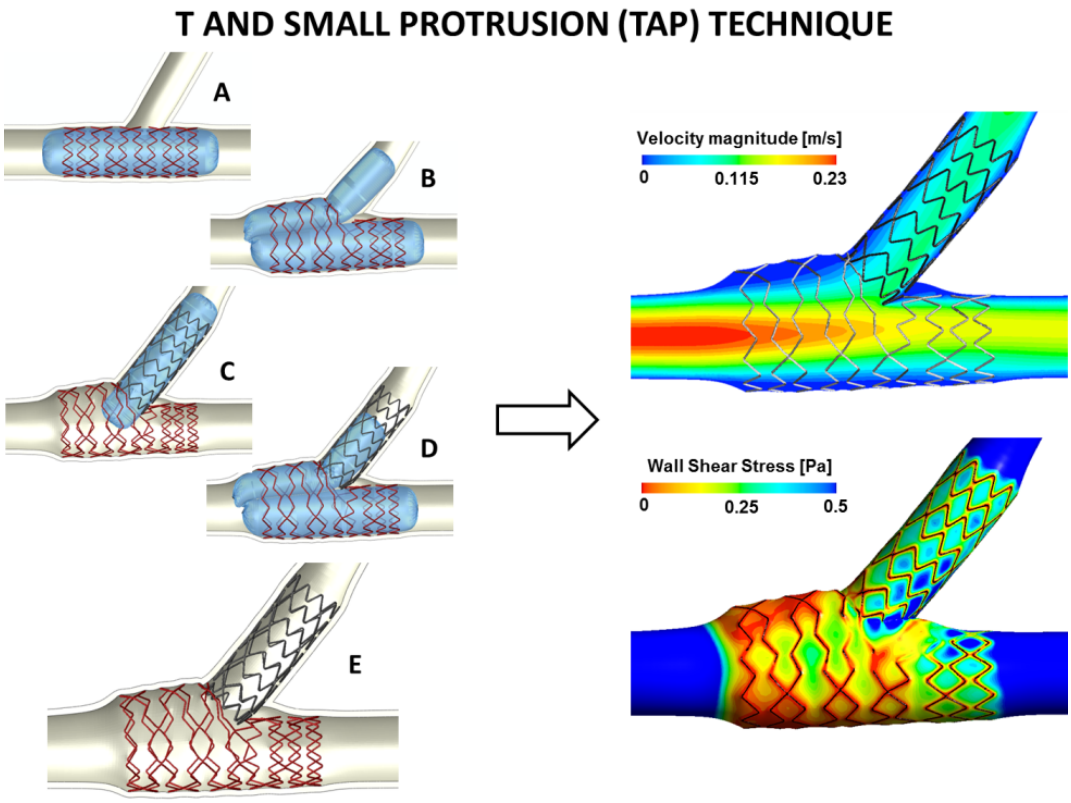

Figure 4.17: *Sequential numerical model of the TAP technique. On the left, the structural simulation of the technique involving three main steps: A) stenting of the MB with a 4.0 mm angioplasty balloon; B) FKB inflation with distal access to the SB; C) positioning and deployment of the SB stent with a perfect alignment to the proximal part of the SB access; D) second FKB inflation; E) final geometrical configuration. On the right, fluid dynamic results: contour maps of the velocity magnitude in the transversal plane (top) and of the WSS field (below).*

and FKB, on the intentional minimal protrusion of the SB stent within the MB. FKB is performed at the end of the procedure. Results of a bench test showed perfect coverage of the bifurcation with minimal stents struts overlap at the proximal part of SB ostium and a small, single layer stent struts, neo-carina not affecting the MB patency. Its main advantages are the possibility of being used within a provisional approach, full coverage of the bifurcation (homogeneous drug elution), minimal overlapping and small struts disturbing the blood flow at the carina. Clinical validity of this approach has been assessed in a recent study [21] where unselected patients underwent DES implantation on bifurcated lesions with a provisional TAP stenting strategy (with a low rate of SB stenting) that appeared to be safe and effective. Results of numerical simulations are presented in Fig. 4.17.

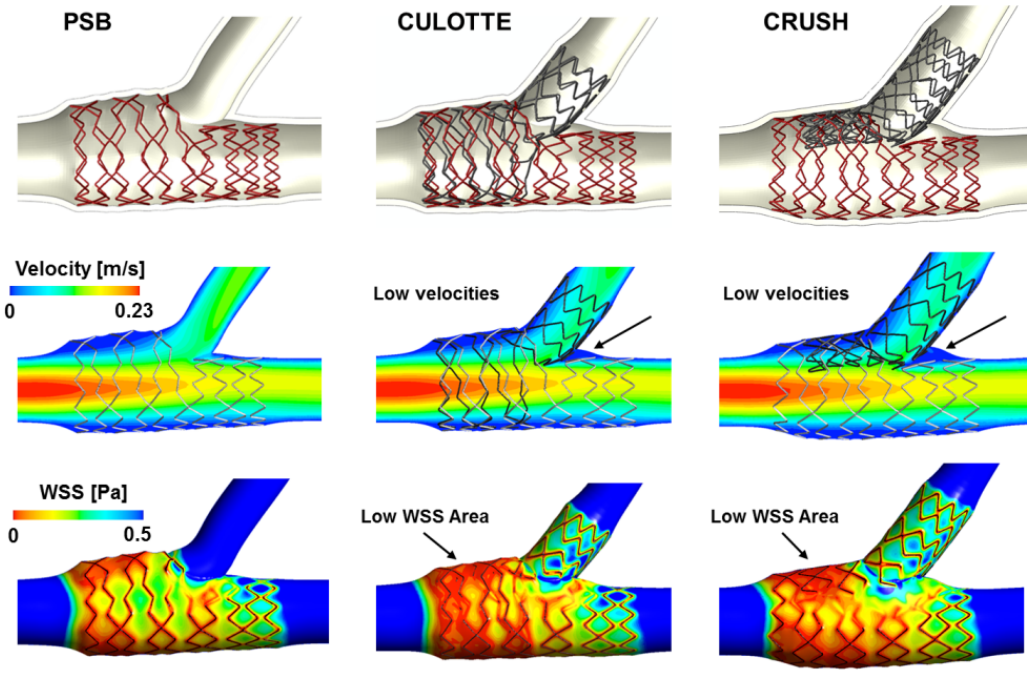

Figure 4.18: *Geometrical configurations (top), velocity magnitude (middle) and WSS contour map (below) achieved at the end of the PSB, CUL and CRU techniques. The influence of double-stenting procedures are evident in the double and triple metallic layers obtained in the proximal part of the MB, the creation of low flow areas at the new metallic carina and the increase of low WSS areas in the proximal MB.*

4.2.3 Discussion

The results of all these simulations can be used to assess the different stenting procedures in terms of several biomechanical variables from both a structural and a fluid dynamic point of view. For sake of brevity, among all the possible comparisons, only four examples are here presented focusing the attention on i) the main differences between single- and double-stenting procedures, ii) the effects of potential procedural errors within the TAP technique, iii) the atypical hemodynamic and biomechanical scenario provoked by the SKS technique and iv) a comparison among the stress/strain influence of different techniques on both the stents and the artery. The results presented should be carefully discussed considering all the limitations included in the numerical models, especially while proposing clinical considerations. In particular, main limitations arise from the idealized geometry of the bifurcations and the steady flows character of the fluid dynamic simulations.

- Single- vs double-stenting procedures

The first comparison proposed aims at investigating different stenting procedures highlighting the effects provoked by the simultaneous presence of two stents in bifurcations. In this case, the double-stenting procedures known as culotte and crush techniques are compared to the PSB approach where on one stent is implanted in the MB. In particular, looking

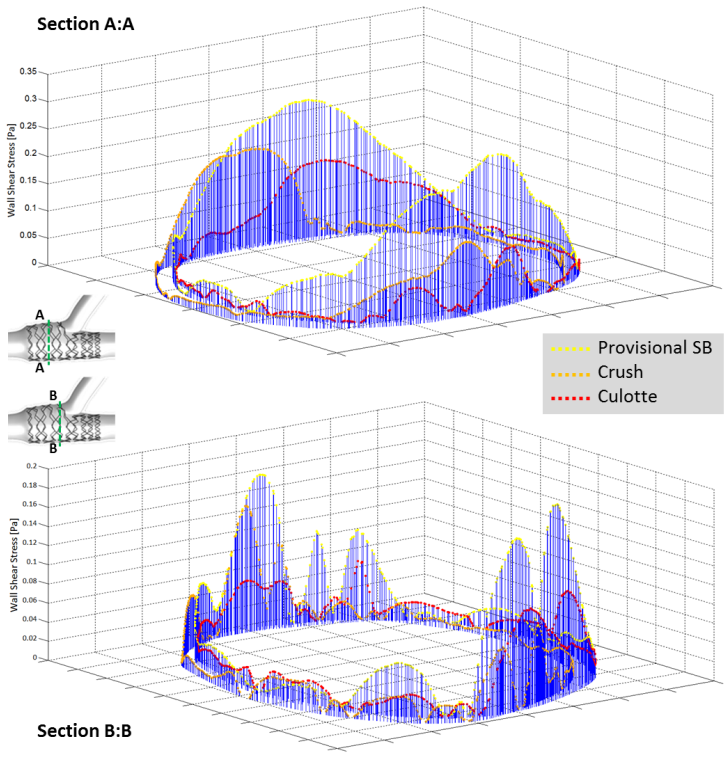

Figure 4.19: *Plot of WSS values obtained in two different sections in the proximal part of the MB after the PSB approach (yellow dotted line), the CRU technique (orange dotted line) and the CUL technique (red dotted line). The influence of the double (CUL) and triple (CRU) metallic layers are evident since WSS values after the PSB approach are generally higher in both sections.*

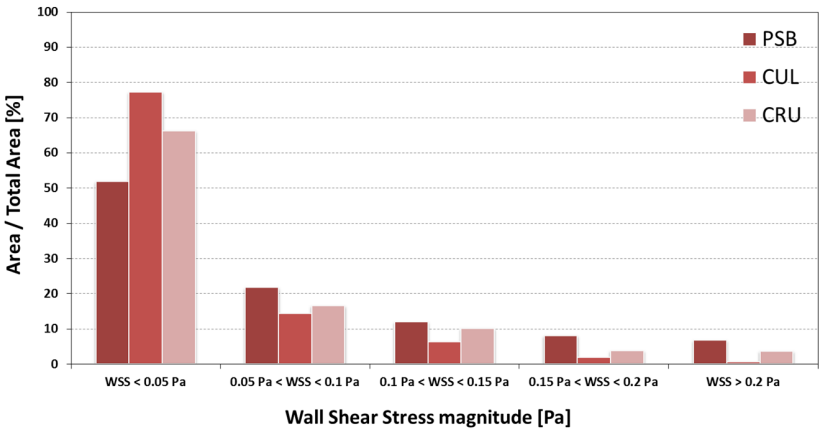

Figure 4.20: *WSS magnitude distribution in the proximal part of the MB in case of PSB, CUL and CRU techniques. The negative influence of the multiple metallic layer occurring in the CRU and mostly in the CUL techniques is evident, especially in the very low WSS area.*

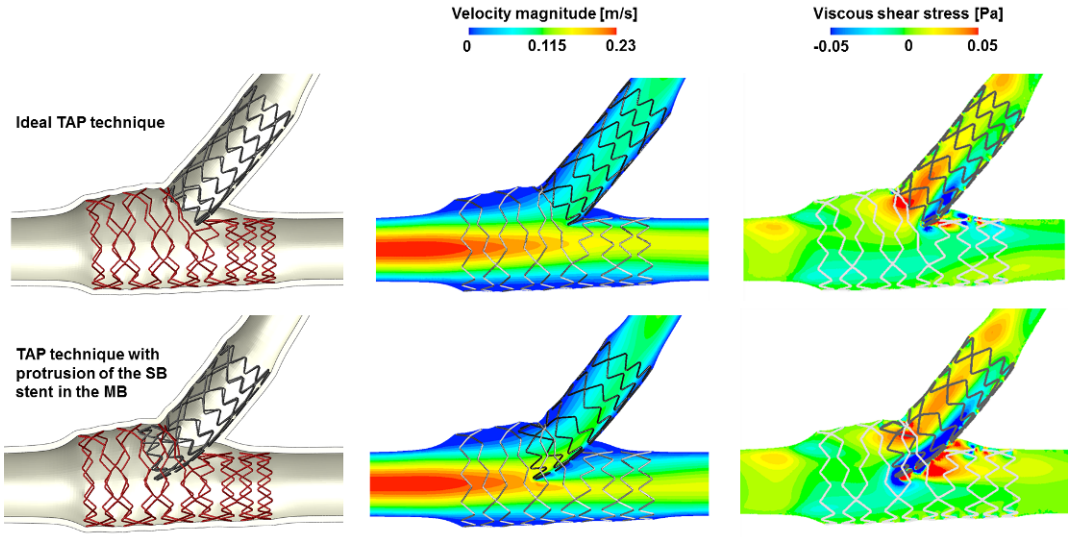

Figure 4.21: *Final geometrical configurations (left), velocity magnitude (middle) and in-plane VSS contour maps (right) obtained at the end of an ideally performed TAP technique (top) and a TAP performed with an incorrect positioning of the SB stent characterized by a high protrusion in the MB. This comparison clearly shows the hemodynamic disturbances provoke by the SB stent struts protruding in the MB.*

at the first row of Fig. 4.18, it is clear how multiple metallic layers and new metallic carinas are frequent occurrences in double-stenting procedures. In particular, focusing on their hemodynamic effect, new metallic carinas create low flow and stagnation regions in the distal part of the bifurcation generating a more favourable scenario for stent thrombosis [17]. Also, from virtual implantations it is evident how the CUL technique is characterized by a wide region of double metallic layer in almost the whole proximal MB while in the CRU technique a triple metallic layer is found in correspondence of the crushed SB stent. Looking at the WSS contour maps of Fig. 4.18, it is possible to notice how low WSS areas (red zones) are wider for double stenting procedures if compared to the PSB approach and mainly localize in correspondence of the multiple metallic layers. A more quantitative analysis is proposed in Fig. 4.19 and 4.20 where the WSS values of two arterial sections are plotted. Results prove that, in case of PSB, WSS values are generally higher than CRU and CUL, the worst scenario. Importance of this investigations arise from the findings of several recent clinical studies that proved how low WSS are positively associated to ISR and, consequently, should be avoided [108].

- Influence of procedural errors in the TAP technique

The second possible use of this sequential models here presented aims at assessing the effects of potential procedural errors. In this case, the ideal procedures of TAP technique is compared to a TAP technique characterized by an incorrect very high protrusion of the SB stent in the MB. In this case, fluid dynamic simulations highlight how the SB stent struts hanging in the MB enhance the hemodynamic disturbances in the MB. This occurrence is

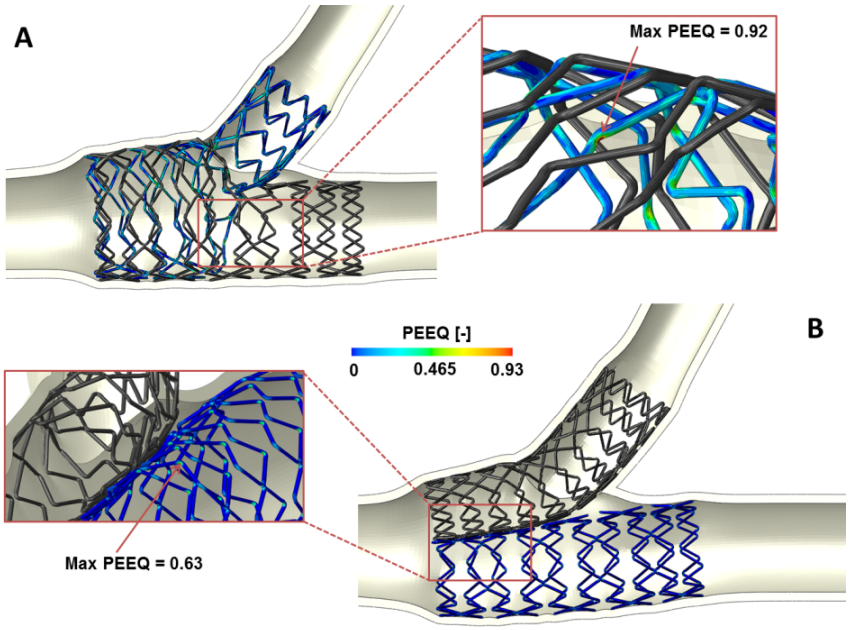

Figure 4.22: *PEEQ contour maps of the most deformed stent implanted in the CUL (A) and SKS (B) techniques. Max values prove how the CUL technique is most demanding procedure for the stent structure if compared to the SKS. Besides mechanical integrity, this evidence also limits the chances of polymer delamination and reduced drug elution capability from highly deformed stent struts.*

particularly clear looking at the velocity and in-plane VSS contour maps in Fig. 4.21. This quantity roughly represents the physical force exerted by the fluid on suspended blood cells. Moreover, a wider low flow area is created downstream the SB stent.

- Analysis of the Simultaneous Kissing Stents technique

The third comparison deals with the SKS technique. This procedure has been invented to allow a simple and fast deployment of two stents in large diameter coronaries without losing the simultaneous access to both branches and without the need of re-crossing stent struts. It involves the synchronised deployment of two devices in both the MB and SB with an overlap of the two stents in the proximal segment of the MB making a new carina proximally [188]. The simulation of the SKS technique with the sequential numerical model presented allows the identification of its main advantages and drawbacks. Among the firsts, since SKS does not require a FKB inflation at the end of the procedure, both stents are deployed at an "ordinary" diameter with normal structural solicitation. This occurrence is evident in Fig. 4.22 where PEEQ contour maps of the most deformed devices are shown in cases of SKS and CUL techniques. From a quantitative point of view, the maximum PEEQ value obtained at the end of SKS is 0.63, far less than values obtained after a CUL technique (0.92) and mainly caused by the FKB inflation. Another important advantage is the lack of multiple metallic layers in contact with the artery decreasing the possibility of arterial injuries during the treatment.

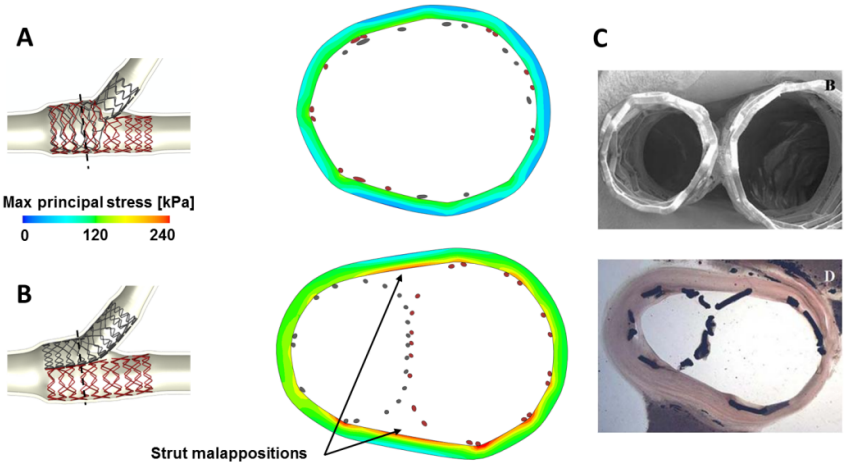

Figure 4.23: *Arterial stresses and geometrical configurations of the stent struts at the end of the CUL (A) and SKS (B) techniques. Strut malappositions and highly elliptical shape characterizing the SKS technique are visible. C) SEM (top) and microscopy (below) images of SKS implantation in the proximal part of a normal pig LM coronary arteries. Images modified with permission from Morton et al. [151].*

On the other hand, SKS technique cannot still be considered an optimal procedure since a few drawbacks are still present. For instance, this particular expansion provokes a huge metallic carina that can be seen in both the numerical simulations displayed in Fig. 4.23b and in the SEM and microscopy images of SKS implantation in normal pig LM coronary arteries published by Morton et al. [151] (Fig. 4.23c). This area contains cervices which may react as nidus for thrombus formation. Also, the stent expansion causes a wide elliptical shape of the proximal MB that resulted in a higher stress field in the arterial wall in comparison with the CUL technique performed with same balloon dimensions and loading rates (Fig. 4.23a). High stress values concentrate in correspondence of the free space between the arterial walls and the malapposed stent struts, a region probably characterized by low drug elution uptakes (no contact and drug diffusion between stent and artery) and a further potential risk of stent thrombosis. Lastly, looking at the fluid dynamic results showed in Fig. 4.24a, it is clear how the low WSS zones occur at the beginning of the stented area and in the free space among the implanted devices in correspondence of the low flow regions, warning on the critic character of this region. This finding is also underlined by the angiographic images of Fig. 4.24b that show an example of restenosis after SKS technique. In particular, the first image shows the angiographic outcome at the end of the SKS technique performed at the LAD/LCX bifurcation with two 3.5x20 mm Taxus DES (Boston Scientific). In the second image, the same patient underwent a follow up control after 8 months showing a high degree of restenosis and necessity of re-treatment. In the third image, the patient underwent another SKS technique with two 3.5x24 mm Taxus showing good immediate angiographic result. In the second and third image, the tissue re-growth in the area between the two stents is clearly visible, matching the considerations made by means of numerical simulations.

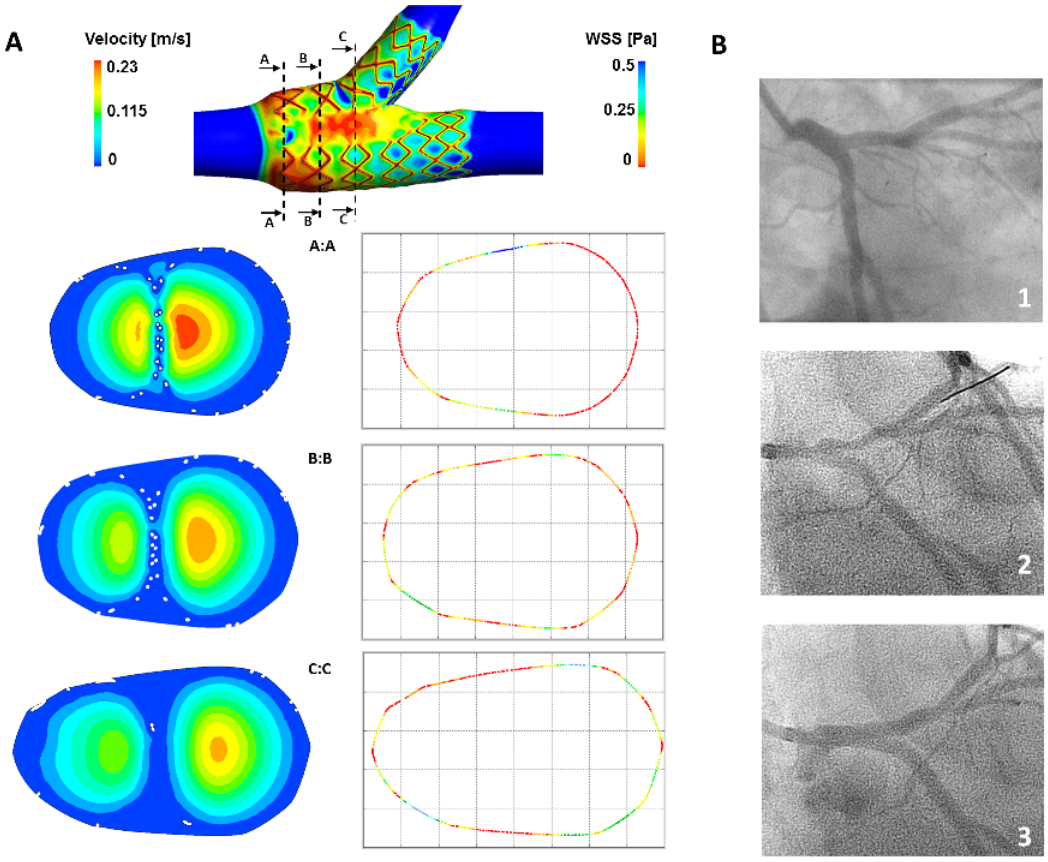

Figure 4.24: *A) Top, contour map of the WSS magnitude resulting in the coronary bifurcation after SKS technique in case of steady flow simulations. Below, velocity and WSS contours in three sections of the proximal part of the MB. The typical separated blood flow characterizing the SKS technique and the risky area characterized by low WSS are shown. C) Angiographic images of a clinical case of in-stent restenosis after SKS: 1) angiographic outcome at the end of the SKS technique performed at the LAD/LCX bifurcation with two 3.5x20 mm Taxus DES; 2) follow up control after 8 months showing a high degree of restenosis in the bifurcation area; 3) second SKS technique with two 3.5x24 mm Taxus showing good immediate angiographic result and the tissue re-growth in the area close to the new metallic carina. Courtesy of Dr. Julian Gunn, University of Sheffield.*

Table 4.1: *Maximum values of PEEQ achieved in the MB and SB stents at the end of the stenting procedures simulated.*

Layer	PSB	CUL	CRU	SKS	TST	TAP
MB stent	0.845	0.927	1.022	0.632	0.834	0.864
SB stent	-	0.843	0.778	0.604	0.481	0.473

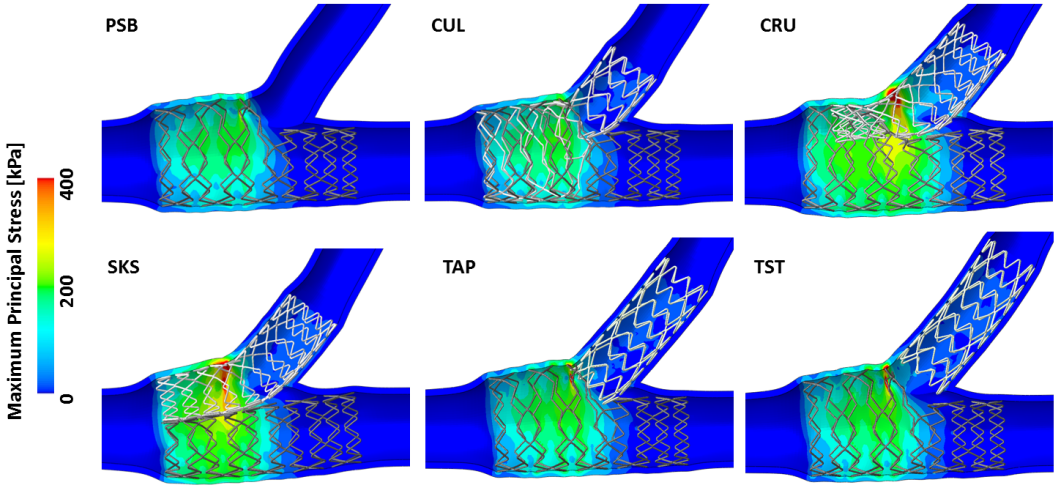

Figure 4.25: *Maximum principal stresses contour maps at the end of the six stenting procedures simulated.*

- Influence of stenting procedures on stress-strain fields

The structural results previously presented prove that stenting procedures have a strongly different biomechanical influence on both the devices implanted and the artery. This occurrence is clear looking at the data presented in Table 4.1 in terms of maximum PEEQ values achieved in the devices and in Fig. 4.25 in terms of maximum principal stresses contour maps. In particular, looking at the maximum PEEQ values obtained in both the MB and SB stents, two major considerations arise. First, the higher PEEQ values occur in those devices that undergo a FKB inflation and, specifically, MB stents implanted through the PSB, CUL, CRU, TST and TAP together with the SB stents implanted via CRU and CUL. According to these results, CUL and CRU seem to be the most demanding cases. Conversely, during SKS the devices undergo expansions at normal diameters resulting in generally lower deformation states. On the other hand, SKS seem to be the most critical technique in terms of stresses provoked in the artery mainly due to its particular expansion that results in a highly elliptical shape of the proximal MB. Together with SKS, high arterial stresses arise after CRU technique and concentrate in the area where SB stent struts crush against the SB wall.

4.2.4 Conclusion

This work demonstrates the feasibility of simulating different single- and double-stenting procedures and of using the numerical results to assess different clinically relevant cases and provide interesting biomechanical insights on the impact of stenting procedures. Four comparisons were proposed highlighting the major complexity and critical nature of double-stenting procedures and underlining how the optimal technique is still missing and new dedicated devices might be required to improve current procedural outcomes. Moreover, interesting potentials of these models involve their use within educational programs for interventional cardiologist to better understand the influence of different interventional options and possible procedural errors.

4.3 New dedicated devices: the Tryton SB stent

Compared to simple lesions, bifurcations were associated with lower procedural success rates, higher adverse event rates, and poorer angiographic and clinical outcomes [181]. Origins of these results may be the procedural errors arising in complex two-stenting techniques or the inability of current devices and techniques to scaffold adequately and preserve the SB ostium. However, such evidences stem from studies using conventional devices and may be challenged by novel technical innovations such as new stents dedicated to bifurcations [78]. The ideal stent for bifurcations should be easy to use, intuitive and simplify the procedure by shortening the procedural time and x-ray exposure and decrease the amount of contrast media. It should be safe, allow permanent SB access and have a high rate of device success with predictable successful ostial SB stenting. It should also provide an optimal long-term outcome with a low rate of restenosis and stent thrombosis. Finally, the ideal dedicated device should be able to treat all kinds of bifurcation lesions [118]. However, the dedicated devices current available on the market are still far from the ideal one and none of them has become widely used in the clinical practice yet. Positioning and alignment issues, complex multi-step procedures and lack of clinical validation are the main reasons of this slow beginning. Only a few devices are currently enrolled in large clinical trials. Among these, the Tryton Side Branch stent (Tryton Medical, Durham, NC, USA), is obtaining promising results [4, 127]. It is a balloon-expandable Co-Cr BMS characterized by low profile stent struts. Its modular design has three different zones; the distal zone has a standard slotted tube workhorse stent design; the central transition zone consists of three panels while the proximal main vessel zone is composed of three undulating fronds that terminate proximally in a circumferential "wedding"band. Through this specific design, Tryton SB stent aims to facilitate the culotte technique in conjunction with a conventional workhorse stent deployed in the MB [126].

During the evaluation of novel interventional devices, virtual modelling techniques based on numerical methods are emerging as a valuable tool for the assessment of several mechanical (arterial wall and stent struts stresses) and hemodynamic variables (shear stresses, drug release) which are hardly detectable by means of *in vitro* or *in vivo* experiments. Accordingly, since the physiological consequences of dedicated stents deployment in bifurcated lesions are scarcely investigated by means of expensive and time consuming clinical studies, we designed the present study aimed to assess the results obtained with PSB stenting procedure, with

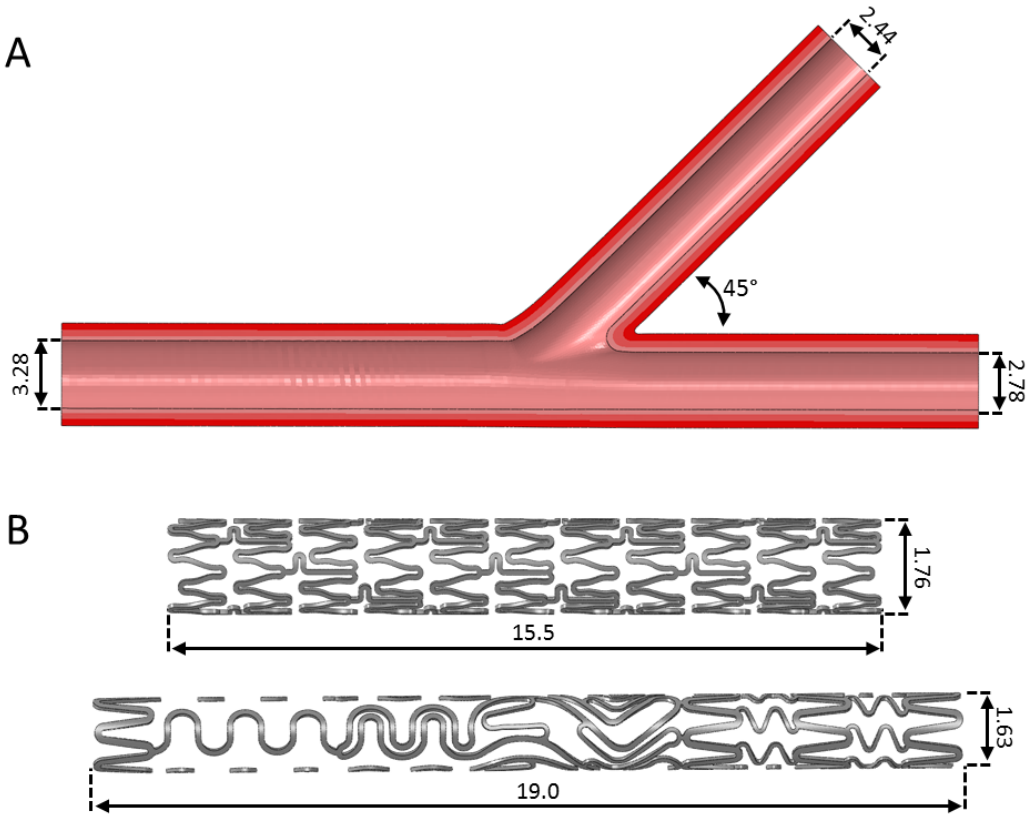

Figure 4.26: *A) 3D model of the coronary bifurcation respecting the dimensional Murray law; B) CAD model of the two stents investigated: the conventional stent Xience V (top) and the dedicated device Tryton Side Branch stent (bottom). All measures reported are in millimetres.*

standard stent-based ("conventional") culotte and Tryton-based culotte using a sequential virtual simulation tool.

First, a numerical model based on the solution of an explicit dynamics problem by means of ABAQUS/Explicit commercial code (Dassault Systemes Simulia Corp., RI, USA) is developed. It involves three main entities: a three-layered hyperelastic bifurcated artery, elastic angioplasty balloon models and elastic-plastic metallic stents (Fig. 4.26a).

4.3.1 Main features of the sequential model

The internal diameters of the bifurcation respect the ratios proposed by the Murray law [155] and are 3.28 mm, 2.78 mm and 2.44 mm for the proximal part of the MB, the distal part of the MB and the SB, respectively. The vessel wall is characterized by a constant thickness of 0.9 mm and the bifurcation angle was 45°Ângioplasty balloons, modelled to behave according to the typical dilation performance of semi-compliant balloons, have a diameter of 3.0 mm for MB and 2.5 mm for SB, respectively. The two examined stents

are designed to resemble the Xience V DES system (Abbott Laboratories, Abbott Park, IL, USA) and the dedicated Tryton Side Branch Stent (Tryton Medical, Durham, NC, USA) (BMS). Stent dimensions are shown in Fig. 4.26b. Positions of the devices, specific boundary conditions and pressure loads have been accurately defined in order to replicate the following stenting procedures:[124]

1. Provisional Side Branch stenting (PSB): a Xience V stent platform crimped to an external diameter of 1.2 mm is positioned across the bifurcation and implanted by inflating a 3.0 mm balloon at 15 atm. After deployment, FKB inflation is simulated by simultaneous inflation of a 3.0 mm balloon in the MB and a 2.5 mm balloon in the SB (accessing the SB through the more distal strut available at SB ostium).

2. Conventional culotte (CUL): a Xience V stent, crimped to an external diameter of 1.2 mm, is implanted across the proximal part of the MB and the SB; then, access to distal MB is achieved by expanding a 3.0 mm balloon through side cells of the SB stent struts. Afterwards, a second Xience V stent is implanted in the MB across the SB take off. Procedure is ended by a FKB inflation using a 3.0 mm balloon in the MB and a 2.5 mm balloon in the SB.

3. Tryton-based culotte (TRY-CUL): the Tryton stent, crimped to an external diameter of 1.2 mm, is implanted across the proximal part of the MB and the SB; access to distal MB is obtained by opening the SB stent struts with a 3.0 mm angioplasty balloon. Then, a Xience V stent is implanted in the MB across the SB take off. Procedure is ended by a FKB inflation using a 3.0 mm balloon in the MB and a 2.5 mm balloon in the SB [102].

As an example of the virtual bench testing modelling used, the complete simulation of the Tryton-based culotte is provided in Fig. 4.27. The metal-to-artery ratios (ratio between the total area of the external surfaces of the stents and the area) at the level of the proximal segment of MB and the PEEQ were calculated and compared between the three investigated stenting techniques to evaluate the effects of stent overlap and the specific stent deformations, respectively.

Additionally, since procedural pitfalls during complex bifurcation stenting procedures may play a major role, the role of SB rewiring site on culotte techniques (a well-established major issue during provisional technique) was investigated. Optimal rewiring should allow the deployment of the second device and maintain free access to both branches, reducing potential procedural complications. Investigation of this issue is performed by evaluating the cross-sectional area available for an optimal rewiring in case of CUL and TRY-CUL technique. While conventional stents have a regular strut pattern, Tryton performances may be influenced by its asymmetric design and cases of Tryton rotated by 30° and 60° (worst scenario possible) are investigated as well.

The final geometrical configurations obtained by virtual bench testing in the coronary bifurcation are used to create the fluid volume for CFD analyses (Fig. 4.28). CFD simulations are focused on near-wall analyses. Blood is defined as an incompressible, non-Newtonian fluid using the Carreau model proposed by Seo et al. [186]. A no slip condition is applied between the fluid and the arterial walls which are assumed to be rigid. A transient velocity profile measured by Davies et al. [36] in a human LAD artery was applied with a constant 70:30 flow split between the MB and SB. Assessment of the velocity field, WSS and RRT [90] in the stented regions are calculated. RRT can be associated to the residence time of the particles near the wall. Moreover it has a more tangible connection to the biological

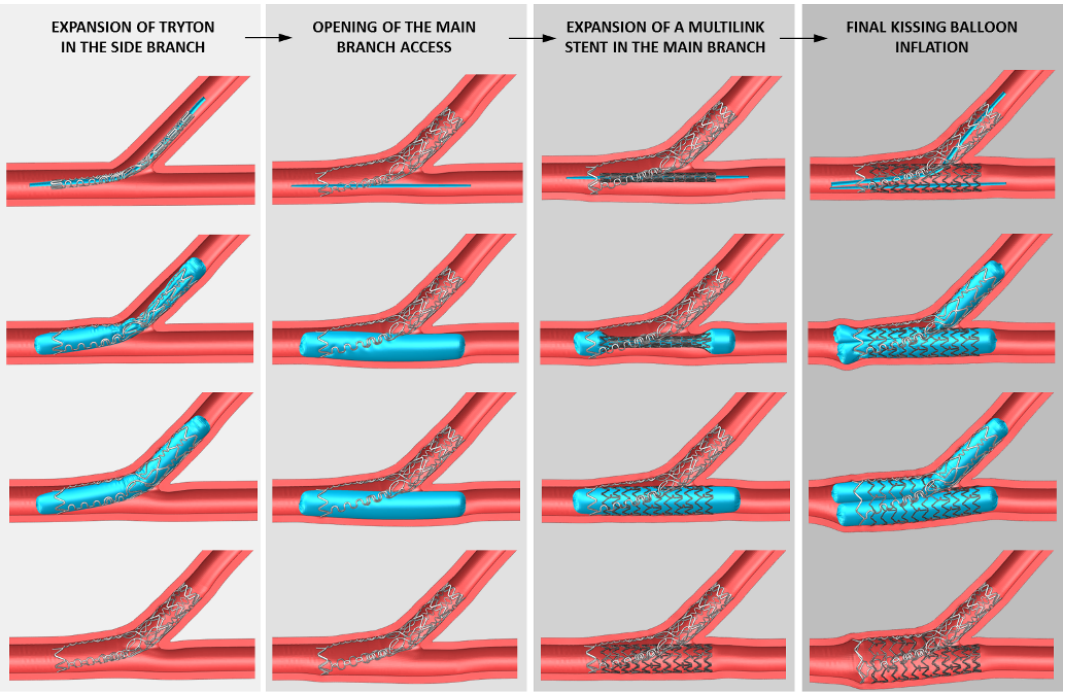

Figure 4.27: *Virtual structural simulation of the Tryton-based culotte technique: implantation of the Tryton stent in the SB with a 2.5 mm balloon; opening of the MB using a 3.0 mm balloon; expansion of a conventional Xience V stent in the MB with a 3.0 mm balloon; FKB inflation performed with a 2.5 mm balloon in the SB and a 3.0 mm balloon in the MB.*

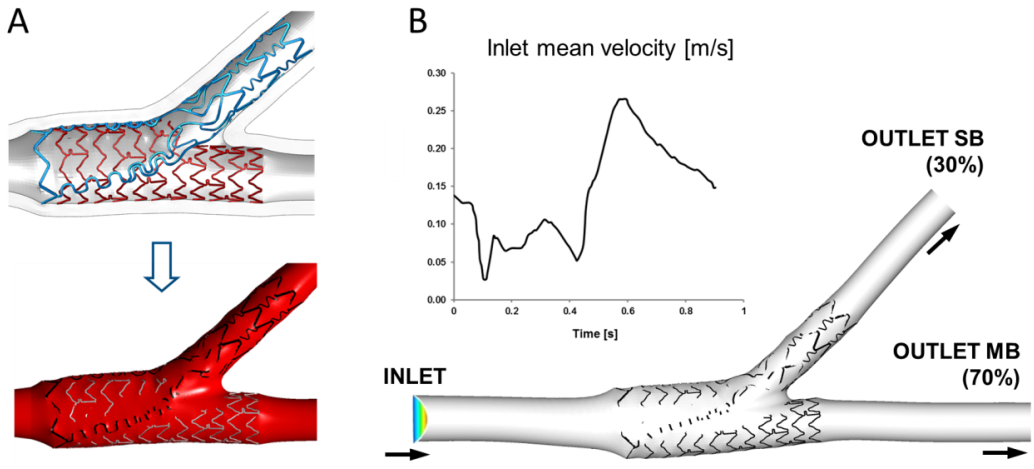

Figure 4.28: *A) Definition of the fluid volume after the structural expansion of Case 3. B) CFD model and velocity tracing applied at the inlet section of the bifurcation.*

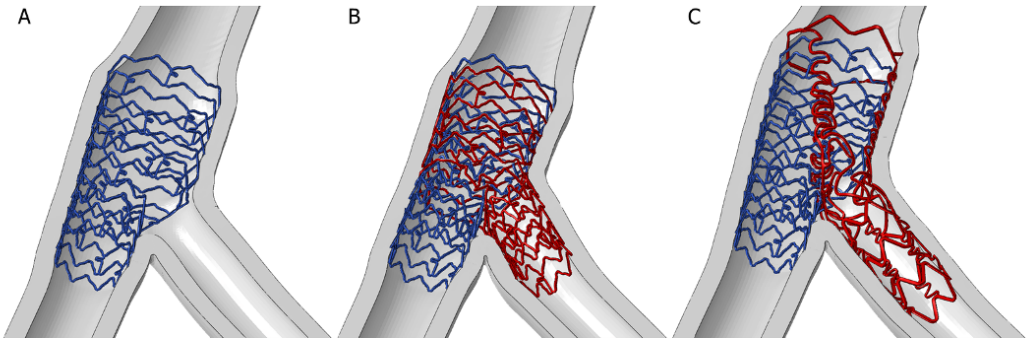

Figure 4.29: *Final deformed geometrical configurations at the end of the three simulated procedures: A) Provisional Side Branch stenting (PSB); B) culotte technique performed with two conventional stents (CUL); C) culotte technique performed with a conventional Xience V stent in the MB and the Tryton stent in the SB (TRY-CUL).*

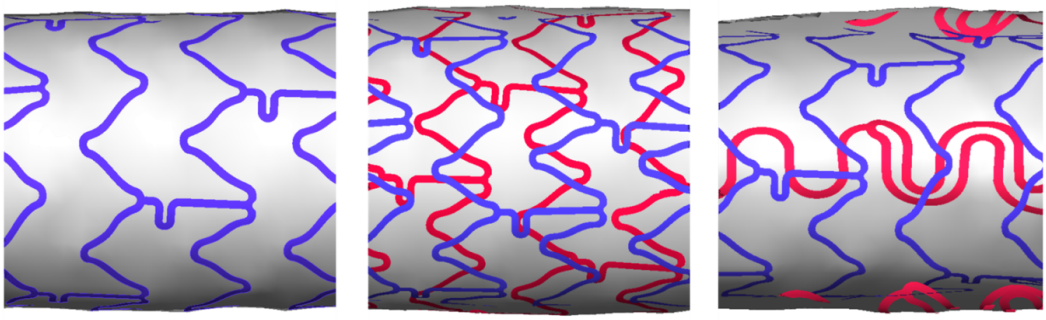

Figure 4.30: *Metal-to-artery ratios for the three cases investigated: PSB (left), CUL (middle) and TRY-CUL (right). The measured ratios in the same region of the proximal MB are 13.2%, 27.4% and 20.6%, respectively.*

mechanisms underlying atherosclerosis than WSS and OSI [90, 117]. Low WSS and high RRT are recognized as critical for the problem of atherogenesis and in-stent restenosis [91, 129].

4.3.2 Results

- Geometrical configurations and physical deformations

Figure 4.29 shows the final geometrical configurations obtained at the end of virtual bench testing. Since all simulated procedures included optimal (distal) SB rewiring and FKB inflation, all the procedures resulted in patent accesses to both the MB and SB.

Metal to artery ratios in the proximal region of the MB are shown in Fig. 4.30. In the PSB approach only one stent is implanted resulting in a metal-to-artery ratio equal to 13.2%. On the other hand, when two conventional devices are implanted as in CUL, the ratio increases to 27.4%. In case of TRY-CUL, the use of the dedicated stent, thanks to the fewer struts in

its proximal design, reduces the ratio to 20.6%.

Regarding stent deformation assessment, the maximum PEEQ obtained at the end of the procedures in the three simulated techniques are reported in Fig. 4.31. In case of PSB stenting, results show that the maximum deformation value (0.75) is obtained in the stent strut at the ostium of the SB opened during the FKB inflation. This final step also influences the deformation state in the proximal part of the MB stent by increasing the max values of PEEQ from 0.33 to 0.43. Similar values of deformations can be found in the MB stents deployed in cases CUL and TRY-CUL. On the other hand, looking at the PEEQ induced in the stents implanted from the proximal MB toward the SB in the two culotte techniques, the conventional stent used in CUL undergoes very high deformations in the strut opened toward the MB (0.95) while the dedicated stent used in the TRY-CUL has overall lower deformation with its higher deformation values (0.65) at the ring of struts located near its proximal end.

- Fluid dynamic analyses: WSS and RRT

Fluid dynamic analyses disclose significant differences between the three investigated technique at the level of proximal MB. Figure 4.32 depicts the contour maps of the TAWSS (left) and RRT (right) in the three cases examined. Overall, contour maps for both parameters concordantly show that better shear stress pattern in the proximal MB is obtained with PSB (single layer of stent struts) while the (higher or lower amount of) double metallic layers associated (respectively) with the CUL and TRY-CUL has an adverse impact on shear stresses by enhancing the areas with low shear stress. In particular, numerical TAWSS analysis show that the percentage areas of the proximal part of MB characterized by TAWSS lower than 0.25 Pa were 56.0%, 88.1% and 71.6% for PSB, CUL and TRY-CUL, respectively. Similar results are obtained in the RRT analysis (Fig. 4.32, numerical data not shown).

- SB stent rewiring: importance of a dedicated design

SB stent rewiring may have a major role in culotte techniques. The available areas for optimal re-crossing of the device are equal to 8.7% after Xience V deployment and 59.4%, 47.6% and 40.8% for the three deployments of Tryton (ideal case, rotation 30° and rotation 60° respectively) (Fig. 4.33). Following, the expansion of a MB balloon results in a patent access to MB in all these cases. As a consequence, the dedicated stent seems to facilitate rewiring. Instead, procedural complications due to sub-optimal re-crossing of a conventional stent seem to be more feasible and may lead to negative geometrical and hemodynamic conditions as illustrated in Fig. 4.34. This case is discussed in more details in the next paragraphs.

4.3.3 Discussion

The combination of the results obtained from the numerical models previously described provides new insights on several aspects of the treatment of coronary bifurcations with single- or double-stenting procedures, conventional or dedicated devices. Tryton stent is characterized by fewer struts in its proximal part and is designed to overcome some of the procedural complications that affect double stenting techniques as, for instance, wide double metallic layers or problematic accesses with the second device.

Firstly, a critical point of double-stenting procedures, particularly evident in the culotte

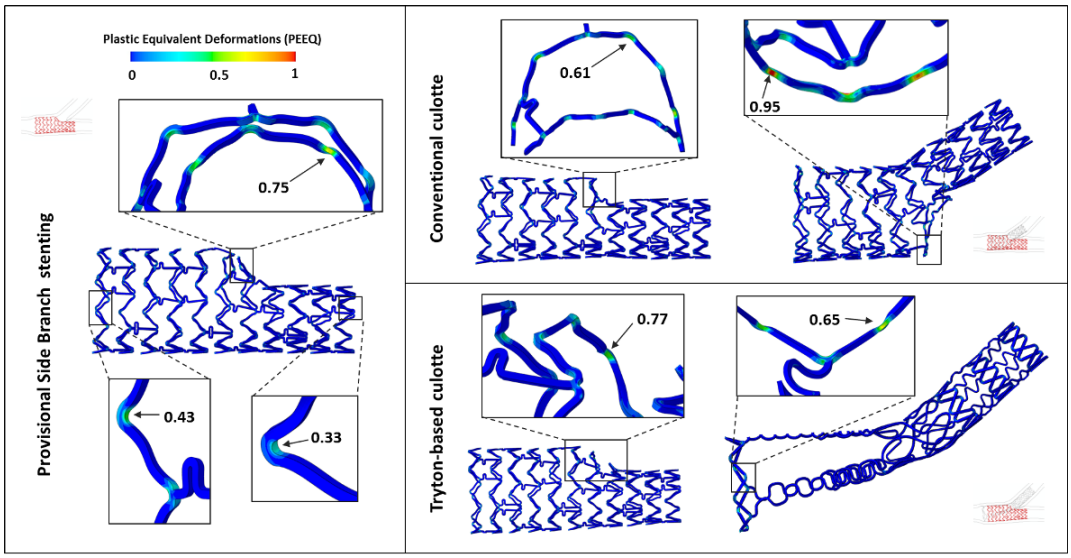

Figure 4.31: *Comparison between the PEEQ values obtained at the end of the stenting procedures in case of PSB stenting (left), CUL (right, top) and TRY-CUL (right, bottom). Magnification areas show maximum values obtained in the devices implanted.*

techniques, is the occurrence of double or even triple metallic layers [114]. These issues might result in higher metal-to-artery ratios, indication of a biomechanical environment more disposed to arterial wall injuries and post-stenting complications. The last three cases investigated show very different metal-to-artery ratios in the proximal part of the MB where the double metallic layer occurs (Fig. 4.30). In particular, the PSB approach results in the lowest metal-to-artery ratio since only one stent is implanted. On the other hand, when two conventional devices are implanted as in the conventional culotte, the ratio doubles. The use of Tryton SB stent, thanks to the fewer struts in its proximal design, reduces this ratio to 20.6%. The presence of a double-metallic layer has a negative influence on the hemodynamic field as well, as proved by the fluid dynamic results illustrated in Fig. 4.32. TAWSS magnitude contour maps of the three cases confirm that the presence of stent struts provokes a decrease of the WSS acting on the arterial wall; this is particularly clear in the regions characterized by the overlapping of the two stents as in case of conventional culotte. If compared to this case, the dedicated device improves the hemodynamic conditions by decreasing the percentage of areas with low WSS from 88.1% of case 2 to 71.6%.

Another critical issue is that conventional devices are designed to reach stresses and deformations that might be potentially exceeded during challenging techniques used in complex geometries such as coronary bifurcations. This occurrence might undermine the mechanical integrity of the devices. Beyond structural integrity and potential stent fracture, other important drawbacks were related to the high deformations achieved during the expansions. Previous reports [79] show that very high deformations in the device might lead to structural damage and delamination of the polymer that covers the stent struts and carries anti-proliferative drugs. Polymer delamination could bring to an inhomogeneous distribution

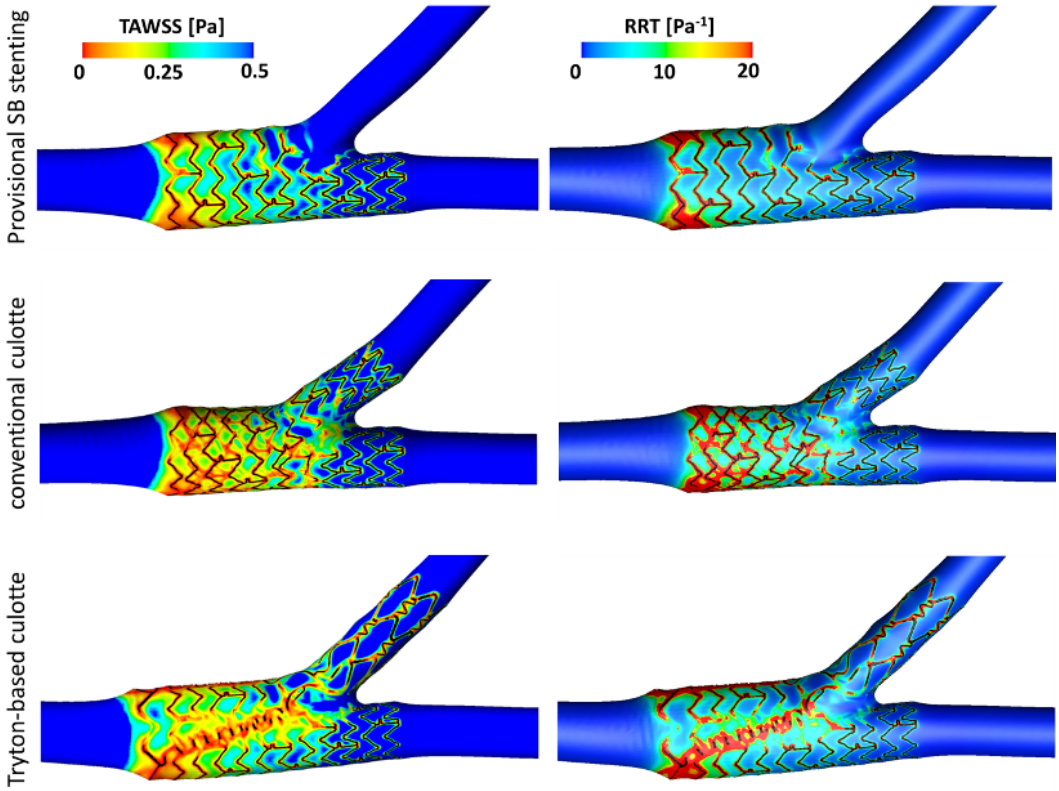

Figure 4.32: *TAWSS and RRT contour maps: comparison between PSB stenting (top), CUL (middle) and TRY-CUL (bottom).*

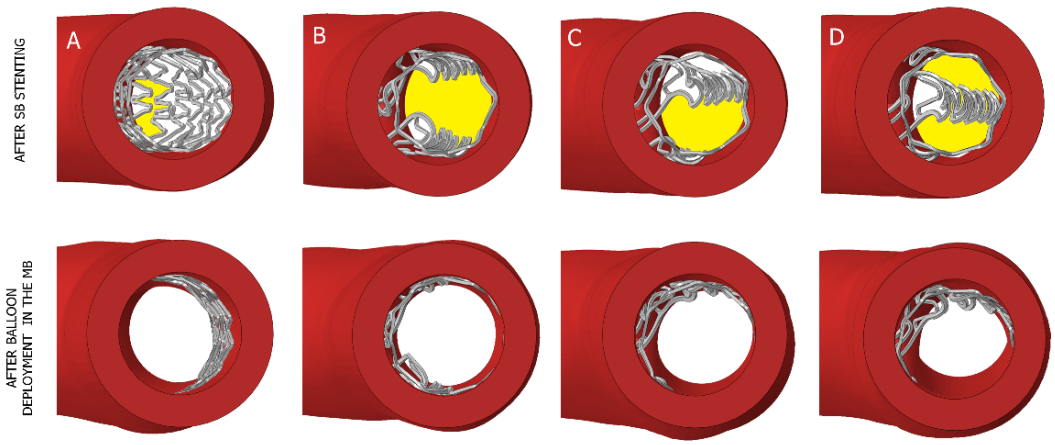

Figure 4.33: *Top) Different accesses to MB after SB stent expansion with a 2.5 mm balloon: deployment of the conventional Xience V stent (A); implantation of the Tryton SB stent in the ideal configuration (B) and rotated of 30° (C) and 60° (D), the worst possible scenario. Yellow areas represent the available area for optimal re-crossing of the device and are equal to 8.7%, 59.4%, 47.6% and 40.8%, respectively. Below) Geometrical configurations after the deployment in the MB of a 3.0 mm balloon.*

of the eluted drug disturbing the correct healing process of the artery. Indeed, structural simulations show that in all the cases, very high stresses and PEEQ are found in the conventional devices deployed (Fig. 4.31). In particular, looking at the MB stent, high plastic deformations are found in all those stent struts rewired with a SB angioplasty balloon and opened during FKB inflations. However, these values, ranging from 0.61 to 0.77, are lower than those obtained in case of conventional culotte after the re-crossing of the SB stent with a 3.0 mm balloon dilated in the MB. PEEQ values are equal to 0.95 and localize at the strut hinges close to the arterial wall opposite to the bifurcation. The same step does not seem to be such critical in case of Tryton-based culotte since lower values of stresses and PEEQ (around 0.65) are found in the dedicated device deployed in the SB. This occurrence proves that a dedicated design might be useful in decreasing the mechanical solicitations of the devices.

Lastly, it is quite reasonable to assume that sub-optimal procedural outcomes could increase the potential risks of post-stenting clinical complications as ISR or ST. Above all, double-stenting procedures seem to be more prone to experience procedural errors mainly due to their technical complexity. In particular, within the culotte techniques a critical point is the crossing of the first device implanted with an angioplasty balloon that enlarges the stent struts and allows the advancement of the second device in the other branch. An optimal balloon insertion should cross the SB stent close to the bifurcation to let the struts adhere to the arterial wall opposite to the bifurcation without hindering the SB access. Looking at the virtual bench test results in Fig. 4.33, it is clear that the dedicated stent provides a wider area (59.4%) available for an optimal re-crossing (Fig. 4.33b) if compared to the standard stent (8.7%) (Fig. 4.33a). Moreover, the highly regular structure of the conventional stent makes the optimal crossing area slightly affected by the uncontrollable rotation of

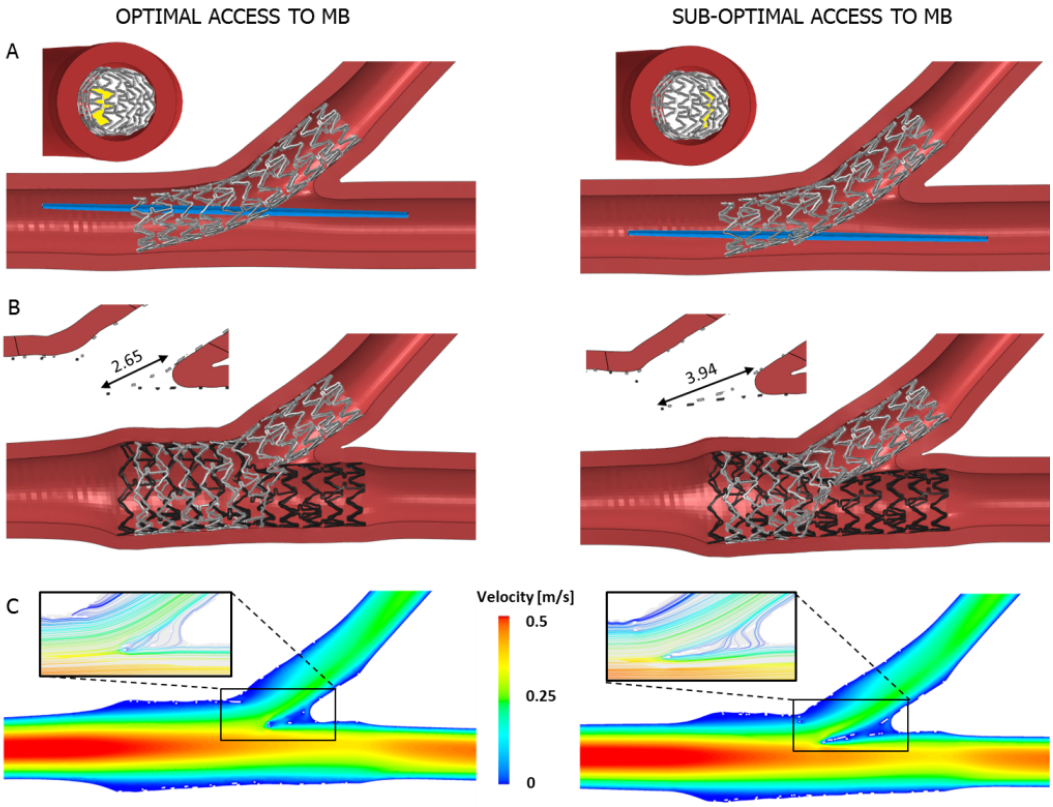

Figure 4.34: *Comparison between an optimal and a sub-optimal access to MB in case of conventional CUL. A) Optimal (left) and sub-optimal (right) crossing of the device with an angioplasty balloon. In the views from the proximal part of the MB, the crossing area is highlighted in yellow. B) Final configuration of the devices after the conventional c technique. A longer new metallic carina is obtained with the sub-optimal access, as underlined in the close-ups of the transversal planes. C) Velocity magnitude contour maps at the maximum flow rate: in the magnification areas, the low velocities and more disturbed flow provoked by the longer metallic carina are visible.*

the device. On the other hand, a sub-optimal procedure performed with the Tryton stent rotated of 30° (Fig. 4.33c) and 60° (Fig. 4.33d) (worst scenario) reduces the crossing area to 47.6% and 40.8% respectively, still enhancing the performances of the conventional device examined. In all these cases, the following MB balloon inflation results in a completely patent access to MB (Fig. 4.33, bottom), thus making rotational alignment of the Tryton SB stent a trivial point. Accordingly, the use of a dedicated device seems to have lower chances of procedural complications due to sub-optimal SB stent rewiring. On the other hand, sub-optimal rewiring of a conventional SB stent seems to be more probable and, when occurring, may lead to negative geometrical and hemodynamic conditions. For instance, Fig. 4.34 provides a comparison between an optimal conventional CUL technique (Fig. 4.34-left) and an example of sub-optimal procedure obtained crossing the stent struts far from the bifurcation (Fig. 4.34-right). In the second case, the result of the MB balloon deployment is a patent MB ostium but a problematic access to SB caused by the presence of several stent struts. In this way, after the MB stent deployment, FKB inflation could only be performed with a proximal access to SB, leading to a greater new metallic carina. Results in terms of geometrical configuration and hemodynamic influence at the end of the whole procedure are visible in Fig. 4.34b and 4.34c, respectively. In particular, differences can be found looking at the longer new metallic carina obtained in the sub-optimal case (3.95 mm) respect to the optimal one (2.65 mm). This new metallic carina has a great influence on the hemodynamic field as proved by the CFD results shown in Fig. 4.34c. In particular, a wider area of low velocities and recirculations is visible close to the bifurcation. Slight increases in the mechanical solicitations on the devices in terms of Von Mises stresses and plastic deformations at the maximum expansion were found as well.

4.3.4 Conclusion

This part of the thesis shows how numerical models might successfully complement the information on stenting procedures obtained with traditional approaches as *in vitro* bench testing or clinical trials. Their ability of providing direct information on clinically interesting biomechanical variables such as mechanical stresses in the artery and the stents could facilitate design process of the devices and clinical planning. In particular, this section confirmed that new dedicated devices, still requiring some improvements in their design and concept, might be an interesting opportunity while stenting coronary bifurcation lesions.

Outside this thesis work, a collaboration with Prof. Paolo Zunino from the University of Pittsburgh and Dr. Elena Cutrí from Politecnico di Milano led to the implementation of a multiscale model able to perform a coupled analysis of fluid dynamics and drug release in stented coronary bifurcations [34]. In this case study, results (Fig. 4.35) showed that major differences in the pattern of drug release are obtained with the three investigated techniques. In particular, it is clear how drug release in the SB is only effective after the implantation of a DES. Furthermore, strut distribution and different stent designs have been shown to highly affect the drug concentration in the arterial walls, especially in the proximal MB where multiple metallic layers occur.

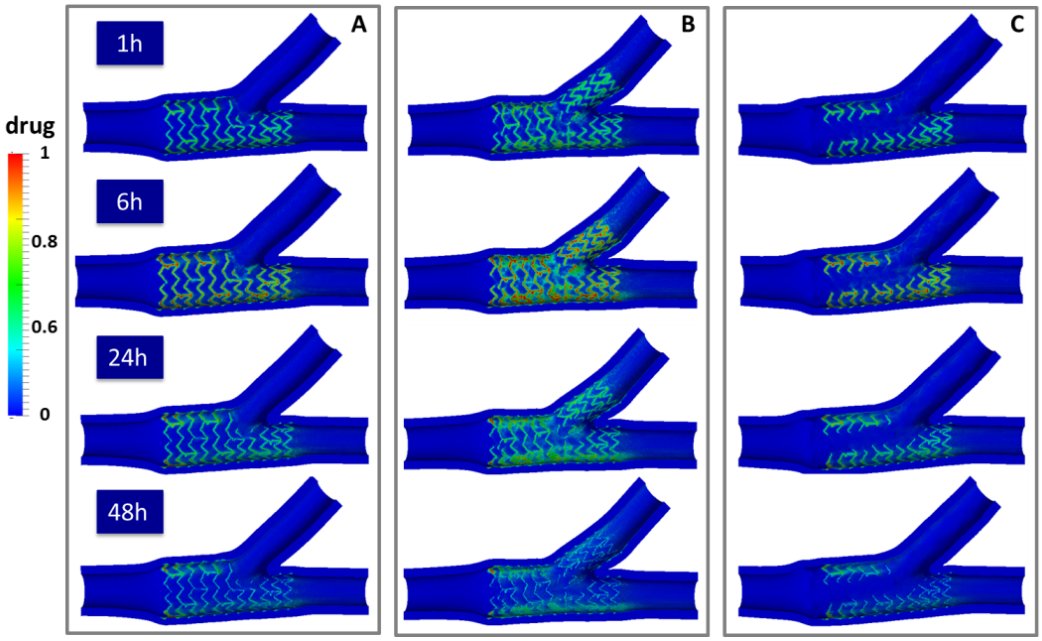

Figure 4.35: *Drug distribution in the arterial wall of the coronary bifurcation evaluated at different time instants (1h, 6h, 24h, 48h) for the PSB stenting (A), conventional CUL (B) and TRY-CUL technique (C). Courtesy of Prof. Zunino and Dr. Cutrí.*

4.4 Study limitations

Despite their continuous improvements and upgrading, numerical models are still affected by a number of limitations that need to be overcome to fully replicate in vivo clinical conditions. Main limitations of the models presented in thi thesis are analyzed in Chapter 3. Hereby, a brief summary of the main assumptions made is proposed:
- Artery: the materials used to define its mechanical behaviour do not consider its anisotropic and inhomogeneous nature. The geometries used in this work have realistic dimensions but only represent idealized models.
- Atherosclerotic plaques have not always been included in the model and, when included, are described as a homogeneous material.
- Stent models could slightly differ from the actual commercial devices. Moreover, only a single conventional stent has been investigated in each case study.
- No image-based reconstructions have been used. Indeed the models implemented cannot provide patient-specific indications but only general guidelines that must be carefully interpreted and adapted to every specific clinical case.

Chapter 5

Experimental and numerical flow patterns in stented and non-stented coronary bifurcations

Contents

5.1 Introduction

Coronary stenting is the most common treatment to restore blood flow in atherosclerotic coronary arteries. However, despite the wide success of this method, several drawbacks are still present such as in-stent restenosis and late thrombosis [51]. From clinical studies, hemodynamic alterations appear to be associated with these failures and a complete understanding of the biomechanical alterations occurring in stented arteries is essential to improve the current interventional strategies and medical devices [108]. At present, *in vivo* imaging systems are not able to provide accurate quantitative information on stented arteries in terms of 3D stent deformations, velocity measurements or arterial stresses occurring during the intervention. As a consequence, *in vitro* experiments and numerical models have become essential and widely adopted tools in this field [147].

Numerical methods such as finite element models or computational fluid dynamics (CFD) utilize mathematical modeling of medical devices and biological tissues to determine the mutual interactions of these components while simulating stenting procedures and the resulting flow environments [132, 146, 153]. Computational methods provide the ability to assess biomechanical quantities such as deformations and stresses acting on both the medical device and biological tissues throughout the entire simulated procedure. Moreover, virtual modeling allows the a priori evaluation and design of new devices without their actual fabrication, thus saving time and money. However, numerical models are often sensitive to assumptions including the geometry, mechanical behavior, and boundary conditions of the system, and therefore need to be accurately verified and validated with *in vivo* or *in vitro* measurements to increase the reliability of results. This process may be challenging, especially in computational biomechanics where complex biological systems are investigated [87].

In vitro bench testing typically consists of the actual deployment of stents in synthetic rigid or compliant arterial models. Subsequently, micro-CT systems may be used to quantify stent deformations [87] while flow measurement techniques, such as Digital Particle Image Velocimetry (DPIV), may be exploited to assess the influence of implanted devices on the hydrodynamics within a model [27, 28, 214]. Such techniques are widely accepted in the interventional cardiology community as they have been used extensively and successfully, having demonstrated their ability to achieve realistic deployments and deliver high fidelity measurements. However, *in vitro* experiments often entail high technical expertise to prepare complex experimental setups and obtain accurate measurements. Consequently, a low number of studies on hemodynamic phenomena [2, 59, 179] and on biomedical devices [8] include both experimental and numerical methodologies despite the shortcomings of each standalone method.

In this light, this study aims to reliably investigate local blood flow patterns in stented and non-stented coronary bifurcation models by employing both experimental [27, 28] and numerical [143] methods. Both stented and non-stented coronary bifurcation models are investigated for three main reasons: i) hemodynamics play a major role in the development of cardiovascular diseases before (atherogenesis) and after stent implantation (in-stent restenosis, late stent thrombosis); ii) coronary bifurcations are characterized by a complex and peculiar hemodynamic scenario including stagnation and recirculation zones [142] that lead to a high probability of cardiovascular diseases in these areas [181]; iii) anatomical com-

plexity and technical difficulties during the interventions result in lower procedural clinical outcomes after stenting deployment with respect to atherosclerotic lesions [68, 181].

One of the major challenges limiting experimental analysis of stented bifurcating vessels is the replication of vessel geometry and stent deployment. To the authors' knowledge, this is the first published *in vitro* investigation using DPIV to quantitatively study flow in stented bifurcating vessels. A total of four different stenting techniques and three bifurcation angles were investigated using both DPIV and CFD, highlighting the critical hemodynamic influence of double-stenting procedures and wider bifurcation angles. Additionally, a full uncertainty analysis is provided for DPIV measurements.

5.2 Materials and methods

This study utilizes both experimental and numerical methods to investigate the bulk flow in bifurcating vessels. The experimental component involves *in vitro* bench tests of four stenting procedures. Non-stented and stented bifurcation models were inserted in a DPIV setup to perform flow measurements and characterize the influence of stenting procedures and bifurcation angles on local blood flow patterns. Secondly, numerical modeling of the experimental cases was performed by means of CFD simulations. A sequential structural and CFD model, based on the ABAQUS/Explicit and ANSYS/Fluent commercial codes, was implemented to examine the stented cases.

5.2.1 Experimental methods

- Stented and non-stented bifurcated silicone models

Bifurcating synthetic models with side branches (SB) angled at 30° 60° and 90° were fabricated through a casting process using PDMS (Dow Corning sylgard 184) at a mixture ratio of 1:10 to match arterial compliance (Fig. 5.1). The resulting bifurcation models had main branch (MB) outer diameters of 4.76 mm and SB diameters of 3.57 mm. The lumen of the model was created using 3.96 mm (MB) and 2.77 mm (SB) steel rods that were fit together at the different angles through an inset hole on the larger rod and centered in a casting mold resulting in a 0.4 mm wall thickness. Only models characterized by a uniform wall thickness and without bubble defects were used to ensure uniform compliance and optical clarity for DPIV purposes.

Commercially available Endeavor Resolute stents (Medtronic, USA) were implanted into four synthetic 60° bifurcated models by an interventional cardiologist using four different stenting techniques (Fig. 5.2). Angioplasty balloons with diameters equal to 4.0 mm and 3.0 mm were used in the MB and SB, respectively. The four techniques [124] investigated herein were:

I. **Provisional Side Branch (PSB):** A stent is deployed in the MB, followed by a Final Kissing Balloon (FKB) inflation to create an opening in the stent for SB flow.

II. **Crush technique (CRU):** First, a stent is deployed in the SB with one third of the stent protruding into the MB. Second, a balloon is inflated in the MB outside of the previously placed stent, and acts to crush the SB stent against the wall of the

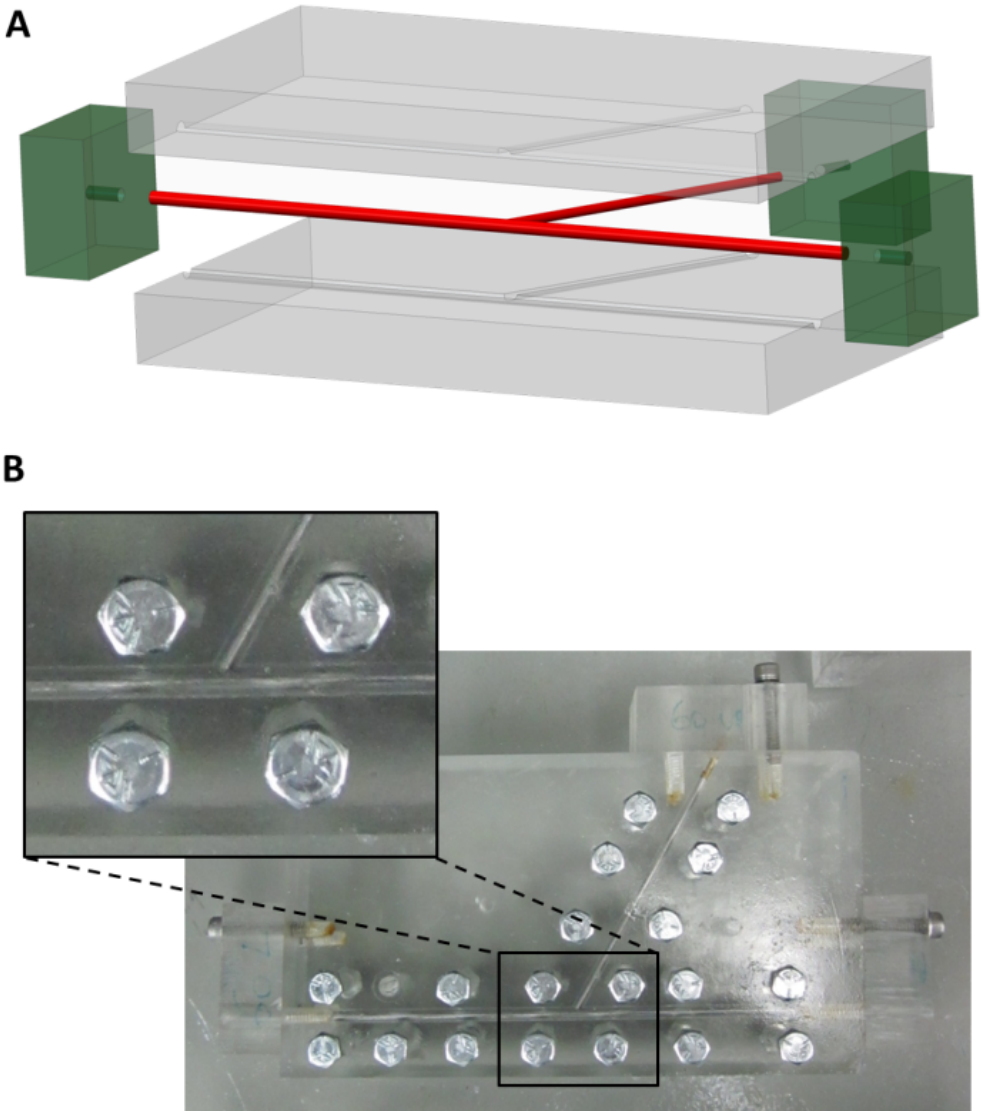

Figure 5.1: *A) Schematic representation of the fabrication process of the synthetic bifurcations. The steel rods are fitted together at a 60° angle (red) and inserted in the acrylic moulds (grey). A 0.4 mm gap exists between the acrylic mould and steel rods and is filled with the silicone polymer. Alignment of internal rods is maintained using spacers (green) at the three ends of the steel rods. All parts are bolted together to secure the assembly and allowed to dry approximately two days. B) The real assembly for the 60° bifurcation is shown highlighting the bifurcation in the magnification zone.*

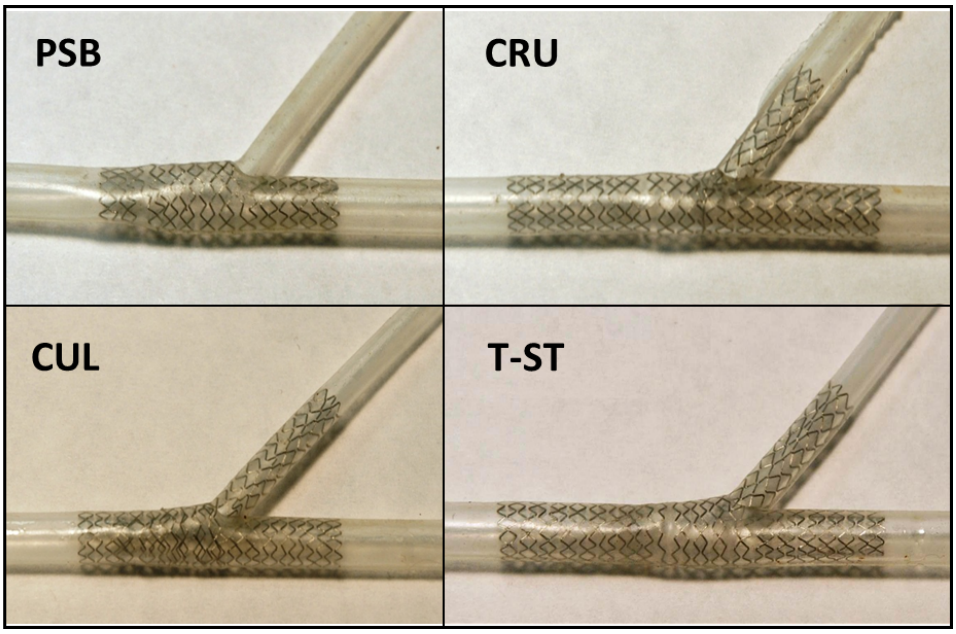

Figure 5.2: *In vitro bench testing of stenting procedures in the fabricated silicone bifurcation models. Top left, provisional side branch stenting; top right, crush technique; bottom left, culotte technique; bottom right, T-stenting technique with high protrusion in the MB.*

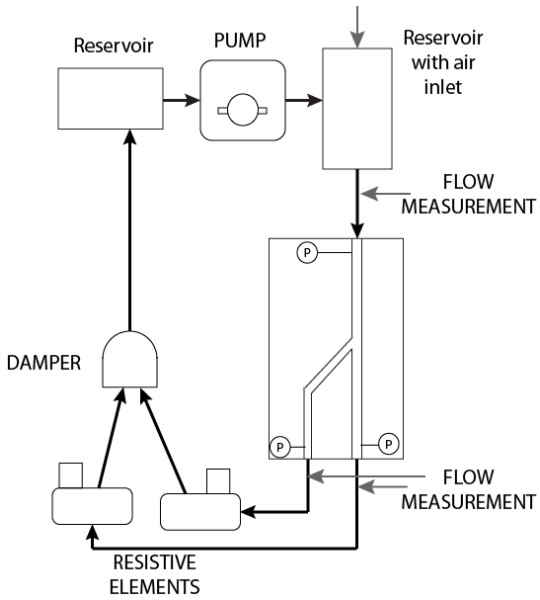

Figure 5.3: *Schematic depiction of the flow loop developed by Charonko et al. [27] modified to examine steady flow cases with a bifurcated region of interest. Resistive elements were placed downstream of the bifurcation model to control the ratio of flow rates between the MB and the SB.*

vessel. Next, a second stent is deployed in the MB and the technique ends with a FKB inflation to reopen the lumens of the MB and SB.

III. **Culotte technique (CUL):** A stent is deployed in the SB with a high protrusion into the proximal region of the MB. Next, a balloon is inflated in the MB through the SB stent struts, which is used to re-open the lumen of the MB. This opening allows access for a second stent to be implanted within the MB and finally, a FKB inflation is performed to reopen MB and SB lumens. High overlap of the two stents occurs in the proximal MB.

IV. **T stenting technique with high protrusion (T-PR):** After performing PSB stenting, a second stent is implanted in the SB with a section of the stent protruding into the MB.

- Flow loop replicating a steady flow

The flow loop shown in Fig. 5.3 and described in Charonko et al. [27] was used to recreate a steady flow condition and modified to account for the presence of a bifurcation in the region of interest. Resistive elements were placed downstream of the bifurcation model, to control the ratio of flow rates between the MB and SB. Pressure was measured at the inlet of the model while flow rates were measured upstream and downstream of the model using an ultrasonic flow meter. A 60%-40% water-glycerine mixture was used as a blood analog to match physiological kinematic viscosity ($3.77\text{x}10^{-6}$ m^2/s). This fluid also filled the test section, and matched the index of refraction of the vessel walls, nearly eliminating optical distortions caused by curvature of the vessel walls and minimizing light reflections. Components of the setup were adjusted to obtain a constant flow rate at the bifurcation inlet with a 84/16 flow split between MB and SB. Pressure conditions were maintained at approximately 100 mmHg. This setup was also used to reproduce physiological pulsatile coronary flow conditions. Preliminary results of these cases are proposed in Appendix 1.

- Digital Particle Image Velocimetry methods

DPIV was performed using a high speed intensified camera (IDT Xs-5i) and a high speed Nd-YAG laser. The bifurcation models were submerged in a reservoir filled with the working fluid to nearly eliminate distortions from the curvature of the wall. The blood analog in the flow loop was seeded with 7 μm fluorescent particles to act as flow tracers. A double pulse strategy (Fig. 5.4a) was adopted to acquire image pairs with a separation time of 200 μm and a sampling frequency of 250 Hz resulting in a peak particle displacement of approximately 8 pixels. For each set of data, a total of 2000 images were acquired, corresponding to an acquisition time of 4 s. The field of view for this study was chosen to visualize flow patterns in the majority of the arterial model resulting in spatial resolution of 7.33 μm/pixels for stented and 4.78 μm/pixels for un-stented cases. The absence of the stent in the latter case allowed for higher magnification although the length of the vessel imaged in the field of view was reduced. DPIV was performed for each stenting technique in 60° bifurcation models as well as in the three non-stented bifurcating models of varying bifurcation angles, resulting in a total of seven cases. For stented cases, stent struts visually blocked several areas in the flow and therefore velocity measurements are not available at these locations. For analysis purposes, stented regions of the velocity fields were masked and excluded from the data analysis after processing was performed.

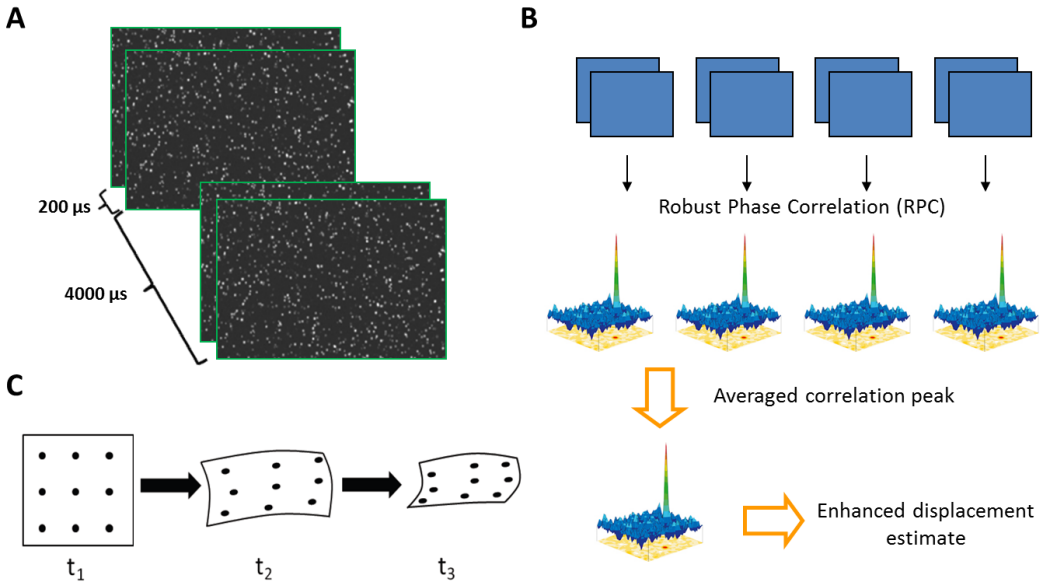

Figure 5.4: *Schematic representation of DPIV methods exploited in this study: A) A double pulse strategy is adopted to acquire image pairs with a frequency of 250 Hz and a separation time of 200 µs. B) Ensemble correlation strategy is used to enhance the displacement estimate in steady flows by averaging several correlation peaks. C) Deformable windows are used to improve the near wall velocity measurements.*

DPIV processing was conducted using Prana ('http://sourceforge.net/projects/qi-tools/'), an in-house software allowing for ensemble correlation processing (Fig. 5.4b) [134] using the Robust Phase Correlation (RPC) [48–50]. The processing method employed includes discrete window offset [209] coupled with a window deformation scheme [182]. Processing methods using window deformation (Fig. 5.4c) are useful for near wall measurements due to shear at these locations and serve to deform the image window based on the local velocities computed in the previous processing passes. Ensemble correlation processing is typically performed to determine velocity information in steady flows as the method improves velocity estimates by averaging DPIV correlations in time [40, 134]. Gaussian windowing is applied to remove aliasing from finite window sizes [49].

Specifically, the background illumination of the images was firstly removed by subtracting the median image in time. Next, ensemble correlation processing was conducted on 1000 image pairs for two passes. The initial pass used a window resolution of 32x32 pixels and an 8-pixel grid resolution and the second pass used a window resolution of 8x8 pixels with a 2-pixel grid resolution. Both passes were iterated three times and a Gaussian filter was used to smooth measurements after each iteration, as is typical for deformable window schemes. Additionally, the universal outlier detection scheme [210] was used to identify erroneous vectors after each pass using a 3x3 vector neighborhood.

Finally, the uncertainty of the measured velocity fields was computed following methods outlined by Charonko et al. [29]. Conventional DPIV experiments often report an error of

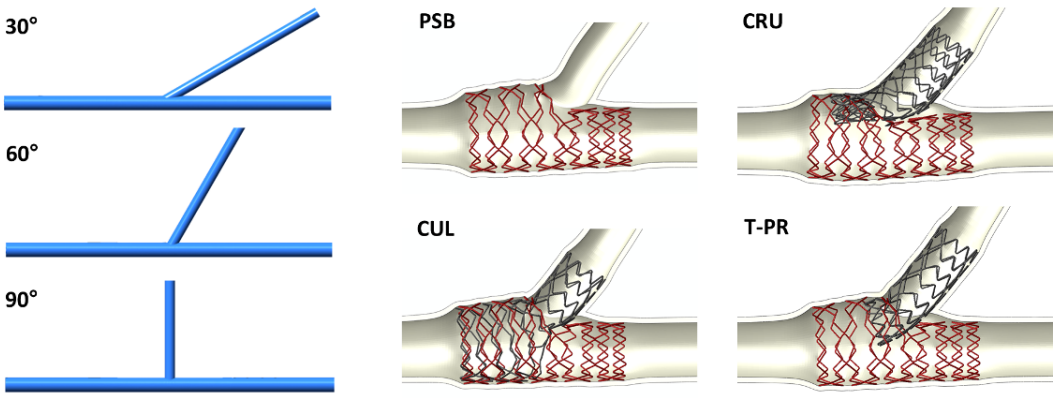

Figure 5.5: *Geometrical configurations of the seven cases used for CFD analyses. On the left, CAD geometries replicating the non-stented 30° 60° and 90° bifurcations. On the right, outcome of the structural simulations of the four stenting procedures investigated. Top left, provisional side branch stenting; top right, crush technique; bottom left, culotte technique; bottom right, T-stenting technique with high protrusion in the MB.*

0.1 pixels. However, this representation is often misleading as error is defined as a deviation from the true value, which is unknown in most circumstances [199]. Alternatively, here the uncertainty (systematic and random) is estimated from the cross-correlation peak ratios (the ratio of the primary to secondary peaks) as opposed to isolating each source of uncertainty. The correlation peak ratio has shown to be a reliable method for outlier detection in standard cross correlation processing as well as an evaluation parameter for signal-to-noise ratio and detectability [104, 112]. Performing uncertainty analysis in such a way allows for the inclusion of unknown sources of error such as instantaneous particle image patterns in the uncertainty analysis. Using this method, uncertainty can be estimated for RPC processing using the ratio of the correlation peaks such that,

$$u_{uncert} = 0.60653\,(Q-1)^{-1} \tag{1}$$

where Q is the ratio of the highest to the second highest peak in the correlation. Additional uncertainties due to magnification and timing of the laser/camera triggering were estimated and propagated to determine the overall reported uncertainty value. For this study, because of the ensemble processing employed, the random error is significantly reduced.

5.2.2 Numerical methods

The seven cases studied by means of DPIV experiments were subsequently simulated via CFD modeling. Geometries, boundary conditions and the blood model were chosen to allow comparison between the cases and the two methods. Numerical replicas of the stenting procedures were implemented by means of finite element modelling strategies described in Chapter 3 and resulted in stent and vessel geometries that were similar to the bench-top models.

- Numerical replica of stenting procedures

A CAD model of the 60° silicone bifurcation was built using the commercial software Rhinoceros 4.0 Evaluation (McNeel and Associates, Indianapolis, IN, USA) to reflect the geometrical features of the bench-top model in terms of bifurcation angle, internal diameters and wall thickness. The bifurcation was then discretized with 112,720 reduced integration C3D8R hexahedral elements and the mechanical behavior was described as a linear elastic material with a Young modulus and a Poisson coefficient equal to 1 MPa and 0.3, respectively.

Stent models resembled the commercial devices Endeavor Resolute (Medtronic, USA) used in the *in vitro* bench tests, which have struts of circular cross section with a diameter of 91 μm. Before deployment, stents had an external nominal diameter of 1.6 mm and a length of 15 mm and were expanded with 4 mm and 3 mm balloons in the MB and SB respectively. The device meshes resulted in a total of 272,384 reduced integration hexahedral elements. Stents were constructed of a cobalt-chromium alloy that was described through a Von Mises-Hill plasticity model with isotropic hardening and the following properties: 233 GPa, 0.35, 414 MPa, 933 MPa and 44.5% in terms of Young modulus, Poisson coefficient, yield stress, stress and deformation at break, respectively [173].

Explicit dynamics finite element models were implemented in ABAQUS/Explicit (v. 6.10, Dassault Systems Simulia Corp., RI, USA) to replicate the four stenting procedures. More details on these models can be found in Gastaldi et al. [65] or Morlacchi et al. [143] Despite the general similarity between how stents were deployed in the physical models and in finite element modeling, some differences exist and are described in the limitations section of the discussion. Lastly, since the double-stenting procedures examined here (CUL, CRU and T-PR) involved the deployment of bent devices in the SB, the stents needed to undergo preliminary simulations of crimping and advancement in order to be correctly positioned in the bifurcated geometries. These preliminary simulations were performed in ABAQUS/Standard and involved the displacement of the stents along an internal cylindrical guide by controlling the axial position of the distal ring of the devices [144].

- Fluid dynamic simulations

The fluid volumes of the three non-stented bifurcations with 30° 60° and 90° were created by means of a CAD software to replicate the fabricated silicone models (Fig. 5.5, left). A structured fully hexahedral mesh was then created with approximately 350,000 elements for the 30ř, 60ř and 90ř bifurcation models. An O-grid was used to discretize the circular section of the vessel with a total of 880 elements, thus enhancing the general quality of the grid at the boundary layers while mesh size was decreased in the bifurcation area. The mesh quality was numerically verified by means of a sensitivity analysis, which indicated that by halving the mesh size, the difference among velocity predictions remained below 1.1% in all cases.

Alternatively, for stented cases, the geometrical configurations of the stents and vessels (Fig. 5.5, right) were achieved with structural simulations and used to create the fluid domain of the stented arteries [143]. A hybrid meshing method composed of hexahedral elements for the core and tetrahedron for the surface was implemented to obtain a computationally efficient calculation grid. Mesh size was chosen in accordance to the sensitivity study presented in Chiastra et al. [31] and resulted in meshes ranging between 2,331,624 elements for the PSB case (1 stent) and 5,081,720 elements for the CUL case (2 stents).

Steady state simulations were carried out by means of the ANSYS/Fluent commercial

software using a parabolic velocity profile at the inlet and a constant flow split as outlet condition in order to replicate the experimental conditions. Specifically, an 85 ml/min inflow was divided with a 84/16 split in the MB and SB. The working fluid was modeled as a Newtonian fluid characterized by a kinematic viscosity of $3.77\text{x}10^{-6}$ m^2/s and a density equal to 1100 kg/m^3. A coupled solver was used with a second-order upwind scheme for the momentum spatial discretization. Under-relaxation factors of 0.3 were applied for the pressure and momentum, and a factor of 1 was applied for the density. The convergence criterion for continuity and velocity residuals was set to 10^{-6}.

5.3 Results

Masked velocity magnitude fields for the non-stented and stented cases are shown in Fig. 5.6 and 5.7, respectively. For non-stented cases, experimental and computational velocity fields display similarities in flow patterns and structures. Specifically, the locations, sizes and shapes of recirculation regions are similar between the two methods. For increasing bifurcation angles, SB recirculation regions grow and protrude inward, toward the lumen centerline. As expected, velocity magnitude in the MB drops off at locations distal to the SB for all cases. For 30° and 90° cases, velocity magnitude values agree between methods. However, the 60° experimental case shows a reduction in velocity magnitude in the MB. This reduction was confirmed in flow rate measurements acquired during image acquisition. Other differences exist between the computational and experimental results, the most obvious being the existence of low flow regions at the MB walls immediately distal to the bifurcation in the experimental cases. This difference can be attributed to the bifurcation model fabrication process causing cloudy regions near the bifurcation due to the junction of metal rods used to form the lumen. As a result the local PIV measurements suffer from reduced signal to noise ratio.

Stented cases shown in Fig. 5.7 also show similarities between the two investigation methods. For the PSB case, which does not include a stented SB, a smaller low flow region is visible in comparison to the other stenting procedures. Additionally, results for double-stented cases (CUL, CRU, T-PR) show flow pattern variation in the distal MB which are manifested as low flow regions protruding inward toward the centerline of the MB and follow the distal surface of the SB stent. This pattern is most obvious in the T-PR case where the SB stent significantly protrudes into the MB lumen. However, several differences are visible between experimental and computational results. First, for experimental cases the field of view contains only stented regions of the bifurcation whereas CFD cases show the transitions between stented and un-stented regions of the vessel. For this reason, CFD results show a decrease in MB velocity over the stented length of the vessel, followed by a recovery of velocity just after the stented portion of the vessel. This decrease and recovery of velocity can be explained by an overexpansion of the stent, which is typical for stenting procedures.

Axial velocity profiles at the SB entrance are shown in Fig. 5.8 in order to quantitatively investigate the influence of bifurcation angles. Both investigation methods show similarly shaped profiles indicating a growth in recirculation area and maximum velocity magnitude for increasing bifurcation angle. Finally, for the T-PR case, velocity magnitude profiles in different locations of the MB and SB are shown in Fig. 5.9. A comparison between numerical

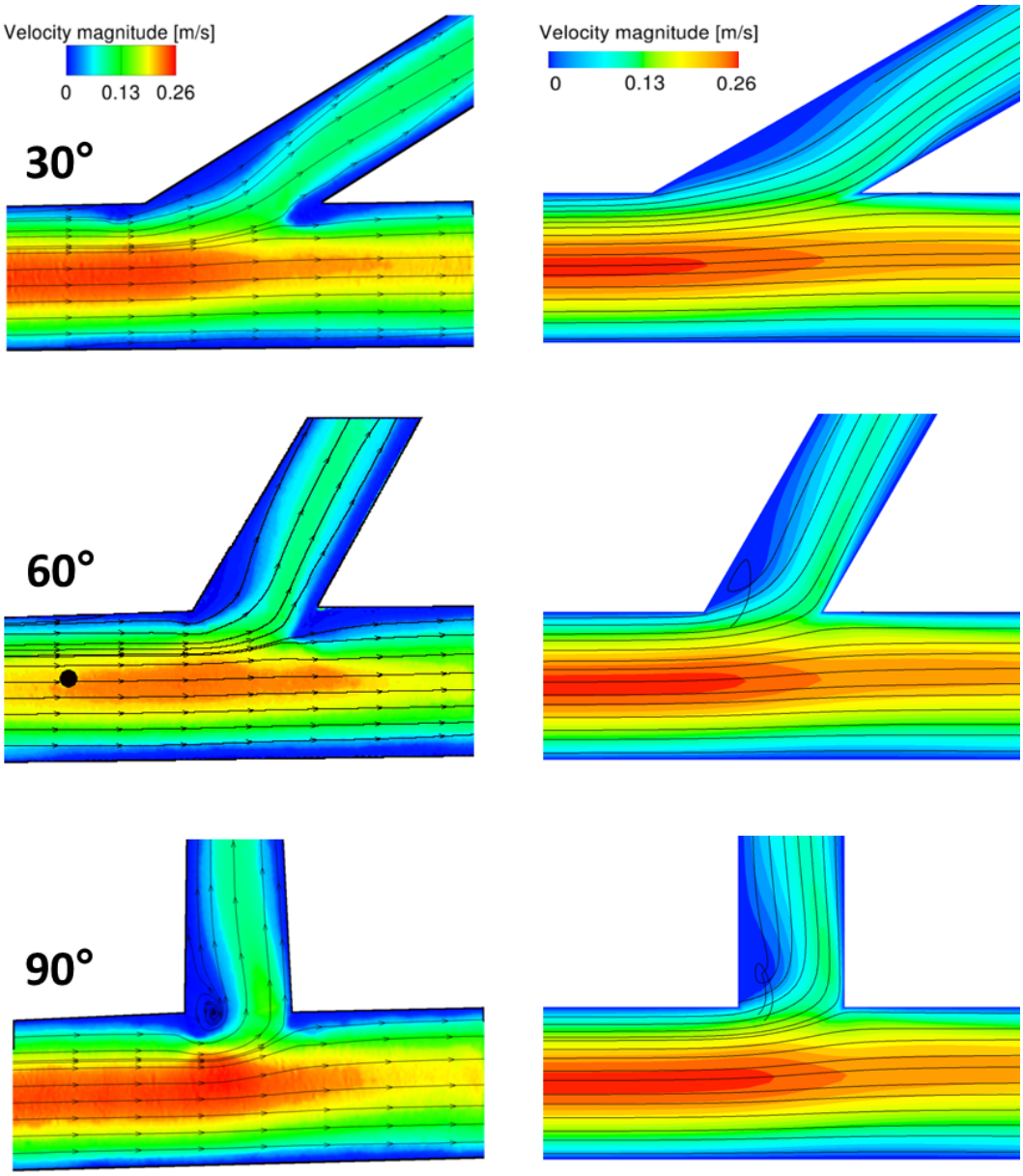

Figure 5.6: *Velocity magnitude fields in* m/s *in the transversal plane of the three non-stented models (top: 30, middle: 60, bottom: 90 degrees). The experimental DPIV measurements are shown on the left, while the numerical results are reported on the right.*

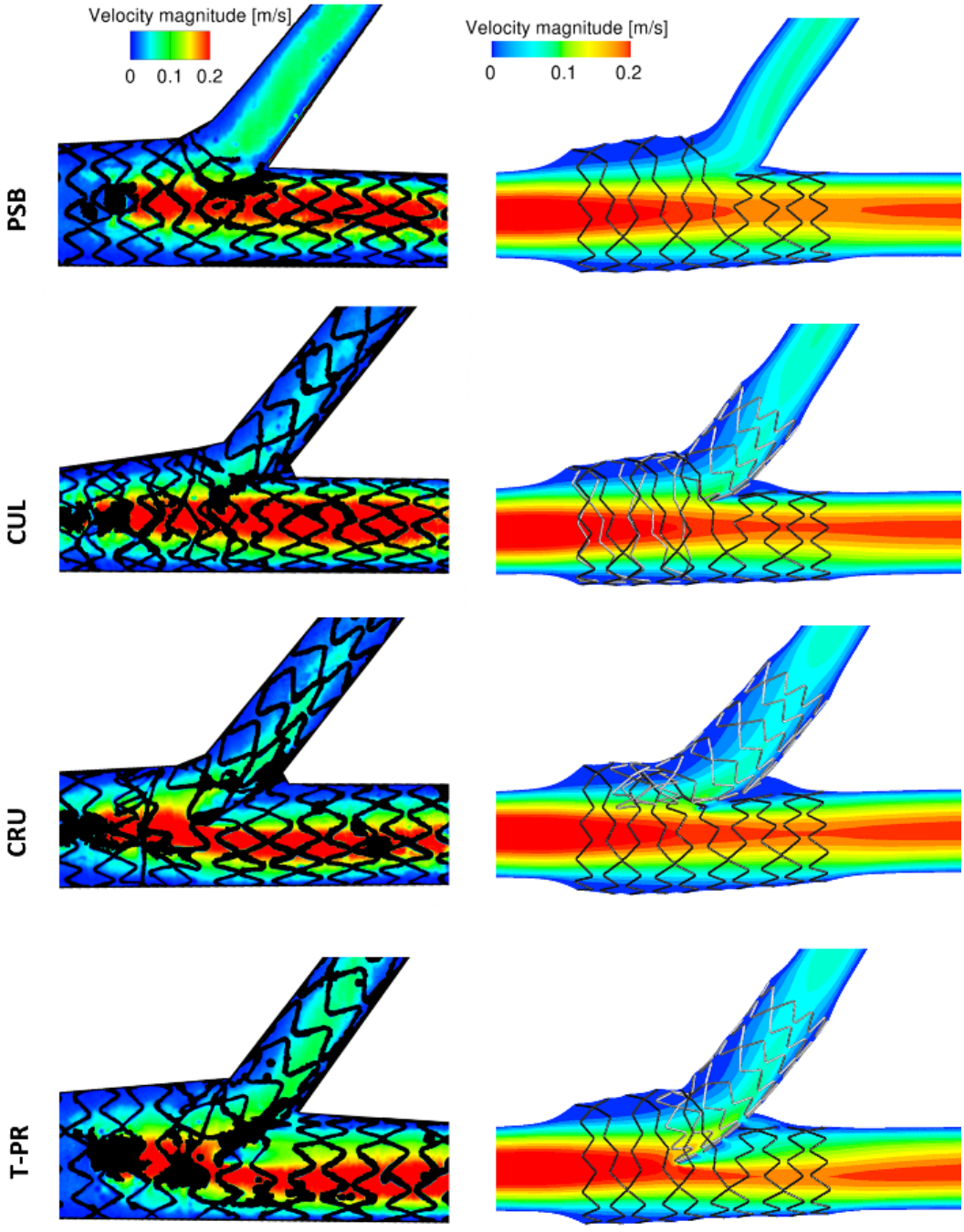

Figure 5.7: *Velocity magnitude fields in m/s in the transversal plane of the four stented models. From top to bottom: PSB, CUL, CRU, and T-PR. The experimental DPIV measurements are shown on the left, while the numerical results are reported on the right.*

and experimental values is reported in the same figures and similar profiles are observed between investigation methods. At the proximal MB location, profiles resemble Poiseuille flow. However, at the first distal MB location, the velocity profile becomes skewed due to a low flow region caused by the SB stent protruding into the MB lumen. Further downstream, the profile skewness is reduced and the velocity returns to a Poiseuille shape.

The uncertainty fields for the T-PR technique and the 60° non-stented case are seen in Fig. 5.10. Problematic regions exist in the MB at high velocity locations, which is consistent for the other data cases. Additionally, increased uncertainty is visible in several small circular regions within the vessel. This increase is due to optical artifacts, which hindered visibility at these locations but did not affect flow inside the model. For brevity, the median uncertainty values of the velocity field for each case are listed in Table 5.1. Larger median uncertainty values are observed for non-stented cases due to the change in spatial resolution.

To better examine the influence of the stenting procedures on the bulk flow, the in-plane Viscous Shear Stress (VSS) has been calculated and reported in Fig. 5.11 for the numerical cases. VSS roughly describes the physical force exerted by the fluid layers on blood cells and is defined as:

$$\mathrm{VSS} = \mu \cdot \left(\frac{\mathrm{dV_x}}{\mathrm{dx}} + \frac{\mathrm{dV_y}}{\mathrm{dy}} \right) \tag{2}$$

where μ is the dynamic viscosity of the fluid while V_x and V_y are the velocities in the principal directions of the transversal plane. For all stent procedures, an increase in VSS magnitude is seen along the vessel wall distal to the bifurcation. Additionally, procedures using multiple stents also display high VSS magnitude values along the region of the SB protruding into the MB lumen. This result is most obvious for the T-PR case, which displays larger regions of high VSS magnitude in the area of the protruding stent. Finally, moderate to high VSS values are seen at the entrance of the SB for each of the stent procedures. Specifically, the PSB procedure, which does not use SB stenting, displays higher VSS values at this location in comparison to the cases using SB stenting.

Additionally, wall shear stress (WSS) was computed for the numerical stented cases and values are reported as area averages in the proximal and distal MB (Fig. 5.12) where for analysis purposes, the division between these areas was chosen to be the centerline of the SB inlet. Secondly, WSS values are reported as line plots (Fig. 5.13) to show the progression of WSS along the length of the MB. WSS values in Fig. 5.13 are reported along three axial wall locations (nearside along the wall adjacent to the SB, far-side, along the wall opposite from the SB, and centerline, along the top wall in the flow direction). Rapid reductions in WSS are observed at locations of the stent struts with maximum WSS values occurring between struts.

For all stenting procedures, WSS is observed to be considerably lower in the proximal region of the MB in comparison to distal areas (Fig. 5.12 and Fig. 5.13). This result is expected, as proximal regions coincide with the over-expansion of the stents caused by the FKB inflation. Results also indicate the detrimental influence of multiple metallic layers on WSS. For instance, CUL performs the worst in the proximal region for both average WSS as well as at each isolated wall location shown in the line plot. Alternatively, the CRU technique has low WSS values localized to the nearside wall at z= 0.016 to 0.018m due to the presence of the triple metallic layer. Results for the PSB case indicate moderate averaged

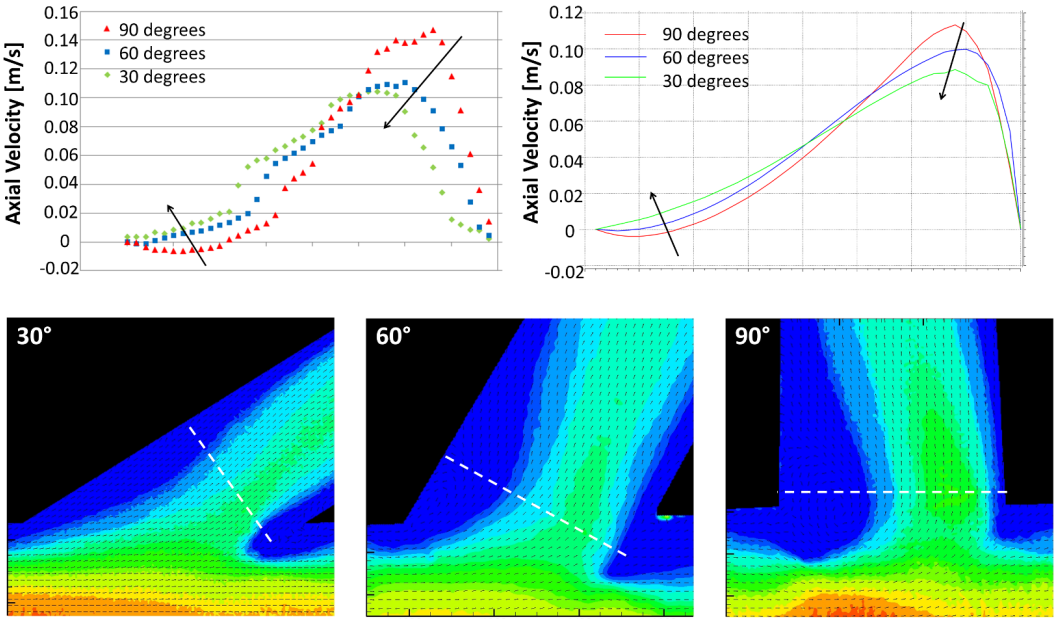

Figure 5.8: *Top: Axial velocity profiles at the SB take-off in the three non-stented cases characterized by a bifurcation angle equal to 90° (red), 60° (blue) and 30° (green). Values are measured at the cross section where the maximal axial velocity is found. The influence of the bifurcation angles in terms of reduction of the peak velocity and recirculation is clear in both the numerical (right) and experimental (left) charts. Bottom: Magnified view of recirculation areas in the SB measured by means of DPIV. Dotted white lines represent the cross section where axial velocity profiles are extracted.*

values without localized regions of low WSS. Finally, the T-PR case indicates higher WSS values, specifically at the far-side wall and in the distal MB, due to the skewness of the velocity profile shown in Fig. 5.9.

5.4 Discussion

DPIV and CFD are commonly adopted methods to assess local bulk flow patterns in coronary arteries both in the scientific literature and in the evaluation processes of cardiovascular implants. Both methods require modeling assumptions that can affect the fidelity of the results. However, comparative investigations of relevant cases can increase the reliability of results and provide a first comparison of CFD models with respect to experimental data, under the targeted flow conditions. Velocity fields presented in Fig. 5.6 and 5.7 and more quantitatively, axial velocity profiles in Fig. 5.8 and 5.9, indicate a general good agreement between the experimental and numerical results despite some point-to-point variations related to intrinsic differences of the two methods (detailed in the limitations section). Although CFD velocity measurements fall outside of DPIV uncertainty values, this analysis is still valuable in order to compare qualitative flow patterns. In fact, most of the following

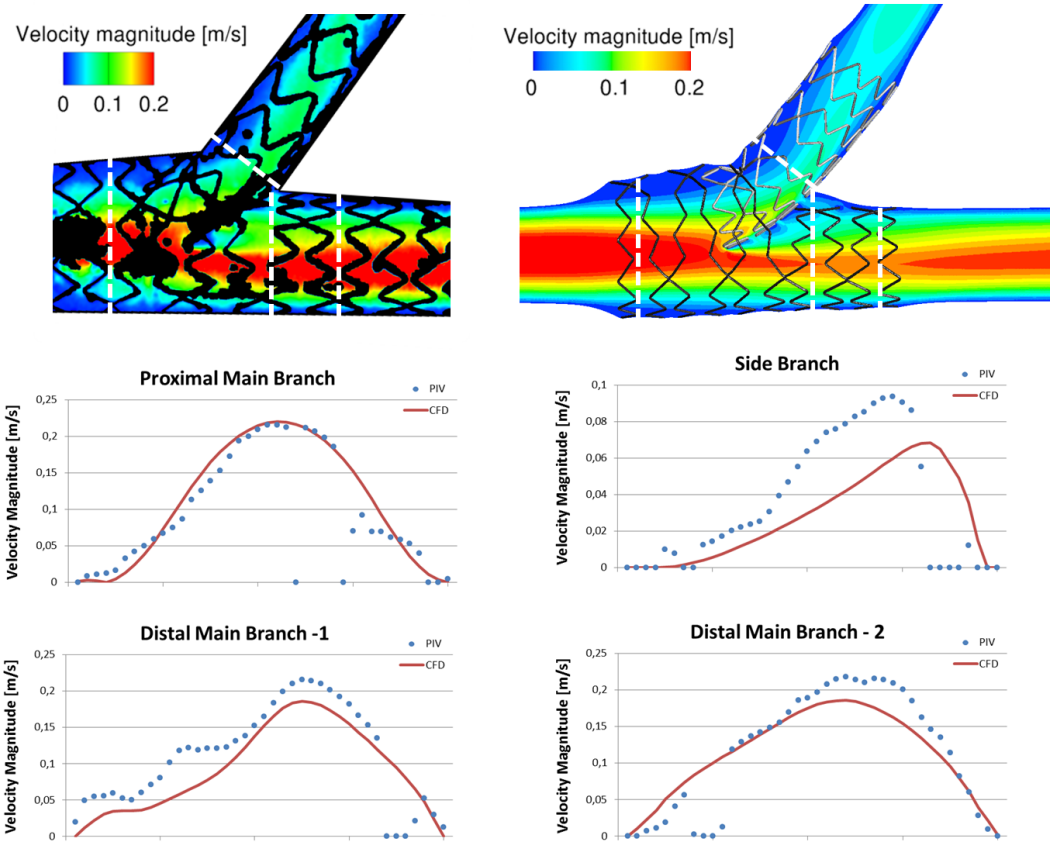

Figure 5.9: *Velocity magnitude profiles measured at four cross sectional locations of the T-PR case for experimental (blue dots) and numerical (red line) studies. Cross sectional locations are highlighted in the contours of the top panel with white dashed lines. Distal Main Branch-1 is located proximal to Distal Main Branch-2.*

Table 5.1: *Median uncertainty values in pixels and velocity magnitude for the seven cases investigated.*

Stent case	Uncertainty[pixels]	Uncertainty[m/s]
No stent 30 degrees	0.16	0.004
No stent 90 degrees	0.20	0.005
No stent 60 degrees	0.15	0.004
Crush	0.04	0.001
Culotte	0.04	0.001
Provisional SB	0.04	0.001
T-stenting with protrusion	0.04	0.001

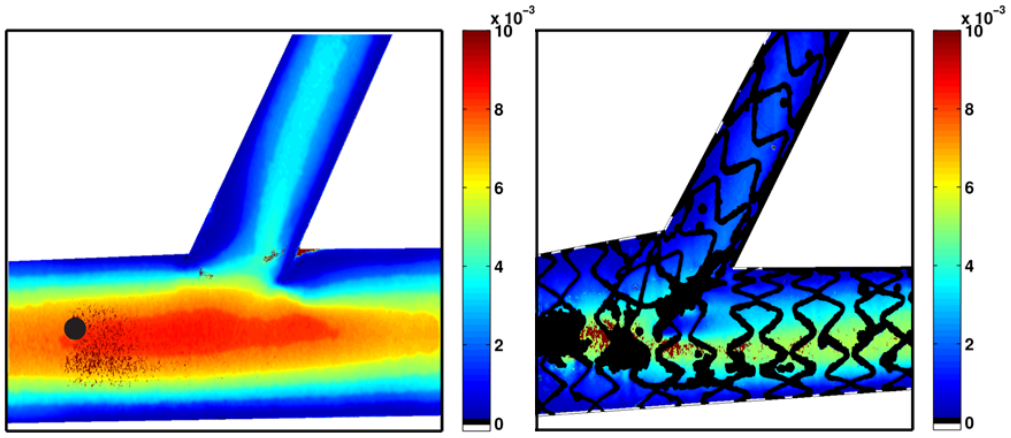

Figure 5.10: *Velocity uncertainty in m/s for the 60° non-stented case and the T-PR technique. Problematic regions exist in the MB at high velocity locations, which is consistent for other data cases.*

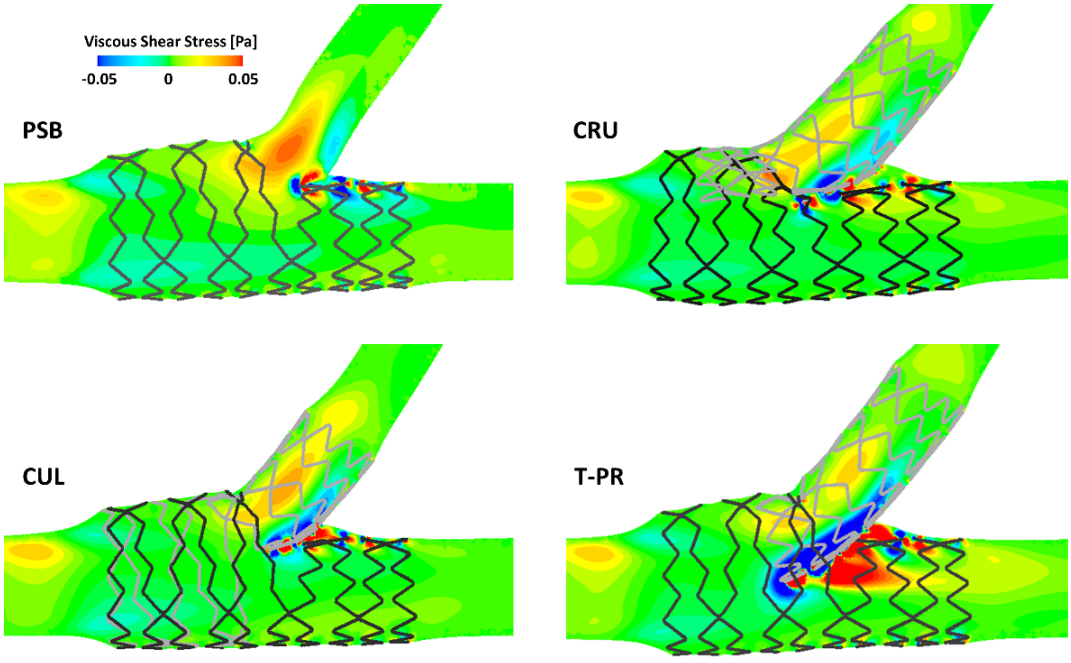

Figure 5.11: *In-plane VSS fields of the numerical results calculated in the transversal plane of the four stented cases. To better visualize fluid structures at different scales, VSS color scale values are bounded between -0.05 and 0.05 Pa. Viscous shear stress is increased by approximately one order of magnitude in regions with close proximity to stent struts.*

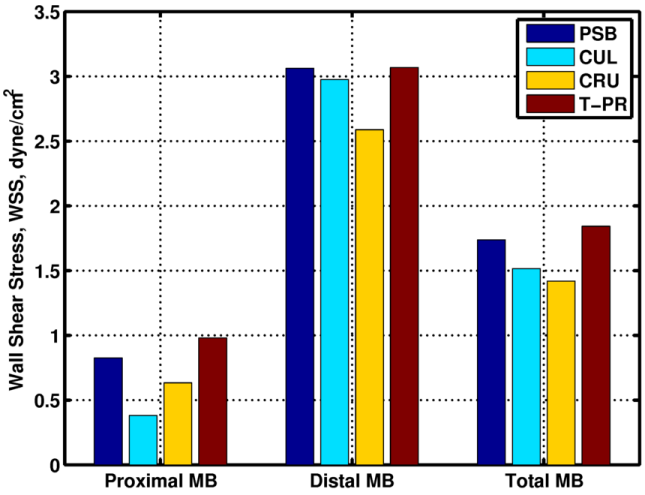

Figure 5.12: *Area averaged WSS for proximal (dark green area), distal (light green area), and entire MB in* dynes/cm^2.

observations related to the influence of bifurcation angles and different stenting procedures can be performed whether considering both experimental and numerical results or just one of the methods.

Specifically, the development of atherosclerotic plaques is mainly localized to the external walls of coronary bifurcations and has been associated with low and recirculating flows as well as low WSS [6, 68]. In particular, the angle of the SB with respect to the MB has been proven to influence the severity of atherosclerosis in coronary bifurcations as larger angles have been associated with increased plaque localization [43, 77]. These findings are in agreement with our experimental and numerical results reported in Fig. 5.6 where velocity magnitude contour maps in the transversal plane are shown for the cases of non-stented bifurcations of 30, 60 and 90 degrees. A wider SB angle is associated with larger recirculation area and, likely, a larger low and negative WSS region. A more quantitative analysis is performed by plotting the axial velocity profiles at the SB cross section (Fig. 5.8). Results indicate that by decreasing the bifurcation angle, both the peak axial velocity and recirculation area decrease, thus describing a less atheroprone hemodynamic environment in comparison to larger angles.

During the bare metal stent (BMS) era, the main concern after stenting procedures was in-stent restenosis, reduction of lumen vessel due to high neo-intimal hyperplasia and migration of smooth muscle cells. The introduction of drug eluting stents (DES) in the clinical field led to a strong reduction of the restenosis rates with respect to BMS [194] but, at the same time, increased the rates of late stent thrombosis (LST) events [54]. LST is defined as a thrombus (or blood clot) formation within a stent occurring more than 30 days after the intervention, mainly caused by a delayed arterial healing and endothelialization. In 2010, Nakazawa et al. [157] observed through human pathologic specimens how bifurcated arteries show a greater incidence of LST, especially at the flow divider region where thrombi originate close to the uncovered stent struts. In this area, delayed healing may be exacerbated by potential flow disturbances induced by stent struts in combination with an impaired drug

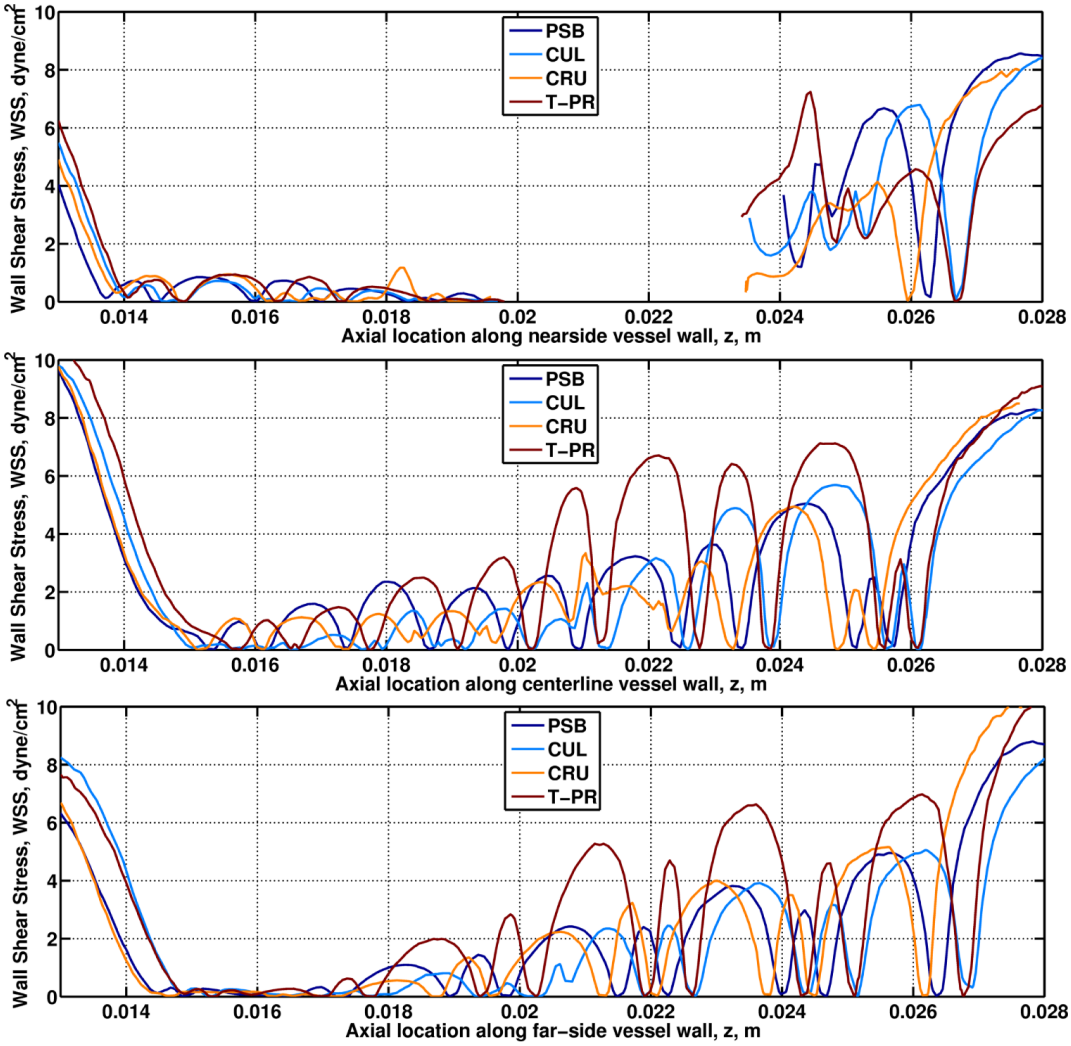

Figure 5.13: *Wall shear stress along nearside (top), centerline (middle) and far-side (bottom) of the MB vessel. Nearside corresponds to wall location on the side of the SB, centerline corresponds to the top wall of the vessel at centerline of the MB, far-side corresponds to the wall location on opposite from the SB.*

elution and altered platelet deposition [215]. With this in mind, an accurate assessment of local blood flow patterns in terms of bulk-flow quantities becomes as crucial as the standard near-wall variables, such as oscillatory indexes or WSS, that are habitually linked to in-stent restenosis.

Alterations in hemodynamic quantities are most noticeable when comparing velocity fields among single (PSB) and double stenting procedures (CUL, CRU, and T-PR). By observing both the *in vitro* expansions (Fig. 5.2) and numerical simulations (Fig. 5.5), it is apparent that the simultaneous presence of two devices in a coronary bifurcation leads to the creation of a new metallic carina between the SB and the distal part of the MB in addition to the presence of a larger number of stent struts at the flow divider. The disturbance created by this geometry is observed in the velocity fields (Fig. 5.7) as well as the VSS (Fig. 5.9) and WSS (Fig. 5.13) measurements, which indicate low velocity and WSS as well as high VSS in and around the region of the flow divider. Problems are also apparent in the proximal MB after double stenting procedures due to increases in strut density, thus causing local values of low WSS. These results are in agreement with the current clinical practice and recent large clinical trials [14] reporting that placing a single stent in the MB should be favored over double stenting procedures for the majority of the cases.

Additionally, results suggest that the hemodynamic conditions also depend on which double stenting technique is performed. Specifically, the cases with high protrusion of the SB into the MB lumen (T-PR and CRU) are observed to have problematic regions distal to the metallic carina. For instance, the T-PR case displays skewed velocity profile with low flow regions occurring distal to the SB stent protrusion within the MB. This skewness causes high WSS values on the far-side wall, but in turn, results in low WSS distal to the metallic carina on the nearside wall and highly disturbed VSS field. This finding is quantified in the axial velocity profiles presented in Fig. 5.9 and in the WSS and VSS measurements (Fig. 5.13 and Fig. 5.11, respectively). Similarly, the CRU case exhibits asymmetrical velocity in the distal MB, but additionally displays low WSS measurements throughout the MB. These findings are supported by Yazdani et al. [215] in an *in vivo* study suggesting that new metallic carinas at the flow divider region may be critical in terms of LST. Lastly, the CUL technique appears to be the least critical among the double stenting procedures in terms of bulk flow quantities, possibly due to the presence of a small protrusion of the SB stent into the MB. However, CUL is also characterized by the lowest WSS values in the proximal MB due to an area of high overlapping stents. This occurrence is also visible in the CRU technique where a triple metallic layer is present near the SB take off MB and correlates to the results proposed by Foin et al.[57] who find a higher risk of stent malapposition within double stenting techniques, especially CRU and CUL technique.

5.4.1 Study limitations

Both the experimental and computational methods presented herein are subject to some intrinsic limitations and assumptions that must be carefully considered when discussing results and drawing conclusions. Two major differences exist between the CFD and experimental models produced by this work. First, the polymeric bifurcation models differ from their numerical replica due to manufacturing inaccuracies. Specifically, due to the molding/casting process, a small extension of polymer remained confined in the bifurcation area

at the connection between MB and SB. This occurrence is mainly evident in the velocity fields of the non-stented cases where low flow areas are present before and after the bifurcation. Concerning the stented cases, geometrical configurations are a result of *in vitro* bench testing performed with real commercial devices deployed by an experienced interventional cardiologist. On the other hand, numerical models are based on virtual simulations that aimed to replicate the same stenting procedures but are characterized by some imprecisions. For instance, the length of the stent used in the numerical models is reduced to decrease the computational cost of each analysis. Moreover, axial positioning and rotation of the devices is only assumed by visual inspection of the *in vitro* expansions and may slightly differ from reality. Second, DPIV experiments are able to catch the compliance of the deformable bifurcated models and the effect of pressure, while rigid wall boundary condition is assumed for all the CFD simulations. However, this difference had only slight influence on the steady cases that have been examined here, but will have more influence on transient flow cases characterized by the typical phase shift between peak pressure and coronary flow.

In addition to the differences between the experimental and numerical methods, other common limitations with regard to the study should be carefully considered, especially if any clinical conclusion is drawn. First, only one stent design and one bifurcation model are analyzed. Moreover, due to manufacturing difficulties, straight vessel branches are designed without considering the physiological diameter reduction and curvature of coronary arteries along each branch. Secondly, only a single steady flow condition is investigated in the current study, while future work will include more physiologically accurate flow environments. Lastly, a Newtonian fluid model is used in both experimental and computational approaches while in reality blood is a non-Newtonian fluid. However, we believe that this limitation might be accepted in this study mainly considering the large vessel diameter and that no discussions on shear stresses at low flow regions are proposed and that within a steady flow conditions Newtonian and non-Newtonian models are proven to be very similar, especially in regions of mid-range to high shear [101].

5.5 Conclusion

This chapter evaluates the fluid dynamic influence of different bifurcation angles and stenting procedures for coronary bifurcations by developing a comprehensive experimental and numerical approach. Results display highly disturbed velocity fields in cases of wider angles and double-stenting procedures. In particular, increasing the bifurcation angles, larger recirculation and stagnation zones are found in the SB area suggesting higher atheroprone environments exist for wider bifurcations. On the other hand, double-stenting procedures result in a higher density of metallic struts in correspondence of the flow dividers. In these areas, both DPIV measurements and CFD predictions highlighted marked low flow regions, very critical for late stent thrombosis.

Besides intrinsic differences and modeling assumptions of the two approaches, the results presented underline how both CFD and DPIV analyses are able to capture the main trends of the fluid flows within both the stented and non-stented cases investigated. These findings suggest that the role of hemodynamics before and after stenting procedures might be accurately assessed with both methods. Nonetheless, both approaches still require a challenging

direct validation against *in vivo* measurements to fully demonstrate their ability to describe the existent hemodynamics of coronary flows. Unfortunately, this step is currently unfeasible due to technical difficulties on *in vivo* imaging systems.

APPENDIX I: Transient cases

In addition to the steady flow conditions used in the presented study, the flow loop developed by Charonko et al.[27] allowed the reproduction of a physiological transient coronary flow as well (Fig. 5.14). In this light, important features of the flow loop were: i) the presence of compliances to simulate the effect of the systemic circulation and ii) a solenoidal valve to clamp the flow in phase with the pump to reproduce the effect of the contractions of myocardium. The pump and the other flow loop components were adjusted to replicate typical flow conditions within the large coronary arteries, including a frequency of 1 Hz and the phase offset between pressure and flow rates visible in Fig. 5.14. Pressure range was maintained within 85 and 115 mmHg causing a modest but visible geometrical variation of the bifurcation.

All seven cases (stented and un-stented) were acquired under this flow condition. However, data from transient acquisitions have yet to be fully processed. As an example of transient data processing and to prove the feasibility of such analyses, preliminary results of the 60° bifurcation without stent are proposed herein. In such flow conditions, post processing was more complex since the standard ensemble correlation techniques that have been exploited for the steady flow cases could not be used with time-varying velocity fields. Indeed, processing of image-pairs was performed following a periodic ensemble technique. This method was graphically described in Fig. 5.15 and consisted in averaging the correlation peaks of image-pairs corresponding to the same instant of the periodic flow. In particular, memory limitations only allowed the acquisition of four seconds corresponding to four consecutive cardiac cycles. In such a way, only four image pairs were ensembled together to improve the estimate of the particle displacement, while for steady cases up to 1000 image-pairs were averaged together for each case.

The preliminary results presented in Fig. 5.16, Fig.5.17 and Fig.5.17 display the velocity magnitude fields and axial velocity profiles at three time instants before and during the reverse flow period. In particular, in Fig. 5.16 the flow is decreasing in both the MB and SB and almost close to zero in the SB. Then the SB flow starts to reverse in the MB (Fig. 5.17) where the flow is still forward. Lastly, in Fig. 5.18 the whole bifurcation experiences a reversed flow. Looking at velocity profiles it is possible to notice in some cases the typical Womersley profile of reversing flows characterized by low or even negative velocity values at the areas close to the wall and a pseudo-parabolic profile in the middle of the vessel.

A full processing of these data will allow a better understanding of the temporal variations of the flow structures that are developing within the bifurcation subjected to a physiological coronary flow. Furthermore, the processing of the data obtained varying the bifurcation angles and the different stenting procedures will lead to recognise their influence on the time-varying local blood flow patterns.

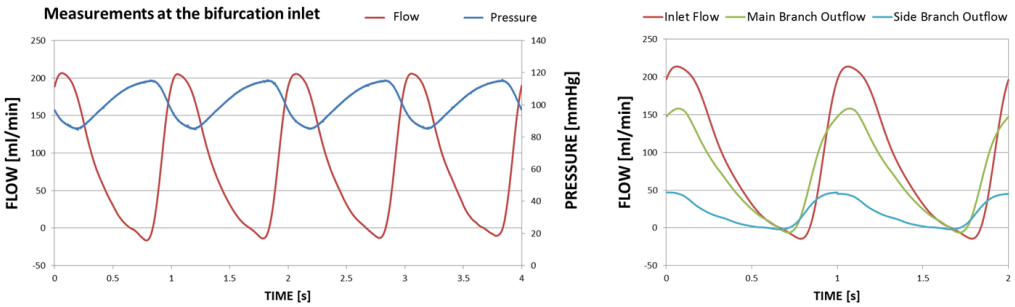

Figure 5.14: *On the left, flow and pressure measurements at the bifurcation inlet in the transient case. The phase shift between flow and pressure is visible. On the right, repartition of the inlet flow between the MB and SB outlet.*

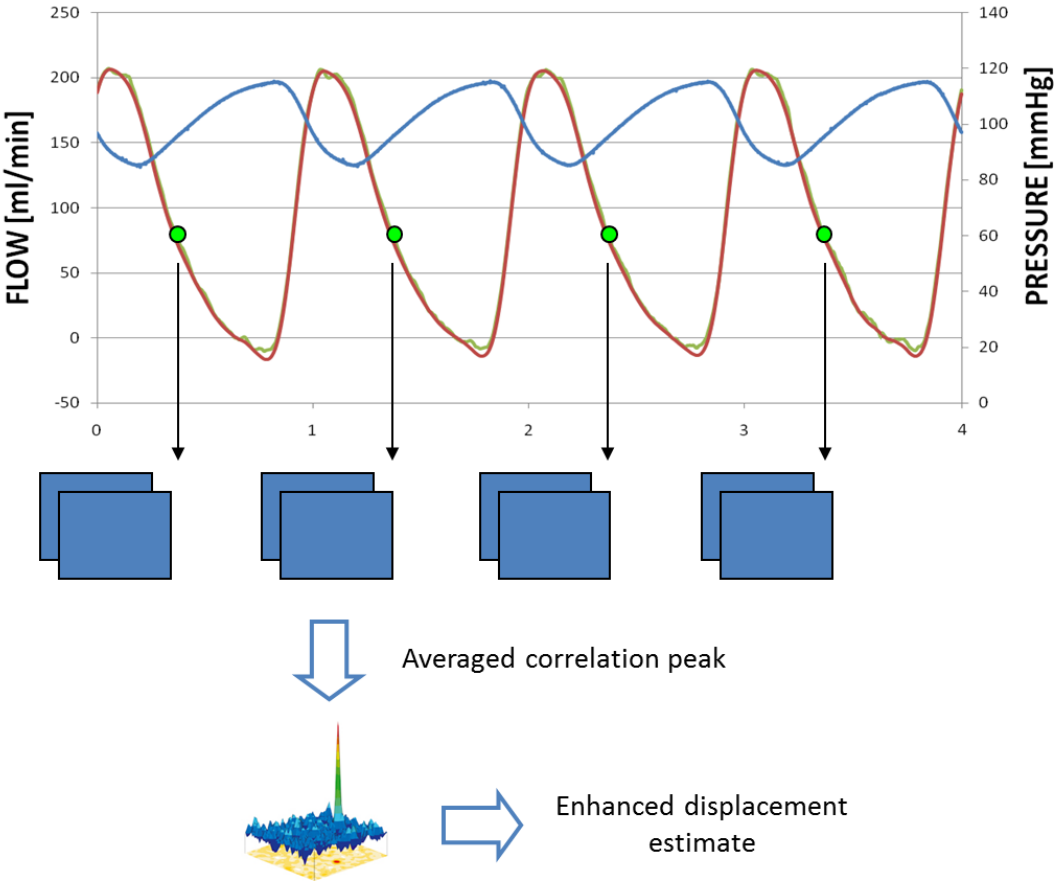

Figure 5.15: *Periodic ensemble technique. Correlation planes of four image-pairs corresponding to the same instant of the four consecutive cycles acquired are averaged together to obtain a better displacement estimate*

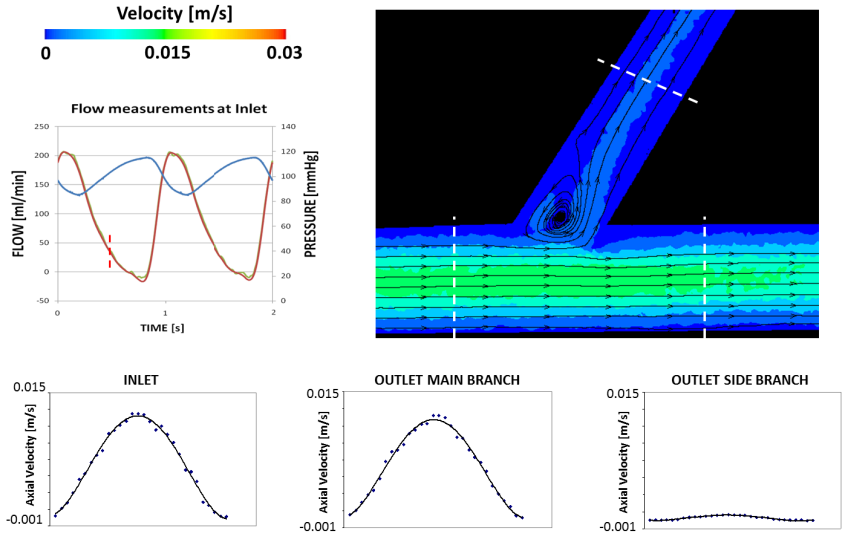

Figure 5.16: *Velocity magnitude field in the transversal plane and axial velocity profiles at the three locations highlighted by the white dotted lines. The time instance is shown with a red line in the velocity tracing graph displayed on the left.*

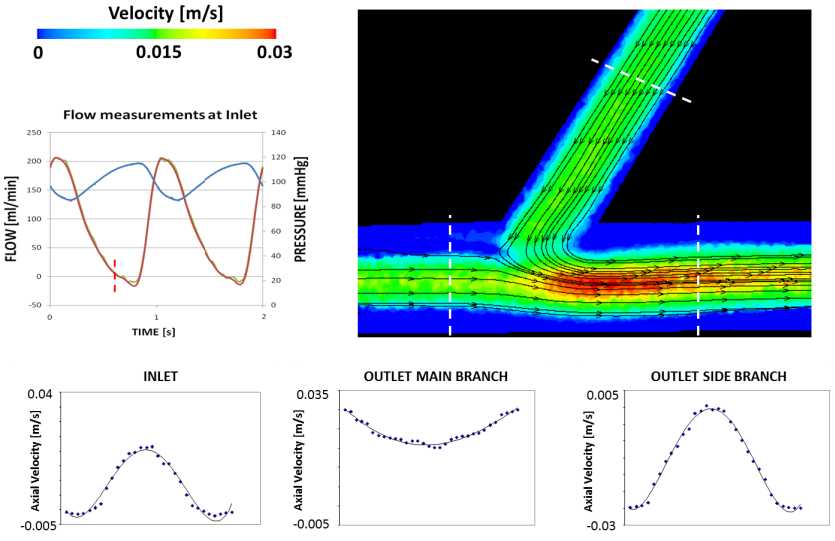

Figure 5.17: *Velocity magnitude field in the transversal plane and axial velocity profiles at the three locations highlighted by the white dotted lines. The time instance is shown with a red line in the velocity tracing graph displayed on the left.*

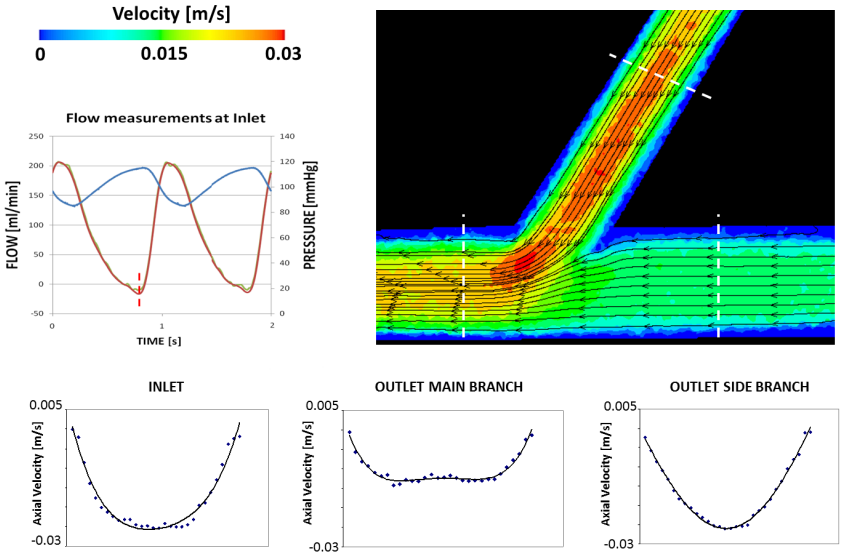

Figure 5.18: *Velocity magnitude field in the transversal plane and axial velocity profiles at the three locations highlighted by the white dotted lines. The time instance is shown with a red line in the velocity tracing graph displayed on the left.*

Chapter 6

Patient specific simulations of real clinical cases

Contents

In the last decade, several numerical models have been implemented to simulate different stenting procedures and provide new information about their biomechanical influence on the surrounding vascular environment [146]. However, important limitations still preclude the current routine application of computational models in the clinical field. Among these limits, the majority of numerical studies until today is still based on highly idealized geometries and only aims at replicating standard stenting procedures. Therefore, such studies can only provide universal guidelines and not patient-specific indications for the planning of each treatment. Conversely, the possibility to compare different procedural options considering the specific anatomical and mechanical properties of each patient before its treatment might help the improvement of the interventional planning and clinical outcome. Recent developments in coronary imaging have paved the way to new methods that are able to create realistic image-based reconstructions of vascular districts [193], potentially useful for patient-specific simulations of stenting procedures.

Thus, in this chapter, a review of the most important methods to create image-based coronary models is firstly presented, highlighting the most recent applications to image-based models of stenting procedure. Secondly, it is proven the feasibility of a new patient-specific virtual model that uses image-based reconstructions of coronary bifurcations and is able to replicate real cases of stenting procedures. Two clinical cases are investigated focusing the attention on the open problems of coronary bifurcations and its main treatment, the PSB approach. Image-based reconstructions are created combining the information from conventional coronary angiography and computed tomography angiography while structural finite element models are implemented by means of the ABAQUS commercial code following the main modelling techniques presented in Chapter 3.

6.1 Coronary imaging for image-based structural models

Much effort has been made over the last decade to reconstruct image-based models of coronary arteries to be used in computational studies [193, 198]. Coronary imaging is still an open challenge for any medical imaging operators. The main reason is that coronary arteries are small (2-4 mm in diameter), have tortuous, complex, 3D paths and are continuously in motion. Besides ordinary requisites, such as complete diagnosis capability, accuracy and limited invasiveness, coronary imaging requires high temporal resolution to resolve the constant motion of the respiratory and the cardiac cycles, and high spatial resolution for the accurate imaging of very small vessels [115]. Nowadays, conventional coronary angiography (CCA) is the standard clinical test for the imaging of diseased coronary arteries, but recently other tomographic imaging systems such as computed tomography angiography (CTA), magnetic resonance imaging (MRI), intravascular ultrasonography (IVUS) and optical coherence tomography (OCT) have been developed and used for coronary imaging. Albeit not being routinely used in clinical practice, these imaging techniques have proven to be able to accurately provide further anatomical and functional information with respect to CCA, such as presence of atherosclerotic plaque, thickness of arterial wall, composition of vascular tissues or even stent struts location. These coronary imaging techniques are listed in 6.1 summarizing some of their main features.

Indeed, while rigid-wall-assumption CFD analyses of coronary arteries only require the

Table 6.1: *Advantages and disadvantages for CCA, CTA, MR, IVUS and OCT. Grading from +++ (most) to - (least); X indicates ability. Table adapted from Lederlin et al. [115], Schmitt et al. [184] and van Soest et al. [205]. Copied with permission from Morlacchi et al. [146].*

Property	CCA	CTA	MRI	IVUS	OCT
Spatial Resolution (μm)	*100-200*	*500-600*	*1000*	*80-120*	*10-20*
Type of radiation	*X-rays*	*X-rays*	*Radio waves*	*Ultrasound*	*Near-IR*
Heavy radiation exposure	*++*	*+++*	-	-	-
Invasiveness	*+++*	*+*	-	*+++*	*+++*
Coronary assessment	*+++*	*++*	*+*	*+++*	*+++*
Plaque detection		*X*	*X*	*X*	*X*
Plaque component detection				*X*	*X*
Stent strut detection					*X*

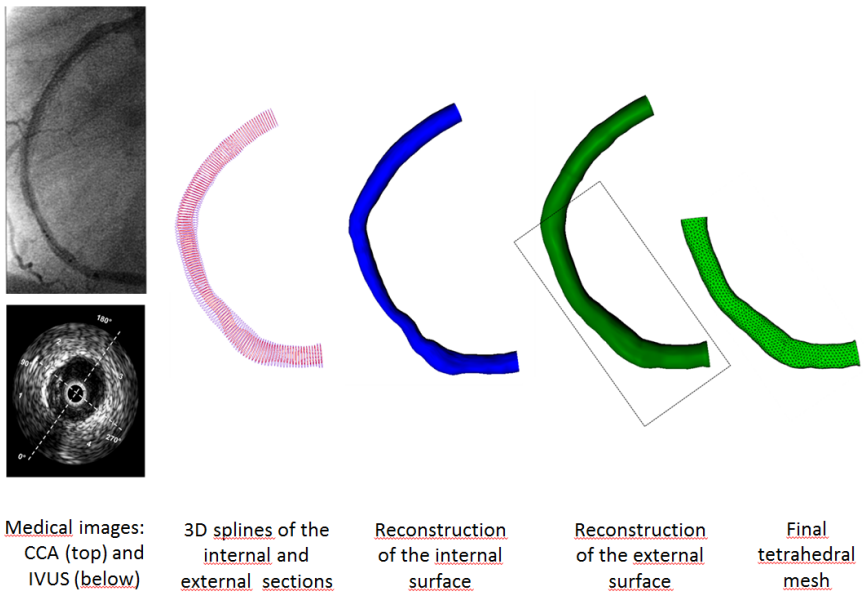

Figure 6.1: *Summary of the main phases required for the construction of an image-based coronary model for structural simulations: from a combination of two medical images (CCA and IVUS) until the final finite-element mesh. Image inspired by Gjisen et al. [69] and Gonzalo et al. [71] with permission.*

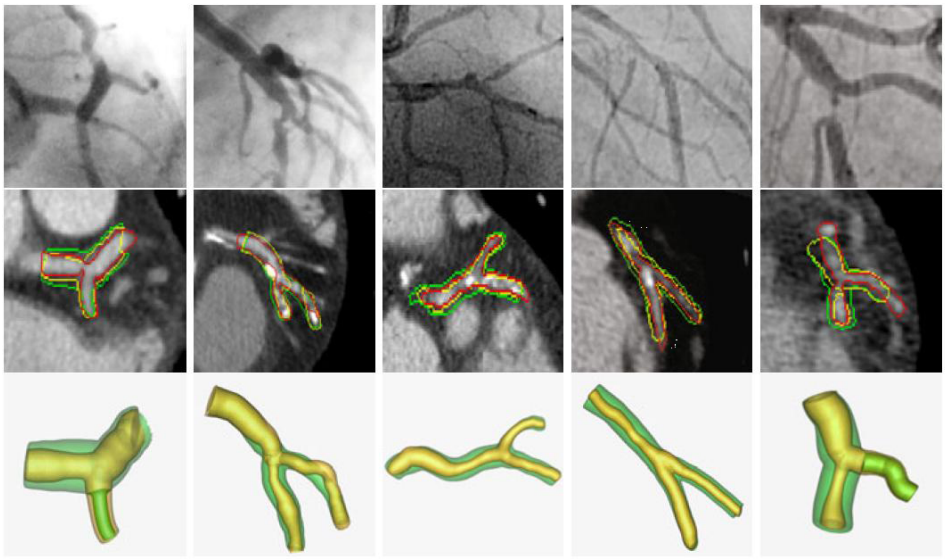

Figure 6.2: *Top row: CCA images of the five coronary bifurcation investigated. Middle row: corresponding bifurcation plane from CTA images with manual segmentation (red), pre- (yellow) and post-operative (green) outlines overlaid. Bottom row: 3D geometrical models of the bifurcations, with inner lumen referred to the pre- (yellow) and the post-operative (green) models. Image copied with permission from Cardenes et al. [25].*

internal arterial surface reconstruction to implement a consistent geometrical model, more complex studies such as image based structural simulations or fluid-structure interaction (FSI) models also require other information like arterial wall thickness, potential presence of atherosclerotic plaques and tissue properties characterization. These data cannot all be obtained via a single imaging technique. As a consequence, recently, several methods able to combine information coming from two different imaging techniques have been developed and proposed in the literature [25, 109, 189]. Lastly, the potential presence of medical devices in the vessels leads to other complications since current major imaging techniques cannot simultaneously detect both biological tissues and metallic objects.

6.1.1 Reconstruction of image-based coronary arteries

The main steps required for an image-based model generation are depicted in Fig. 6.1, where the image-based reconstruction of a stenotic RCA is shown as an example [69, 71].

The first phase in the image-based modelling process is the extraction of the vessel skeleton and the subsequent surface reconstruction from medical images of the vascular anatomy. Some 3D imaging techniques such as CTA or MRI allow a direct 3D reconstruction of the internal or external vessel geometry by providing a series of aligned 2D cross-sections of the arteries. On the other hand, cross-sectional images obtained with IVUS and OCT need to be associated with other imaging systems like CCA in order to reconstruct a realistic vessel path in the 3D space. Depending on the type of images available, the skeleton is reconstructed manually or with computer-assisted segmentation of individual image slices using

the boundaries of the lumen and/or the vessel outer wall. The vessel boundary is then defined to generate the surface of a solid model. Surfaces of vessels without lateral branches are directly reconstructed by connecting splines describing the vessel circumferences. For bifurcating or branching vessels the surface generation is more complicated: a common approach is to reconstruct each branch separately and then merge the vessels via CAD software.

After the vessel reconstruction process, the final phase is the discretization of the complex model into finite elements to be used in numerical analysis. Geometries that are topologically equivalent to straight tubes, such as coronary artery segments with no branches, are easily discretized with structured or even unstructured hexahedral meshes. Such meshes may also be computed for bifurcations, but more effort is required to ensure the element quality [39]. Unstructured tetrahedral meshes are more popular and easier to be computed but may result in lower convergences speeds of the analysis and less reliable results.

In the next paragraphs, some of the published image-based reconstruction strategies are outlined, starting from those able to reconstruct the inner wall only and, then, focusing on those able to reconstruct both the inner and the outer arterial walls.

The methods that only reconstruct the inner wall of the vessels are mainly used for CFD simulations while their application for FSI or structural models is subject to the geometrical approximation of the external wall. In 2002 Antiga et al. [5] were able to reconstruct various arterial bifurcations using only CTA images, proposing a fast, accurate and reproducible technique. Their study developed a methodology able to build and analyse patient-specific 3D geometrical models and to semi-automatically generate high quality hexahedral meshes. In 2010, Galassi et al. [60] proposed a 3D reconstruction of coronary bifurcations based on 2D CCA images, obtained in standard clinical tests. Their novel 3D reconstruction system well reproduced a solid image starting from simple biplane angiographies. Dvir et al. [47] also successfully generated 3D models of coronary bifurcations using 2D angiographies taken from different angles of projection. Subsequently, authors used the solid geometries to investigate morphological changes occurring after the treatment. Other groups combined outcomes from different imaging systems taking advantage of each technique to overcome the limitations of the other. In 2011, Cardenes et al. [25] developed for the first time a method to combine CTA and CCA for the reconstruction of the internal wall of coronary artery bifurcations (Fig. 6.2). These authors analysed vessels that underwent stenting surgery examining pre- and post-operative conditions. Correspondence between CCA, CTA images and the realistic 3D bifurcation geometries is shown in Fig. 6.2. Limitations of this reconstruction technique are the assumption of circular cross section for the arteries and the limited information regarding the different composition of vascular tissues and the outer arterial wall shape.

On the other hand, the use of IVUS or OCT imaging techniques paves the way to the simultaneous reconstruction of both the internal and external arterial walls. In 1996, Krams et al. [109] demonstrated the feasibility of combining CCA and IVUS. This technique, validated and used in many investigations [69, 207], has the main advantage that CCA and IVUS imaging acquisitions are simultaneous. Moreover, it does not rely on manual selection and matching of anatomical landmarks [204]. The vessel path is identified from 2D angiographies while IVUS images provide the cross-sections to obtain accurate geometries of both the inner and outer wall. Outputs of their imaging procedure consisted of arterial contours that were subsequently positioned perpendicular to the reconstructed 3D catheter pathto loft a 3D solid model. The 3D reconstruction of the lumen and the vessel wall is generated with a

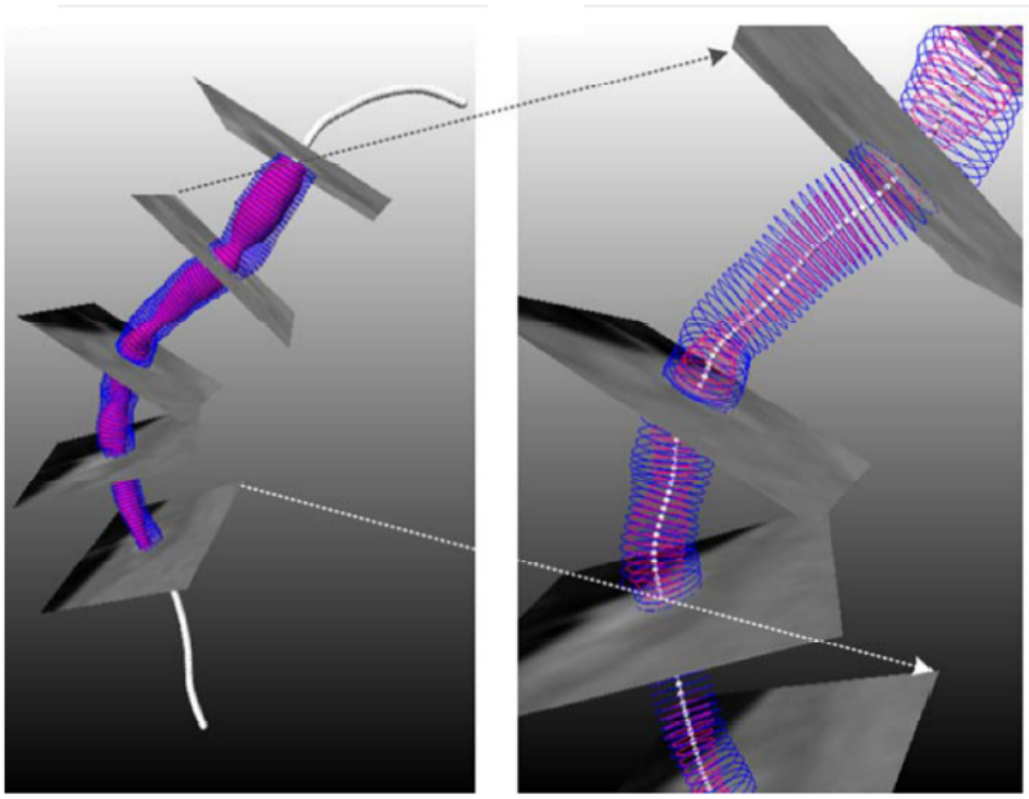

Figure 6.3: *The IVUS 2D images are placed on the CTA derived centreline at correct locations, generating the coronary artery geometry. Pink curves represent the internal lumen, blue ones the exterior wall. On the right, a magnification of the 3D contours. Reprinted with permission from Van der Giessen et al. [204].*

CAD software utilizing B-splines and the mesh was then created using tetrahedral elements. Other research groups have also combined CCA and IVUS to obtain 3D reconstructions of coronary arteries, as well [19, 189]. Subsequently, van der Giessen et al. [204] presented another interesting framework that merges IVUS and CTA and can be used to derive 3D lumen and wall geometries in which the relationship between WSS and atherosclerosis can be investigated (Fig. 6.3). Recently, in 2011, Tu et al. [201] published a study where a new co-registration approach able to combine X-ray angiography and IVUS/OCT imaging is presented. This strategy allows a straightforward and reliable solution for the assessment of the extent of coronary artery disease and the reconstruction of the coronary tree providing detailed information about lumen area and plaque size at every position along the vessel of interest. Limitation of this new approach is that OCT is not routinely gated to the cardiac motion and *in vivo* validation has been limited. However, the use of OCT may be the next important step in image-based reconstruction of coronary models. Indeed, OCT is able to precisely detect geometrical configurations of both atherosclerotic plaques and arterial walls

and distinguish among their different biological components (lipid deposits, necrotic core, calcifications, stratification of the arteries etc.).

6.1.2 Image-based structural models of stenting procedures

The first image-based structural model of stenting procedures that appeared in the literature was presented by Holzapfel et al. in 2005 [93]. This study investigated the effect of geometrical parameters such as stent cell size and strut thickness on the biomechanical impact of the three different stents expanded within a realistic, patient-specific model of an iliac linear stenotic artery. The 3D reconstruction was based on high resolution MRI of a postmortem iliac artery segment presenting stenosis. The medical images, coupled with histological analysis, allowed the detection of eight different tissue types. For each scanned MRI cross sectional image, the borders of the arterial components were traced automatically by a set of points. These points were then fitted by non-uniform rational B-splines (NURBS) curves, which were combined along the arterial axis in order to obtain the boundary surfaces of the different tissue components. In order to model the material response, each component of the stenotic segment was assumed to behave as a composite reinforced by two families of collagen fibers. Finite element meshes were generated using a built-in software, able to parameterize and automatically generate differently dense meshes. Three commercially available stent models were expanded in the reconstructed geometry applying pressure directly on the inner surface of the struts, exhibiting different mechanical and geometrical results [93]. The results are shown in Fig. 6.4, highlighting the circumferential stress distribution. The presented study gave a new perspective to structural computational analysis of stent deployment, highlighting the potential of FEM utilizing realistic, patient-specific diseased vessels.

Then, Gijsen et al. (2008) [69] investigated the effect of a stent expansion within a patient specific model of a stenotic coronary artery. The reconstruction was based on biplane angiography and IVUS of a RCA achieved prior to the stenting intervention. First, the CCA images were selected at end-diastole, to eliminate respiratory and cardiac motion artifacts. Secondly, the IVUS frames were analysed and segmented semi-automatically, to detect lumen contours and the media/adventitia interface. Subsequently, the IVUS cross sectional images were positioned perpendicularly onto the reconstructed 3D catheter path and finally the coronary artery segment was generated utilizing B-splines. The stent was positioned in the stenotic area and expanded by means of a pressure directly applied on the inner surface, as shown in Fig. 6.5. Although the stenosis is relevant, no plaque is considered in this work. Results in terms of morphology changes and Von Mises stresses on the arterial wall are shown in Fig. 6.6. The great innovation brought by Gijsen et al. is the use of one of the most advanced reconstruction techniques, utilizing CCA and IVUS, for structural purpose. Once the medical images are taken, the intervention results can be predicted computationally.

More recently, other image-based studies were presented focusing on more complex geometries and vascular districts. For instance, Auricchio et al. (2010) [7] simulated a carotid artery stenting procedure on a bifurcated arterial model based on CTA images. The CTA images of a stenotic carotid bifurcation were processed in order to select the region of interest and remove secondary branches. Since the medical images did not contain information on the vessel wall thickness, the 3D model was reconstructed considering the thickness as

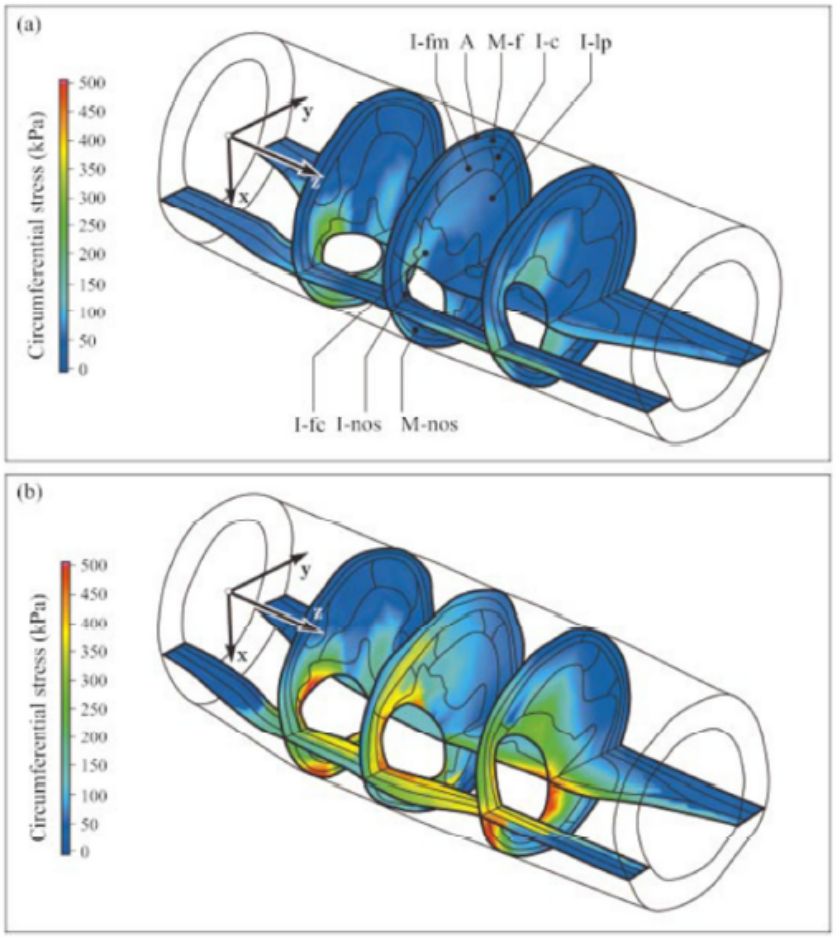

Figure 6.4: *Circumferential Cauchy stress distribution in the stenotic arterial wall before (a) and after (b) stenting procedure. The top figure highlights the eight tissue types detected. Reprinted with permission from Holzapfel et al. [93].*

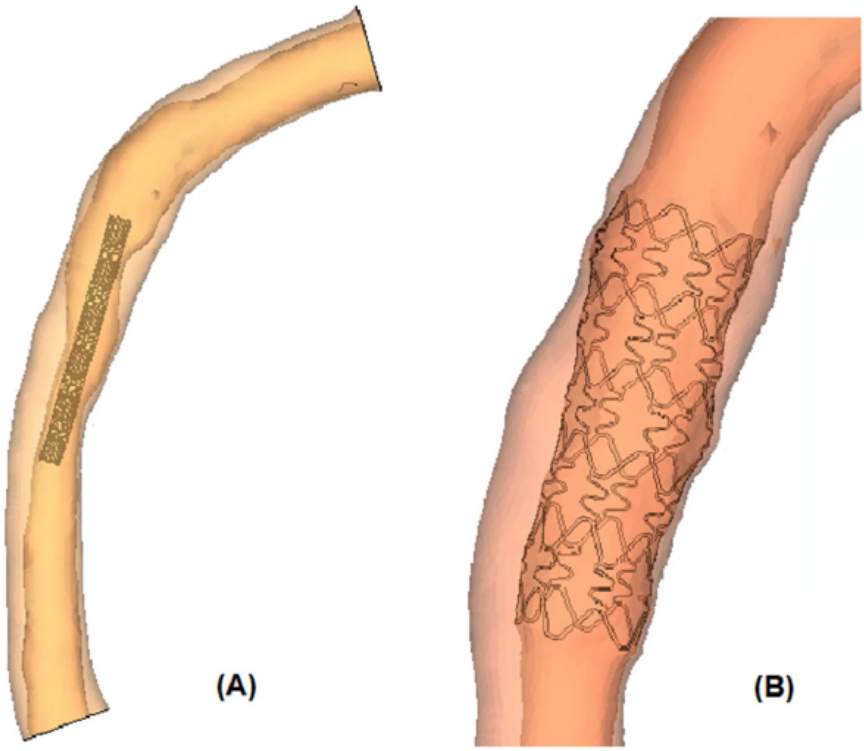

Figure 6.5: *Positioning of the coronary stent (A) and subsequent expansion in the patient-specific geometry (B). Reprinted with permission from Gijsen et al. [69].*

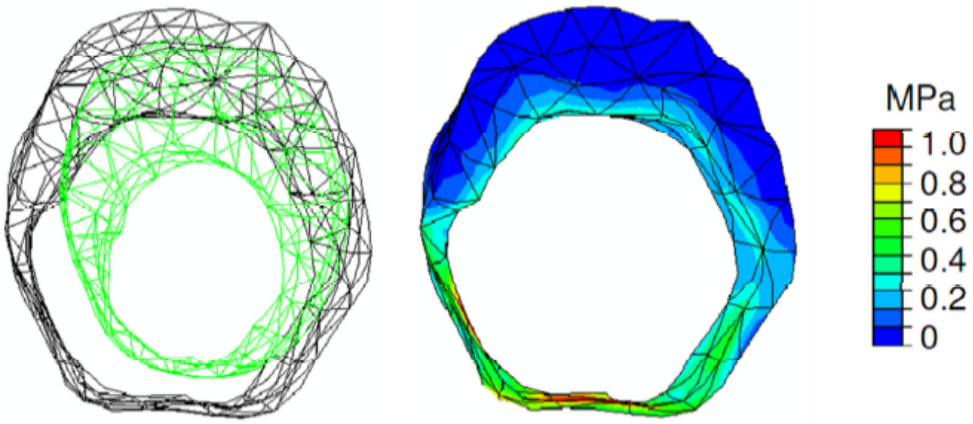

Figure 6.6: *Results of the computational work carried out by Gijsen et al. [69] On the left, lumen shape in the most stenotic cross section before (green) and after (black) the stenting procedure. On the right, the corresponding Von Mises stresses on the arterial wall. Reprinted with permission from Gijsen et al. [69].*

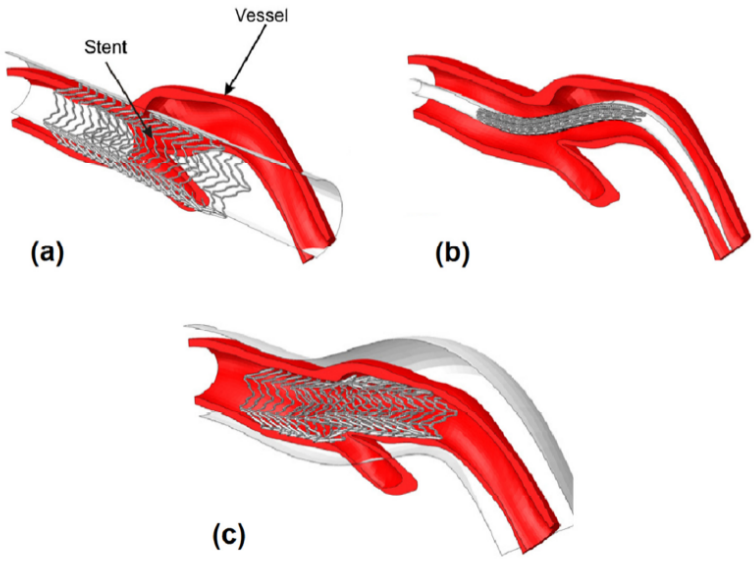

Figure 6.7: *Stent deployment in the patient-specific bifurcation. Original configuration in (a), crimping and bending in (b) and expansion in (c). Reprinted with permission from Auricchio et al. [7].*

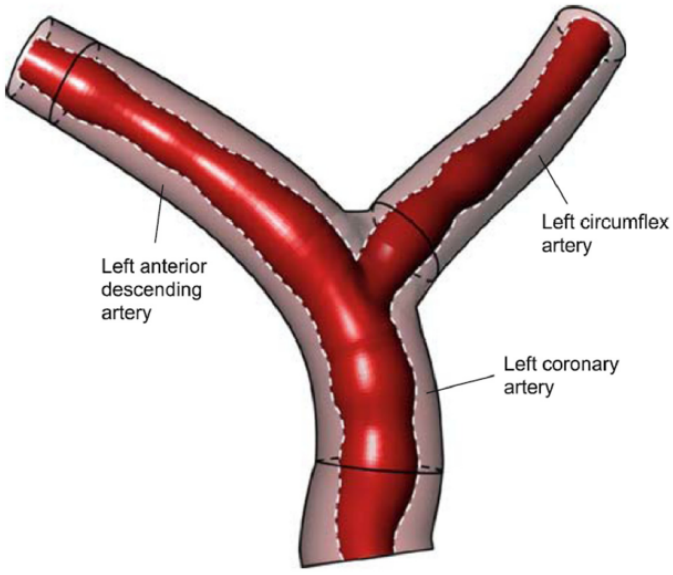

Figure 6.8: *3D reconstruction of the coronary bifurcation obtained by rotational angiography. The circular cross sections used for the outer wall creation are shown. Reprinted with permission from Mortier et al. [149].*

a percentage (i.e. 30%) of the vessel radius. To fit in such a complex geometry, the stent was first crimped and subsequently bent. The stent deployment was then simulated in an idealized way, by imposing radial displacement to an internal catheter, as shown in Fig. 6.7. Another recent work involving arterial bifurcations was carried out by Mortier et al. (2009) [149], where the expansion of three commercially available stents was compared utilizing a 3D coronary model based on a patient-specific angiographic data. To generate the outer wall, a circular approximation was obtained by scaling selected luminal circles, using a scaling factor of 1.6, based on anatomical data for healthy coronary arteries. The second NURBS surface allowed the creation of a structured hexahedral mesh of the vessel wall. The mesh was then split into three layers of equal thickness, corresponding to the three vessel layers, without considering plaque. Anisotropy of the arterial wall was implemented. The 3D model generated is shown in Fig. 6.8. The intravascular stents were expanded applying an increasing pressure to a tri-folded balloon and the effect different stent designs was investigated, focusing on arterial wall stress distributions and morphology changes following the modeled intervention procedure.

6.2 Numerical model of real clinical cases: materials and methods

In this light, the aim of this work is to prove the feasibility of implementing patient-specific structural models starting from image-based reconstructions of atherosclerotic coronary arteries. The replicas of two real clinical cases are simulated by following the procedural indications of the physician who actually performed the interventions. In particular, the two studied cases involved coronary bifurcations of the LAD coronary artery since such regions are very critical from a biomechanics point of view [142] and are still affected by lower clinical and procedural outcomes [181]. Interventions were performed at University Hospital Doctor Peset in Valencia (Spain) and patients were treated with a PSB stenting without FKB inflation. This strategy consists of deploying a stent in the MB across the bifurcation followed by the optional treatment of the SB in the case of sub-optimal clinical results. Due to its simplicity and better clinical outcomes if compared to complex techniques, PSB is at the moment the most adopted stenting procedure in the clinical field [119]. Pre-stenting acquisitions with CTA and CCA are used to generate image-based models of the atherosclerotic bifurcations at the University Pompeu Fabra in Barcelona [25]. These models are subsequently discretized with fully hexahedral meshes. Atherosclerotic plaques are included in the model, monitoring the distance from each node to the centerline of the external wall. Curvature and tortuosity of the coronaries entail the development of preliminary structural analyses to accurately crimp and advance the devices to the correct position. Afterwards, stressed configurations of the devices are used within the final structural simulations, replicating the actual stenting procedures by means of a finite element commercial code [65]. Lastly, for one case, the final geometrical configuration obtained in silico is compared with the image-based reconstruction of post-stenting geometry providing a qualitative validation of the proposed numerical approach.

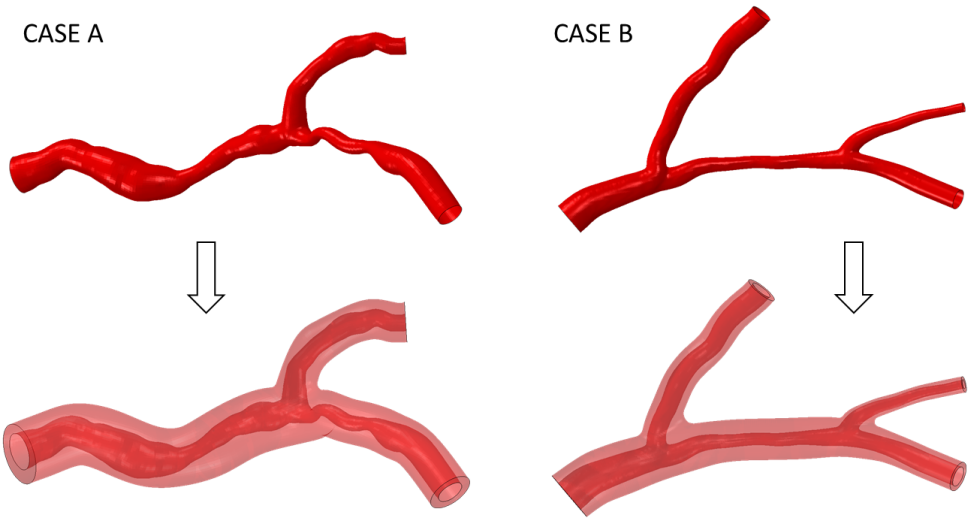

Figure 6.9: *Geometrical reconstructions of the two LAD coronary arteries investigated: from medical images (top) to 3D solid models (below).*

6.2.1 Image-based coronary bifurcations models

Two clinical cases of adult females are investigated in this work, after informed patient consent and approval of the hospital ethical committee for this study. In both cases, the patients underwent percutaneous coronary stent implantation. In particular, the first case investigated (Case A) involves the proximal section of the LAD while in the second case (Case B) both the proximal and mid part of LAD are included. Pre-treatment CCA and CTA are used to reconstruct the internal surfaces of the pre-stenting geometries following the methodology proposed by Cárdenes et al. [25]. The combination of these two imaging systems allows a more realistic reconstruction of coronary bifurcations than just using one of them alone. CTA provides the 3D trajectories followed by the arteries while CCA provides accurate lumen radius estimations. The internal surfaces are then used to construct 3D solid models of the two coronary bifurcations investigated (Fig. 6.9). First, the open-source software package VMTK [200] is used to identify the centerline of the internal wall reconstruction. Second, due to the lack of imaging data, external wall surfaces are created by smoothly connecting circumferential cross sections perpendicular to the centerlines using the CAD software Rhinoceros 4.0 Evaluation (McNeel & Associates, Indianapolis, IN, USA). To allow a better description of arteries and correctly localize potentially asymmetric atherosclerotic plaques, cross sections are only defined in those regions where, by angiographic inspection, no plaques or symmetric plaques are recognized. The diameters of the external wall are chosen in order to comply with the internal diameter and physiological wall thicknesses of healthy coronary branches [74]. Regarding case A, external wall diameters vary from a maximum of 5.2 mm at the inlet of the MB to 1.6 mm at the outlet of the second SB. For case B, external diameters at the inlet and the outlet of the MB are equal to 5.43 mm and 4.0 mm, respectively. In this case, the external diameter of the SB resulted

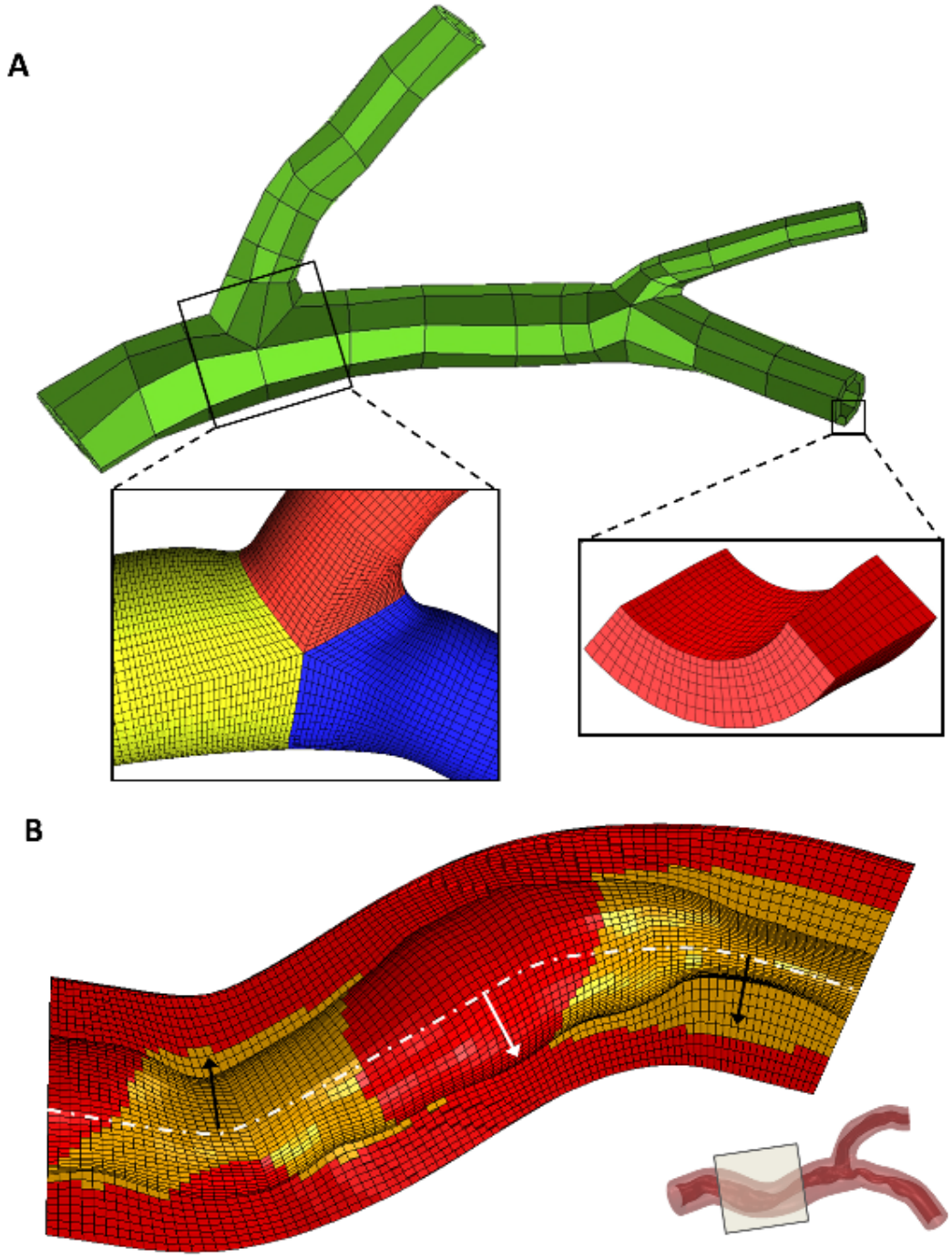

Figure 6.10: *A) Discretization process of an image-based coronary model. On the top, the arterial wall is subdivided in regions topologically equivalent to parallelepipeds that have been subsequently subdivided in hexahedral elements. Below, in the details, the refinement of the mesh close to the internal surface and the bifurcated region are depicted. B) Plaque identification process based on the calculation of the distance between each mesh node and the centerline of the external wall. Black arrows indicate some nodes characterized by lower distances than the physiological lumen radius of a healthy LAD.*

in 3.49 mm.

The 3D geometries are discretized using Ansys ICEM CFD (ANSYS Inc., Canonsburg, PA, USA) with fully hexahedral meshes (Fig. 6.10a). Mesh density is increased in the bifurcation area and close to the internal surface of the arterial wall. In this way, the areas characterized by lower stress gradients such as the external layers of the arterial wall and the regions far from the stented area are less densely meshed; mesh-independency of the results is guaranteed without excessively increasing the computational cost. Indeed, our results are very similar in terms of mesh density to those reported and verified by Capelli et al. [24] for a similar coronary artery model. A total of 120,344 and 187,326 elements is used to discretize the arterial geometries of case A and B, respectively.

The combination of CCA and CTA cannot provide adequate information on the typology of biological tissues characterizing the arterial wall and, in particular, it cannot identify the precise location of atherosclerotic plaques and its composition. For this reason, a method based on the calculation of the distance between each node of the mesh and the centerline of the external wall (Fig. 6.10b) is implemented. With this approach, if the calculated distance is lower than a reference radius of a healthy artery (black arrows, Fig. 6.10b), that node will be considered part of the atherosclerotic plaque; otherwise (white arrow, Fig. 6.10b), it will be considered as part of the arterial wall. The reference radius linearly decreases along the artery considering the intrinsic diameter reduction occurring in the reconstructed arteries. Stenosis is measured by dividing the area of the atherosclerotic plaque by the area of the arterial lumen of the same cross-section, obtained removing the elements belonging to the plaque itself. Different sections perpendicular to the centerline are assessed in cases A and B. Following this qualitative method, the local maximum degrees of stenosis obtained are 84% and 73% for cases A and B, respectively.

The material properties used for the arterial wall and the plaques replicate the mechanical behavior in the circumferential direction of the media layer and cellular plaques, respectively. The hyperelastic constitutive models implemented are based on the experimental values described in Holzapfel et al. [92] for the arterial wall and in Loree et al. [123] for the atherosclerotic plaques. In the plaque model, perfect plasticity is associated to the hyperelastic strain energy density function to roughly simulate the plaque rupture at the experimental tensile stress values measured in the referenced study (about 400 kPa). More details on these material models can be found in Gastaldi et al. [65].

For the reconstruction of the post-treatment anatomy of the vessel, immediate post-treatment CCA and post-operative CTA performed after six months are used to reconstruct the internal surfaces of the post-stenting geometries following the previously described methodology [25]. This post-stenting geometry will give us an insight on the similarity between our numerically simulated model and the one obtained from real images, and it is only available for case A since the patient of case B did not undergo any follow-up CTA.

6.2.2 Stent and balloon angioplasty models

In the two cases investigated, two different stents are used in the interventions (Fig. 6.11). Their geometrical models are obtained using the previously mentioned CAD software and resemble the Xience Prime (Abbott Lab., USA) stent for case A and the Endeavor Resolute (Medtronic, USA) device in case B. Considering its un-crimped configuration, the Multilink

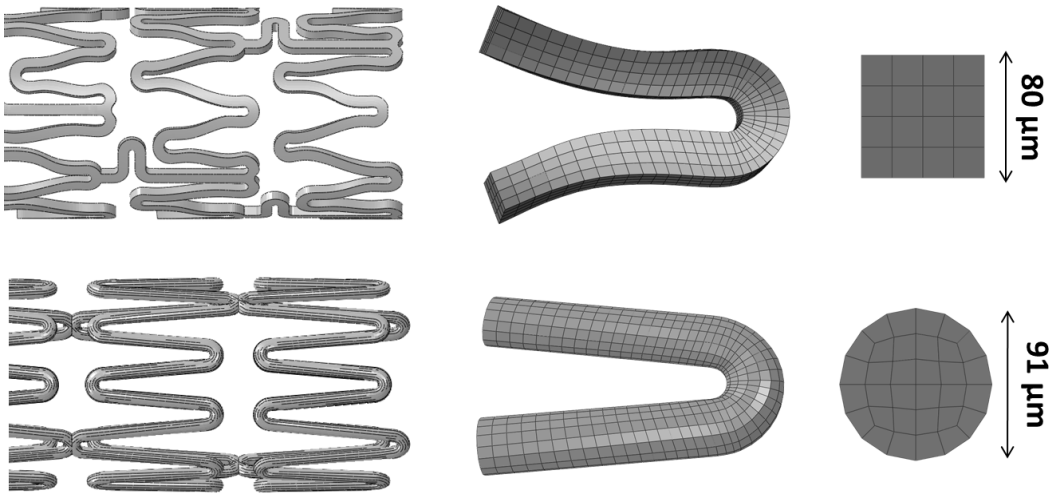

Figure 6.11: *On the top, geometrical model of a stent resembling the commercial Xience Prime (Abbott Lab., USA) used in case A and characterized by a length of 28 mm and an external diameter of 1.76 mm. Below, geometrical model resembling the Endeavor Resolute stents (Medtronic, USA) used in case B and characterized by a circular cross-section. On the right, details of the hexahedral discretization of these stent models.*

Vision stent is characterized by an external diameter of 1.76 mm, a strut thickness of 80 μm and a length of approximately 28 mm. The Endeavor Resolute stent model has a circular section with a diameter of 91 μm and in the un-crimped configuration is characterized by an external diameter of 1.6 mm and a length of 15 mm. The meshes of the devices are partially shown in Fig. 6.11 and result in a total amount of 448,424 and 272,384 reduced integration hexahedral elements for the Xience and the Endeavor stents, respectively. Both stents are constructed of a cobalt-chromium alloy that is described through a Von Mises-Hill plasticity model with isotropic hardening, with the following properties: 233 GPa, 0.35, 414 MPa, 933 MPa and 44.5% in terms of Young modulus, Poisson coefficient, yield stress, ultimate stress and deformation at break, respectively [173].

Polymeric angioplasty balloons with different diameters (from 1.5 to 3 mm) and lengths (from 17 to 30 mm) are created. In the virtual implantations, the balloon models are selected to exactly match those used by the clinical operators in the actual interventions. Similarly to the models previously described in Gastaldi et al. [65], angioplasty balloons are created in the expanded configuration, discretized with quadrilateral membrane elements and deflated to achieve a multi-folded configuration.

6.2.3 Preliminary simulations: crimping and bending

To precisely position the stents in the complex patient-specific geometries, preliminary simulations of crimping and bending of the devices are performed using the implicit finite element commercial code ABAQUS/Standard (Dassault Systemes Simulia Corp., RI, USA) and the modelling techniques presented in Chapter 3. At the end of each simulation, the

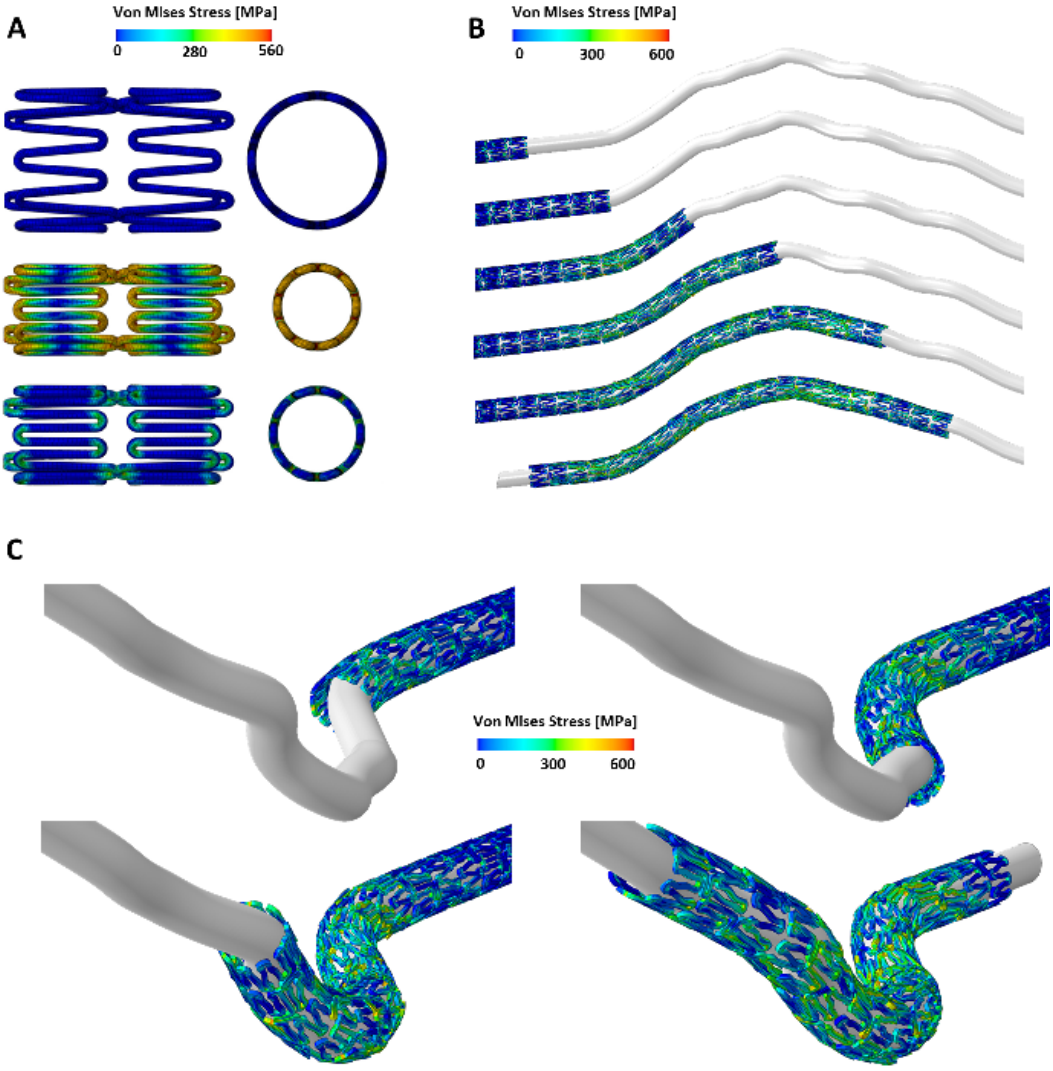

Figure 6.12: *Preliminary structural simulations: A) Crimping of the Endeavor Resolute stent model, for clarity only two stent struts are shown. The initial stent geometry (top) is crimped to an external diameter of 1 mm by controlling the radial displacement of a rigid cylindrical surface (middle); after the elastic recoil, the final stent diameter is about 1.11 mm; B) Bending simulations of case B where a Xience-Prime stent is advanced onto a cylindrical internal guide following the vessel centerline and characterized by a 0.8 mm diameter.*

stressed configurations of the devices are passed to the subsequent steps in order to keep track of the history of stress modifications.

At first, the initial configurations of the devices are crimped to an external diameter of 1.00 mm by controlling the radial displacement of a cylindrical surface in contact with the stents (Fig. 6.12a). After elastic recoil, crimped configurations of the stents are imported in the bending simulation (Fig. 6.12b). Since the arterial tracts preceding the coronary bifurcations have greater diameters and higher curvature radii, stent advancement in these regions is assumed to be negligible for the stent final positioning and stressed state. Therefore, two cylindrical internal guides are created following the centerline of the two patient-specific bifurcations obtained after the simulation of the angioplasty procedures (see section 2.4). The guides are discretized with rigid homogeneous shell elements. At this point, to simulate stent advancement and obtain realistic stress distributions on the bent struts, the stents are pushed against the guide imposing longitudinal displacement to the nodes positioned close to the links. Such boundary conditions are removed once the links approach the first curve in order to let the stent freely bend along the guide. Contacts are set to have a friction coefficient equal to 0.3 and the normal behavior is modeled with a "softened" contact relationship in which the contact pressure is a linear function of the clearance between the surfaces. In the last step of the bending simulations, even the last displacement boundary condition is removed and one stent node on the distal end is constrained to its current position allowing the stent to adapt to the bending guide and reach a minimum-energy final static equilibrium. More discussion on this stent advancement models have been presented in Chapter 3. Simulations of crimping and bending of cases A and B require a simulation time of 38 and 13 hours, respectively, using two nodes of a high computing cluster, each of them characterized by a 2 Quad-Core Intel Xeon E5620 processor, 24 GB of RAM and InfiniBand Mellanox for the main interconnections.

Lastly, the creation of the curved configurations of the balloons is also required to position the balloons inside the curved geometries that characterize the stents after the bending and before the implantation. To achieve this goal, advancement simulations similar to those used for the stents are implemented in ABAQUS/Explicit. In this case, however, the balloons are not pulled by means of displacement boundary conditions but via concentrated forces applied at the distal nodes of the balloon.

6.2.4 Final simulations: replica of two clinical cases

Numerical simulations of the stents deployment are simulated as quasi-static processes using the explicit dynamics solver implemented in ABAQUS/Explicit. To ensure this condition, the ratio of kinetic to internal energy should be monitored to avoid that any inertial effect in the solution influences the dynamic equilibrium, thus guaranteeing the reliability of the structural results obtained. An adequate semi-automatic mass scaling governs the stable time increment in order to reduce the computational cost while viscous pressure is applied to the external surfaces of the arterial and stent models to dampen dynamic oscillations. More details on these models can be found in Chapter 3 of this thesis. The procedural indications adopted in the two clinical cases are used to assign specific loading and boundary conditions as follows:

- *Case A:* pre-dilatation at 10atm with a 2x20 mm long angioplasty balloon, a Xience

Table 6.2: *Summary and description of the steps implemented for the simulation of Case A. Loads, boundary conditions and contacts are reported.*

Step	Description	Loads	Contacts	Boundary Conditions
1	Angioplasty Balloon Inflation	Pressure of 10 atm acting on the 2x20 mm balloon	Balloon - catheter, balloon - artery	
2	Elastic recoil post-angioplasty	No loads applied	Interactions removed	
3	Stent expansion	Pressure of 14 atm acting on the 3x32 mm balloon	Balloon - stent, balloon - artery, balloon - catheter, stent - artery	Artery: end nodes constrained in the longitudinal direction. Catheter guides: fully constrained.
4	Elastic recoil post expansion	No loads applied	Stent - artery	
5	Proximal expansion	Pressure of 18 atm acting on the proximal 3.5x20 mm balloon	Balloon - stent, balloon - artery, balloon - catheter, stent - artery	
6	Elastic recoil post expansion	No loads applied	Stent - artery	

Prime stent characterized by a length of 28 mm is deployed across the bifurcation between the LAD and the first diagonal branch by inflating a 3x32 mm angioplasty balloon at 14 atm. The procedure ends with a post-dilatation at 18 atm in the proximal part of the MB using a 3.5x20 mm balloon.

- *Case B:* two Endeavor stents are implanted across the two bifurcations between the LAD and the first and second diagonal branches. After a pre-dilatation at 13 atm with a 2.5x15 mm angioplasty balloon, the distal device is inserted and expanded at 12 atm with a 2.75x18 mm angioplasty balloon. Afterwards, the proximal stent is implanted across the first bifurcation with a 3x18 mm angioplasty balloon inflated at 14 atm resulting in a small overlap of about 2.00 mm with the previously implanted device.

The different steps of the simulations are summarized in Tables 6.2 and 6.3 for cases A and B, respectively, reporting the loads, boundary conditions and contact domains implemented. Contacts involving the arterial surface are all modeled using a hard normal behaviour and a frictional tangential behaviour with penalty of 0.06 [46]. All other contacts are characterized by a friction coefficient of 0.2 [1]. Final simulations of cases A and B require a computational time of 60 and 56 hours, respectively, using two nodes of the previously described high computing cluster.

Table 6.3: *Summary and description of the steps implemented for the simulation of Case B. Loads, boundary conditions and contacts are reported.*

Step	Description	Loads	Contacts	Boundary Conditions
1	Angioplasty Balloon Inflation	Pressure of 13 atm acting on the 2.5x15 mm balloon	Balloon - catheter, balloon - artery	Artery: end nodes constrained in the longitudinal direction. Catheter guides: fully constrained.
2	Elastic recoil post-angioplasty	No loads applied	No Interactions	
3	Distal stent expansion	Pressure of 12 atm acting on the 2.75x18 mm distal balloon	Balloon - stent, balloon - artery, balloon - catheter, stent - artery	
4	Elastic recoil post distal expansion	No loads applied	Stent - artery	
5	Proximal stent expansion	Pressure of 14 atm acting on the 3x18 mm proximal balloon	Balloon - stents, balloon - artery, balloon - catheter, stents - artery, MB stent - SB stent	
6	Elastic recoil post proximal expansion	No loads applied	Stents - artery, MB stent - SB stent	

6.3 Numerical model of real clinical cases: results and discussion

Before analyzing any mechanical result, the quasi-static condition has been verified for each simulation by checking that the ratio between kinetic and internal energy is maintained below 2%. In this way, the reliability of the simulations performed with an explicit dynamic model is guaranteed. Figures 6.13 and 6.14 show the sequential steps of the two clinical cases simulated. In agreement with the post-stenting clinical evidence, in both cases virtual stenting implantations succeed in re-opening the arterial lumen by providing an adequate structural support to the arterial wall and restoring the vessel patency at the end of the procedures. In particular, the degree of stenosis in the most critical section of case A changes from 84% to 76% after the angioplasty procedure, enlarging the free lumen and allowing an easier advancement of the device. Concerning case B, the simulated angioplasty results in a reduction of the stenosis from 73% to 64%. In both cases, no stenosis is present at the end of the stenting procedures.

6.3.1 Straightening of the arterial wall

In Fig. 6.15, a visualization of the post-treatment coronary angiography is presented for both the models. The position of the 3D models is manually adjusted to match the viewpoint of the angiography. The visualization of the stent on the angiography is poor due to its low opacity. For this reason, the position of the stent is obtained by visual inspection of the complete image sequence and highlighted in the second frame of Fig. 6.15. In the third frame an overlay of the 3D model of the stent and the angiography with matching viewpoints is reported while the 3D numerical outcomes of the stent inside the vessel lumen model is presented in the last frame. For case A we observe a good matching between the stent implanted in the patient and the simulation. In case B, where two stents are implanted, we observe that the distal side of the stent implanted distally is slightly dislocated with respect to the real one. This should be mainly attributed to the motion of the coronaries (heart pulsation and respiration) and the fact that the reconstructed model does not account for this motion. Still, the mismatch is limited to the final portion of the stent showing a good resemblance in the remaining locations and for case A.

In both cases, post-stenting straightening of the arterial wall occurs. In literature, this phenomenon is frequently reported in *in vivo* studies [121, 208]. This occurrence is clinically relevant since it is also identified as a valid predictor for major adverse cardiac events such as death, acute myocardial infarction, or target lesion revascularization [82]. Since then, flexibility of coronary stents has become a key point during the design of coronary stents and several numerical models have been implemented to investigate this issue [149, 169]. Fig. 6.16 provides a qualitative representation of the influence of stent implantation on the arterial geometries. In order to more quantitatively assess this issue, a tortuosity index (TI) [171] has been evaluated for each of the cases and defined as

$$\mathrm{TI} = \frac{\mathrm{L}}{\mathrm{L}'} - 1 \tag{1}$$

where L is the length of the centreline of the coronary arteries and L' is the distance

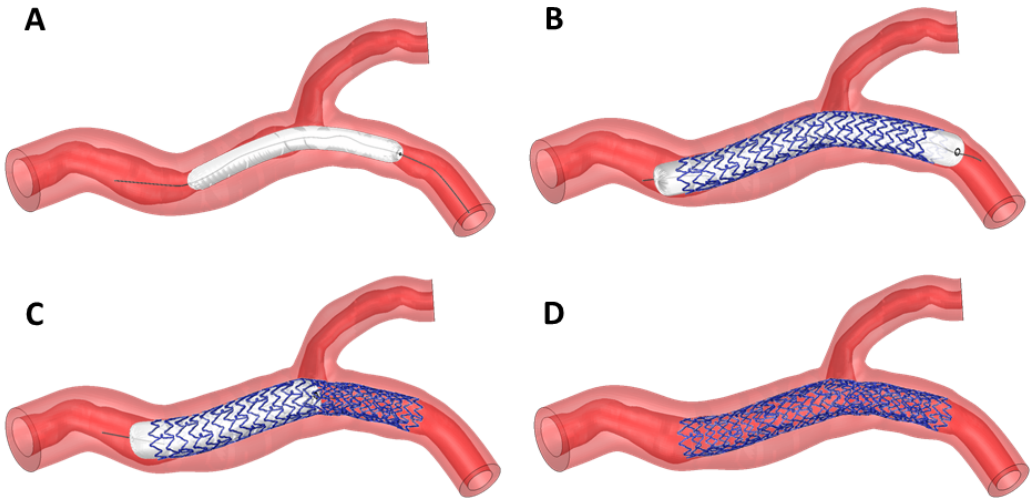

Figure 6.13: *Clinical case A. Steps of the final numerical simulation: A) Angioplasty procedure with a 2.0 mm balloon expanded at 10 atm; B) Deployment of the Xience Prime stent with a 3.0 mm balloon at 14 atm; C) Proximal optimization technique with a 3.5 mm balloon deployed in the proximal part of the MB at 18 atm; D) Final geometrical configuration at the end of the stenting procedure.*

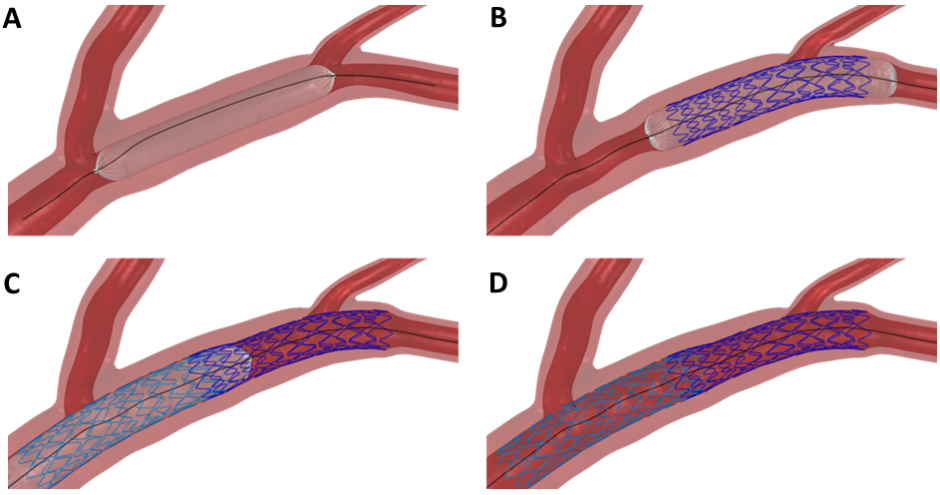

Figure 6.14: *Clinical case B. Steps of the final numerical simulation: A) Angioplasty procedure with a 2.5 mm balloon expanded at 13atm; B) Expansion of an Endeavor stent across the distal bifurcation with a 2.75 mm balloon inflated at 12 atm; C) Deployment of a second Endeavor stent across the proximal bifurcation with a 3.0 mm balloon at 14 atm; D) Final geometrical configuration at the end of the stenting procedure.*

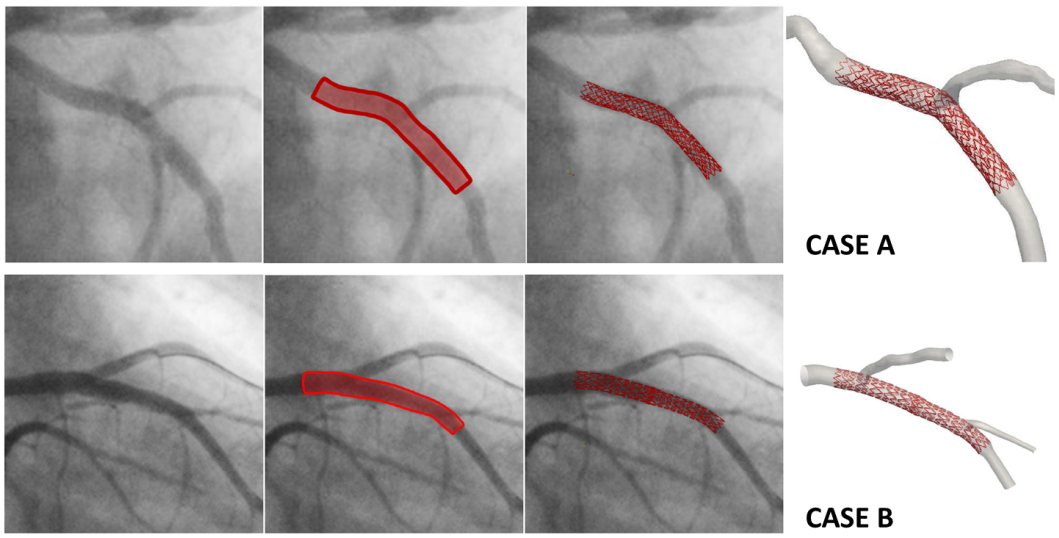

Figure 6.15: *Visualization of the post-treatment coronary angiography for cases A (top) and B (bottom). The position of the 3D models is manually adjusted to match the viewpoint of the angiography. From left to right: the post-treatment CCA alone, the angiography with the position of the stent highlighted, the angiography with the superimposed visualization of the stents from the FEM simulation, and the result of the simulation with the stent inside the deformed vessel model.*

between the extremes of the region of interest. TI has a value of zero for a straight vessels and increases with vessel curvature. Regarding case A, after the stenting procedure, TI changed from 0.119 to 0.085(-28.6%) while for case B TI decreases from 0.054 to 0.044 (-18.5%).

For case A only, an image-based post-stenting geometry is reconstructed combining the information of 6 months post-intervention CTA to extract the vessel centerline and CCA acquired immediately after the intervention to obtain the artery diameters. This geometrical model can be considered a realistic model of the patient because it is based on actual measurements on image patient data, and because no in-stent restenosis is clinically observed after 6 months. Thus, it is fairly acceptable that the diameters of the artery did not greatly change in this period. Therefore, similarities of this reconstruction with respect to our numerical model obtained by replicating the intervention, provide a first evidence of the success of our methodology. Figure 6.17 clearly illustrates the similarities between the numerical and image-based reconstructions of the stented bifurcations. To quantitatively measure the straightening effect, the TI is computed in each case resulting in values of 0.085 and 0.089 for the numerical and image-based geometries, respectively.

For case A only, an image-based post-stenting geometry was reconstructed combining the information of 6 months post-intervention CTA for the vessel centreline and CCA acquired immediately after the intervention for the artery diameters. Consistency of this reconstruction is guaranteed by the fact that significant in-stent restenosis was not found after 6 months; thus, it is fairly acceptable that diameters of the artery did not greatly change in this period. Figure 6.17 shows the comparison between the numerical and image-based reconstructions

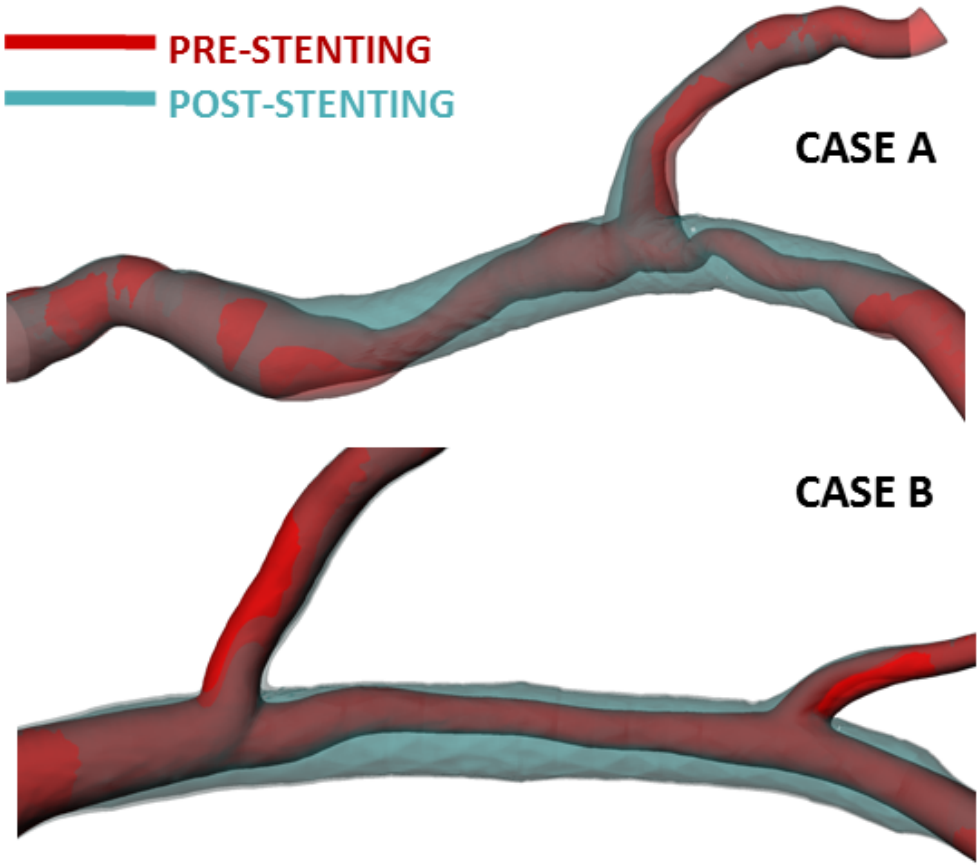

Figure 6.16: *Comparison of the pre-stenting (red) and post-stenting (blue) configurations for case A (top) and case B (below). The straightening of the arterial wall is visible in both cases.*

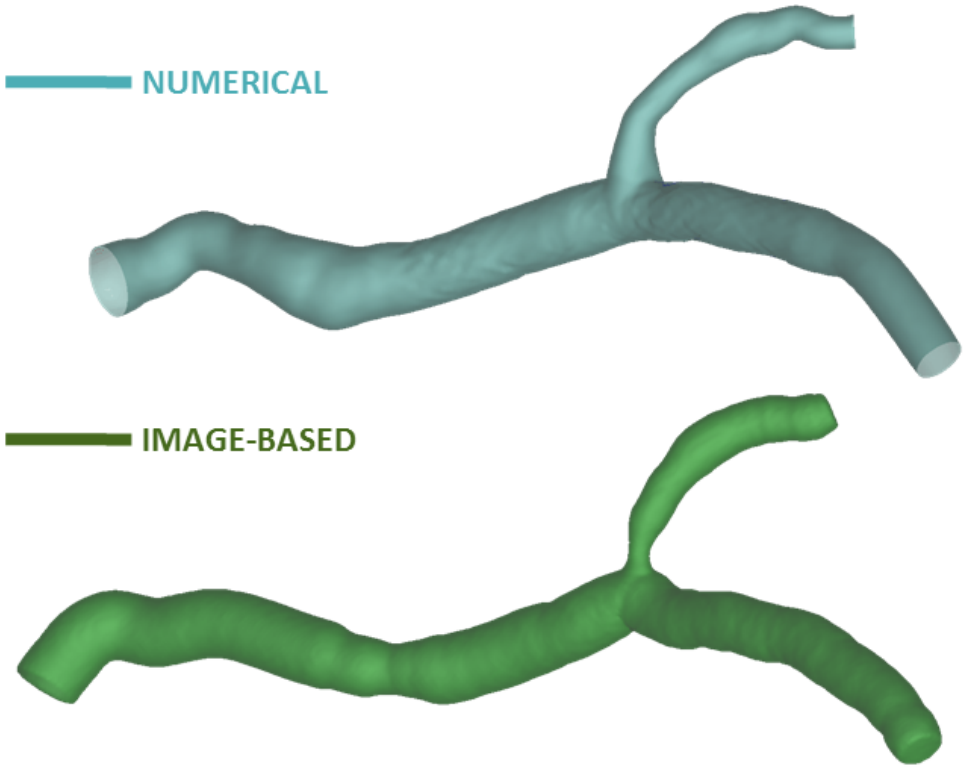

Figure 6.17: *Post-stenting geometrical configuration: comparison between the numerical outcome (blue) and the reconstruction from medical images (color).*

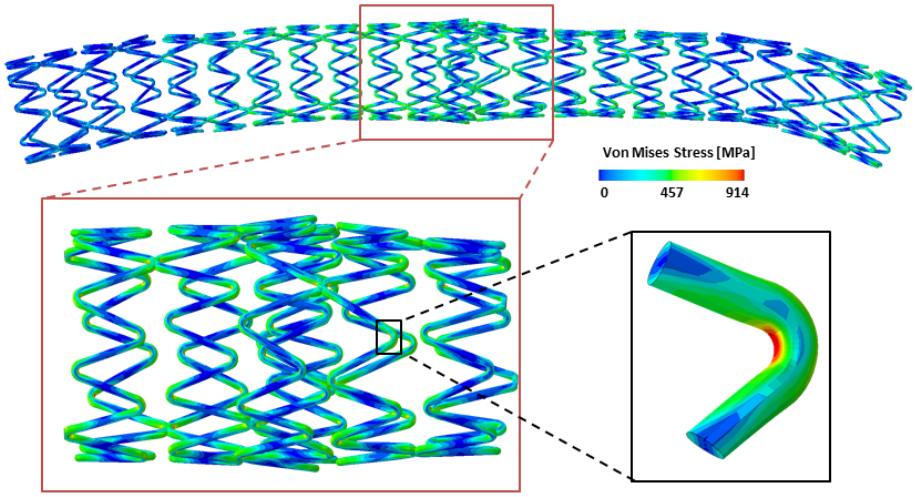

Figure 6.18: *Contour maps of the Von Mises stresses in the two stents at the end of the stenting procedure of case B. In the magnification areas below, details of the stresses in the overlapping region and in the strut with the highest stress.*

of the stented bifurcations. Estimation of TI results in values of 0.085 and 0.089 for the numerical and image-based geometries, respectively.

In conclusion, it is shown quantitatively and qualitatively how the straightening of the vessel is properly simulated, proving the reliability of finite element simulations in predicting patient-specific stenting intervention geometrical outcomes. Certain regions of the numerically simulated model differ more clearly from the image-based model, such as a narrowing at the beginning of the SB, and in the MB at the proximal part of the stent. This can be explained by plaque shift in these regions, a phenomenon that is actually expected looking at CCA images, and that is not included in our current numerical modeling capabilities.

6.3.2 Effect of overlapping stents

In case B, the clinical procedure performed consists of a sequential implantation of two devices across the first and second diagonal branches of the LAD. At first, the distal stent is expanded by means of deployment of a 2.5 mm angioplasty balloon. Then, a second device is implanted with a 2.75 mm balloon allowing a small overlap between the devices. This occurrence is not uncommon in the case of long atherosclerotic lesions even if it has been associated to delayed healing [178] and emerging structural issues like coronary stent fracture [156].

The biomechanical results obtained in this study highlight the criticisms provoked by two overlapping stents. For instance, the peak values of the von Mises stresses both at the maximum expansion of the second device (917MPa) and at the end of the procedure (904 MPa) can be found in the overlapping region of the distal stent (Fig. 6.18). These values are very close to the ultimate stress at break (933 MPa) showing the potential risk of rupture at

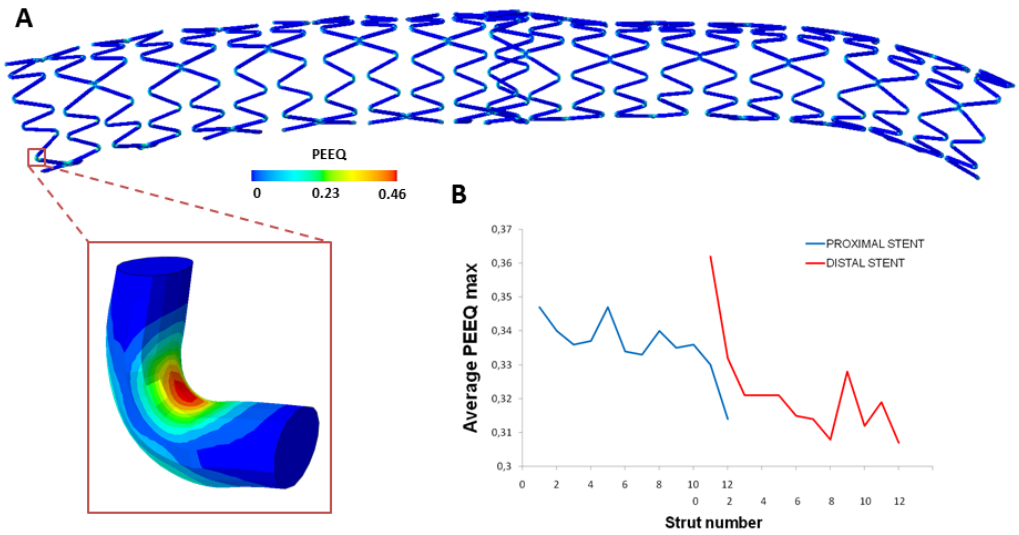

Figure 6.19: *A) Contour maps of the PEEQ in the two stents at the end of the stenting procedure of case B. In the magnification area below, details of the most deformed strut. B) Plot of the average PEEQ calculated in every ring of struts for the proximal (blue) and distal (red) stent. Peak values are obtained in the first struts of the proximal stent, in those located at the bifurcations (yellow circles) and in the overlapping struts of the distal stent.*

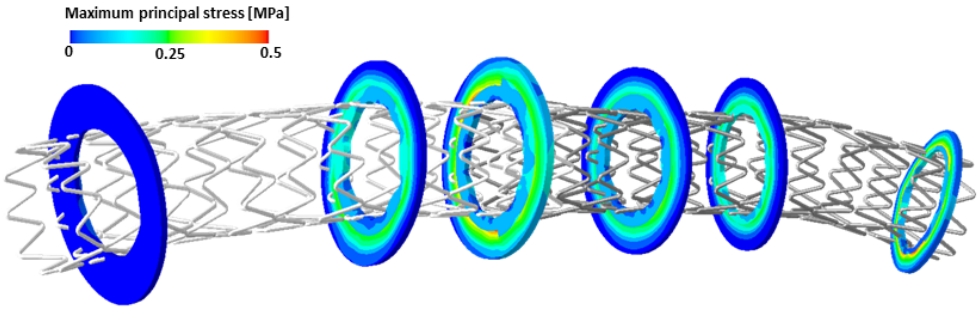

Figure 6.20: *Contour maps of the maximum principal stresses in the artery at the end of the stenting procedure of case B. For clarity of view, only some sections are shown. Higher values are obtained in the overlapping region.*

these locations. The same region is proven to be mechanically risky considering the plastic equivalent strains (PEEQ) as well.This quantity is a scalar representation of the amount of plastic strains that stent struts undergo during expansion while providing structural support to the arterial wall and preventing its immediate full recoil. The PEEQ peak value at the end of the procedure is located in the first ring of the proximal stent (Fig. 6.19a) and equals 0.454. A total of two stent struts, both located in the first ring of the proximal stent, exceed the ultimate tensile strain limit of the material model implemented (0.445). Figure 6.19b reports the values of the mean PEEQ calculated averaging the maximum values obtained along the whole ring of the struts. Besides the overlapping region where the firstly implanted device is over expanded by the deployment of the second device, high values of averaged PEEQ can be found in the first struts of the proximal stent and in the struts located level with the bifurcations (black lines) as well. In these areas, the absence of plaques and the origin of the SB decrease the radial forces acting on the expanded stent and allow the device to expand and deform more. Besides structural integrity of the metallic devices, high deformation areas are also critical for the potential damage or delamination of the polymer coating and consequent impairment of drug supply to the arterial wall, as shown by Guerin et al. in 2009 [79].

Beside the influence on the devices, the overlapping region also results in an increase of stresses in the arterial wall. Figure 6.20 depicts the contour maps of the maximum principal stresses in different sections of the arterial wall at the end of the procedure. The maximum value is found in the central section of the overlapping area reaching 525 kPa at the maximum expansion of the second device and 374 kPa at the end of the procedure.

In summary, the major biomechanical influence of overlapping stents has been proven in several clinical studies in terms of delayed arterial healing [56], risk of stent fracture due to fatigue failure [156] and more frequent target lesion revascularization [178], especially looking at angiographic long-term clinical outcomes. In particular, Raber et al. [178] proved how focal in-stent restenosis predominantly occurred in the overlapping stent zone after multiple DES implantation. The results of our models seem to match these considerations proving the criticism of overlapping stent in terms of higher stresses and deformation occurring both in the devices and the arterial wall. Furthermore, an increased metal-to-artery ratio of the overlapping area will likely result in a widely modified hemodynamic field as well.

6.3.3 Preliminary fluid dynamic numerical models

Preliminary patient-specific CFD analyses for the clinical case B have been implemetned applying the methodology of the sequential model described in Chpater 3. In particular, due to lack of patient-specific measurements, a steady state flow of 60 ml/min is applied at the inlet of the domain imposing a 70:30 flow split at the outlets of the two bifurcations. The Carreu's non-Newtonian model for blood and rigid wall conditions are used. Preliminary fluid dynamic results (Fig. 6.21) prove that, besides structural considerations, the overlapping of two stents is a critical region from a hemodynamic point of view, as well. Infact, low WSS are found in this area together with the predictable low WSS regions occurring close to the external walls of the bifurcations. However, pulsatile fluid dynamic analyses will be implemented in the future to increase the reliability of these considerations and better investigate the phenomon.

6.3.4 Model limitations

Some limitations are present in the implemented numerical models. Firstly, the image-based reconstructions still present some simplifications such as, for instance, the circular cross-section hypothesized along the whole geometry and the assumed smooth configuration of the external wall. This study lacks information on the biological tissues composition of the two patient-specific cases. Furthermore, the artery is considered isotropic and homogeneous, even though the vessel wall is anisotropic due to the collagen fibers orientation and is characterized by different layers. Also, plaque positioning is only hypothesized and entirely modeled as soft cellular plaque. Moreover, the computational simulations does not consider the in vivo stretch affecting the coronary wall (generally about 6-10 kPa). Also, arterial blood pressure (averaged 100 mmHg) inside the vessels is neglected.

The mechanical behavior of the exact Co-Cr alloys used to fabricate the commercial devices is not available due to manufacturer industrial policies. Also, post production surface treatments are not taken into account and modeled in this study. Hence, a typical Co-Cr medical alloy mechanical behavior is used for both the devices. This limitation has to be considered while discussing the presented results and stress values may only be used in a qualitative or comparative way.

In light of these considerations, further developments of the presented model could surely provide more accurate results and additional information for both the clinical and the industrial point of view. First, the use of anisotropic arterial wall modeling, taking into consideration the collagen fibers orientation, could improve the biological tissues material models; secondly, a more detailed and differentiated reconstruction of arterial geometry could be possible using more recent vascular imaging techniques, such as IVUS and OCT, also capable of the identification of various plaque components and wall composition. Furthermore, the combination of structural analyses with computational fluid dynamics [31, 143] or drug eluting models, if used [34, 35], could be helpful in completing the picture and better understanding the biomechanical influence of stenting procedure in patient-specific cases.

Lastly, since the main limitations that currently restrict the adoption of finite element models in clinical practice are their complex implementation and their high computational cost, automatic methods of image-based geometrical reconstruction and discretization should be matched with less computationally demanding modeling techniques such as the use of beam elements for the stents or shell elements for the arteries. In such a way, quicker simulations and comparisons of different optional treatments might be implemented fostering the use of these models during the interventional planning. In this light, the complex numerical methods here presented might be used to validate these more rapid but less accurate modeling tools.

6.4 Conclusions

The study presented shows the feasibility of implementing a patient-specific virtual model replicating two actual clinical cases. This step may be considered a step forward towards the routine application of such models in the clinical field that, however, is still limited by some restrictions such as the computational cost and complex preparation of the models itself. In both the cases presented, the straightening of the arterial wall due to stent implantation

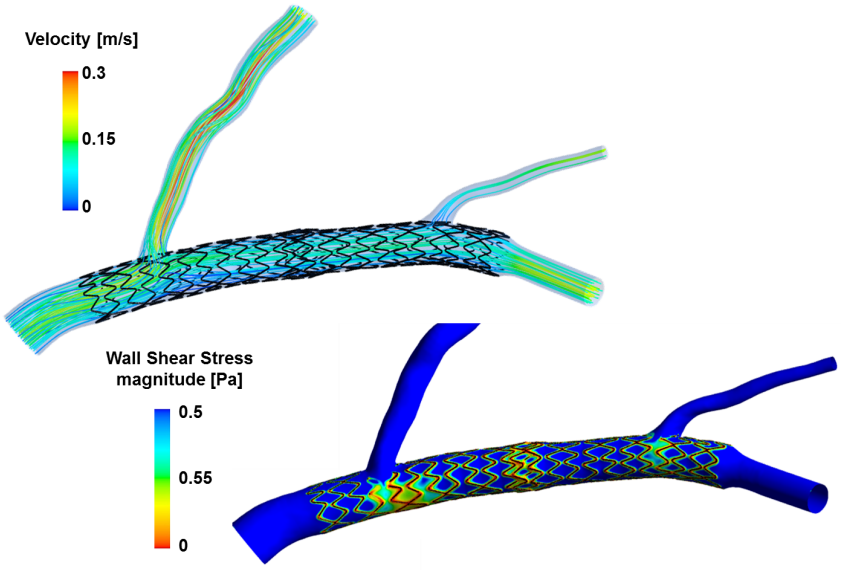

Figure 6.21: *Preliminary steady state fluid dynamics analyses of the post-interventional models: A) graphical representation of velocity streamlines; B) contour map of WSS magnitude. Low WSS areas are evident at the overlapping region and near the arterial walls opposite to the bifurcations.*

is in agreement with previous experimental studies and with the image-based post-stenting configuration of the second case studied, reconstructed after the 6 months follow-up. Then, the presence of overlapping stents proved to be a critical occurrence from a biomechanical point of view because of higher mechanical stresses both in the device and the arterial wall and a higher metal-to-artery ratio due to the double metallic layer. These findings seems to be in agreement with some in vivo studies that recognized overlapping stents as an independent factor of coronary stent fractures [156] and delayed healing [178].

Ideally, the routine application of patient-specific numerical models could help clinicians in their intervention strategies, well predicting *in vivo* outcomes. Various stenting procedural options could be simulated for patient-specific cases, comparing results in terms of lumen re-opening and the mechanical behavior of the intravascular devices and of the arterial wall. In this way, interventional planning could be greatly facilitated and optimized. Moreover, coronary stent designers could also rely on such results to improve strut geometries and materials, decreasing local stresses on the struts or on the arterial wall.

Chapter 7

Final remarks

7.1 Main conclusions

The main hypothesis of this thesis is that a better understanding of the biomechanics occurring in coronary bifurcations before and after stenting procedures may be useful to improve the current clinical state of the art in interventional cardiology. In fact, several studies proved that biomechanics plays a major role both in the formation of atherosclerotic diseases in coronary bifurcations and the development of post-stenting drawbacks such as in-stent restenosis and stent thrombosis. As a consequence, in this thesis a sequential structural and fluid dynamic model is developed to better investigate clinically interesting issues related to stenting procedures for coronary bifurcations. Particular attention is paid to the creation of the fluid volume based on the geometrical configurations after the structural simulations.

Despite consensus on some topics related to coronary bifurcations has been reached, several issues are still under debate and the optimal procedure or device suitable for all the different lesions and anatomic variations of coronary bifurcations has not been found, yet. Three main cases are investigated in this thesis. At first, results from numerical simulations highlight the advantages of the FKB inflation in terms of better flow pattern and access to the SB but also its drawbacks mainly due to the overexpansion of the proximal part of the MB. In particular, FKB provokes greater stresses in the arterial wall and a wider region characterized by low and oscillating WSS. This work shows that the use of a tapered balloon deployed in the SB during FKB might improve the main drawbacks of this procedure. Second, the sequential numerical model is applied to investigate the most common single- or double-stenting procedures involving conventional devices. A few comparisons among techniques are proposed highlighting the major complexity and critical nature of double-stenting procedures and underlining how the the optimal technique is still missing and new dedicated devices might be required to improve current procedural outcomes. Lastly, a new dedicated stent for coronary bifurcations is compared to a conventional device within the culotte stenting approach. Results prove that, still requiring some improvements in their design and concept, dedicated devices might be an interesting opportunity while stenting coronary bifurcation lesions. In summary, these results prove that the implemented models may provide useful insights for both the industry to enhance the commercially available devices (includ-

ing the design of new dedicated stents) and for the clinical world to better understand the different outcome of different stenting procedures. Moreover, interesting potentials of these models involve their use within educational programs for interventional cardiologist to better understand the influence of different interventional options and potential procedural errors.

Then, local blood flow patterns in stented and non-stented coronary bifurcation models have been investigated in a comparative study among DPIV measurements and structural-based CFD analyses. Beside intrinsic differences and modelling assumptions of the two approaches, both CFD and DPIV analyses proved to be able to capture the main features of the fluid flows, highlighting the influence of different bifurcation angles or stenting procedures. These findings suggest that the hemodynamic scenario before and after stenting procedures might be accurately assessed with both methods. Nonetheless, both approaches still require a challenging direct validation against *in vivo* measurements to fully demonstrate their ability to describe the existent hemodynamics of coronary flows. However, this process is currently not feasible due to technical challenges related to accurate *in vivo* measurements in small and complex geometries such as stented coronary arteries.

Lastly, a feasibility study of image-based numerical models that are able to replicate real cases of stenting procedures is presented. This may be considered a step forward towards the routine application of such models in the clinical field that, however, is still limited by some restrictions such as the computational cost and complex preparation of the models itself. In both the cases presented, the straightening of the arterial wall due to stent implantation is in agreement with previous experimental studies and with the image-based post-stenting configuration of the first case studied, reconstructed after the 6 months follow-up. Then, the presence of overlapping stents in the second case investigated proved to be a critical occurrence from a biomechanical point of view because of higher mechanical stresses both in the device and the arterial wall and a higher metal-to-artery ratio due to the double metallic layer. These findings seem to be in agreement with some *in vivo* studies that recognized overlapping stents as an independent factor of coronary stent fractures and delayed arterial healing.

7.2 Future developments

From the issues previously outlined, it is evident that stent modelling is still an ongoing wide research area. Innovations of interventional procedures and new medical devices may still obtain benefits from computational studies. Further developments are still required to investigate the arising clinical problems and technological advancements.

Degradable stents is an area where efforts should be directed as these devices could represent the third revolution for cardiovascular intervention after the introduction of BMS and DES. In this regards, in the literature some modelling studies on polymeric [72, 73, 141, 190, 191] and metallic stents [66, 76, 212, 213] were performed but should be applied to more realistic cases and more accurately validated (Fig. 7.1). The main issues involving degradable devices are the mechanical properties of polymeric stents resulting in thicker stent struts, and the sub-optimal degradation rates both for metallic and polymeric devices. In particular, stents fabricated in magnesium alloys seem to have a fast degradation rate while biodegradable polymers (mainly poly-l-lactic acid, PLLA) are too slowly absorbed in

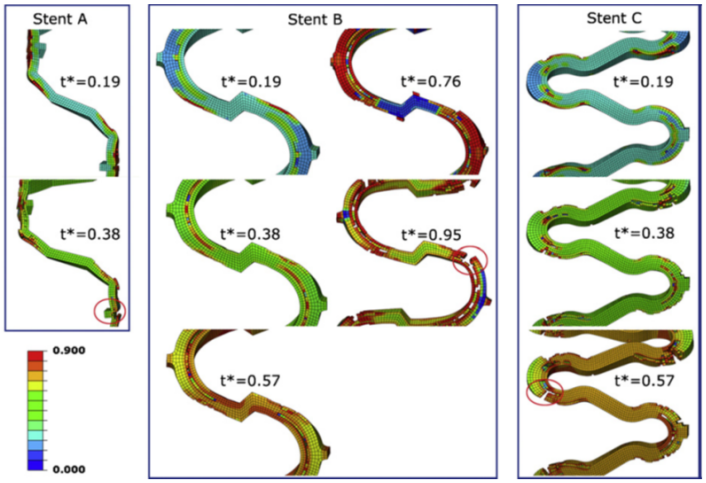

Figure 7.1: *Computational model of DES for a two stents technique: a) 3D geometry of the DESs implanted in the coronary bifurcation via a structural finite element model; b) 1D model of DESs built from the 3D geometry; c) drug concentration in the arterial wall (blue to red code), blood velocity in the arterial lumen (streamlines) and 1D geometry of the two DESs. Image copied with permission from Wu et al. [212].*

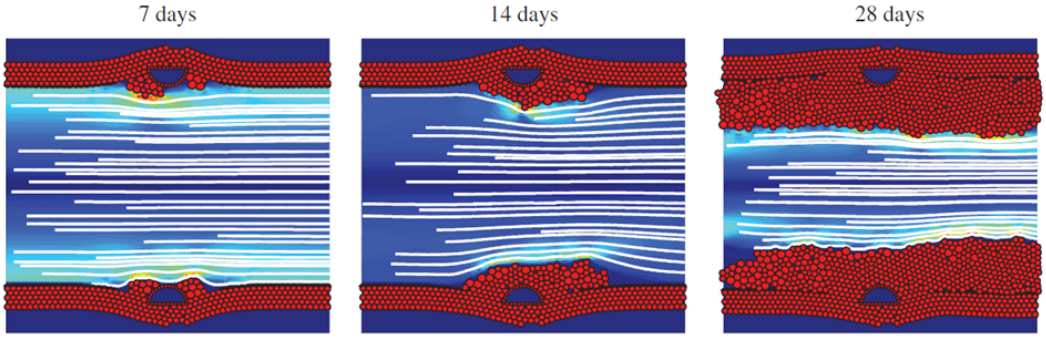

Figure 7.2: *Example of multi-scale model of the in-stent restenosis process after stent deployment. Simulation results of a rounded strut deployed at 90* mm*, showing neointimal growth after 7, 14 and 28 days after the stent deployment. Reprinted with permission from Tahir et al. [196].*

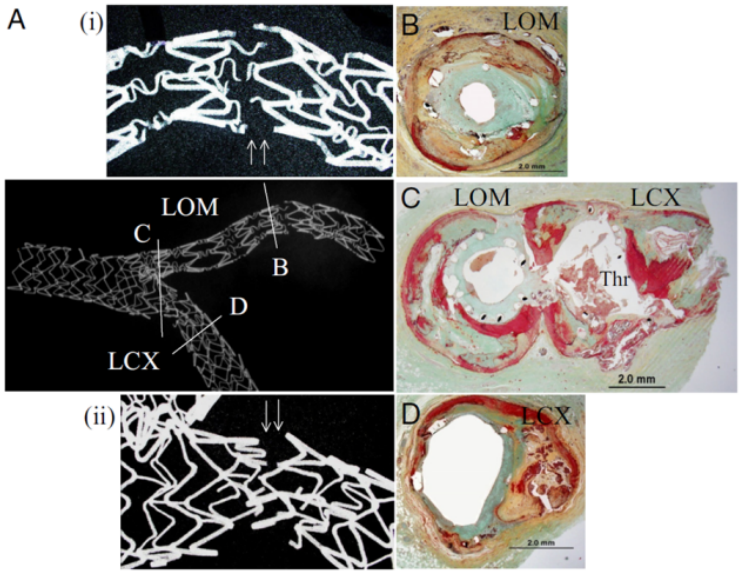

Figure 7.3: *A Case of Grade V Cypher and Taxus Stent Fracture. At 172 days following implantation the patient died from stent thrombosis in the LCX coronary artery. (A) Radiograph of the stented left circumflex and left obtuse marginal (LOM) artery. Note, presence of grade V Cypher stent fracture highlighted in magnified image (i) and another grade V fracture at the bifurcation site in the Taxus stent (ii). (B) Cypher stent in LOM with grade V fracture was associated with restenosis. (C) Taxus stent fracture in LCX was located in the area close to the bifurcation site where the thrombus was located (Thr). (D) The stented LCX segment distal to the fracture was widely patent. Reprinted with permission from Nakazawa et al. [156].*

the human body (12-18 months) [62]. In this light, numerical methods coupled with shape optimization methods may be helpful in finding innovative solutions to improve the stent mechanical properties or degradation process.

Another aspect worth of deeper investigation is the multi-scale modelling of in-stent restenosis after coronary artery stenting. This complex multi-physics and multi-scale phenomenon is not fully understood, and identification of how different biomechanical factors correlate to in-stent restenosis may pave the way to computer-aided design of stent-based therapies. An example of these studies is proposed by Caiazzo et al. [22] where a multi-scale model system is implemented as a collection of single-scale models that operate on different temporal and spatial scales. These single-scale models for stent deployment, blood flow, vascular smooth muscle cells and drug diffusion communicate with each other via smart conduits. In Tahir et al. [196], a 2D version of this model is implemented (Fig. 7.2); their results were compared to an available porcine dataset. Authors found a strong correlation between strut thickness and the rate of smooth muscle cell proliferation. Moreover, simulation results suggest that the growth of the restenotic lesion is strongly dependent on the stent strut cross-sectional profile.

Coronary stent failure due to fatigue fracture is also emerging as one of the critical issues for the stent success [156, 167, 195]. Clinical studies proved that some factors such as stent

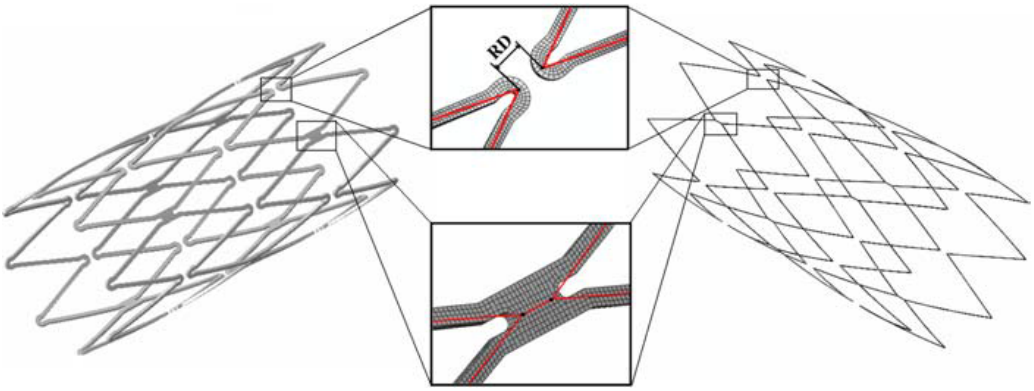

Figure 7.4: *FEM 3D and 1D models of the stent. In the middle, some details showing the approximation of 1D model (red lines) and reference points (bold dots). The value of the RD is 0.26 mm. Image copied by Bernardini et al. [16].*

design, length of the device, specific vascular districts or stenting procedures were identified as independent causes of coronary stent fracture (Fig. 7.3). Computational studies can be valuable to identify the critical areas prone to fracture and improve the treatment or the choice of the device. In 2006, the study by Marrey et al. [131] proposed a damage-tolerant analysis of a coronary Co-Cr stent, where the design life is conservatively evaluated using a fracture mechanics methodology. In future studies, this phenomenon might be better predicted using patient-specific or image-based models as demonstrated for stented valves by Schievano et al. [183]. Moreover, cardiac wall dynamics and its cyclic loadings on the implanted devices should not be neglected while investigating this issue.

Efforts should also be dedicated towards methodological aspects aiming to overcome the obstacles that limit the current use of numerical models in the clinical field. First, computational analyses should be more accessible to inexpert operators such as clinicians. In fact, simulations at the current state of the art are difficult to implement and highly dependent on the operator skills, especially in the construction of geometrical models and their discretization. Simplification of the use of such models may help in the virtual planning process by comparing the performances of different devices or procedural options. Another great limitation is related to the computational time required to run complex simulations. Stenting procedures are real-time interventions and the computational cost should be reduced as much as possible. In this light, a promising solution may be the use of simplified elements such as beams (Fig. 7.4) which have been demonstrated able to predict similar maximum and minimum stresses along a stent at significantly reduced computational costs [16, 23, 83]. Lastly, more accurate and detailed image-based geometrical models should be pursued to increase the realism of the simulations leading to highly patient-specific models in terms of both geometries and boundary conditions. A very recent study by Raber and colleagues [177] showed how offline fusion of co-registered IVUS and OCT, for example, can potentially improve the diagnostic accuracy of plaque characterization and offer an ideal platform to elaborate more realistic geometries that can be used for computer simulations.

Bibliography

[1] *http://engineershandbook.com*, (Accessed 20 September 2011).

[2] G. Acevedo-Bolton, L. Jou, B. Dispensa, M. Lawton, R. Higashida, A. Martin, W. Young, and D. Saloner, *Estimating the hemodynamic impact of interventional treatments of aneurysms: Numerical simulation with experimental validation: Technical case report*, Neurosurgery, 59 (2006), pp. E429–E430.5.

[3] T. Adriaenssens, R. Byrne, A. Dibra, R. Iijima, J. Mehilli, O. Bruskina, A. Schamig, and A. Kastrati, *Culotte stenting technique in coronary bifurcation disease: Angiographic follow-up using dedicated quantitative coronary angiographic analysis and 12-month clinical outcomes*, European Heart Journal, 29 (2008), pp. 2868–2876.

[4] P. Agostoni, D. Foley, M. Lesiak, A. Belkacemi, J. Dens, I. Kumsars, B. Scott, P. Oemrawsingh, C. Dubois, E. Garcia, T. Lefevre, and P. Stella, *A prospective multicentre registry, evaluating real-world usage of the tryton side branch stent: Results of the e-tryton 150/benelux registry*, EuroIntervention, 7 (2012), pp. 1293–1300.

[5] L. Antiga, B. Ene-Iordache, L. Caverni, G. Cornalba, and A. Remuzzi, *Geometric reconstruction for computational mesh generation of arterial bifurcations from ct angiography*, Computerized Medical Imaging and Graphics, 26 (2002), pp. 227–235.

[6] T. Asakura and T. Karino, *Flow patterns and spatial distributions of atherosclerotic lesions in human coronary arteries*, Circulation Research, 66 (1990), pp. 1045–1066.

[7] F. Auricchio, M. Conti, M. De Beule, G. De Santis, and B. Verhegghe, *Carotid artery stenting simulation: From patient-specific images to finite element analysis*, Medical Engineering and Physics, 33 (2011), pp. 281–289.

[8] M. Babiker, L. Gonzalez, J. Ryan, F. Albuquerque, D. Collins, A. Elvikis, and D. Frakes, *Influence of stent configuration on cerebral aneurysm fluid dynamics*, Journal of Biomechanics, 45 (2012), pp. 440–447.

[9] B. Balakrishnan, J. Dooley, G. Kopia, and E. Edelman, *Intravascular drug release kinetics dictate arterial drug deposition, retention, and distribution*, Journal of Controlled Release, 123 (2007), pp. 100–108.

[10] B. Balakrishnan, J. Dooley, G. Kopia, and E. Edelman, *Thrombus causes fluctuations in arterial drug delivery from intravascular stents*, Journal of Controlled Release, 131 (2008), pp. 173–180.

[11] B. Balakrishnan, A. Tzafriri, P. Seifert, A. Groothuis, C. Rogers, and E. Edelman, *Strut position, blood flow, and drug deposition: Implications for single and overlapping drug-eluting stents*, Circulation, 111 (2005), pp. 2958–2965.

[12] R. Balossino, F. Gervaso, F. Migliavacca, and G. Dubini, *Effects of different stent designs on local hemodynamics in stented arteries*, Journal of Biomechanics, 41 (2008), pp. 1053–1061.

[13] R. Balossino, G. Pennati, F. Migliavacca, L. Formaggia, A. Veneziani, M. Tuveri, and G. Dubini, *Computational models to predict stenosis growth in carotid arteries: Which is the role of boundary conditions?*, Computer Methods in Biomechanics and Biomedical Engineering, 12 (2009), pp. 113–123.

[14] M. Behan, N. Holm, N. Curzen, A. Erglis, R. Stables, A. De Belder, M. Niemela, N. Cooter, D. Chew, T. Steigen, K. Oldroyd, J. Jensen, J. Lassen, L. Thuesen, and D. Hildick-Smith, *Simple or complex stenting for bifurcation coronary lesions : A patient-level pooled-analysis of the nordic bifurcation study and the british bifurcation coronary study*, Circulation: Cardiovascular Interventions, 4 (2011), pp. 57–64.

[15] A. Bernardini, I. Larrabide, H. Morales, G. Pennati, L. Petrini, S. Cito, and A. Frangi, *Influence of different computational approaches for stent deployment on cerebral aneurysm haemodynamics*, Interface Focus, 1 (2011), pp. 338–348.

[16] A. Bernardini, I. Larrabide, L. Petrini, G. Pennati, E. Flore, M. Kim, and A. Frangi, *Deployment of self-expandable stents in aneurysmatic cerebral vessels: Comparison of different computational approaches for interventional planning*, Computer Methods in Biomechanics and Biomedical Engineering, 15 (2012), pp. 303–311.

[17] D. Bluestein, C. Gutierrez, M. Londono, and R. Schoephoerster, *Vortex shedding in steady flow through a model of an arterial stenosis and its relevance to mural platelet deposition*, Annals of Biomedical Engineering, 27 (1999), pp. 763–773.

[18] A. Borghi, E. Foa, R. Balossino, F. Migliavacca, and G. Dubini, *Modelling drug elution from stents: Effects of reversible binding in the vascular wall and degradable polymeric matrix*, Computer Methods in Biomechanics and Biomedical Engineering, 11 (2008), pp. 367–377.

[19] C. Bourantas, I. Kourtis, M. Plissiti, D. Fotiadis, C. Katsouras, M. Papafaklis, and L. Michalis, *A method for 3d reconstruction of coronary arteries using biplane angiography and intravascular ultrasound images*, Computerized Medical Imaging and Graphics, 29 (2005), pp. 597–606.

[20] F. Burzotta, H.-C. Gwon, J.-Y. Hahn, E. Romagnoli, J.-H. Choi, C. Trani, and A. Colombo, *Modified t-stenting with intentional protrusion of the side-branch stent within the main vessel stent to ensure ostial coverage and facilitate final kissing balloon: The t-stenting and small protrusion technique (tap-stenting). report of bench testing and first clinical italian-korean two-centre experience*, Catheterization and Cardiovascular Interventions, 70 (2007), pp. 75–82.

[21] F. Burzotta, G. Sgueglia, C. Trani, G. Talarico, S. Coroleu, S. Giubilato, G. Niccoli, M. Giammarinaro, I. Porto, A. Leone, R. Mongiardo, M. Mazzari, G. Schiavoni, and F. Crea, *Provisional tap-stenting strategy to treat bifurcated lesions with drug-eluting stents: One-year clinical results of a prospective registry*, Journal of Invasive Cardiology, 21 (2009), pp. 532–537.

[22] A. Caiazzo, D. Evans, J. Falcone, J. Hegewald, E. Lorenz, B. Stahl, D. Wang, J. Bernsdorf, B. Chopard, J. Gunn, R. Hose, M. Krafczyk, P. Lawford, R. Smallwood, D. Walker, and A. Hoekstra, *A complex automata approach for in-stent restenosis: Two-dimensional multiscale modelling and simulations*, Journal of Computational Science, 2 (2011), pp. 9–17.

[23] C. Capelli, G. Biglino, L. Petrini, F. Migliavacca, D. Cosentino, P. Bonhoeffer, A. Taylor, and S. Schievano, *Finite element strategies to satisfy clinical and engineering requirements in the field of percutaneous valves*, Annals of Biomedical Engineering, In press (2012), pp. 1–11.

[24] C. Capelli, F. Gervaso, L. Petrini, G. Dubini, and F. Migliavacca, *Assessment of tissue prolapse after balloon-expandable stenting: Influence of stent cell geometry*, Medical Engineering and Physics, 31 (2009), pp. 441–447.

[25] R. Cardenes, J. Diıez, I. Larrabide, H. Bogunovic, and A. Frangi, *3d modeling of coronary artery bifurcations from cta and conventional coronary angiography.*, Medical image computing and computer-assisted intervention, 14 (2011), pp. 395–402.

[26] C. Caro, J. Fitz-Gerald, and R. Schroter, *Arterial wall shear and distribution of early atheroma in man [18]*, Nature, 223 (1969), pp. 1159–1161.

[27] J. Charonko, S. Karri, J. Schmieg, S. Prabhu, and P. Vlachos, *In vitro, time-resolved piv comparison of the effect of stent design on wall shear stress*, Annals of Biomedical Engineering, 37 (2009), pp. 1310–1321.

[28] J. Charonko, S. Karri, J. Schmieg, S. Prabhu, and P. Vlachos, *In vitro comparison of the effect of stent configuration on wall shear stress using time-resolved particle image velocimetry*, Annals of Biomedical Engineering, 38 (2010), pp. 889–902.

[29] J. Charonko and P. Vlachos, *Estimation of uncertainty bounds from cross correlation peak ratio for individual piv measurements*, Proceedings of the ASME Fluids Engineering Summer Meeting, Puerto Rico, USA, (2012).

[30] S. Chen, J. Zhang, F. Ye, Y. Chen, T. Patel, K. Kawajiri, M. Lee, T. Kwan, G. Mintz, and H. Tan, *Study comparing the double kissing (dk) crush with classical*

crush for the treatment of coronary bifurcation lesions: The dkcrush-1 bifurcation study with drug-eluting stents, European Journal of Clinical Investigation, 38 (2008), pp. 361–371.

[31] C. Chiastra, S. Morlacchi, S. Pereira, G. Dubini, and F. Migliavacca, *Computational fluid dynamics of stented coronary bifurcations studied with a hybrid discretization method*, European Journal of Mechanics, B/Fluids, 35 (2012), pp. 76–84.

[32] A. Colombo, E. Bramucci, S. SaccaŠ, R. Violini, C. Lettieri, R. Zanini, I. Sheiban, L. Paloscia, E. Grube, J. Schofer, L. Bolognese, M. Orlandi, G. Niccoli, A. Latib, and F. Airoldi, *Randomized study of the crush technique versus provisional side-branch stenting in true coronary bifurcations: The cactus (coronary bifurcations: Application of the crushing technique using sirolimus-eluting stents) study*, Circulation, 119 (2009), pp. 71–78.

[33] A. Colombo, G. Stankovic, D. Orlic, N. Corvaja, F. Liistro, F. Airoldi, A. Chieffo, V. Spanos, M. Montorfano, and C. Di Mario, *Modified t-stenting technique with crushing for bifurcation lesions: Immediate results and 30-day outcome*, Catheterization and Cardiovascular Interventions, 60 (2003), pp. 145–151.

[34] E. CutriŠ, P. Zunino, S. Morlacchi, C. Chiastra, and F. Migliavacca, *Drug delivery patterns for different stenting techniques in coronary bifurcations: a comparative computational study*, Biomechanics and Modelling in Mechanobiology, In press (2012).

[35] C. D'Angelo, P. Zunino, A. Porpora, S. Morlacchi, and F. Migliavacca, *Model reduction strategies enable computational analysis of controlled drug release from cardiovascular stents?*, SIAM Journal on Applied Mathematics, 71 (2011), pp. 2312–2333.

[36] J. Davies, Z. Whinnett, D. Francis, C. Manisty, J. Aguado-Sierra, K. Willson, R. Foale, I. Malik, A. Hughes, K. Parker, and J. Mayet, *Evidence of a dominant backward-propagating "suction" wave responsible for diastolic coronary filling in humans, attenuated in left ventricular hypertrophy*, Circulation, 113 (2006), pp. 1768–1778.

[37] M. De Beule, P. Mortier, S. Carlier, B. Verhegghe, R. Van Impe, and P. Verdonck, *Realistic finite element-based stent design: The impact of balloon folding*, Journal of Biomechanics, 41 (2008), pp. 383–389.

[38] G. De Santis, M. Conti, B. Trachet, T. De Schryyer, M. De Beule, J. Degroote, J. Vierendeels, F. Auricchio, P. Segers, P. Verdonck, and B. Verhegghe, *Haemodynamic impact of stent-vessel (mal)apposition following carotid artery stenting: mind the gaps!*, Computer methods in biomechanics and biomedical engineering, In press (2012).

[39] G. De Santis, M. De Beule, P. Segers, P. Verdonck, and B. Verhegghe, *Patient-specific computational haemodynamics: generation of structured and conformal hexahedral meshes from triangulated surfaces of vascular bifurcations.*, Computer methods in biomechanics and biomedical engineering, 14 (2011), pp. 797–802.

[40] E. Delnoij, J. Westerweel, N. Deen, J. Kuipers, and W. Van Swaaij, *Ensemble correlation piv applied to bubble plumes rising in a bubble column*, Chemical Engineering Science, 54 (1999), pp. 5159–5171.

[41] V. Deplano, C. Bertolotti, and P. Barragan, *Three-dimensional numerical simulations of physiological flows in a stented coronary bifurcation*, Medical and Biological Engineering and Computing, 42 (2004), pp. 650–659.

[42] C. Di Mario, N. Morici, C. Godino, O. Goktekin, C. Tamburino, R. Barbagallo, D. Antoniucci, E. Grube, F. Airoldi, G. Zoccai, A. Colombo, and G. Sangiorgi, *Predictors of restenosis after treatment of bifurcational lesions with paclitaxel eluting stents: A multicenter prospective registry of 150 consecutive patients*, Catheterization and Cardiovascular Interventions, 69 (2007), pp. 416–424.

[43] Z. Ding, T. Biggs, W. Seed, and M. Friedman, *Influence of the geometry of the left main coronary artery bifurcation on the distribution of sudanophilia in the daughter vessels*, Arteriosclerosis, Thrombosis, and Vascular Biology, 17 (1997), pp. 1356–1360.

[44] J. Dodge Jr, B. Brown, E. Bolson, and H. Dodge, *Lumen diameter of normal human coronary arteries: Influence of age, sex, anatomic variation, and left ventricular hypertrophy or dilation*, Circulation, 86 (1992), pp. 232–246.

[45] P. Doriot, P. Dorsaz, L. Dorsaz, E. De Benedetti, P. Chatelain, and P. Delafontaine, *In-vivo measurements of wall shear stress in human coronary arteries*, Coronary Artery Disease, 11 (2000), pp. 495–502.

[46] A. Dunn, T. Zaveri, B. Keselowsky, and W. Sawyer, *Macroscopic friction coefficient measurements on living endothelial cells*, Tribology Letters, 27 (2007), pp. 233–238.

[47] D. Dvir, H. Marom, A. Assali, and R. Kornowski, *Bifurcation lesions in the coronary arteries: early experience with a novel 3-dimensional imaging and quantitative analysis before and after stenting.*, Eurointervention, 3 (2007), pp. 95–99.

[48] A. Eckstein, J. Charonko, and P. Vlachos, *Phase correlation processing for dpiv measurements*, Experiments in Fluids, 45 (2008), pp. 485–500.

[49] A. Eckstein and P. Vlachos, *Assessment of advanced windowing techniques for digital particle image velocimetry (dpiv)*, Measurement Science and Technology, 20 (2009).

[50] A. Eckstein and P. Vlachos, *Digital particle image velocimetry (dpiv) robust phase correlation*, Measurement Science and Technology, 20 (2009).

[51] E. Edelman and C. Rogers, *Pathobiologic responses to stenting*, American Journal of Cardiology, 81 (1998), pp. 4E–6E.

[52] L. Ellwein, H. Otake, T. Gundert, B. Koo, T. Shinke, Y. Honda, J. Shite, and J. LaDisa Jr, *Optical coherence tomography for patient-specific 3d artery reconstruction and evaluation of wall shear stress in a left circumflex coronary artery*, Cardiovascular Engineering and Technology, 2 (2011), pp. 212–227.

[53] F. Etave, G. Finet, M. Boivin, J. Boyer, G. Rioufol, and G. Thollet, *Mechanical properties of coronary stents determined by using finite element analysis*, Journal of Biomechanics, 34 (2001), pp. 1065–1075.

[54] A. Farb and A. Boam, *Stent thrombosis redux - the fda perspective*, New England Journal of Medicine, 356 (2007), pp. 984–987.

[55] M. Fernandez, J. Goicolea, C. Garcida, J. Garcida, A. Crespo, J. Rodriguez, and J. Goicolea, *Influence of shear stress on in-stent restenosis: In vivo study using 3d reconstruction and computational fluid dynamics [influencia de la tensiÃşn de cizallamiento en la reestenosis intra-stent: Estudio in vivo con reconstrucciÃşn 3d y dinÃąmica de fluidos computacional]*, Revista Espanola de Cardiologia, 59 (2006), pp. 20–27.

[56] A. Finn, F. Kolodgie, J. Harnek, L. Guerrero, E. Acampado, K. Tefera, K. Skorija, D. Weber, H. Gold, and R. Virmani, *Differential response of delayed healing and persistent inflammation at sites of overlapping sirolimus- or paclitaxel-eluting stents*, Circulation, 112 (2005), pp. 270–278.

[57] E. Foin, N ANS Alegria-Barrero, R. Torii, P. Chan, N. Viceconte, J. Davies, and C. Di Mario, *Crush, culotte, t and protrusion: Which 2-stent technique for treatment of true bifurcation lesions?: Insights from in vitro experiments and micro-computed tomography*, Circulation Journal, 77 (2013), pp. 73–80.

[58] N. Foin, R. Torii, P. Mortier, M. De Beule, N. Viceconte, P. Chan, J. Davies, X. Xu, R. Krams, and C. Di Mario, *Kissing balloon or sequential dilation of the side branch and main vessel for provisional stenting of bifurcations: Lessons from micro-computed tomography and computational simulations*, JACC: Cardiovascular Interventions, 5 (2012), pp. 47–56.

[59] M. Ford, H. Nikolov, J. Milner, S. Lownie, E. DeMont, W. Kalata, F. Loth, D. Holdsworth, and D. Steinman, *Piv-measured versus cfd-predicted flow dynamics in anatomically realistic cerebral aneurysm models*, Journal of Biomechanical Engineering, 130 (2008).

[60] A. Galassi, S. Tomasello, D. Capodanno, D. Seminara, L. Canonico, M. Occhipinti, and C. Tamburino, *A novel 3-d reconstruction system for the assessment of bifurcation lesions treated by the mini-crush technique*, Journal of Interventional Cardiology, 23 (2010), pp. 46–53.

[61] S. Garg and P. Serruys, *Coronary stents: Current status*, Journal of the American College of Cardiology, 56 (2010), pp. S1–S42.

[62] S. Garg and P. Serruys, *Coronary stents: Looking forward*, Journal of the American College of Cardiology, 56 (2010), pp. S43–S78.

[63] T. Gasser and G. Holzapfel, *Modeling plaque fissuring and dissection during balloon angioplasty intervention*, Annals of Biomedical Engineering, 35 (2007), pp. 711–723.

[64] T. Gasser, R. Ogden, and G. Holzapfel, *Hyperelastic modelling of arterial layers with distributed collagen fibre orientations*, Journal of the Royal Society Interface, 3 (2006), pp. 15–35.

[65] D. Gastaldi, S. Morlacchi, R. Nichetti, C. Capelli, G. Dubini, L. Petrini, and F. Migliavacca, *Modelling of the provisional side-branch stenting approach for the treatment of atherosclerotic coronary bifurcations: Effects of stent positioning*, Biomechanics and Modeling in Mechanobiology, 9 (2010), pp. 551–561.

[66] D. Gastaldi, V. Sassi, L. Petrini, M. Vedani, S. Trasatti, and F. Migliavacca, *Continuum damage model for bioresorbable magnesium alloy devices - application to coronary stents*, Journal of the Mechanical Behavior of Biomedical Materials, 4 (2011), pp. 352–365.

[67] F. Gervaso, C. Capelli, L. Petrini, S. Lattanzio, L. Di Virgilio, and F. Migliavacca, *On the effects of different strategies in modelling balloon-expandable stenting by means of finite element method*, Journal of Biomechanics, 41 (2008), pp. 1206–1212.

[68] G. Giannoglou, A. Antoniadis, K. Koskinas, and Y. Chatzizisis, *Flow and atherosclerosis in coronary bifurcations*, EuroIntervention, 6 (2010), pp. J16–J23.

[69] F. Gijsen, F. Migliavacca, S. Schievano, L. Socci, L. Petrini, A. Thury, J. Wentzel, A. van der Steen, P. Serruys, and G. Dubini, *Simulation of stent deployment in a realistic human coronary artery*, BioMedical Engineering Online, 7 (2008).

[70] W. Gomes and E. Buffolo, *Coronary stenting and inflammation: Implications for further surgical and medical treatment*, Annals of Thoracic Surgery, 81 (2006), pp. 1918–1925.

[71] N. Gonzalo, H. Garcia-Garcia, E. Regar, P. Barlis, J. Wentzel, Y. Onuma, J. Ligthart, and P. Serruys, *In vivo assessment of high-risk coronary plaques at bifurcations with combined intravascular ultrasound and optical coherence tomography*, JACC: Cardiovascular Imaging, 2 (2009), pp. 473–482.

[72] N. Grabow, C. Bunger, K. Steinberg, S. Mews, K. Schmohl, and K. Schmitz, *Mechanical properties of a biodegradable balloon-expandable stent from poly(l-lactide) for peripheral vascular applications*, Journal of Medical Devices, Transactions of the ASME, 1 (2007), pp. 84–88.

[73] N. Grabow, M. Schlun, K. Sternberg, N. Hakansson, S. Kramer, and K. Schmitz, *Mechanical properties of laser cut poly(l-lactide) micro-specimens: Implications for stent design, manufacture, and sterilization*, Journal of Biomechanical Engineering, 127 (2005), pp. 25–31.

[74] I. Gradus-Pizlo, B. Bigelow, Y. Mahomed, S. Sawada, K. Rieger, and H. Feigenbaum, *Left anterior descending coronary artery wall thickness measured by high-frequency transthoracic and epicardial echocardiography includes adventitia*, American Journal of Cardiology, 91 (2003), pp. 27–32.

[75] M. Grassi, G. Pontrelli, L. Teresi, G. Grassi, L. Comel, A. Ferluga, and L. Galasso, *Novel design of drug delivery in stented arteries: A numerical comparative study*, Mathematical Biosciences and Engineering, 6 (2009), pp. 493–508.

[76] J. Grogan, B. O'Brien, S. Leen, and P. McHugh, *A corrosion model for bioabsorbable metallic stents*, Acta Biomaterialia, 7 (2011), pp. 3523–3533.

[77] P. Grottum, A. Svindland, and L. Walloe, *Localization of atherosclerotic lesions in the bifurcation of the main left coronary artery*, Atherosclerosis, 47 (1983), pp. 55–62.

[78] M. Grundeken, P. Stella, and J. Wykrzykowska, *Why the provisional single-stent approach is not always the right strategy; arguments for the development of dedicated bifurcation devices*, EuroIntervention, 7 (2012), pp. 1249–1253.

[79] P. Guerin, P. Pilet, G. Finet, Y. Goueffic, J. N'Guyen, D. Crochet, I. Tijou, P. Pacaud, and G. Loirand, *Drug-eluting stents in bifurcations: Bench study of strut deformation and coating lesions*, Circulation: Cardiovascular Interventions, 3 (2010), pp. 120–126.

[80] T. Gundert, A. Marsden, W. Yang, D. Marks, and J. LaDisa Jr, *Identification of hemodynamically optimal coronary stent designs based on vessel caliber*, IEEE Transactions on Biomedical Engineering, 59 (2012), pp. 1992–2002.

[81] T. Gundert, S. Shadden, A. Williams, B. Koo, J. Feinstein, and J. Ladisa Jr, *A rapid and computationally inexpensive method to virtually implant current and next-generation stents into subject-specific computational fluid dynamics models*, Annals of Biomedical Engineering, 39 (2011), pp. 1423–1437.

[82] M. Gyongyosi, P. Yang, A. Khorsand, and D. Glogar, *Longitudinal straightening effect of stents is an additional predictor for major adverse cardiac events*, Journal of the American College of Cardiology, 35 (2000), pp. 1580–1589.

[83] G. Hall and E. Kasper, *Comparison of element technologies for modeling stent expansion*, Journal of Biomechanical Engineering, 128 (2006), pp. 751–756.

[84] F. Harewood, J. Grogan, and P. McHugh, *A multiscale approach to failure assessment in deployment for cardiovascular stents*, Journal of Multiscale Modeling, 2 (2010), pp. 1–22.

[85] F. Harewood and P. McHugh, *Modeling of size dependent failure in cardiovascular stent struts under tension and bending*, Annals of Biomedical Engineering, 35 (2007), pp. 1539–1553.

[86] I. Hariton, G. deBotton, T. Gasser, and G. Holzapfel, *Stress-modulated collagen fiber remodeling in a human carotid bifurcation*, Journal of Theoretical Biology, 248 (2007), pp. 460–470.

[87] H. Henninger, S. Reese, A. Anderson, and J. Weiss, *Validation of computational models in biomechanics*, Proceedings of the Institution of Mechanical Engineers, Part H: Journal of Engineering in Medicine, 224 (2010), pp. 801–812.

[88] Hibbit, Karlsson, and Sorensen, *Theory manual*, Abaqus 6-10 Documentation, (Abaqus Inc., RI, USA).

[89] D. Hildick-Smith, J. Lassen, R. Albiero, T. Lefevre, O. Darremont, M. Pan, M. Ferenc, G. Stankovic, and Y. Louvard, *Consensus from the 5th european bifurcation club meeting*, EuroIntervention, 6 (2010), pp. 34–38.

[90] H. Himburg, D. Grzybowski, A. Hazel, J. LaMack, X.-M. Li, and M. Friedman, *Spatial comparison between wall shear stress measures and porcine arterial endothelial permeability*, American Journal of Physiology - Heart and Circulatory Physiology, 286 (2004), pp. H1916–H1922.

[91] Y. Hoi, Y.-Q. Zhou, X. Zhang, R. Henkelman, and D. Steinman, *Correlation between local hemodynamics and lesion distribution in a novel aortic regurgitation murine model of atherosclerosis*, Annals of Biomedical Engineering, 39 (2011), pp. 1414–1422.

[92] G. Holzapfel, G. Sommer, C. Gasser, and P. Regitnig, *Determination of layer-specific mechanical properties of human coronary arteries with nonatherosclerotic intimal thickening and related constitutive modeling*, American Journal of Physiology - Heart and Circulatory Physiology, 289 (2005), pp. H2048–H2058.

[93] G. Holzapfel, M. Stadler, and T. Gasser, *Changes in the mechanical environment of stenotic arteries during interaction with stents: Computational assessment of parametric stent designs*, Journal of Biomechanical Engineering, 127 (2005), pp. 166–180.

[94] D. Hose, A. Narracott, B. Griffiths, S. Mahmood, J. Gunn, D. Sweeney, and P. Lawford, *A thermal analogy for modelling drug elution from cardiovascular stents.*, Computer methods in biomechanics and biomedical engineering, 7 (2004), pp. 257–264.

[95] A. Hoye, C. Van Mieghem, A. Ong, J. Aoki, G. Granillo, M. Valgimigli, K. Tsuchida, G. Sianos, E. McFadden, W. Van Der Giessen, P. De Feyter, R. Van Domburg, and P. Serruys, *Percutaneous therapy of bifurcation lesions with drug-eluting stent implantation: The culotte technique revisited*, International Journal of Cardiovascular Interventions, 7 (2005), pp. 36–40.

[96] Y. Huo, G. Finet, T. Lefevre, Y. Louvard, I. Moussa, and G. Kassab, *Which diameter and angle rule provides optimal flow patterns in a coronary bifurcation?*, Journal of Biomechanics, 45 (2012), pp. 1273–1279.

[97] C. Hwang, D. Wu, and E. Edelman, *Physiological transport forces govern drug distribution for stent-based delivery*, Circulation, 104 (2001), pp. 600–605.

[98] I. Iakovou, L. Ge, and A. Colombo, *Contemporary stent treatment of coronary bifurcations*, Journal of the American College of Cardiology, 46 (2005), pp. 1446–1455.

[99] I. Iakovou, T. Schmidt, E. Bonizzoni, L. Ge, G. Sangiorgi, G. Stankovic, F. Airoldi, A. Chieffo, M. Montorfano, M. Carlino, I. Michev, N. Corvaja, C. Briguori, U. Gerckens, E. Grube, and A. Colombo, *Incidence, predictors and outcome of thrombosis after succesful implantation of drug-eluting stents*, Journal of the American Medical Association, 293 (2005), pp. 2126–2130.

[100] M.-H. Jim, H.-H. Ho, A.-O. Chan, and W.-H. Chow, *Stenting of coronary bifurcation lesions by using modified crush technique with double kissing balloon inflation (sleeve technique): Immediate procedure result and short-term clinical outcomes*, Catheterization and Cardiovascular Interventions, 69 (2007), pp. 969–975.

[101] B. Johnston, P. Johnston, S. Corney, and D. Kilpatrick, *Non-newtonian blood flow in human right coronary arteries: Steady state simulations*, Journal of Biomechanics, 37 (2004), pp. 709–720.

[102] A. Kaplan and H. Davis, *Tryton side-branch stent*, Eurointervention, 2 (2006), pp. 270–271.

[103] G. Kassab, *Functional hierarchy of coronary circulation: Direct evidence of a structure-function relation*, American Journal of Physiology - Heart and Circulatory Physiology, 289 (2005), pp. H2559–H2565.

[104] R. Keane and R. Adrian, *Theory of cross-correlation analysis of piv images*, Applied Scientific Research, 49 (1992), pp. 191–215.

[105] Y.-H. Kim, D.-W. Park, I.-W. Suh, J.-S. Jang, E.-S. Hwang, Y.-H. Jeong, S.-W. Lee, S.-W. Lee, W. Cheol, M.-K. Hong, J.-J. Kim, S.-W. Park, and S.-J. Park, *Long-term outcome of simultaneous kissing stenting technique with sirolimus-eluting stent for large bifurcation coronary lesions*, Catheterization and Cardiovascular Interventions, 70 (2007), pp. 840–846.

[106] D. Kiousis, A. Wulff, and G. Holzapfel, *Experimental studies and numerical analysis of the inflation and interaction of vascular balloon catheter-stent systems*, Annals of Biomedical Engineering, 37 (2009), pp. 315–330.

[107] V. Kolachalama, E. Levine, and E. Edelman, *Luminal flow amplifies stent-based drug deposition in arterial bifurcations*, PLoS ONE, 4 (2009).

[108] K. Koskinas, Y. Chatzizisis, A. Antoniadis, and G. Giannoglou, *Role of endothelial shear stress in stent restenosis and thrombosis: Pathophysiologic mechanisms and implications for clinical translation*, Journal of the American College of Cardiology, 59 (2012), pp. 1337–1349.

[109] R. Krams, J. Wentzel, J. Oomen, R. Vinke, J. Schuurbiers, P. De Feyter, P. Serruys, and C. Slager, *Evaluation of endothelial shear stress and 3d geometry as factors determining the development of atherosclerosis and remodeling in human coronary arteries in vivo: Combining 3d reconstruction from angiography and ivus (angus) with computational fluid dynamics*, Arteriosclerosis, Thrombosis, and Vascular Biology, 17 (1997), pp. 2061–2065.

[110] D. Ku, *Blood flow in arteries*, Annual Review of Fluid Mechanics, 29 (1997), pp. 399–434.

[111] D. Ku, D. Giddens, C. Zarins, and S. Glagov, *Pulsatile flow and atherosclerosis in the human carotid bifurcation. positive correlation between plaque location and low and oscillating shear stress*, Arteriosclerosis, 5 (1985), pp. 293–302.

[112] B. Kumar and L. Hassebrook, *Performance-measures for correlation filters*, Applied optics, 29 (1990), pp. 2997–3006.

[113] A. Latib and A. Colombo, *Management of bifurcation lesions*, Controversies and Consensus in Imaging and Intervention, 5 (2007), p. C212.

[114] A. Latib and A. Colombo, *Bifurcation disease. what do we know, what should we do?*, JACC: Cardiovascular Interventions, 1 (2008), pp. 218–226.

[115] M. Lederlin, J. Thambo, V. Latrabe, O. Corneloup, H. Cochet, M. Montaudon, and F. Laurent, *Coronary imaging techniques with emphasis on ct and mri*, Pediatric Radiology, 41 (2011), pp. 1516–1525.

[116] J. Lee and N. Smith, *The multi-scale modelling of coronary blood flow*, Annals of Biomedical Engineering, In press (2012), pp. 1–15.

[117] S.-W. Lee, L. Antiga, and D. Steinman, *Correlations among indicators of disturbed flow at the normal carotid bifurcation*, Journal of Biomechanical Engineering, 131 (2009).

[118] T. Lefevre, B. Chevalier, and Y. Louvard, *Is there a need for dedicated bifurcation devices?*, EuroIntervention, 6 (2010), pp. J123–J129.

[119] T. Lefevre, O. Darremont, and R. Albiero, *Provisional side branch stenting for the treatment of bifurcation lesions*, EuroIntervention, 6 (2010), pp. J65–J71.

[120] T. Lefevre, Y. Louvard, M. Morice, P. Dumas, C. Loubeyre, A. Benslimane, R. Premchand, N. Guillard, and J. Piechaud, *Stenting of bifurcation lesions: Classification, treatments, and results*, Catheterization and Cardiovascular Interventions, 49 (2000), pp. 274–283.

[121] R. Liao, N. Green, S. Chen, J. Messenger, A. Hansgen, B. Groves, and J. Carroll, *Three-dimensional analysis of in vivo coronary stent - coronary artery interactions*, International Journal of Cardiovascular Imaging, 20 (2004), pp. 305–313.

[122] D. Lim, S. Cho, W. Park, A. Kristensson, J. Ko, S. Al-HAssani, and H. Kim, *Suggestion of potential stent design parameters to reduce restenosis risk driven by foreshortening or dogboning due to non-uniform balloon-stent expansion*, Annals of Biomedical Engineering, 36 (2008), pp. 1118–1129.

[123] H. Loree, *Static circumferential tangential modulus of human atherosclerotic tissue*, Journal of Biomechanics, 27 (1994), pp. 195–204.

[124] Y. Louvard, M. Thomas, V. Dzavik, D. Hildick-Smith, A. Galassi, M. Pan, F. Burzotta, M. Zelizko, D. Dudek, P. Ludman, I. Sheiban, J. Lassen, O. Darremont, A. Kastrati, J. Ludwig, I. Iakovou, P. Brunel, A. Lansky, D. Meerkin, V. Legrand, A. Medina, and T. Lefevre, *Classification of coronary artery bifurcation lesions and treatments: Time for a consensus!*, Catheterization and Cardiovascular Interventions, 71 (2008), pp. 175–183.

[125] M. Lovich and E. Edelman, *Computational simulations of local vascular heparin deposition and distribution*, American Journal of Physiology - Heart and Circulatory Physiology, 271 (1996), pp. H2014–H2024.

[126] M. Magro and R. Van Geuns, *The tryton side branch stent*, EuroIntervention, 6 (2010), pp. J147–J150.

[127] M. Magro, J. Wykrzykowska, P. Serruys, C. Simsek, S. Nauta, M. Lesiak, K. Stanislawska, Y. Onuma, E. Regar, R. Van Domburg, S. Grajek, and R. Geuns, *Six-month clinical follow-up of the tryton side branch stent for the treatment of bifurcation lesions: A two center registry analysis*, Catheterization and Cardiovascular Interventions, 77 (2011), pp. 798–806.

[128] E. Maher, A. Creane, S. Sultan, N. Hynes, C. Lally, and D. Kelly, *Tensile and compressive properties of fresh human carotid atherosclerotic plaques*, Journal of Biomechanics, 42 (2009), pp. 2760–2767.

[129] A. Malek, S. Alper, and S. Izumo, *Hemodynamic shear stress and its role in atherosclerosis*, Journal of the American Medical Association, 282 (1999), pp. 2035–2042.

[130] M. Markl, F. Wegent, T. Zech, S. Bauer, C. Strecker, M. Schumacher, C. Weiller, J. Hennig, and A. Harloff, *In vivo wall shear stress distribution in the carotid artery effect of bifurcation eometry, internal carotid artery stenosis, and recanalization therapy*, Circulation: Cardiovascular Imaging, 3 (2010), pp. 647–655.

[131] R. Marrey, R. Burgermeister, R. Grishaber, and R. Ritchie, *Fatigue and life prediction for cobalt-chromium stents: A fracture mechanics analysis*, Biomaterials, 27 (2006), pp. 1988–2000.

[132] D. Martin and F. Boyle, *Computational structural modelling of coronary stent deployment: A review*, Computer Methods in Biomechanics and Biomedical Engineering, 14 (2011), pp. 331–348.

[133] A. Medina, J. Suarez de Lezo, and M. Pan, *A new classification of coronary bifurcation lesions [1] [una clasificacion simple de las lesiones coronarias en bifurcacion]*, Revista Espanola de Cardiologia, 59 (2006), p. 183.

[134] C. Meinhart, S. Wereley, and J. Santiago, *A piv algorithm for estimating time-averaged velocity fields*, Journal of Fluids Engineering, Transactions of the ASME, 122 (2000), pp. 285–289.

[135] I. Meredith, S. Worthley, R. Whitbourn, M. Webster, P. Fitzgerald, and J. Ormiston, *First-in-human experience with the medtronic bifurcation stent system*, EuroIntervention, 7 (2011), pp. 662–669.

[136] F. Migliavacca, F. Gervaso, M. Prosi, P. Zunino, S. Minisini, L. Formaggia, and G. Dubini, *Expansion and drug elution model of a coronary stent.*, Computer methods in biomechanics and biomedical engineering, 10 (2007), pp. 63–73.

[137] F. Migliavacca, L. Petrini, M. Colombo, F. Auricchio, and R. Pietrabissa, *Mechanical behavior of coronary stents investigated through the finite element method*, Journal of Biomechanics, 35 (2002), pp. 803–811.

[138] F. Migliavacca, L. Petrini, V. Montanari, I. Quagliana, F. Auricchio, and G. Dubini, *A predictive study of the mechanical behaviour of coronary stents by computer modelling*, Medical Engineering and Physics, 27 (2005), pp. 13–18.

[139] R. Mongrain, I. Faik, R. Leask, J. Rodes-Cabau, E. Larose, and O. Bertrand, *Effects of diffusion coefficients and struts apposition using numerical simulations for drug eluting coronary stents*, Journal of Biomechanical Engineering, 129 (2007), pp. 733–742.

[140] R. Mongrain, R. Leask, J. Brunette, I. Faik, N. Bulman-Feleming, and T. Nguyen, *Numerical modeling of coronary drug eluting stents*, Studies in Health Technology and Informatics, 113 (2005), pp. 443–458.

[141] J. Moore Jr, J. Soares, and K. Rajagopal, *Biodegradable stents: Biomechanical modeling challenges and opportunities*, Cardiovascular Engineering and Technology, 1 (2010), pp. 52–65.

[142] J. Moore Jr, L. Timmins, and J. Ladisa Jr, *Coronary artery bifurcation biomechanics and implications for interventional strategies*, Catheterization and Cardiovascular Interventions, 76 (2010), pp. 836–843.

[143] S. Morlacchi, C. Chiastra, D. Gastaldi, G. Pennati, G. Dubini, and F. Migliavacca, *Sequential structural and fluid dynamic numerical simulations of a stented bifurcated coronary artery*, Journal of Biomechanical Engineering, 133 (2011).

[144] S. Morlacchi, S. Colleoni, R. CÃąrdenes, C. Chiastra, J. Diez, I. Larrabide, and F. Migliavacca, *Patient-specific simulations of stenting procedures in coronary bifurcations: Two clinical cases*, Medical Engineering and Physics, (2013), pp. 1–10. Article in Press.

[145] S. Morlacchi, B. Keller, P. Arcangeli, M. Balzan, F. Migliavacca, G. Dubini, J. Gunn, N. Arnold, A. Narracott, D. Evans, and P. Lawford, *Hemodynamics and in-stent restenosis: Micro-ct images, histology, and computer simulations*, Annals of Biomedical Engineering, 39 (2011), pp. 2615–2626.

[146] S. Morlacchi and F. Migliavacca, *Modeling stented coronary arteries: Where we are, where to go*, Annals of Biomedical Engineering, (2012), pp. 1–17. Article in Press.

[147] P. Mortier, M. De Beule, G. Dubini, Y. Hikichi, Y. Murasato, and J. Ormiston, *Coronary bifurcation stenting: Insights from in vitro and virtual bench testing*, EuroIntervention, 6 (2010), pp. J53–J60.

[148] P. Mortier, M. De Beule, D. Van Loo, B. Verhegghe, and P. Verdonck, *Finite element analysis of side branch access during bifurcation stenting*, Medical Engineering and Physics, 31 (2009), pp. 434–440.

[149] P. Mortier, G. Holzapfel, M. De Beule, D. Van Loo, Y. Taeymans, P. Segers, P. Verdonck, and B. Verhegghe, *A novel simulation strategy for stent insertion and deployment in curved coronary bifurcations: Comparison of three drug-eluting stents*, Annals of Biomedical Engineering, 38 (2010), pp. 88–99.

[150] P. Mortier, D. Van Loo, M. De Beule, P. Segers, Y. Taeymans, P. Verdonck, and B. Verhegghe, *Comparison of drug-eluting stent cell size using micro-ct: important data for bifurcation stent selection.*, EuroIntervention : journal of EuroPCR in collaboration with the Working Group on Interventional Cardiology of the European Society of Cardiology, 4 (2008), pp. 391–396.

[151] A. Morton, A. Siotia, N. Arnold, P. Korgul, J. Bowles, J. Heppenstall, and J. Gunn, *Simultaneous kissing stent technique to treat left main stem bifurcation disease*, Catheterization and Cardiovascular Interventions, 69 (2007), pp. 209–215.

[152] M. Movahed, K. Kern, H. Thai, R. Ebrahimi, M. Friedman, and M. Slepian, *Coronary artery bifurcation lesions: a review and update on classification and interventional techniques*, Cardiovascular Revascularization Medicine, 9 (2008), pp. 263–268.

[153] J. Murphy and F. Boyle, *A numerical methodology to fully elucidate the altered wall shear stress in a stented coronary artery*, Cardiovascular Engineering and Technology, 1 (2010), pp. 256–268.

[154] J. Murphy and F. Boyle, *Predicting neointimal hyperplasia in stented arteries using time-dependant computational fluid dynamics: A review*, Computers in Biology and Medicine, 40 (2010), pp. 408–418.

[155] C. Murray, *The physiological principle of minimum work: I. the vascular system and the cost of blood volume*, Proceedings of the National Academy of Sciences of the United States of America, 12 (1926), pp. 207–214.

[156] G. Nakazawa, A. Finn, M. Vorpahl, E. Ladich, R. Kutys, I. Balazs, F. Kolodgie, and R. Virmani, *Incidence and predictors of drug-eluting stent fracture in human coronary artery. a pathologic analysis*, Journal of the American College of Cardiology, 54 (2009), pp. 1924–1931.

[157] G. Nakazawa, S. Yazdani, A. Finn, M. Vorpahl, F. Kolodgie, and R. Virmani, *Pathological findings at bifurcation lesions. the impact of flow distribution on atherosclerosis and arterial healing after stent implantation*, Journal of the American College of Cardiology, 55 (2010), pp. 1679–1687.

[158] M. Niemela, K. Kervinen, A. Erglis, N. Holm, S. James, H. Miettinen, J. Lassen, and L. Thuesen, *Randomized comparison of final kissing balloon dilatation versus no final kissing balloon dilatation in patients with coronary bifurcation lesions treated with main vessel stenting: The nordic-baltic bifurcation study iii*, Circulation, 123 (2011), pp. 79–86.

[159] B. O'Connell, T. McGloughlin, and M. Walsh, *Factors that affect mass transport from drug eluting stents into the artery wall*, BioMedical Engineering Online, 9 (2010).

[160] B. O'Connell and M. Walsh, *Demonstrating the influence of compression on artery wall mass transport*, Annals of Biomedical Engineering, 38 (2010), pp. 1354–1366.

[161] J. Ormiston, E. Currie, M. Webster, P. Kay, P. Ruygrok, J. Stewart, R. Padgett, and M. Panther, *Drug-eluting stents for coronary bifurcations: Insights into the crush technique*, Catheterization and Cardiovascular Interventions, 63 (2004), pp. 332–336.

[162] J. Ormiston, M. Webster, S. El Jack, P. Ruygrok, J. Stewart, D. Scott, E. Currie, M. Panther, B. Shaw, and B. O'Shaughnessy, *Drug-eluting stents for coronary bifurcations: Bench testing of provisional side-branch strategies*, Catheterization and Cardiovascular Interventions, 67 (2006), pp. 49–55.

[163] J. Ormiston, M. Webster, P. Ruygrok, J. Stewart, H. White, and D. Scott, *Stent deformation following simulated side-branch dilatation: A comparison of five stent designs*, Catheterization and Cardiovascular Interventions, 47 (1999), pp. 258–264.

[164] C. Oviedo, A. Maehara, G. Mintz, H. Araki, S. Choi, K. Tsujita, T. Kubo, H. Doi, B. Templin, A. Lansky, G. Dangas, M. Leon, R. Mehran, S. Tahk, G. Stone, M. Ochiai, and J. Moses, *Intravascular ultrasound classification of plaque distribution in left main coronary artery bifurcations where is the plaque really located?*, Circulation: Cardiovascular Interventions, 3 (2010), pp. 105–112.

[165] M. Pan, A. Medina, J. Suarez De Lezo, M. Romero, J. Segura, P. Martn, J. Suarez De Lezo, E. Hernandez, F. Mazuelos, A. Moreno, D. Pavlovic, S. Ojeda, F. Toledano, and C. Leon, *Coronary bifurcation lesions treated with simple approach (from the cordoba and las palmas [corpal] kiss trial)*, American Journal of Cardiology, 107 (2011), pp. 1460–1465.

[166] S. Pant, N. Bressloff, and G. Limbert, *Geometry parameterization and multidisciplinary constrained optimization of coronary stents*, Biomechanics and Modeling in Mechanobiology, 11 (2012), pp. 61–82.

[167] A. Papayannis and E. Brilakis, *Stent fracture: Broken stents-broken hearts*, Catheterization and Cardiovascular Interventions, 78 (2011), pp. 1106–1107.

[168] I. Pericevic, C. Lally, D. Toner, and D. Kelly, *The influence of plaque composition on underlying arterial wall stress during stent expansion: The case for lesion-specific stents*, Medical Engineering and Physics, 31 (2009), pp. 428–433.

[169] L. Petrini, F. Migliavacca, F. Auricchio, and G. Dubini, *Numerical investigation of the intravascular coronary stent flexibility*, Journal of Biomechanics, 37 (2004), pp. 495–501.

[170] T. Pflederer, J. Ludwig, D. Ropers, W. Daniel, and S. Achenbach, *Measurement of coronary artery bifurcation angles by multidetector computed tomography*, Investigative Radiology, 41 (2006), pp. 793–798.

[171] M. Piccinelli, A. Veneziani, D. Steinman, A. Remuzzi, and L. Antiga, *A framework for geometric analysis of vascular structures: Application to cerebral aneurysms*, IEEE Transactions on Medical Imaging, 28 (2009), pp. 1141–1155.

[172] R. Pietrabissa, S. Mantero, T. Marotta, and L. Menicanti, *A lumped parameter model to evaluate the fluid dynamics of different coronary bypasses*, Medical Engineering and Physics, 18 (1996), pp. 477–484.

[173] P. Poncin, C. Millet, J. Chevy, and J. Proft, *Comparing and optimizing co-cr tubing for stent applications*, Proceedings of the Materials and Processes for Medical Devices Conference, (2004).

[174] G. Pontrelli and F. de Monte, *A multi-layer porous wall model for coronary drug-eluting stents*, International Journal of Heat and Mass Transfer, 53 (2010), pp. 3629–3637.

[175] M. Prosi, K. Perktold, Z. Ding, and M. Friedman, *Influence of curvature dynamics on pulsatile coronary artery flow in a realistic bifurcation model*, Journal of Biomechanics, 37 (2004), pp. 1767–1775.

[176] A. Quarteroni and A. Veneziani, *Analysis of a geometrical multiscale model based on the coupling of odes and pdes for blood flow simulations*, Multiscale Modeling and Simulation: A SIAM Interdisciplinary Journal, 1 (2003), pp. 173–195.

[177] L. Raber, J. Heo, M. Radu, H. Garcia-Garcia, G. Stefanini, A. Moschovitis, J. Dijkstra, H. Kelbaek, S. Windecker, and P. Serruys, *Offline fusion of co-registered intravascular ultrasound and frequency domain optical coherence tomography images for the analysis of human atherosclerotic plaques*, Eurointervention, 8 (2012), pp. 98–108.

[178] L. Raber, P. Juni, L. Loffel, S. Wandel, S. Cook, P. Wenaweser, M. Togni, R. Vogel, C. Seiler, F. Eberli, T. Luscher, B. Meier, and S. Windecker, *Impact of stent overlap on angiographic and long-term clinical outcome in patients undergoing drug-eluting stent implantation*, Journal of the American College of Cardiology, 55 (2010), pp. 1178–1188.

[179] M. Raschi, F. Mut, G. Byrne, C. Putman, S. Tateshima, F. Vinuela, T. Tanoue, K. Tanishita, and J. Cebral, *Cfd and piv analysis of hemodynamics in a growing intracranialaneurysm*, International Journal for Numerical Methods in Biomedical Engineering, 28 (2012), pp. 214–228.

[180] E. Romagnoli, S. De Servi, C. Tamburino, A. Colombo, F. Burzotta, P. Presbitero, L. Bolognese, L. Paloscia, P. Rubino, G. Sardella, C. Briguori, F. Ettori, G. Franco, D. Di Girolamo, I. Sheiban, L. Piatti, C. Greco, S. Petronio, B. Loi, E. Lioy, A. Benassi, A. Patti, A. Gaspardone, D. Capodanno, G. Biondi-Zoccai, and G. Sangiorgi, *Real-world outcome of coronary bifurcation lesions in the drug-eluting stent era: Results from the 4,314-patient italian society of invasive cardiology (sici-gise) italian multicenter registry on bifurcations (i-bigis)*, American Heart Journal, 160 (2010), pp. 535–542.e1.

[181] H. Routledge, T. Lefevre, A. Colombo, K. Oldroyd, C. Hamm, G. Guagliumi, W. von Scheidt, V. Guetta, W. Ruzyllo, K. Wittebols, D. Goedhart, and P. Serruys, *Three-year clinical outcome of percutaneous treatment of bifurcation lesions in multivessel coronary artery disease with the sirolimus-eluting stent: Insights from the arterial revascularisation therapies study, part ii (arts ii)*, EuroIntervention, 5 (2009), pp. 190–196.

[182] F. Scarano, *Interative image deformation methods in piv*, Measurement Science and Technology, 13 (2002), pp. R1–R19.

[183] S. Schievano, A. Taylor, C. Capelli, P. Lurz, J. Nordmeyer, F. Migliavacca, and P. Bonhoeffer, *Patient specific finite element analysis results in more accurate prediction of stent fractures: Application to percutaneous pulmonary valve implantation*, Journal of Biomechanics, 43 (2010), pp. 687–693.

[184] J. Schmitt, D. Kolstad, and C. Petersen, *Intravascular optical coherence tomography opens a window onto coronary artery disease*, Optics and Photonics News, 15 (2004), pp. 20–25.

[185] L. Schwer, *Guide for verification and validation in computational solid mechanics*, American Society of Mechanical Engineers, (2006).

[186] T. Seo, L. Schachter, and A. Barakat, *Computational study of fluid mechanical disturbance induced by endovascular stents*, Annals of Biomedical Engineering, 33 (2005), pp. 444–456.

[187] G. Sgueglia and B. Chevalier, *Kissing balloon inflation in percutaneous coronary interventions*, JACC: Cardiovascular Interventions, 5 (2012), pp. 803–811.

[188] S. Sharma, A. Choudhury, J. Lee, M. Kim, E. Fisher, A. Steinheimer, and A. Kini, *Simultaneous kissing stents (sks) technique for treating bifurcation lesions in medium-to-large size coronary arteries*, American Journal of Cardiology, 94 (2004), pp. 913–917.

[189] C. Slager, J. Wentzel, J. Schuurbiers, J. Oomen, J. Kloet, R. Krams, C. Von Birgelen, W. Van Der Giessen, P. Serruys, and P. De Feyter, *True 3-dimensional reconstruction of coronary arteries in patients by fusion of angiography and ivus (angus) and its quantitative validation*, Circulation, 102 (2000), pp. 511–516.

[190] J. Soares, J. Moore, and K. Rajagopal, *Constitutive framework for biodegradable polymers with applications to biodegradable stents*, ASAIO Journal, 54 (2008), pp. 295–301.

[191] J. Soares, K. Rajagopal, and J. Moore Jr, *Deformation-induced hydrolysis of a degradable polymeric cylindrical annulus*, Biomechanics and Modeling in Mechanobiology, 9 (2010), pp. 177–186.

[192] G. Stankovic, O. Darremont, M. Ferenc, D. Hildick-Smith, J. Lassen, Y. Louvard, R. Albiero, M. Pan, and T. Lefevre, *Percutaneous coronary intervention for bifurcation lesions: 2008 consensus document from the fourth meeting of the european bifurcation club*, EuroIntervention, 5 (2009), pp. 39–49.

[193] D. Steinman, *Image-based computational fluid dynamics modeling in realistic arterial geometries*, Annals of Biomedical Engineering, 30 (2002), pp. 483–497.

[194] G. Stone, J. Moses, S. Ellis, J. Schofer, K. Dawkins, M. Morice, A. Colombo, E. Schampaert, E. Grube, A. Kirtane, D. Cutlip, M. Fahy, S. Pocock, R. Mehran, and M. Leon, *Safety and efficacy of sirolimus- and paclitaxel-eluting coronary stents*, New England Journal of Medicine, 356 (2007), pp. 998–1008.

[195] C. Sweeney, P. McHugh, J. McGarry, and S. Leen, *Micromechanical methodology for fatigue in cardiovascular stents*, International Journal of Fatigue, 44 (2012), pp. 202–216.

[196] H. Tahir, A. Hoekstra, E. Lorenz, P. Lawford, R. Hose, J. Gunn, and D. Evans, *Multi-scale simulations of the dynamics of in-stent restenosis: Impact of stent deployment and design*, Interface Focus, 1 (2011), pp. 365–373.

[197] L. Tan, D. Webb, K. Kormi, and S. Al-Hassani, *A method for investigating the mechanical properties of intracoronary stents using finite element numerical simulation*, International Journal of Cardiology, 78 (2001), pp. 51–67.

[198] C. Taylor and D. Steinman, *Image-based modeling of blood flow and vessel wall dynamics: Applications, methods and future directions: Sixth international bio-fluid mechanics symposium and workshop, march 28-30, 2008 pasadena, california*, Annals of Biomedical Engineering, 38 (2010), pp. 1188–1203.

[199] L. Timmins, M. Miller, F. Clubb Jr, and J. Moore Jr, *Increased artery wall stress post-stenting leads to greater intimal thickening*, Laboratory Investigation, 91 (2011), pp. 955–967.

[200] V. M. Toolkit", *http://www.vmtk.org/*, (accessed 10 December 2011).

[201] S. Tu, N. Holm, G. Koning, Z. Huang, and J. Reiber, *Fusion of 3d qca and ivus/oct.*, The international journal of cardiovascular imaging, 27 (2011), pp. 197–207.

[202] G. Vairo, M. Cioffi, R. Cottone, G. Dubini, and F. Migliavacca, *Drug release from coronary eluting stents: A multidomain approach*, Journal of Biomechanics, 43 (2010), pp. 1580–1589.

[203] A. van der Giessen, H. Groen, P. Doriot, P. de Feyter, A. van der Steen, F. van de Vosse, J. Wentzel, and F. Gijsen, *The influence of boundary conditions on wall shear stress distribution in patients specific coronary trees*, Journal of Biomechanics, 44 (2011), pp. 1089–1095.

[204] A. van der Giessen, M. Schaap, F. Gijsen, H. Groen, T. Van Walsum, N. Mollet, J. Dijkstra, F. Van De Vosse, W. Niessen, P. De Feyter, A. Van Der Steen, and J. Wentzel, *3d fusion of intravascular ultrasound and coronary computed tomography for in-vivo wall shear stress analysis: A feasibility study*, International Journal of Cardiovascular Imaging, 26 (2010), pp. 781–796.

[205] G. Van Soest, T. Goderie, E. Regar, S. Koljenovic, G. Van Leenders, N. Gonzalo, S. Van Noorden, T. Okamura, B. Bouma, G. Tearney, J. Wolter Oosterhuis, P. Serruys, and A. Van Der Steen, *Atherosclerotic tissue characterization in vivo by optical coherence tomography attenuation imaging*, Journal of Biomedical Optics, 15 (2010).

[206] J. Wentzel, J. Kloet, I. Andhyiswara, J. Oomen, J. Schuurbiers, B. De Smet, M. Post, D. De Kleijn, G. Pasterkamp, C. Borst, C. Slager, and R. Krams, *Shear-stress and wall-stress regulation of vascular remodeling after balloon angioplasty: Effect of matrix metalloproteinase inhibition*, Circulation, 104 (2001), pp. 91–96.

[207] J. Wentzel, R. Krams, J. Schuurbiers, J. Oomen, J. Kloet, W. Van Der Giessen, P. Serruys, and C. Slager, *Relationship between neointimal thickness and shear stress after wallstent implantation in human coronary arteries*, Circulation, 103 (2001), pp. 1740–1745.

[208] J. Wentzel, D. Whelan, W. Van Der Giessen, H. Van Beusekom, I. Andhyiswara, P. Serruys, C. Slager, and R. Krams, *Coronary stent implantation changes 3-d vessel geometry and 3-d shear stress distribution*, Journal of Biomechanics, 33 (2000), pp. 1287–1295.

[209] J. Westerweel, D. Dabiri, and M. Gharib, *The effect of a discrete window offset on the accuracy of cross-correlation analysis of digital piv recordings*, Experiments in Fluids, 23 (1997), pp. 20–28.

[210] J. Westerweel and F. Scarano, *Universal outlier detection for piv data*, Experiments in Fluids, 39 (2005), pp. 1096–1100.

[211] A. Williams, B. Koo, T. Gundert, P. Fitzgerald, and J. J. LaDisa, *Local hemodynamic changes caused by main branch stent implantation and subsequent virtual side branch balloon angioplasty in a representative coronary bifurcation*, Journal of Applied Physiology, 109 (2010), pp. 532–540.

[212] W. Wu, D. Gastaldi, K. Yang, L. Tan, L. Petrini, and F. Migliavacca, *Finite element analyses for design evaluation of biodegradable magnesium alloy stents in arterial vessels*, Materials Science and Engineering B: Solid-State Materials for Advanced Technology, 176 (2011), pp. 1733–1740.

[213] W. Wu, L. Petrini, D. Gastaldi, T. Villa, M. Vedani, E. Lesma, B. Previtali, and F. Migliavacca, *Finite element shape optimization for biodegradable magnesium alloy stents*, Annals of Biomedical Engineering, 38 (2010), pp. 2829–2840.

[214] S. Yazdani, J. Moore Jr, J. Berry, and P. Vlachos, *Dpiv measurements of flow disturbances in stented artery models: Adverse affects of compliance mismatch*, Journal of Biomechanical Engineering, 126 (2004), pp. 559–566.

[215] S. Yazdani, M. Nakano, F. Otsuka, F. Kolodgie, and R. Virmani, *Atheroma and coronary bifurcations: Before and after stenting*, EuroIntervention, 6 (2010), pp. J24–J30.

[216] H. Zahedmanesh, D. Kelly, and C. Lally, *Simulation of a balloon expandable stent in a realistic coronary artery-determination of the optimum modelling strategy*, Journal of Biomechanics, 43 (2010), pp. 2126–2132.

[217] S. Zhao, L. Gu, and S. Froemming, *Finite element analysis of the implantation of a self-expanding stent: Impact of lesion calcification*, Journal of Medical Devices, Transactions of the ASME, 6 (2012).

[218] P. Zunino, *Multidimensional pharmacokinetic models applied to the design of drug-eluting stents*, Cardiovascular Engineering, 4 (2004), pp. 181–191.

[219] P. Zunino, C. D'Angelo, L. Petrini, C. Vergara, C. Capelli, and F. Migliavacca, *Numerical simulation of drug eluting coronary stents: Mechanics, fluid dynamics and drug release*, Computer Methods in Applied Mechanics and Engineering, 198 (2009), pp. 3633–3644.

List of Figures

List of Tables

Summary of publications

Publications on international journals

2010

- Gastaldi D., **Morlacchi S.**, Nichetti R., Capelli C., Dubini G., Petrini L. and Migliavacca F. Modelling of the provisional side-branch stenting approach for the treatment of atherosclerotic coronary bifurcations: effects of stent positioning. *Biomechanics and Modelling in Mechanobiology.* 9(5):551-561, 2010.

2011

- **Morlacchi S.**, Keller B., Arcangeli P., Balzan M., Migliavacca F., Dubini G., Gunn J., Arnold N., Narracott A., Evans D. and Lawford P. Hemodynamics and In-stent Restenosis: Micro-CT Images, Histology and Computer Simulations. *Annals of Biomedical Engineering.* 39(10):2615-26, 2011.

- **Morlacchi S.**, Chiastra C., Gastaldi D., Pennati G., Dubini G. and Migliavacca F. Sequential Structural and Fluid Dynamic Numerical Simulations of a Stented Bifurcated Coronary Artery. *Journal of Biomechanical Engineering.* 133(12):121010, 2011.

- Dubini G et al. Trends in biomedical engineering: Focus on patient specific modeling and life support systems. *Journal of Applied Biomaterials and Biomechanics.* 9(2):109-117, 2011.

- D'Angelo C., Zunino P., Porpora A., **Morlacchi S.** and Migliavacca F. Model reduction strategies enable computational analysis of controller drug release from coronary stents. *SIAM Journal od Applied mathematics.* 71:2312, 2011.

2012

- Chiastra C., **Morlacchi S.**, Pereira S., Dubini G. and Migliavacca F. Computational fluid dynamics of stented coronary bifurcations studied with a hybrid discretization method. *European Journal of Mechanics - B/Fluids.* 35:76-84, 2012.

- Cutrí E., Zunino P., **Morlacchi S.**, Chiastra C., and Migliavacca F. Drug delivery pat-

terns for different stenting techniques in coronary bifurcations: a comparative computational study. *Biomechanics and Modelling in Mechanobiology.* Online first. Doi: 10.1007/s10237-012-0432-5.

- **Morlacchi S.** and Migliavacca F. Modelling stented coronary arteries: where we are, where to go. *Annals of biomedical engineering.* Online first. Doi: 10.1007/s10439-012-0681-6.

2013

- **Morlacchi S.**, Colleoni S.G., Cardenes R., Chiastra C., Diez J.L., Larrabide I. and Migliavacca F. Patient-specific simulations of stenting procedures in coronary bifurcations: two clinical cases. *Medical Engineering and Physics.* Submitted on July 20, 2012.

- **Morlacchi S.**, Chiastra C., Cutrí E., Zunino P., Burzotta F., Dubini G. and Migliavacca F. Stent deformation, physical stress, and drug elution obtained with provisional stenting, conventional culotte and tryton-based culotte to treat bifurcations: a virtual simulation study. *Eurointervention.* Submitted on October 1, 2012.

- Chiastra C., **Morlacchi S.**, Gallo D., Morbiducci U., Cardenes R., Larrabide I. and Migliavacca F. Computational fluid dynamic simulations of patient-specific stented coronary bifurcations. *Interface Focus.* Submitted on October 30, 2012.

Publications on conference proceedings

2011

- **Morlacchi S.**, Chiastra C., Dubini G. and Migliavacca F. Numerical analysis of the culotte stenting technique: comparison between a standard and a dedicated device. *Proceedings of the 2011 SCATh Joint Workshop on New Technologies for Computer/Robot Assisted Surgery.* July 11-13, 2011, Graz, Austria.

- Chiastra C., **Morlacchi S.**, Dubini G. and Migliavacca F. A Structural and Fluid Dynamic Approach to Investigate a New Angioplasty Balloon Dedicated to Bifurcation Lesions. *Proceedings of the 2011 SCATh Joint Workshop on New Technologies for Computer/Robot Assisted Surgery.* July 11-13, 2011, Graz, Austria.

- Cattaneo L., Chiastra C., Cutrí E., Migliavacca F., **Morlacchi S.** and Zunino P. An immersed boundary method for drug release applied to drug eluting stents dedicated to arterial bifurcations. *Proceedings of Enumath 2011 - European Conference on Numerical Mathematics and Advanced Applications.* September, 2011, Leicester, UK.

- Chiastra C., **Morlacchi S.**, Dubini G., Zunino P. and Migliavacca F. A Structural and Fluid Dynamic Approach to Design a New Tapered Balloon Dedicated to Stenting Procedure in Coronary Bifurcations. *Proceedings of Cardiovascula Fluid mechanics 2011 - from theoretical aspects to diagnostic and therapeutic support.* June 27-29, 2011, University of Cagliari, Italy.

2012

- Chiastra C., **Morlacchi S.**, Dubini G. and Migliavacca F. A comparison between stan-

dard and dedicated stents for coronary bifurcations: structural and fluid dynamic numerical simulations. *The Proceedings of the 10th International Symposium on Computer Methods in Biomechanics and Biomedical Engineering.* April 11-14, 2012, Berlin, Germany.

- Cutrí E., Zunino P., **Morlacchi S.**, Chiastra C. and Migliavacca F. Drug release in coronary bifurcation stenting. *The Proceedings of the 10th International Symposium on Computer Methods in Biomechanics and Biomedical Engineering.* April 11-14, 2012, Berlin, Germany.

List of abbreviations

0D	zero-dimensional
1D	mono-dimensional
2D	bi-dimensional
3D	three-dimensional
ASME	American society of mechanical engineering
BMS	bare metal stent
C3D8R	3D 8-nodes reduced integration brick element
CAD	computer aided design
CCA	conventional coronary angiography
CFD	computational fluid dynamics
Co-Cr	Coblat-Cromium
CRU	crush technique
CT	X-ray computed tomography
CTA	computed tomography angiography
CUL	culotte technique
DES	drug eluting stent
DPIV	digital Particle Image Velocimetry
EBC	European bifurcation club
FEM	finite element method
FKB	final kissing balloon
FKBmod	modified final kissing balloon
FKBstd	standard final kissing balloon
FSI	fluid-structure interaction
ISR	in-stent restenosis
IVUS	intra-vascular ultrasound
LAD	left anterior descending
LCA	left coronary artery
LCX	left circumflex
LM	left main
LOM	left obtuse marginal
MB	main branch

MBst	stenting of the MB
microCT	micro-computed tomography
MRI	magnetic resonance imaging
OCT	optimal coherence tomography
OSI	oscillatory shear index
PEEQ	plastic equivalent deformation
PET	polyethylene terephthalate
PIV	particle image velocimetry
PLLA	poly-l-lactic-acid
PSB	provisional side branch
RCA	right coronary artery
RPC	robust phase correlation
RRT	relative residence time
SB	side branch
SEM	scanning electron microscopy
SKS	simultaneous kissing stents
ST	sub-acute thrombosis
TAP	T after small protrusion technique
TAWSS	time-averaged wall shear stress
TI	tortuosity index
TRY-CUL	Tryton-based culotte
TST	T-stenting technique
UOD	universal outlier detection
VSS	viscous shear stress
WSS	wall shear stress